Holistic Management of Energy Storage System for Electric Vehicles

by

Eugene Kim

A dissertation submitted in partial fulfillment
of the requirements for the degree of
Doctor of Philosophy
(Computer Science and Engineering)
in The University of Michigan
2018

Doctoral Committee:

Professor Kang G. Shin, Chair
Associate Professor Ella Atkins
Professor Wei Lu
Associate Professor Thomas Wenisch

Eugene Kim

kimsun@umich.edu

ORCID iD: 0000-0002-1923-235X

To my family and friends

ACKNOWLEDGEMENTS

First, I would like to express my sincere gratitude to my advisor, Professor Kang G. Shin, for his constant support and encouragement and invaluable advice and guidance during my doctoral study. I have benefited tremendously from his vision, technical insights, and insightful comments, and more importantly, his logical and scientific thinking process, provided me with invaluable preparation for future challenges. I would also like to thank my committee members, Professor Wei Lu, Professor Ella Atkins and Professor Thomas Wenisch, for their valuable and insightful comments and feedbacks to help me improve the quality and depth of my dissertation.

I would like to especially thank my mentor and collaborator, Professor Jinkyu Lee, for guiding me during graduate study and collaborating in co-authoring conference and journal papers. I would also like to thank my collaborators in LG Chem, Dr. Wontae Cho and Dr. Changhyun Sung, for their valuable insights and feedback for my research during my graduate study and summer intership at LG Chem. I am also grateful to my many talented and friendly RTCL/cyber physical system group members, Professor Liang He, Bin Wu and Youngmoon Lee, for their kind support and collaboration in co-authoring conference papers, and other former/current members.

Finally and most importantly, my sincere gratitude goes to my family. My father, Joohyung Kim, my mother, Soohyang Lee, my sister, Haeun Kim, and my fiance, Kaitlin Keane, always gave me the unconditional love and support through this journey.

TABLE OF CONTENTS

LIST OF FIGURES

Figure

LIST OF TABLES

Table

ABSTRACT

While electric vehicles (EVs) have recently gained popularity owing to their economic and environmental benefits, they have not yet dominated conventional combustion-engine vehicles in the market. This is due mainly to their short driving range, high cost and/or quick battery performance degradation. One way to mitigate these shortcomings is to optimize the driving range and the degradation rate with a more efficient battery management system (BMS).

This dissertation explores how a more efficient BMS can extend EVs' driving range during their warranty periods. Without changing the battery capacity/size, the driving range and the degradation rate can be optimized by adaptively regulating main operational conditions: battery ambient temperature (T), the amount of transferred battery energy, discharge/charge current (I), and the range of operating voltage (min/max V). To this end, we build a real-time adaptive BMS from a cyber-physical system (CPS) perspective. This adaptive BMS calculates target operation conditions (T, I, min/max V) based on: (a) *a battery performance model* that captures the effects of operational conditions on the degradation rate and the driving range; (b) *a real-time battery power predictor*; and (c) *a temperature and discharge/charge current scheduler* to determine target battery operation conditions that guarantee the warranty period and maximize the driving range. Physical components of the CPS actuate battery control knobs to achieve the target operational conditions scheduled by the batteries cyber components of CPS. There are two sub-

components for each condition (T, I): (d) *a battery thermal management system* and (e) *a battery discharge/charge current management system* that consists of algorithms and hardware platforms for each sub-system.

This dissertation demonstrates that a more efficient real-time BMS can provide EVs with necessary energy for the specified period of time while slowing down performance degradation. Our proposed BMS adjusts temperature and discharge/charge current in real time, considering battery power requirements and behavior patterns, so as to maximize the battery performance for all battery types and drivers. It offers valuable insight into both current and future energy storage systems, providing more adaptability and practicality for various mobile applications such as unmanned aerial vehicles (UAV) and cellular phones with new types of energy storages.

CHAPTER I

Introduction

1.1 Motivation of Building a Good BMS

Electric vehicles (EVs) are gaining popularity for their environmental friendliness and potential economic benefits. Since EVs are powered by batteries, rather than fossil fuel, like internal combustion engines (ICEVs), they can reduce fuel dependency and economically harmful fuel by-products [105]. However, they have not yet replaced ICEVs for three main reasons.

First, EVs are much more expensive than ICEVs. An EV that has comparable performance to ICEVs requires a high rate of voltage and current since its powertrain must drive large motors in order to move its heavy vehicle body and load. To supply a high rate of current with high voltage, thousands of small cylindrical battery cells or hundreds/thousands of large battery pouches are connected. For example, the GM 2010 Chevy Volt requires 288 pouch Li-ion battery cells, while the Tesla Motors Model S (85 Kwh) requires 7,104 cylindrical cells. These result in an upfront price difference of thousands of dollars between similar EVs and ICEVs, lowering consumers' interest. Second, the battery capacity monotonically decreases with time, and its degradation rate is larger than that of gasoline tanks and engines in ICEVs. As a result, EVs must be equipped with enough batteries to maintain the required

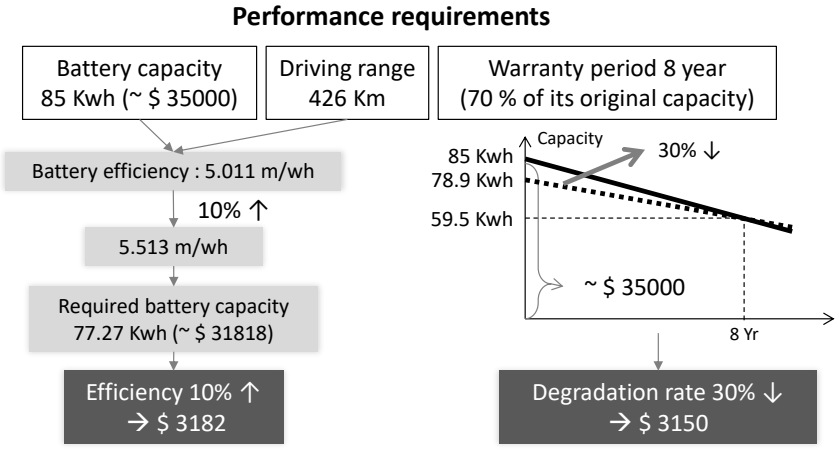

Figure 1.1: Motivation on battery cost

capacity throughout their warranty period. This capacity fast degradation may also require battery replacements for most EVs, incurring an additional (maintenance) cost. Finally, the charging infrastructure for EVs is not yet ready; while more than 120,000 gas stations in the US have been deployed, there are only 16,533 battery charging stations for EVs as of November 2017 [5, 8, 42, 107, 108].

Therefore, a large number of battery cells in EVs must be managed effectively for delivery of the required power within a desired operational range over their warranty period to address several of the challenges facing EVs. Efficient charging/discharging could reduce the required number of battery cells and the charging frequency (hence battery cost); robust cell protection/balancing could prevent battery quick capacity degradation and malfunction under extreme conditions (enhancing battery protection) [17, 72]. A more efficient BMS would better manage factors that reduce driving range and battery degradation. This would result in fewer replacement batteries, reduced charging frequency, and reduced initial and battery maintenance cost for both producers and consumers. For instance, Tesla Motors Model S (85 Kwh), which currently contains 7,104 Li-ion battery cells, guaranteed to power vehicles up to 426 km (265 miles) for eight years with unlimited miles. Figure 1.1 shows the battery ca-

pacity changes during the warranty period when it degrades constantly. This rate of degradation is typical for the current BMS. Normally, the battery should be replaced when its capacity drops below 70% of its original capacity. Hence, the manufacturer must be able to guarantee that the battery will be larger than 59.5 Khw at the end of the warranty period. In this scenario, an increase of 10% of driving range would save $3,182 of the batterys cost, because the vehicle would need fewer cells (only 6,468) to guarantee the required driving range. There could be an additional cost reduction of $3,150 with a 30% reduction in capacity degradation rate. With a reduced degradation rate, the initial battery cells (up to 6,474) operate at a higher capacity for a longer period of time, maintaining the driving range farther during the warranty period, as shown in Figure 1.1. This dissertation develops a real-time battery management framework that both extends driving range and reduces its degradation rate during the warranty period, including a hardware architecture for battery management.

1.2 Background and Related Work

This section introduces the background for building the effective BMS. We first review the factors affecting battery's driving range and its degradation rate, and then previous efforts for optimizing those factors.

1.2.1 Critical factors affecting battery efficiency and its degradation

Battery efficiency and degradation depend on the operating conditions, such as temperature (T), dis/charge current (I_c, I_d) and operating voltage range (V_c, V_d).

Discharge/charge current effects

Among the various reasons for battery performance degradation, the discharge/charge current (I_d, I_c) is the most critical [85, 63]. Continuous exposure to high discharge

current leads to extensive energy consumption and capacity degradation rate, thereby deteriorating battery performance. However, high discharge/charge current is often inevitable, because EVs require large power requirements (power supplement) to power the motor, especially during acceleration, and store energy from the regenerative braking system (RBS) when vehicles decelerate. Hence, most EVs estimate a power capability, how much power the battery can supply and accommodate, during driving, and limit the accelerations requiring high power and/or regenerating power from RBS. To mitigate discharge/charge stress affecting the battery capacity and life without limiting power requirement and energy generations from RBS, researchers have focused on hybrid energy storage systems (HESSes) built with two or more types of energy storage devices. The main principle of HESS is to use the power-dense battery including ultra-capacitor (UC) as an energy buffer to smooth rapid power fluctuations in and out of the battery of an EV [25, 65, 109, 111, 114]. High-energy batteries supply the average power required to operate vehicles, while power-dense batteries provide the sudden power surges required for acceleration and also accommodate instantaneous regenerative energy from the RBS.

Thermal effects

Temperature is another critical factor in the design and operation of EV's batteries [13, 32, 63, 85]. Temperature (T) can alter the battery's efficiency due to the dependence of the chemical reaction rate on the absolute temperature. As a rough approximation, for many reactions happening at around room temperature, the rate of reaction doubles for every 10 ^oC rise in temperature, improving battery efficiency. However, if the battery is used continuously at a high temperature, the performance degradation rate will also increase due to the accelerated side chemical reactions. Extremely low temperatures may lead to lower reaction rates and ion mobility, thereby

resulting in low energy capacity and a severe voltage drop. Existing BMSes have thus employed thermal management policies to prevent battery cells from very high and low temperatures which may result in capacity degradation and malfunction, respectively. A BMS monitors the temperature of battery cells and triggers the thermal control when temperature deviates from the normal operational range (note that the normal operation range of battery cells can be determined by thoroughly testing battery cells' performance in thermal chambers) via "thermal fins", an "air cooling system", or a "liquid coolant system" [35, 70, 99, 115]. This control includes both cooling and heating, and existing controls and systems are all or nothing. To cool the battery, the radiator is used to transfer heat from the fluid inside the battery to the air outside, thereby cooling the fluid, which, in turn, cools the battery [99]. To heat the battery, an electric heater is embedded in vehicles to heat the coolant. GM's Chevy Volt uses 144 thermal fins to cool/heat 288 lithium-ion cells with a coolant flow valve controlling cooled/heated coolant flows [99].

Voltage effects

The operating battery voltage range, also, significantly affects battery efficiency and degradation rate. The maximum amount of energy the battery can store is determined by the minimum discharged voltage (V_d) and maximum charged voltages (V_c). If the voltage range is extended, we can use more extended capacity of batteries because we can store more energy in the battery within the extended voltage range. However, the extension of operating voltage range accelerates battery degradation. According to the experimental results in some literature, the most damaging conditions are the high charge cut-off voltage and the charging period at a high voltage [84, 140]. Therefore, battery manufacturers test the batteries for various voltage ranges to optimize them given performance requirements such as the required battery

warranty period and charge capacity. Then, the BMS maintains batteries within the recommended voltage range during the battery pack operates.

1.2.2 Conventional BMS

Battery management is crucial because batteries in EVs must power the motors and other devices efficiently without severe damages within the specific operation ranges. A standard procedure for BMS designers, especially in automotive industry, is to (i) test and evaluate battery energy capacity degradation and internal resistance in different operating environments, and tabulate the battery performance parameters along with the associated operating conditions; (ii) based on these parameters, determine efficient and safe operating conditions within which the batteries can power the system without suffering fast capacity degradation or quick internal resistance increase; and (iii) estimate battery states and operating conditions to keep the batteries efficient and safe after their release.

However, every vehicle operates under different conditions, including temperature, voltage discharge/charge-rate, and at different locations or by different drivers throughout its warranty period. Also, every battery has different properties and may show different efficiency and degradation characteristics [56]. So, the battery operating condition bounds based on the battery degradation pattern identified offline may not be effective for all battery systems, thus necessitating online construction of a battery degradation model that captures the impact of operating conditions [91].

1.3 Dissertation Goal and Overview

The goal of this dissertation is to design a more effective BMS that improves battery pack performance, 1) maximizing the usable energy capacity of the battery pack and 2) lowering the battery performance degradation rate within the EVs warranty

period. With a larger energy capacity, the same number of batteries extends the driving range. The battery warranty period is defined as the duration (measured in the number of cycles or elapsed time) of a rechargeable battery until it degrades irreversibly to 70% of its initial capacity and cannot hold a useful capacity. By increasing individual battery's warranty period, the high cost of replacing a battery within the EV's warranty period is reduced. Slowing the capacity degradation of batteries can reduce the overall cost of purchasing and maintaining EVs, both for producers and consumers. Improved battery capacity may also result in additional battery cost savings, like reduction in the number of battery cells required, which further reduces EV costs.

Thus, this dissertation has built a holistic BMS for the optimization dynamic & adaptive battery operating conditions as shown in Fig. 1.2. Unlike the conventional BMS, the proposed BMS must be able to (i) diagnose batteries and identify their degradation rate with respect to the operating conditions; (ii) estimate the battery power requirement for electric loads and supply from energy sources; (iii) optimize the operating conditions (T, V_c, V_d, I_c, I_d) for supplying the required power and accommodating the regenerated power to maximize battery efficiency during the warranty period; and (iv) control the operating conditions to achieve the optimized conditions. This dissertation not only proposes optimal algorithms for determining battery operating conditions but also implements hardware circuits and relevant control algorithms to realize the optimizations.

1.4 Dissertation Organization

The disseration is organized as follows. Chapter II examines how to estimate the required conditions/power to accurately predict an EV's power requirement in real

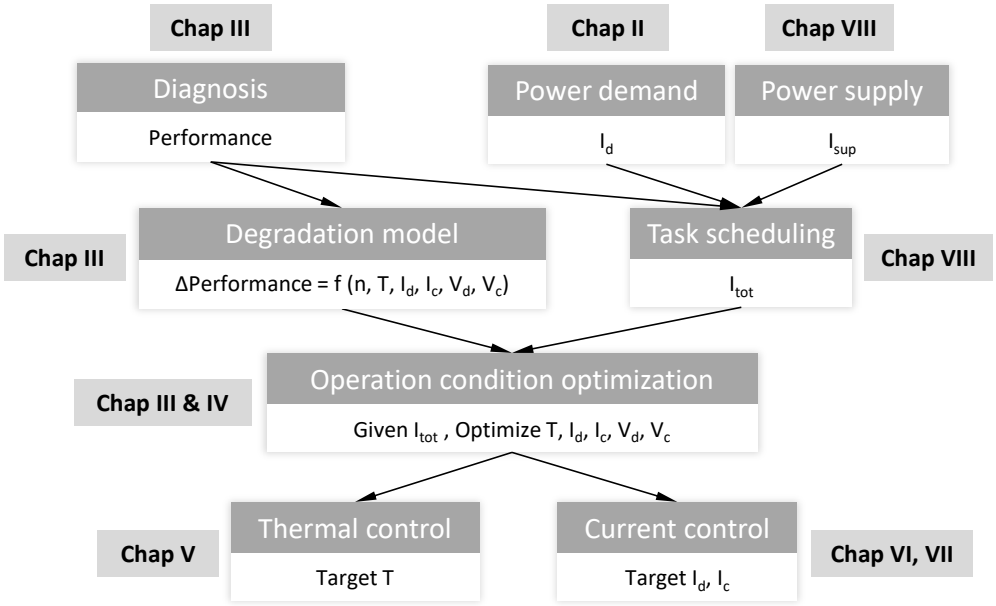

Figure 1.2: Overall approach and thesis organization

time. This prediction enables the BMS to keep cells within their operating limits and schedule battery cells to be discharged and recharged more effectively while balancing them. Chapter III and Chapter IV describe the process to model battery behavior based on the required power and temperature conditions. Based on the power requirement prediction and the battery's behavior model, Chapter IV also describes how to determine optimal discharge-rate and temperature for better battery management. Chapter V first analyzes the effect of temperature on the basic operation of a battery cell, and then shows how the effect can cause thermal and general problems, e.g., a thermal runaway that results in the explosion of battery cells, and unbalanced state of charge (SoC) which degrades battery cells' performance. Based on this understanding of thermal behavior, we finally develop temperature control approaches and a battery thermal management system. Chapter VI and Chapter VII first explore a contemporary energy storage system for EVs to capture the physical dynamics that affect the battery discharge/charge rate. Based on this

understanding of the effects of discharge/charge rate in an energy storage system, we devise control knobs to manipulate the discharge/charge rate. Then, we design an adaptive algorithm that manages the discharge/charge rate, reconfiguring the energy storage architecture. Chapter VIII develops a power scheduling framework for a reliable energy storage system with multiple power-supply sources and multiple power-demand operations. First, we provide an offline power-supply guarantee such that every power-demand operation completes its execution in time while the sum of power required by individual operations does not exceed the total power supplied by the entire energy storage system at any time. Second, we propose online power management that efficiently utilizes the surplus power (available at run-time) for system performance improvement. Chapter IX concludes this dissertation and outlines future directions for BMSes.

CHAPTER II

Real-Time Prediction of Battery Power Requirements for Electric Vehicles

2.1 Introduction

An effective battery management system (BMS) is a must in addressing the above-mentioned challenges of EVs in Chapter I. To do this efficiently, processing units in the BMSes need accurate and appropriate physical state information around/in the battery cells. While existing approaches assume that the physical states, such as the cell discharging rate (i.e., the required EV load), are constant or change slowly with time [72, 80], this assumption is not realistic as EVs' power requirements usually change abruptly and significantly. That is, simple measurement of past power consumption cannot accurately predict power demands in future for efficient battery management. Furthermore, the calculation of power requirement should be done fast and used to (re)configure the connection of battery cells; otherwise, the calculated power requirement may become obsolete at the time of its use for battery management. It is therefore necessary for the BMS to predict the power requirement accurately and in real time.

The main goal of this chapter is to develop a systematic way of accurately predicting an EV's power requirement in *real time*, which will then enable the BMS to keep cells within their operating limits and schedule battery cells to be discharged and

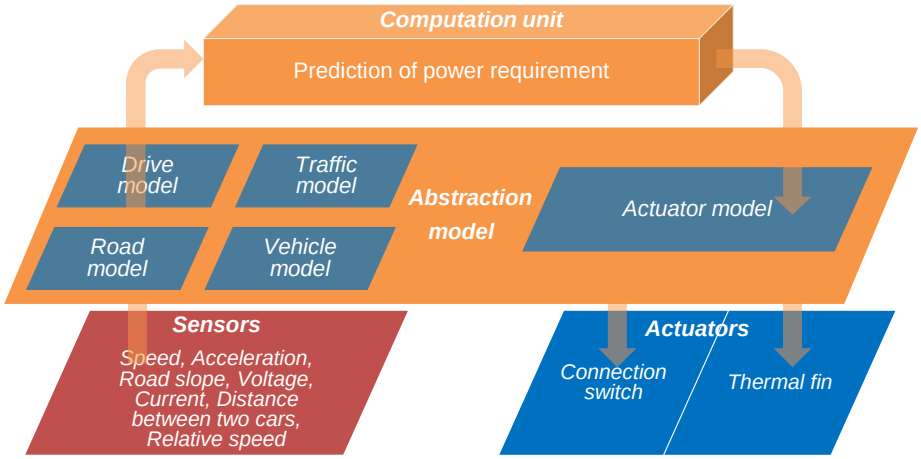

Figure 2.1: Cyber-Physical System for PRP

recharged more effectively while balancing them. To show the utility of our power requirement prediction, we also propose an advanced BMS equipped with the power requirement predictor (PRP). Note, however, that this prediction is difficult since the power requirement depends on many *physical elements* such as traffic conditions, traffic regulations, the operator's driving pattern, the vehicle's state and the road condition. Therefore, *cyber elements* in PRP that compute the power requirements should capture their coupling with the physical elements. To achieve this, we add an interface that abstracts the physical elements as shown in Fig. 2.1; the input and output of the interface are directly connected to physical components like sensors and actuators.

To facilitate the prediction of power requirements, we introduce a power requirement model with parameters that dictate the required power, and predict each parameter from the corresponding *physical* model in the abstraction layer. Although many power requirement models have been proposed, such as [22, 119, 10], we use the simple and widely-used model with real-time adaptation (i.e., history-based energy-usage model in [48]) to different vehicles and operational environments. With the model, our PRP operates as follows. First, we update the parameters in the power

requirement model according to the performance of the vehicle's physical components and structure by periodically estimating the parameters based on the driving pattern and the power demand data. Second, we pre-calculate changes in the parameters related to the road information using a pre-downloaded map. Finally, to predict the changes of acceleration, the most challenging step, we make three key observations that affect the acceleration pattern: the traffic flow, the operator's driving behavior, and the traffic regulations. Then, we develop acceleration prediction methods that address these observations, and propose a unified method that exploits the prediction methods.

Our evaluation with actual experimentation and realistic simulation demonstrates that the proposed PRP with the unified acceleration prediction method yields the actual required power more accurately than a widely-used heuristic approach by up to 69.2%.

The proposed PRP differs from other approaches in that it

- predicts the operator's driving pattern in real time;
- estimates parameters adaptively for the prediction of power requirements;
- reduces the complexity of computation; and
- reflects traffic flows, the driver's behavior, and traffic regulations.

The chapter is organized as follows. Section 2.2 presents our PRP, and Section 2.3 details the acceleration prediction schemes developed for the PRP. Section 2.4 evaluates our acceleration prediction using experimentation and simulation. Finally, the chapter concludes with Section 2.5.

	a (m/s^2)	V (m/s)	m (kg)	g (m/s^2)	K_r	α (degree)	ρ_{air} (kg/m^2)	C_d	A (m^2)
Dynamics	Extremely high	High	Extremely low	Extremely low	High	High	Low	Extremely low	Extremely low
Dependency	Driver, Road, Traffic	Driver, Road, Traffic	Vehicle structure	Altitude	Tire, Road	Road	Altitude	Vehicle structure	Vehicle structure

Table 2.1: Characteristics of parameters in the power requirement model

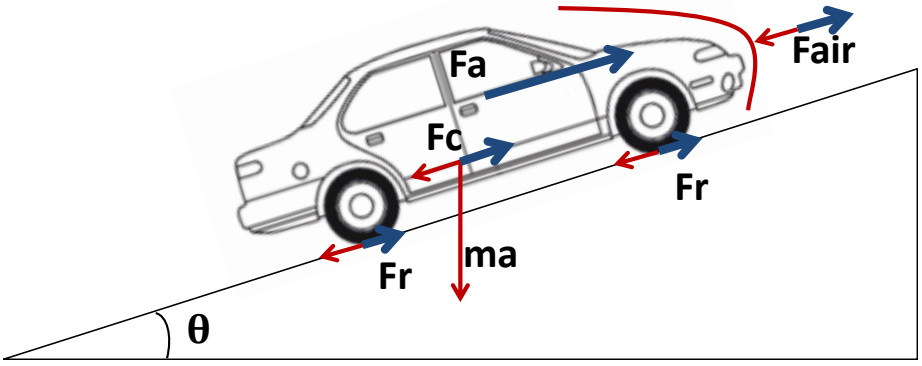

Figure 2.2: Forces in the power requirement model

2.2 Power Requirement Prediction

We first present an existing power requirement model we adopt for the power requirement predictor (PRP), and then describe how to predict all the parameters in the model. To this end, we identify the parameters' characteristics, and then use them to design the PRP. Finally, we present how the PRP is placed in an advanced BMS.

2.2.1 Power requirement model

We use a polynomial power requirement model [123] that accounts for power demand according to physical laws. Fig. 2.2 illustrates the model where F_a, F_{air}, F_c, and F_r denote, respectively, the force for acceleration, the aerodynamic force, a load related to steepness, and rolling resistance. The total power requirement (P_{total}) is then calculated as the sum of all forces multiplied by the vehicle's forward speed (V):

$$P_{total} = F_a \cdot V + F_{air} \cdot V + F_c \cdot V + F_r \cdot V$$

$$= m \cdot a \cdot V + \frac{1}{2} \cdot \rho_{air} \cdot C_d \cdot A \cdot V^3 + m \cdot g \cdot \sin\theta \cdot V + m \cdot g \cdot K_r \cdot V, \tag{2.1}$$

where θ denotes the slope angle, and all other parameters will be detailed in Section 2.2.2.

Simplicity is the primary reason for adopting this model. Since the model depends only on some physical parameters, we can obtain their actual values from measurement or calculation. Moreover, the calculation of the power requirement in Eq. (2.1) requires only basic operations, facilitating the real-time prediction of power requirements. In Section 2.4, we will show that the model, albeit simple, yields good accuracy in estimating the required power.

2.2.2 Characteristics of the model parameters

To estimate the amount of power that the BMS should provide during the next time interval, we need to predict all the parameters in Eq. (2.1). Such prediction requires the knowledge of (i) the frequency of change in each parameter and (ii) the information necessary to predict each parameter. One can then tailor prediction schemes to this knowledge. Table 2.1 summarizes the parameter characteristics which are then used to categorize the parameters as

C1. *stable*: mass of the vehicle (m), gravitational acceleration (g), air density (ρ_{air}), drag coefficients (C_d) and frontal area (A);

C2. *dynamic but easy to predict*: rolling resistance coefficient (K_r) and road slope (θ); and

C3. *dynamic and difficult to predict*: acceleration (a) and speed (V).

The parameters in C1, such as m, C_d and A, rarely change as they depend only on the vehicle itself. Also, g and ρ_{air} change very slowly. The parameters in C2 depend on the car's location on the road. We can thus accurately predict the parameters by

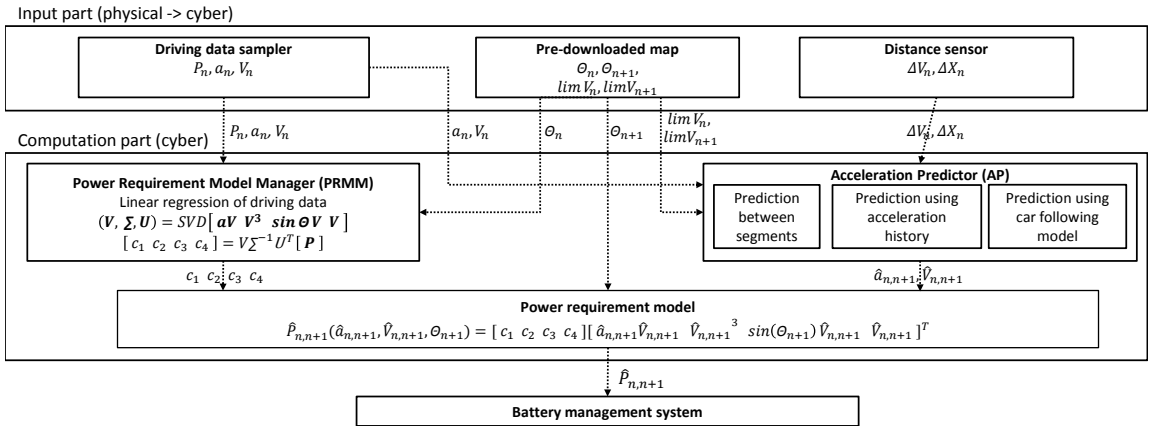

¡Notations¿ P_n, a_n, V_n: power demand, acceleration, speed *measured* at step n

$\hat{P}_{n,n+1}$, $\hat{a}_{n,n+1}$, $\hat{V}_{n,n+1}$: power demand, acceleration, speed at step $n+1$ *estimated* at step n

$\theta_n, limV_n$: road slope, speed limit at step n obtained from a pre-downloaded map

ΔV_n, ΔX_n: relative speed and distance between the leading and my cars *measured* at step n

Figure 2.3: Overall structure of the power requirement predictor (PRP)

using offline information of the roads (e.g., Google Map [6]) and real-time location information (e.g., GPS). For example, we can get the information of road type and slope *a priori* from a pre-downloaded map, thus acquiring K_r and θ for a given location. By incorporating the static information into real-time location information, we can easily predict the parameters in C2 despite their dynamic variation.

In contrast, the two parameters a and V in C3 dynamically change and are difficult to predict, since they depend not only on road information, such as the road type and slope, but also on the operator's driving pattern, which are difficult to predict and analyze. In particular, drivers have their own driving patterns related to complex human decision-making processes, and the pattern might change with their mood or physical condition. Besides, the driver should obey traffic regulations and consider traffic conditions, which significantly affect the two parameters.

As a result, we need two different approaches in predicting the parameters in C1, C2, and C3 as detailed in the next subsection.

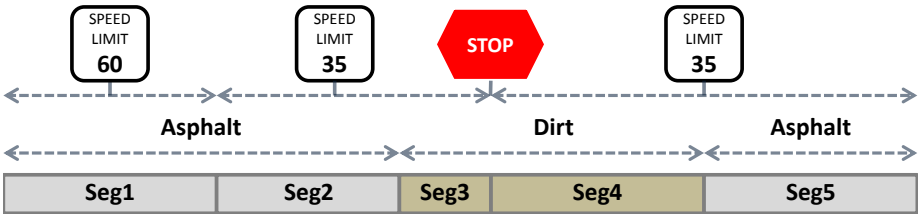

Figure 2.4: Example of road segmentation

2.2.3 Design of the power requirement predictor

Here we present the design of PRP. As shown in Fig. 2.3, PRP estimates the next (step $n+1$) power requirement during the current time interval (step n), and consists of input and computation parts. The input part provides all measured data of the current step and all pre-calculated data for the next step. Using this data, the computation part estimates all the parameters in C1–C3, and then outputs the estimated power requirement for the next step (i.e., $\hat{P}_{n,n+1}$) using the power requirement model in Eq. (2.1).

Before detailing these two parts, we first define a *road segment*, which is used for the computation part. A road segment is a continuous road interval in which road conditions and traffic regulations are uniform. Fig. 2.4 shows an example. The concept of road segment is important, since some parameters in the power requirement model vary with road segment.

The computation part estimates the parameters in two different ways. As discussed in Section 2.2.2, the parameters in C1 and C2 are either slowly changing or predictable, but the parameters in C3 are difficult to estimate. Considering the different parameter characteristics, the power requirement model manager (PRMM) and the acceleration predictor (AP) predict the parameters in C1 and C2, and those of C3, respectively, as detailed next.

The parameters in C1 change slowly, and K_r in C2 is constant within a road

segment. So, after segmentation of the road, we can abstract K_r and the parameters in C1 into four coefficients, thus reducing the number of input parameters for the power requirement model as follows.

$$P_{total}(a, V, m, g, K_r, \theta, \rho, C_d, A) = \text{the RHS of Eq. (2.1)}$$

$$\Rightarrow P_{total}(a, V, \theta) = c_1 \cdot a \cdot V + c_2 \cdot V^3 + c_3 \cdot sin\theta \cdot V + c_4 \cdot V. \tag{2.2}$$

Then, Eq. (2.2) depends only on the coefficients c_1—c_4, acceleration (a), speed (V) and road slope (θ). Since θ is given by the pre-downloaded map, we only need to estimate the coefficients, and acceleration and speed. For coefficients, PRMM adopts a popular history-based estimation—linear regression, calculating the coefficients based on the past data of all parameters in Eq. (2.2). For this, PRMM receives the current data of power requirement (P_n), acceleration (a_n), speed (V_n), and rode slope (θ_n) as shown in Fig. 2.3, and estimates the four coefficients for prediction at the next interval.

On the other hand, AP outputs acceleration and speed for the next interval, and needs additional information on the relative speed and distance between the leader and the follower cars (ΔV_n and ΔX_n) as shown in Fig. 2.3, which abstract the traffic flow. Of the two parameters a and V, we will focus on the prediction of a since we can calculate V in the next interval once we know a and V in the current interval. To predict a in the next interval, we identify factors that affect the acceleration pattern, develop schemes to address the factors, and finally combine the schemes towards a unified, effective prediction. We will detail the acceleration prediction in Section 2.3.

As shown in Fig. 2.3, the input part in PRP provides measured or pre-calculated data to PRMM, AP, or the power requirement model directly, and consists of three components: (i) the driving data sampler for the power consumption (P_n), accelera-

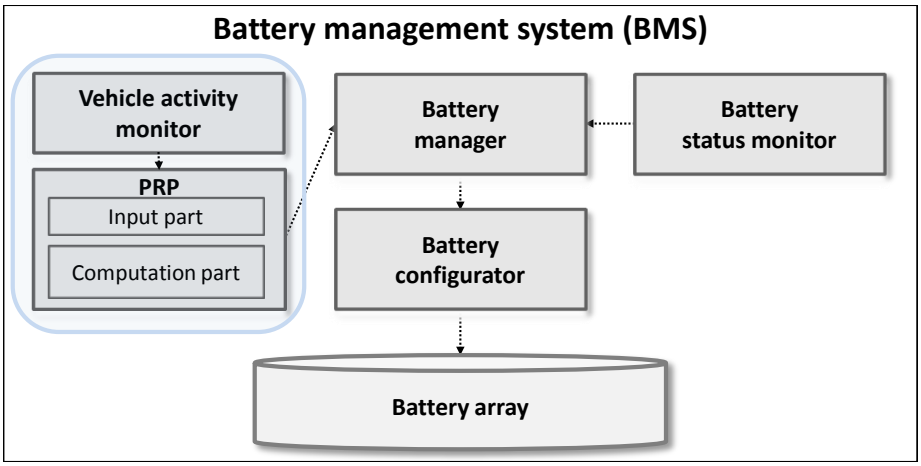

Figure 2.5: Structure of proposed BMS.

tion (a_n), and speed (V_n); (ii) the pre-downloaded map for the current and next road slopes (θ_n and θ_{n+1}), and the current and next speed limits ($limV_n$ and $limV_{n+1}$); and (iii) the distance sensor for the relative speed and distance between the leader and the follower cars (ΔV_n and ΔX_n).

2.2.4 Advanced BMS

To manage large-scale batteries for EVs in the presence of nonlinear, complex battery dynamics [85], existing BMSes [17, 72, 80, 120, 71, 73] usually consist of the battery status monitor, the battery manager, and the battery configurator as shown in Fig. 2.5. The battery status monitor periodically reports each cell/pack's state, such as SoC (State of Charge), temperature, and open circuit voltage. Then, the battery manager calculates each cell's discharge rate and rest period, and then sends the results to the battery configurator. The configurator sets the connection of battery cells as instructed by the battery manager at the circuit level.

One of the key features of BMSes is to schedule and allocate battery cells to meet the EV's power demand in an effective and safe way. To do this, we have (in the previous subsection) developed the PRP, which forms additional parts of a

BMS as shown in Fig. 2.5. That is, the advanced BMS contains the vehicle activity monitor, which reports the vehicle's driving information, including all the variables provided by the input part. Then, the PRP in Fig. 2.3 calculates the vehicle's next power demand, which is then sent to the battery manager for more efficient and safe battery (connection) arrangement. We will briefly discuss how the proposed PRP in this chapter is placed with the advanced BMS in Section 2.5.

2.3 Acceleration Predictor

As discussed in Section 2.2, it is difficult to predict a vehicle's acceleration since it depends not only on static information such as the road type and slope as well as traffic regulations, but also on dynamic one such as the operator's driving pattern and the traffic flow near the car. For accurate acceleration prediction, we first make three key observations that affect the acceleration pattern. Then, we develop acceleration prediction schemes that account for some of these observations. Finally, we combine these prediction schemes to devise a unified acceleration prediction method.

2.3.1 Observations of acceleration pattern

We make three key observations that determine the acceleration pattern: the traffic flow around the car, the operator's driving behavior, and the traffic regulations. We also corroborate the observations with experiments. The observations will be a basis for acceleration prediction schemes to be developed in Section 2.3.2.

O1. The leader car affects the follower's acceleration pattern.

As long as car A does not pass the front car B, the average speed of A cannot exceed that of B. Therefore, as shown in Fig. 2.6,[1] the average relative speed between A and B is almost zero. If the relative speed is negative (positive), A tries to catch

[1] We obtained Figs. 2.6, 2.7 and 2.8 using the evaluation tools to be described in Section 2.4.

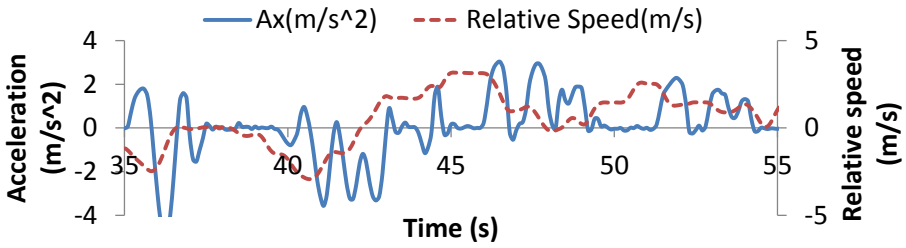

Figure 2.6: Acceleration of a car and relative speed between the car and the leader car; we chose a car and the car in front on the US-101 highway.

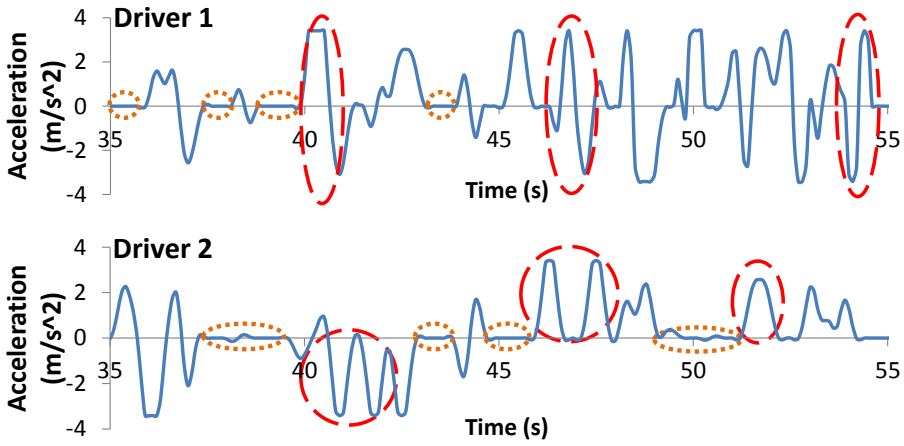

Figure 2.7: Reaction strength and time; we picked two cars on the US-101 highway.

up (distance itself from) with B by acceleration (deceleration). Therefore, the front car B determines an average behavior of the follower car A's acceleration.

O2. The operator's driving behavior affects the acceleration pattern.

We capture each operator's driving pattern with two variables: *reaction strength*—how quickly the operator/driver accelerates to achieve a desired speed, and *reaction time*—how long it takes for the driver to react to a given situation, which are represented in Fig. 2.7, respectively, by the slope of acceleration and the duration during which the acceleration is zero. For instance, some drivers press the acceleration pedal aggressively until the vehicle reaches the desired speed, but others gradually increase/decrease speed with a long acceleration time. Although the reaction strength varies with drivers, we found that the reaction strength of a driver remains

prediction methods	previous acceleration	previous acceleration with reaction strength	correlation with past accelerations	car following model	road segmentation
addressed observations	O2 (implicitly)	O2 (implicitly) and reaction strength in O2	O2 (implicitly)	O1	O3
limit to application	no limitation	no limitation	no limitation	no limitation	segment transfer
sampling rate	dependent	dependent	dependent	independent	independent
calculation cost	low	low	high	low	low
input data	a_n	a_n, reaction strength	$a_{n-q}, \cdots, a_n$	ΔV_n, ΔX_n	V_n, $limV_{n+1}$

Table 2.2: Properties of the acceleration prediction methods

similar all time. The reaction time also depends on the driver. While drivers with a long reaction time tend to maintain their vehicles' speed instead of acceleration or deceleration, others with a short reaction time immediately respond to a given situation, e.g., the front car's slowdown.

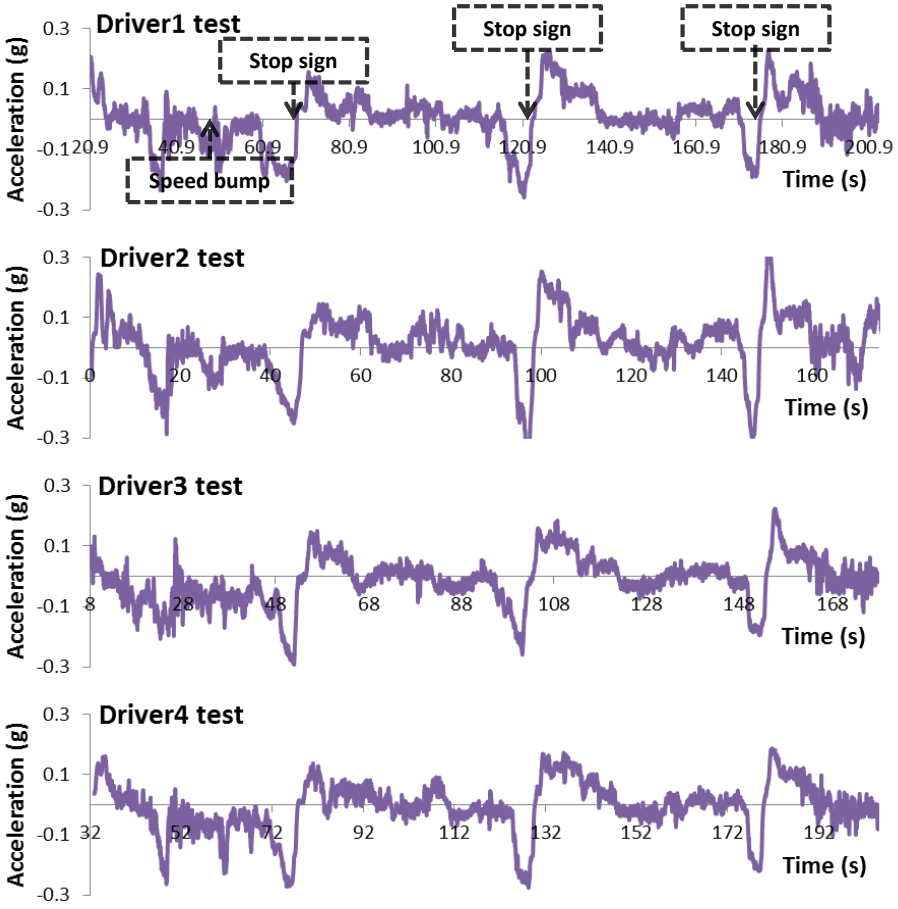

Figure 2.8: Acceleration pattern between road segments; four different drivers drove around the University of Michigan campus and the path includes three stop signs and a speed bump.

O3. The traffic regulations affect the acceleration pattern.

The traffic regulations include speed limit, traffic lights and other traffic signs, and have a great impact on acceleration. For example, every driver is supposed to decelerate at a stop sign or speed bump, and hence, this is independent of drivers as shown in Fig. 2.8. Using offline profiling of road information, we can predict the impact of traffic regulations on the acceleration pattern.

2.3.2 Acceleration prediction methods

To predict an operator's acceleration pattern, we present five methods, each with its own properties. The first three methods utilize the history of previous acceleration patterns, thus indirectly/directly addressing O2. On the other hand, the next two methods address O1 and O3, respectively, by using an existing traffic flow model and road segmentation based on traffic regulations. The five methods are summarized in Table 2.2. Considering the fact that the five methods are effective for different environments/situations, we combine them to devise a unified acceleration prediction method, exploiting advantages of the five individual methods.

Previous acceleration

In this method, the current acceleration is used as the next acceleration prediction. Its advantage is simplicity. This method, although naive, results in accurate prediction in case of slow acceleration fluctuation, or high sampling frequency with an almost zero battery reconfiguration time. However, this method alone cannot cope with abrupt changes in acceleration in many practical situations.

Previous acceleration with reaction strength

To improve the simple acceleration method that uses the previous acceleration, we incorporate the reaction strength in O2. To do this, we calculate the accelera-

tion slope when the driver starts acceleration, and use it for the next acceleration prediction as follows:

$$\hat{a}_n = a_{n-1} + k \cdot (a_{n-1} - a_{n-2}), \tag{2.3}$$

where k is the sensitivity coefficient for the acceleration slope (reaction strength). This additional consideration yields more accurate prediction than the previous acceleration method while requiring only two more basic operations.

Correlation with past accelerations

While the two history-based methods focus on the previous acceleration, this method employs a linear filter that correlates a long history of earlier accelerations with the next acceleration. For this, we first measure and record time-stamped accelerations, and then generate correlation factors based on the errors between recorded (input) and predicted accelerations. Finally, we predict the next acceleration by inner-product of the input and the correlation vectors. This method is useful when the next acceleration is highly correlated with earlier accelerations. It achieves higher accuracy than the two history-based methods at the expense of high computational complexity. Note that all history-based methods including this depend on the data sampling rate, because the higher rate can mask rapid changes of acceleration.

Car following model

Many transportation researchers studied microscopic driver behavior to describe a real traffic flow. The car following model [29, 81], a well-known microscopic traffic flow model, describes the vehicle's acceleration in terms of the relative speed and distance between a car and the leading car in front. Among existing car following models [29, 100, 14, 95], we choose the popular one in [14], which extends the classic model [29] based on the observation for optimal velocity. The main advantage of

prediction with the car following model is its independence of the sampling frequency. Although this model provides which action is needed to maintain a relative speed of zero and a constant desired distance between the two cars, it does not directly provide the vehicle's acceleration, resulting in inaccurate prediction.

Road segmentation

To address the effect of traffic regulations, we segment the road based on traffic regulations, and then predict the acceleration pattern when a car transits from a segment to another. This method enhances the accuracy of acceleration prediction between road segments; for example, if the next segment's speed limit is higher or lower than the current one, we can predict the acceleration during the segment transition by calculating of the difference in speed (limits) between the current and next segments. Since the traffic regulation information can be extracted from a pre-downloaded map, it does not depend on the data sampling frequency.

Unified prediction of acceleration

As shown in Table 2.2, each of the above methods has its own characteristics and advantages: (i) the history-based (the first three) methods depend on the sampling rate and are effective when the rate is high; (ii) the method based on the car following model is independent of the sampling rate and thus more widely applicable; and (iii) the road segmentation method is specialized for segment transition.

Considering these characteristics, we propose a unified method that predicts the acceleration in the next interval as follows: (a) when the car crosses a segment boundary, it uses the road segmentation method to predict acceleration; (b) otherwise, it predicts acceleration using a combination of methods based on acceleration history and car-following model.

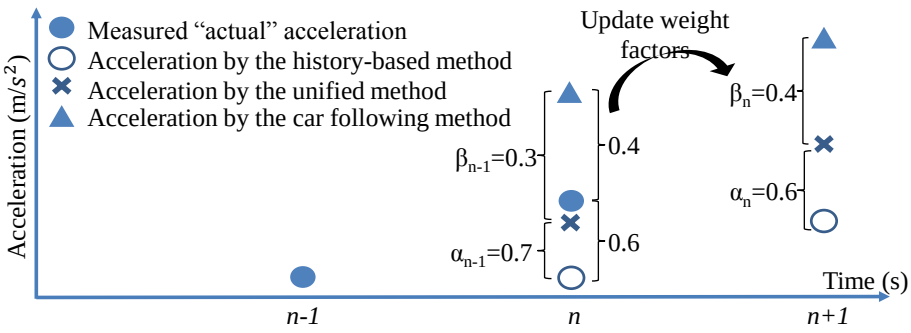

Figure 2.9: Update of the weight factors and calculation of the next acceleration using the weight factors

There are two variables that affect the decision of (b): the sampling rate and the reaction time. As to the sampling rate, the history-based methods (the method with the car following model) are more effective than the counterpart under a higher (lower) sampling rate, because the car following model guarantees the same level of accuracy even under a low sampling rate, while the prediction accuracy of the history-based methods is proportional to the sampling rate. As to the reaction time, the history-based methods are accurate for a long reaction time, because drivers with a long reaction time tend to maintain their speed. On the other hand, the acceleration by drivers with short reaction time can be described well by the car following model as the drivers react immediately to a given traffic situation.

Considering the two variables, the unified method handles the situation (b) via the weights α and β (such that $\alpha + \beta = 1$), which are respectively the weight of one of the history-based methods and that of the method with the car following model. The weights can be calculated adaptively so as to reduce the error in predicting the next acceleration. Fig. 2.9 shows an example of the process of updating the weights. Suppose that the weights at step $n-1$ are set to $\alpha_{n-1} = 0.7$ and $\beta_{n-1} = 0.3$, and the method uses them to predict the acceleration of step n. Then, at step n, the actual acceleration is different from the predicted; if the weights were $\alpha_{n-1} = 0.6$ and

$\beta_{n-1} = 0.4$, the prediction would have no error. Using this information, the method updates the weights at step n for the acceleration prediction of step $n+1$ as shown in the figure.[2] In Section 2.4 we will compare the accuracies of acceleration prediction by the unified and the other methods.

2.4 Evaluation

We now evaluate the proposed power requirement predictor. We first describe tools and settings used for the evaluation. Then, we demonstrate the accuracy of acceleration predictor (AP) and power requirement predictor (PRP).

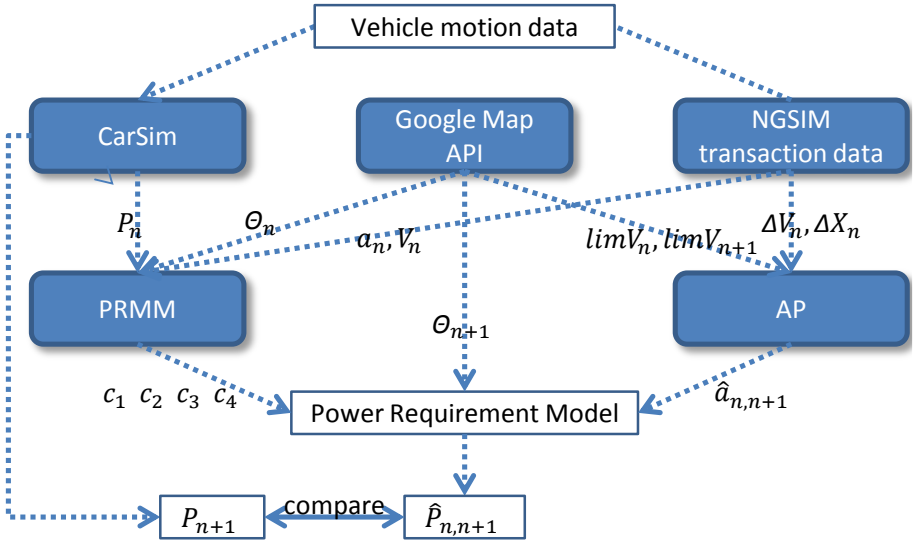

Figure 2.10: Block diagram of the PRP evaluation system

2.4.1 Evaluation tools and settings

To evaluate PRP, three types of offline/driving data are needed as inputs of PRP: (i) road information (θ, $limV$), (ii) real driving data (a, V, ΔX, ΔV), and (iii) the measured power consumption (P). We designed an emulator of PRP, which provides actual or realistic data from three popular tools as shown in Fig. 2.10: Google Maps

[2]While the unified method calculates average prediction error of x previous steps for the update of weights, we illustrate $x = 1$ for simplicity of presentation.

API [6], NGSIM [7], and CarSim [4].

Google Maps API enables developers to build map-based applications which allow us to access the road information database including the road type, the speed limit, and the elevation along with the GPS data, thus providing road information (i).

NGSIM (next generation simulation program) was initiated by the US DOT, and accompanied by a core of open behavioral algorithms in support of traffic simulation with a primary focus on microscopic modeling. NGSIM collects high-quality primary traffic and trajectory data to test new algorithms, thus providing real driving data (ii). We use the vehicle trajectory data including vehicle identification number, instantaneous velocity and acceleration of the vehicle, and distance between the front-center of a vehicle and that of the preceding vehicle.

CarSim is a vehicle model simulator that allows users to design, develop, test, and plan vehicle programs in a variety of environments. It can simulate the dynamic behavior of passenger cars, racecars, light trucks, and utility vehicles, under specified road type and slope. CarSim provides animations, and outputs the required power, which can be plotted, analyzed, and exported to other software such as MATLAB, Excel, and other optimization tools. In our emulator, CarSim receives the vehicle motion data from NGSIM, and then generates the required power, as shown in Fig. 2.10.

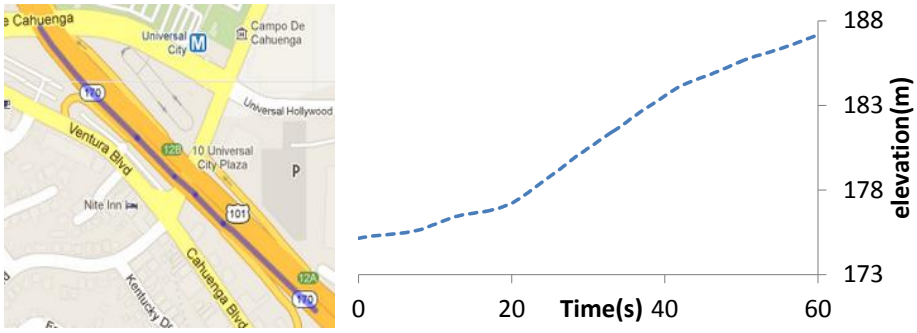

Figure 2.11: Road location and slope

For NGSIM and CarSim, we use a hatchback-type car with 205/55 R16 tires, assuming a paved road. We also assume that there is no regenerative break system, and therefore, the required power is always non-negative. For road information, we select the southbound US-101 highway in Los Angeles, CA from Google Maps API as shown in Fig. 2.11, and NGSIM tested the car on the road with traffic of June 15th, 2005.

2.4.2 Evaluation results

In this subsection, we evaluate the accuracy of AP and PRP. We first discuss hardware factors that may degrade accuracy, such as the sampling rate of the required data, the times for computing the required power and reconfiguring the connection of battery cells. All of these factors are related to manufacturing costs; if a BMS is equipped with high-performance sensors, processors, and quickly-reconfigurable systems, the undesirable effect of these factors on prediction accuracy will be reduced. However, BMS designers are required to use cheap and low-powered devices to reduce the cost and power consumption of a BMS, which will in turn lower accuracy of PRP. While the degree of inaccuracy caused by these factors varies with hardware, it is inevitable for a BMS to spend time for sensing physical data, calculating the required power, and incorporating them into the BMS. To address this latency, we abstract these factors as a sampling rate, and evaluate it with three different rates: 2Hz, 5Hz, and 10Hz.

Such a finite sampling rate causes prediction error as shown in Fig. 2.12. That is, even if PRP exactly predicted the required power for step n at step $n-1$, the required power between steps n and $n+1$ varies, resulting in some error. This also holds for acceleration prediction. So, let Opt-P (Opt-A) denote this perfect prediction of power (acceleration) with the inherent error due to the finite sampling rate.

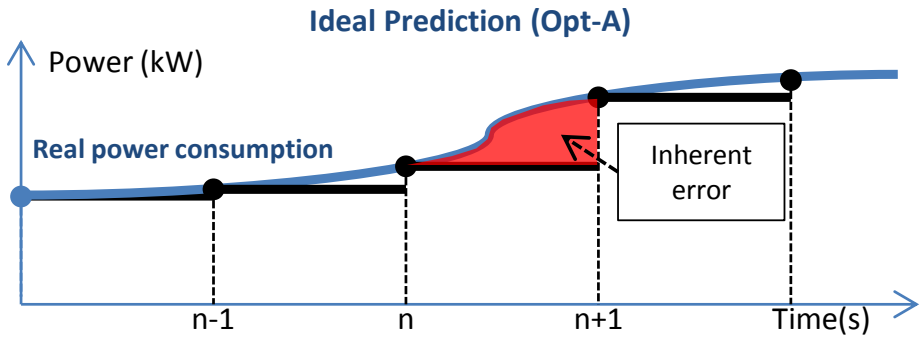

Figure 2.12: Inherent error due to finite sampling frequency

We now show the accuracy of AP and PRP with the following acceleration prediction methods, compared to Opt-A.

- Prev (previous acceleration) in Section 2.3.2,
- Prev+ (previous acceleration with reaction strength) in Section 2.3.2,
- Corr (correlation with past accelerations) in Section 2.3.2,
- CF (car following model) in Section 2.3.2,
- RS (road segmentation) in Section 2.3.2, and
- Uni(H) (the unified prediction of acceleration with one of the history-based methods, i.e., H is either Prev, Prev+, or Corr) in Section 2.3.2.

Accuracy of AP

We first compare the acceleration prediction methods when the car is within a single road segment. To evaluate the accuracy of acceleration prediction, we used the driving record produced by NGSIM, and adapted each prediction method to predict the vehicle's next acceleration. To compare the performance of each prediction method, we calculated the average of absolute prediction errors, as shown in Table 2.3. Overall, the higher sampling rate, the more accurate prediction because more information is available to predict the next acceleration. At a low sampling

rate, prediction by CF shows less prediction error since CF is the only method that is independent of the sampling rate. On the other hand, history-based acceleration predictions, such as Prev, Prev+, and Corr, performed well at a high sampling rate. Uni($\cdot$), in general, yields more accurate acceleration prediction than other methods irrespective of the sampling rate. One exception is the prediction by CF at 2Hz, because there are a limited number of driving information samples at 2Hz and then errors of Uni($\cdot$) are likely to occur during the learning of the driver's reaction.

	Average error (m/s^2)		
Prediction methods	2Hz	5Hz	10Hz
Opt-A	0.795	0.369	0.168
Prev	1.518	0.989	0.556
Prev+	1.566	1.128	0.461
Corr	1.465	1.016	0.444
CF	0.984	1.070	0.985
Uni(Prev+)	1.154	0.992	0.433
Uni(Corr)	1.162	0.948	0.448

Table 2.3: Average error of acceleration prediction

Now, we show how RS is useful when a car crosses segment boundaries. To predict the acceleration between road segments, we picked two drivers from NGSIM trajectory data. The leading car passes a traffic light just before the light turns to red, but the following car stops at the traffic light since it just turned to red. Then, we compare the accuracy of acceleration prediction with/without RS when CF is used as the baseline prediction method. Since the the following car cannot accelerate due to the traffic light, CF's prediction of the following car's acceleration shows a large average error as shown in Fig. 2.13. However, the road segmentation can provide a chance to predict acceleration accurately between different road segments as shown in the figure. The average errors of acceleration prediction are 1.912 and 1.262, respectively, for CF and CF with RS.

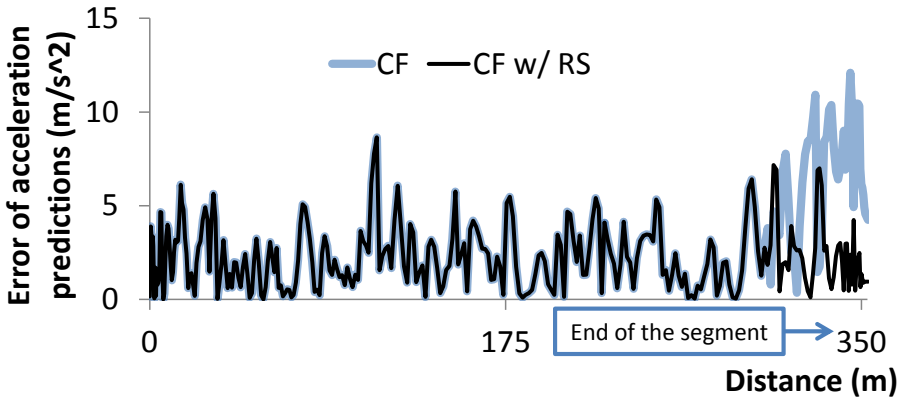

Figure 2.13: Acceleration prediction between segments

	Average error (m/s^2)		
Prediction methods	2 Hz	5 Hz	10 Hz
Opt-P	8.671	3.861	1.705
PRP with Opt-A	9.186	4.448	2.458
Actual previous power	15.884	10.461	5.904
PRP with Prev+	17.198	11.212	5.202
PRP with Corr	12.567	10.368	4.962
PRP with CF	10.464	11.006	10.630
PRP with Uni(Prev+)	12.138	10.425	4.916
PRP with Uni(Corr)	10.891	10.220	5.068

Table 2.4: Average error of power prediction

Accuracy of PRP

We first evaluate the power requirement model in Eq. (2.1). Since Opt-P and Opt-A are the most accurate power and acceleration predictions achievable for a given sampling frequency, we compare Opt-P, and PRP with Opt-A. As shown in Table 2.4, the difference in average error between the two is marginal, meaning that the power requirement model we employed yields accurate enough prediction of the required power.

Since Opt-P and Opt-A are ideal power and acceleration predictions (thus infeasible), we need to employ one of acceleration prediction methods with PRP; Table 2.4 summarizes the prediction errors, and Fig. 2.14 plots the prediction. We included one heuristic (actual previous power) that uses the current actual power consump-

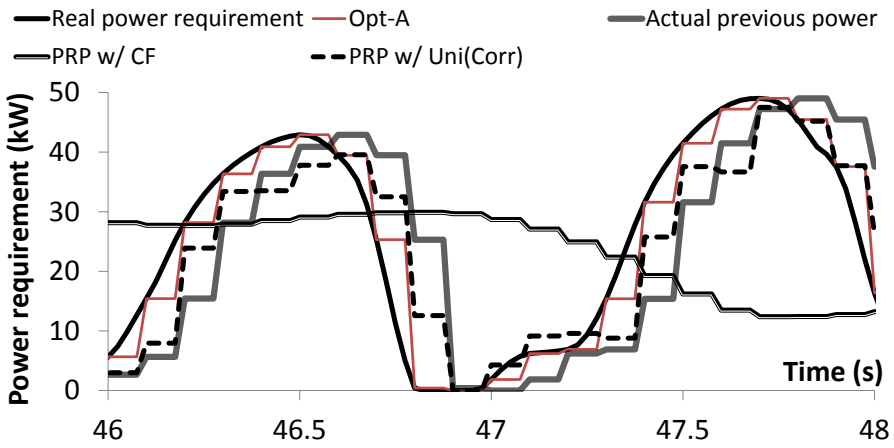

Figure 2.14: Prediction of power requirement with 10Hz sampling

tion as the next power requirement. Note that this scheme does not use our PRP. Compared to the heuristic, PRP with Uni(Corr) shows an improvement of prediction accuracy by 69.2% at 2Hz, 3.7% at 5Hz, and 19.9% at 10Hz within a road segment. If we compare PRP with different acceleration prediction methods, the trend will be similar to the accuracy of AP, because the error in predicting the power requirements is dominated by that of acceleration prediction. For example, Uni(Corr) is in general (one of) the best methods for predicting acceleration that corresponds to the required power associated with PRP. In particular, compared to PRP with CF, PRP with Uni(Corr) predicts closer to the actual required power by 11.0% at 5Hz, and 62.3% at 10Hz.

2.5 Conclusion

Increasing demand to make EVs lighter and less expensive places stringent restrictions on battery size and capacity. It is thus important to devise advanced BMS extending battery capacity without increasing its size. A number of BMSes have been proposed to exploit nonlinear battery characteristics, including recovery and rate-capacity effects.

To introduce adaptability and efficiency into existing BMSes, we have proposed the battery power requirement predictor (PRP). It predicts the amount of required battery power that enables BMSes to allocate battery cells to power EVs efficiently and safely. While recording and linearly regressing vehicle activities such as speed, acceleration, road slope and power consumption, PRP updates the (near) static parameters of the battery power requirement model for EVs. In the meantime, PRP estimates the acceleration, perhaps the most important dynamic parameter of the model, in real time, by accounting for the driver's acceleration pattern, traffic flows and regulations. Our evaluation with actual experimentation and realistic simulation has shown that PRP makes a significant improvement in acceleration prediction over a simple heuristic method often seen in the existing BMSes.

Since PRP was developed to be used in an advanced BMS in Fig. 2.5, we plan to develop a new battery manager that exploits the predicted power by PRP. We can then find how much PRP with the new battery manager can improve the life and operation time of existing BMSes. It would also be interesting to explore ways of improving PRP. For example, we can enhance the accuracy of the acceleration prediction by sensing the driver's motion on the acceleration pedal. Besides, we may employ more accurate power requirement models, such as those in [22, 119, 10]. Since these models are complex, it would be interesting to investigate how to adapt them for real-time prediction.

CHAPTER III

Adaptive Battery Diagnosis/Prognosis for Efficient Operation Control

3.1 Introduction

Battery diagnosis and prognosis — via accurate estimation of battery characteristics, such as maximum power capability and end-of-life (EOL) [88, 146, 84] — are crucial to their reliable operation [141, 91]. Therefore, battery management system (BMS) designers must test and evaluate battery performance in different operating environments. Based on the degradation patterns, BMS designer can figure out the the battery degradation model and determine efficient and safe operating conditions. The BMS estimates battery states and operating conditions to keep the batteries efficient and safe after releasing products.

The challenges in building such a battery degradation model are three-fold. First, it requires a comprehensive understanding on battery operation, which is a rather complex electro-chemical process that affects the battery's energy efficiency in many aspects. Second, most efficiency-related battery parameters change over time, and thus those dominating the battery degradation, together with their relationship with batteries' potential operating conditions (i.e., V, I, T), must be identified in real time. This is because the operating conditions affect batteries' internal reactions — and thus their efficiency and degradation — significantly, rendering battery degradation a

complex process. This makes simple battery models deficient in describing/predicting their current/future health states [91, 84]. Third, directly checking the material states of a battery is expensive and destructive, e.g., disassembling a battery pack entails additional labor and cost. An ideal battery diagnosis/prognosis system must be able to indirectly figure out the states of battery health (SOH) in a pack without taking intrusive measures nor requiring a significant amount of time, both of which degrade users' convenience and experience.

Numerous approaches have been proposed to estimate battery state-of-health (SOH) by identifying battery degradation states with non-destructive data-driven approaches [57, 88, 30, 143, 125]. Most of them assessed battery SOH in terms of energy capacity and internal resistance. Based on the degradation profiles of battery energy capacity and internal resistance under different operating conditions, they construct a degradation model as a function of operating conditions and cycles/time. Battery's energy capacity and internal resistance, albeit crucial, cannot fully represent the important parameters that affect battery SOH. The authors of [84] proposed a comprehensive degradation model based on a physical electro-chemical model and validated it in several domains. However, applying their model to the real world requires certain cell information related to the electro-chemical battery model, which is usually proprietary to cell manufactures and thus has limited availability.

In particular, we propose an adaptive battery diagnosis/prognosis system for efficient battery control via charging diagnosis and based on a newly constructed adaptive battery degradation model. This system monitors battery behaviors during charging, which are then used to estimate battery SOH. The thus-obtained SOH profiles are recorded along with the corresponding number of operation cycles and the operating conditions (V, I, T) which are used to construct a battery degradation

model. The degradation model allows the BMS to predict battery EOL (end-if-life) and search for the optimal battery operating conditions, so as to maximize battery performance within a given warranty period.

The main contributions of this chapter include:

- proposal of a diagnostic charging system that identifies and collects battery SOH information during charging;
- development of an adaptive battery degradation model which represents the relationship between the degradation rates of performance parameters and the operating conditions applicable to vehicles/mobile systems;
- prediction of battery EOL based on the constructed degradation model; and
- construction of a holistic framework for battery diagnosis/prognosis and demonstration of its efficiency via in-depth experimental evaluation.

The rest of this chapter is organized as follows. Sec. 3.2 provides the background of battery model and degradation, and Sec. 3.3 formally states our problem and solution approach. Sec. 3.4 describes how to estimate battery model parameters related to battery performance and SOH during charging. Sec. 3.5 describes the construction of battery degradation models for predicting batteries' future states and their use to predict battery EOL. Sec. 3.6 evaluates the proposed battery diagnosis/prognosis system. The chapter concludes in Sec. 3.7.

3.2 Background

We present the necessary background on battery management here.

3.2.1 Li-ion Battery Operation and Modeling

Let us first consider how battery operates during discharging and charging. When discharging a battery, Li-ions in the active materials of its negative electrode (i)

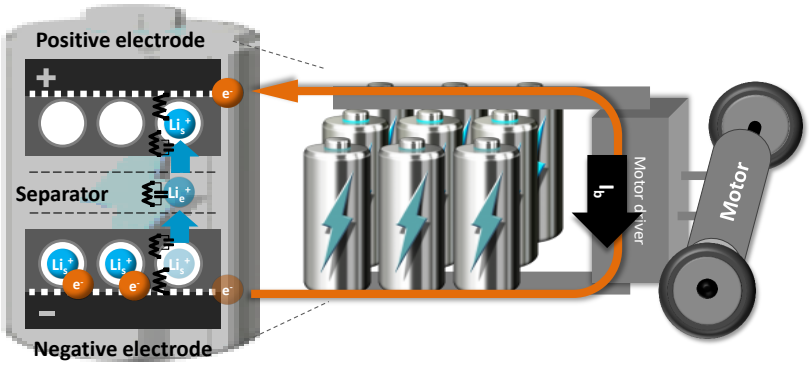

Figure 3.1: Discharging process of Li-ion batteries.

diffuse to the surface in which they move from the solid phase to the electrolyte phase; and then (ii) travel to the positive electrode where they react with, and enter inside the active material. During this process, the electrons released in the negative electrode travel through the external circuit to generate a flow of current, as shown in Fig. 3.1. This process occurring in the positive and negative electrodes will be reversed during charging. When current flows through a battery cell during discharging/charging, there are a number of factors causing its voltage drops from the equilibrium open-circuit voltage (OCV) — commonly called "overpotential", including: (i) ohmic drop due to electronic or ionic current flow (i.e., Ohm's law), (ii) concentration overpotential due to the buildup of concentration gradients in a battery, and (iii) surface overpotential needed to drive the reactions. Based on the overpotential and operating principles of battery, we develop the equivalent circuit model shown in Fig. 3.2.

Equivalent Circuit Model

Typically, a large capacitor or a dependent voltage source is used to represent the OCV; the rest of the circuit simulates (i) the battery's ohmic resistance (R_0) due to the ohmic and surface overpotential, and (ii) the dynamic voltage behaviors ($R_1, C_1, \ldots, R_n, C_n$) caused by the concentration overpotential when battery is dis-

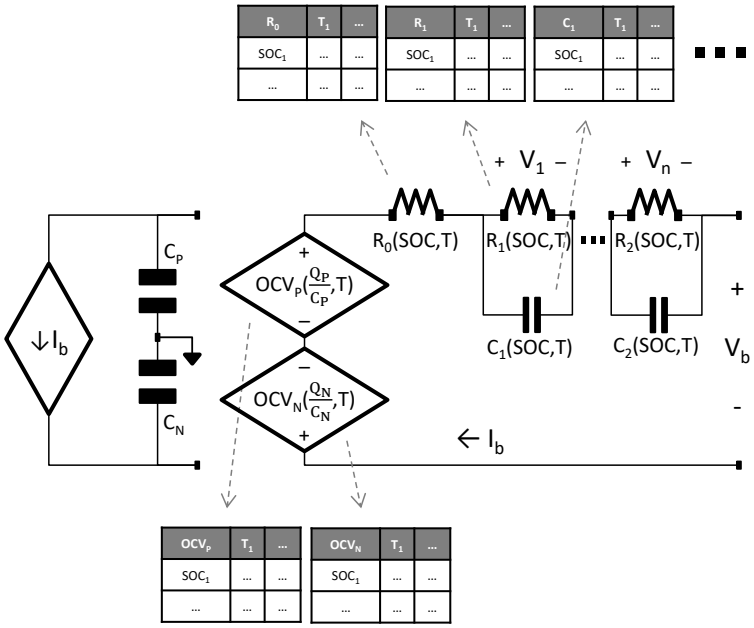

Figure 3.2: Equivalent circuit battery model.

charged/charged at the rate I_b. These battery parameters (i.e., OCV, R_0, R_1, C_1, ...) are representative of a particular battery type, and is in general a nonlinear function of state-of-charge (SOC) and temperature (T) [31]. The number of RC branches in the equivalent circuit model determines the model's accuracy and complexity. In this chapter, we use the RC branch (R_1, C_1) to describe the dynamic voltage behavior for simplicity.

Parametric Open-Circuit Voltage (OCV) Model

Battery OCV is determined by the potential difference between OCVs of the positive (OCV_P) and the negative electrodes (OCV_N). Thus, a parametric OCV model has been proposed to describe the battery's entire OCV in terms of $\text{OCV}_P(\frac{Q_P}{C_P})$ and $\text{OCV}_N(\frac{Q_P}{C_P})$ [21, 41], based on the stored charge capacity (Q_N, Q_P) and the total

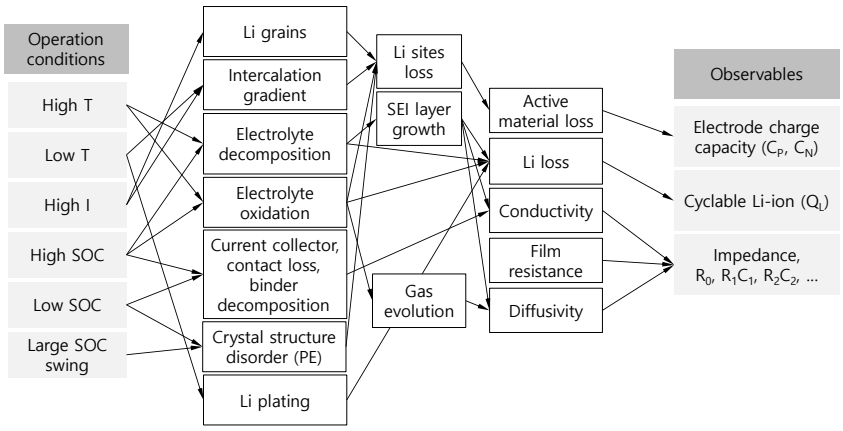

Figure 3.3: Degradation factors and their impacts.

maximum charge capacity (C_N, C_P) as:

$$\text{OCV} = \text{OCV}_P(\frac{Q_L^P}{C_P}) + \text{OCV}_N(\frac{Q_L^N}{C_N}) \tag{3.1}$$

$$Q_L = Q_L^P + Q_L^N,$$

where Q_L^P and Q_L^N are the amounts of Li-ion that are inter-calated in positive and negative electrodes' active material, respectively, and C_P and C_N are the maximum charge capacities of the active materials to store Li-ions without over- or under-voltage in the positive and negative electrodes, respectively. Based on the parametric OCV model, battery's total charge capacity can be assessed with three important parameters: the capacity of positive and negative active material (C_P and C_N), and the amount of cyclable Li-ion (Q_L). These parameters decrease slowly over time due to side chemical reactions in the battery.

3.2.2 Changes of Battery Parameters due to Degradation

Battery performance degrades over cycles/time, observed as not only charge capacity decrease, but also as internal resistance increase (R_0, R_1) and capacitance decrease (C_1). An increase in internal resistance leads to larger voltage drop, and a decreased internal capacitance causes faster voltage drop, both degrading battery's

power capability. The changes of these parameters rely heavily on battery's operating conditions as shown in Fig. 3.3, including high/low temperature, high/low SOC, large charge/discharge current, frequent discharge/charge cycles [140], etc., which accelerate the side chemical reactions related to solid electrolyte interfaces (SEI) layer growth, lithium plating, gas and precipitation generation, electrolyte oxidation and decomposition. Along with these chemical side reactions, mechanical stress on the electrodes during charge/discharge cycles also leads to contact loss, particle cracking, and structure disorder. These chemical and mechanical stresses affect the parameters closely related to battery performance over cycles.

3.3 Problem Statement and Proposed Approach

Thus far, we have discussed the necessary background to understand the battery model, state-of-health (SOH) and degradation factors. Electrodes' capacities (C_P, C_N) and the amount of Li-ion (Q_L) must be identified because they closely relate to battery's energy capacity. We must also extract battery internal resistances (R_0, R_1) and capacitance (C_1) to describe the battery's dynamic behavior such as voltage drop and recovery effect. Moreover, the degradation of these parameters over time relies on the battery's operating conditions (V, I, T). Therefore, the underlying diagnosis system must identify them accurately, and the prognosis system should capture the relationship between their degradation and operating conditions (V, I, T). Presented below are a formal statement of our diagnosis/prognosis problem and the overview of the proposed solution.

3.3.1 Problem Statement

With the above system model, assumptions and notations, our problem can be formally stated as:

Using battery data measured in the charging titration period,

Develop an adaptive battery diagnosis/prognosis system that identifies the battery parameters related to the energy capacity (C_P, C_N, Q_L) and internal resistance (R_0, R_1, C_1), figure out the battery parameters' degradation rates and establish the relationship between and the operating conditions (V, I, T) and the parameters' degradation rates so as to

Predict *battery degradation pattern* and *end-of-life (EOL)*, and

Optimize *battery operating conditions* (V, I, T).

Considering users' convenience and cost, the diagnosis system should be able to estimate parameters $(C_P, C_N, Q_L, R_0, R_1, C_1)$ based only on measured data without disassembling a battery pack or any other destructive measurements. The prognosis system must complete the development of a battery degradation model based on the diagnostic data.

3.3.2 Overview of Proposed Solution

Fig. 3.4 shows the overall diagnosis/prognosis process. First, battery current–voltage characteristics are captured periodically through a titration technique [87]. Based on these characteristics, the model parameters are estimated and stored in tables with the corresponding operating conditions (V, I, T) and the number of cycles (n). For this step, the system needs a parameter estimation technique, which will be detailed later. The prognosis system then develops the battery degradation model based on the collected diagnosis information. The degradation model, in turn, is used to predict battery's *end-of-life* (EOL), defined as when the battery performance has dropped significant enough (e.g., to 50˜80% of its initial capacity [142, 38]). Here, we use the 70% level of the initial energy capacity to define EOL. Also, the degradation

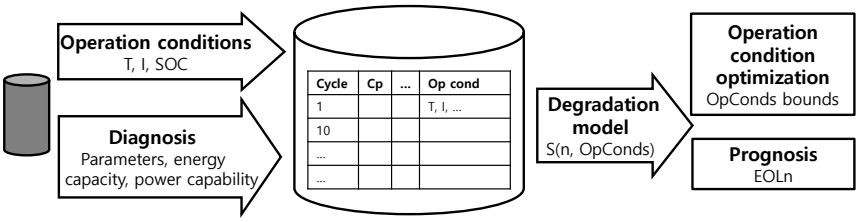

Figure 3.4: Overall process for the proposed diagnosis/prognosis

model with respect to operating conditions allows the management system to search for "effective" operating conditions to ensure smooth system operation throughout the warranty period.

3.3.3 State-of-the-Art and Limitations

Various approaches to parameter identification have been developed over the last decade or so. Electrical parameter estimation via electrochemical impedance spectroscopy (EIS) and time constant analysis are well-known to describe the dynamic voltage transient with respect to discharge/charge current [51, 139, 9]. A parameteric OCV model was proposed to determine battery active material capacities and the amount of cyclable Li-ion [41, 21]. In this chapter, we propose the battery diagnosis system that facilitates parameter estimation for battery management and prognosis, especially for EVs. We first introduce the applicable battery diagnosis techniques, and then develop applicable algorithms for real vehicles.

For battery prognosis, most existing degradation model studies focused on searching for the optimal model coefficients of the pre-defined form of degradation model as shown in Fig. 3.5. The pre-defined models are selected based on the observations during a large number of offline degradation tests under various operating conditions. To describe the non-linear property of battery degradation, they used exponential, polynomial, or power functions, because these functions can fit the degradation patterns in their test environments. A non-linear regression or neural network was

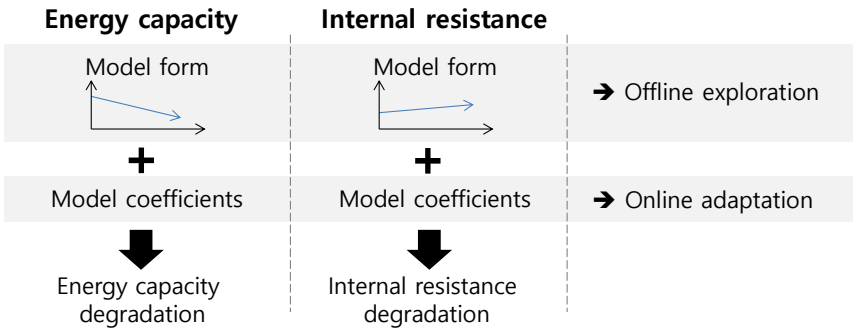

Figure 3.5: Conventional battery degradation modeling.

utilized to identify the coefficients of the pre-defined model.

Fig. 3.6 shows the overall procedure of our battery degradation modeling approach. Instead of battery's total capacity and internal resistance, we develop a more detailed degradation model consisting of positive/negative electrode capacity, resistances and capacitance. Also, to construct a more adaptive degradation model, we take an additional step to select a generic model-form instead of using a pre-defined model form. In addition to identifying degradation patterns, the system also focuses on the impact of operating conditions on the battery degradation rate as:

$$D_x = f_x(V, I, T),$$

where x is the battery model parameters including $\{C_P, C_N, Q_L, R_0, R_1, C_1\}$ and D_x is the degradation rate of x. $\{V, I, T\}$ are measurable and controllable operating conditions related to battery degradation.

3.4 Diagnostic Charging System

We now detail the battery diagnostic charge system in which the amount and duration of charge current are controllable. Fig. 3.7 shows an example diagnosis procedure to estimate the battery model parameters.

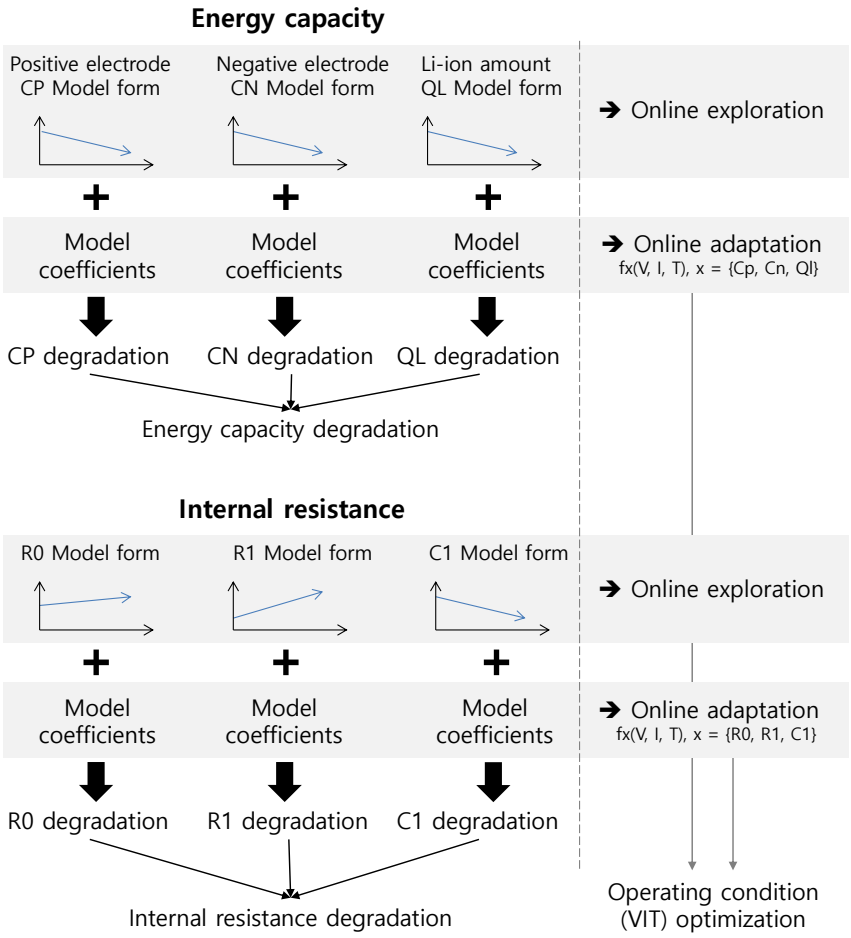

Figure 3.6: Proposed battery degradation modeling.

3.4.1 Parameter Estimation of Equivalent Circuit Battery Model

The titration procedure in the algorithm normally consists of a series of charge current pulses, followed by a relaxation time. During a charge current pulse, the battery voltage first quickly increases to a value proportional to its ohmic internal resistance (R_0), and then the voltage slowly increases further due to the constant charge pulse and a charge migration and diffusion effect which is described by additional resistance and capacitance ($R_1, C_1, \ldots$). We record these voltage change profiles to estimate battery internal parameters (R_0, R_1, C_1). Based on the captured voltage–current characteristics, we determine $R_0(\mathrm{SOC}, T)$, $R_1(\mathrm{SOC}, T)$, $C_1(\mathrm{SOC}, T)$

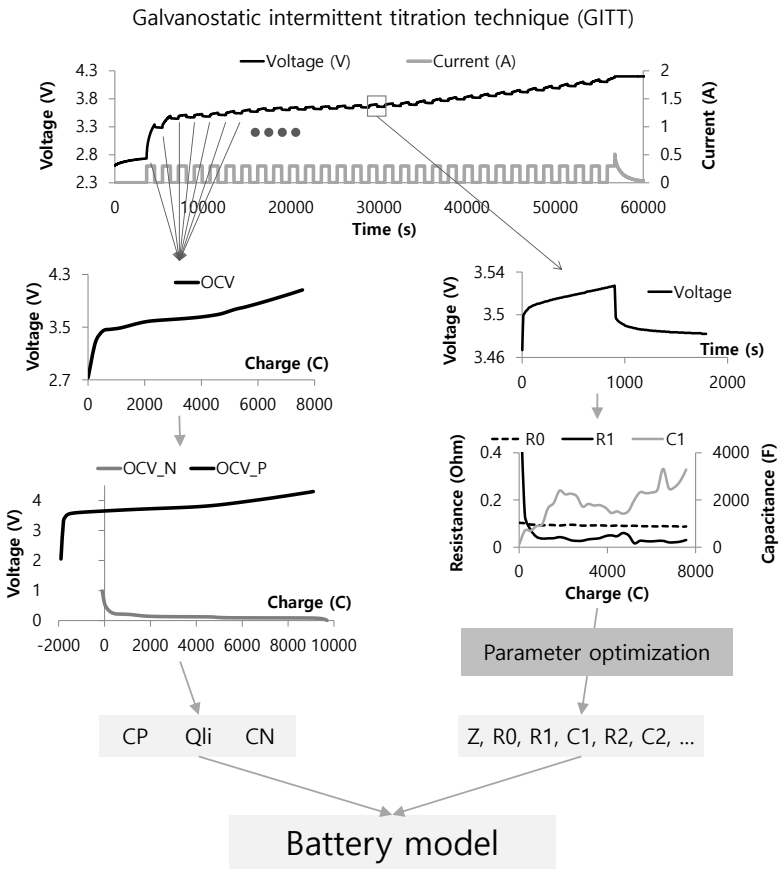

Figure 3.7: Model-based battery diagnosis.

over battery SOC and temperature T [30] as shown in Fig. 3.7. After a charging period, during the relaxation time, the voltage first suddenly decreases to a value proportional to the internal resistance (R_0), and then slowly decreases until output voltage in equilibrium is reached. These equilibrated voltages are recorded since they are close to battery's open circuit voltages (OCV(SOC, T)) at the corresponding SOC and temperature (T) levels. Such charge-and-relaxation procedure is applied repeatedly until the battery is fully charged ($V_o = 4.2V$), obtaining the OCV characteristics over a full range of battery SOC.

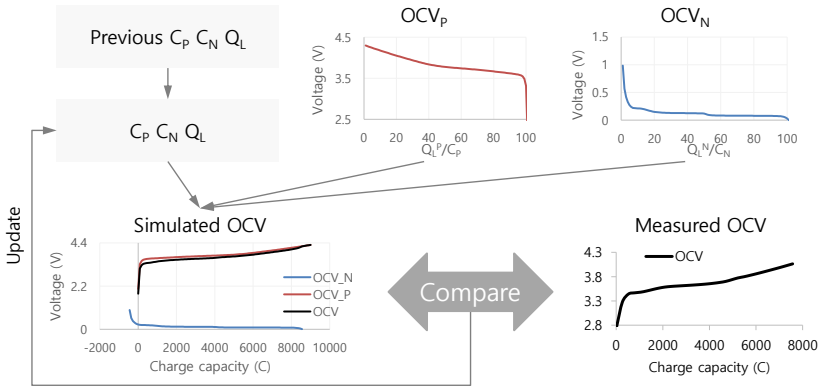

Figure 3.8: Model-based battery OCV parameter estimation.

3.4.2 Estimation of OCV Model Parameters

Battery electrodes' capacities and cyclable Li-ion amount decrease over time due to side chemical reactions in the battery. While the battery's maximum capacity decreases, the SOC and OCV will change faster even with the same charge current, because the decreased capacity will be filled in quickly. Also, OCVs (OCV_P, OCV_N) and SOCs ($\frac{Q_P}{C_P}, \frac{Q_N}{C_N}$) are closely related. The parametric OCV model enables the analysis of battery OCV in terms of active materials' charge capacities.

Fig. 3.8 provides a search procedure for C_P, C_N, Q_L based on the OCV–charge capacity curves ($\text{OCV}_P(x)$ and $\text{OCV}_N(x)$) [41, 21]. We first synthesize the OCV curve based on OCV_P and OCV_N with the capacity parameters (C_P, C_N, Q_L). Battery $\text{OCV}_N(\frac{Q_L^N}{C_N})$ and $\text{OCV}_P(\frac{Q_L^P}{C_P})$ depend on active materials' maximum charge capacity (C_P, C_N) and the amount of charge (Q_L^N, Q_L^P) in the active materials [41, 21]. Note that the $\text{OCV}_N(\frac{Q_L^N}{C_N})$ and $\text{OCV}_P(\frac{Q_L^P}{C_P})$ curves are very different functions in terms of charge concentration $(\frac{Q_L}{C})$ [41, 21]. Next, we compare the measured and synthesized OCVs with respect to the charge capacity (Q). The algorithm keeps searching the parameter set (C_P, C_N, Q_L) until the difference between the measured and synthesized OCVs becomes lower than the pre-specified value.

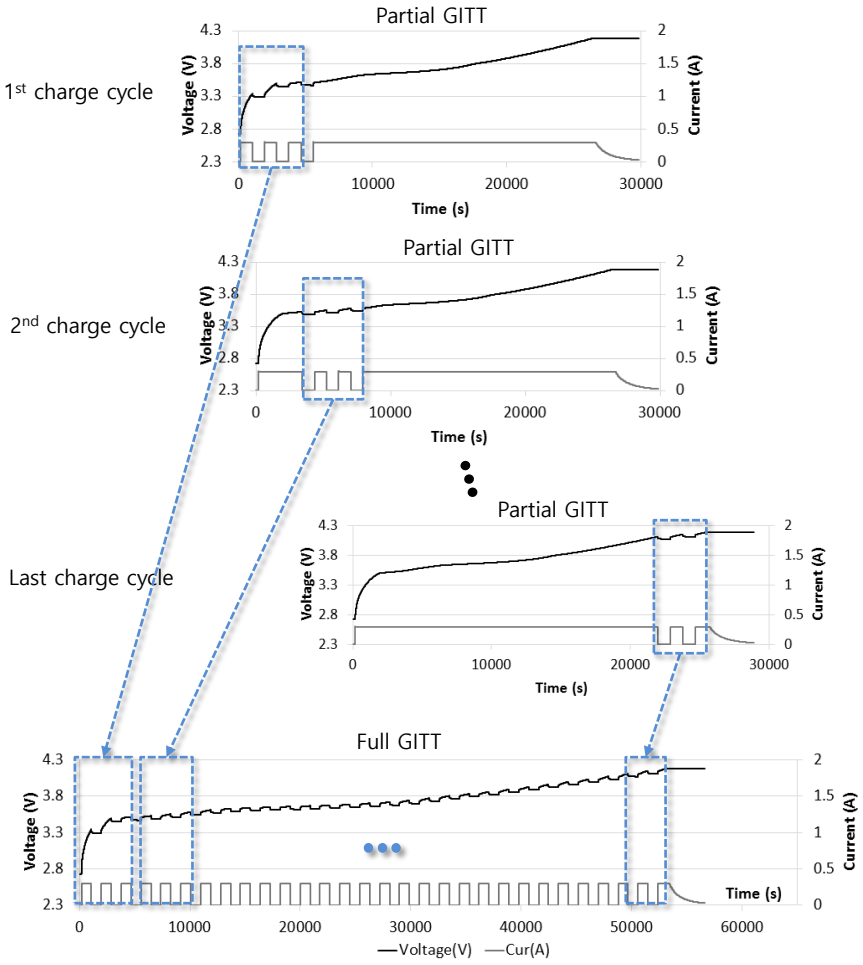

Figure 3.9: GITT for the battery system over the full range of SOC.

3.4.3 Diagnostic Charging System

One may wonder if a series of charge current pulses may interrupt the vehicle's operation. We resolve this problem by only applying the charge current pulses during night when EV batteries are charged from the wall power while parked. Also, a few hours may not be sufficient to apply the entire series of charge current pulses; we divide the series into several intervals, which can be applied in different days. This is valid because battery behaviors are similar between several consecutive days as shown in Fig. 3.9.

For the first charge cycle, partial GITT (Galvanostatic intermittent titration tech-

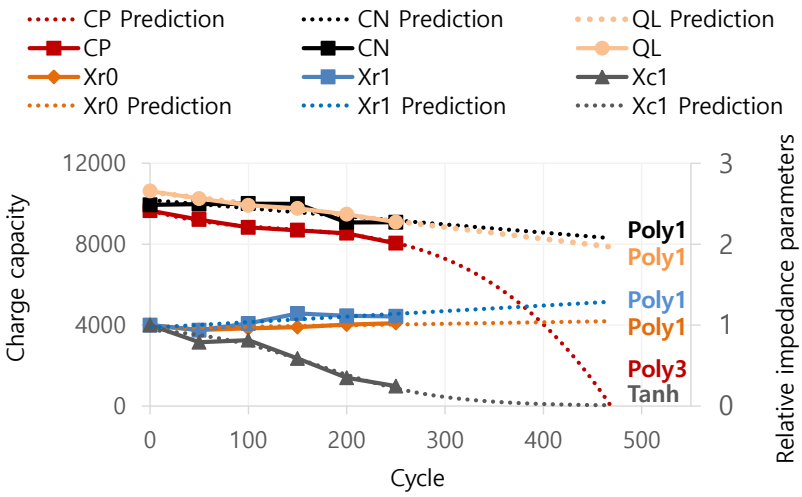

Figure 3.10: Example model parameter degradations during 250 discharge/charge cycles. Operating temperature is $23°C$, battery C–rate is $2{,}300mA$, charge current is $2A$, max charge voltage is $4.2V$, average discharge current ($E(I_d)$) is $2A$, and root mean square of discharge current ($RMS(I_d)$) is $2.45A$. Dotted lines show the degradation predictions of model parameters

nique, as shown in Fig. 3.7) is performed for diagnosis at the lowest SOC. In case the system cannot perform GITT over the full SoC range due to limited available charge time, GITT is applied only to a partial SoC range. In following charge cycles, the charge system applies GITT to identify battery parameters at the other SoC ranges until the system collects the full SOC range of diagnostic information. Fig. 3.10 shows an example of parameter estimations during the first 250 cycles.

3.5 Prognosis system

Thus far, we have explored the diagnosis system for battery model parameters related to SOH and performance. Here we propose how to prognose the battery based on the diagnosis results, and address when the battery is expected to die before the warranty expires. Fig. 3.11 represents the overall procedure for the proposed battery prognosis system. First, the system constructed the battery degradation models adaptively with respect to the operating conditions. Then, the system predicts the battery EOL and regulates the operating conditions so as to maximize battery per-

formance within the warranty period.

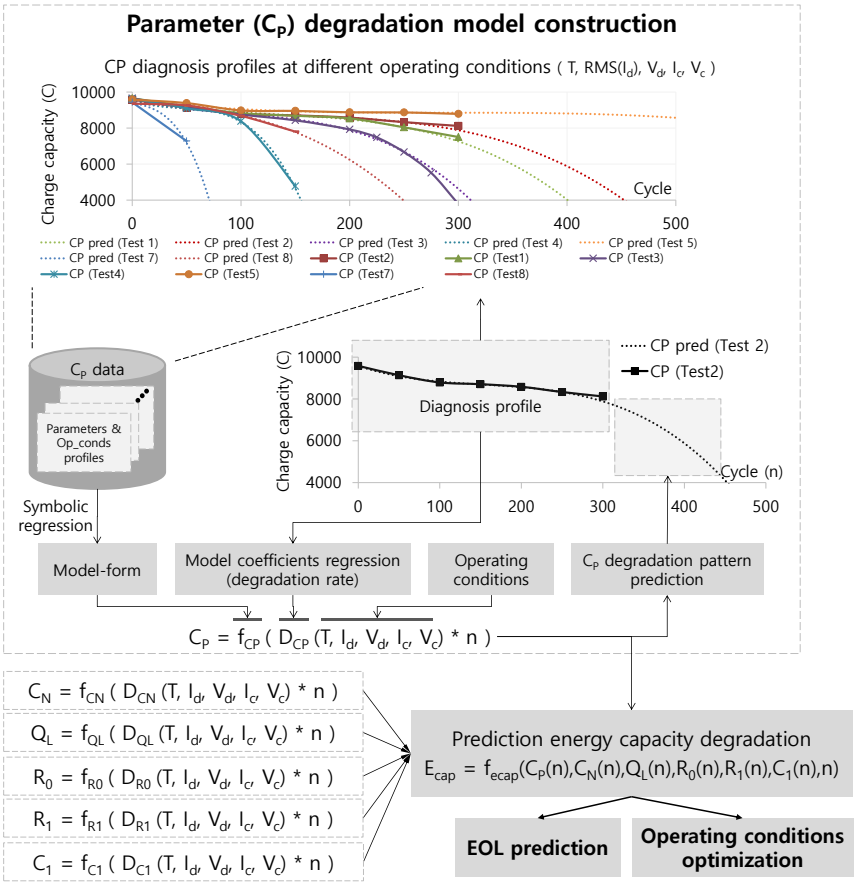

Figure 3.11: Overall procedure for battery prognosis

3.5.1 Adaptive performance degradation model

The degradation state ($\mathbf{S}$) includes the charge capacity parameters (C_P, C_N, Q_L), relative internal resistances and capacitances ($X_{R_0}, X_{R_1}, X_{C_1}, \ldots$). The parameter degradation models (f_S) can be represented by functions of operating conditions and the number of cycles (n) as:

$$\begin{aligned}\mathbf{S} &= (C_P, C_N, Q_L, X_{R_0}, X_{R_1}, X_{C_1}, ...), \\ &= f_S(D_S(\mathbf{x}) \cdot n), \\ \mathbf{x} &= [T, RMS(I_d), V_d, V_c, I_c],\end{aligned}$$

where $\mathbf{x}$ is an operating condition vector including battery temperature (T), discharge stress ($RMS(I_d)$), minimum discharge voltage (V_d), maximum charge voltage (V_c) and charge current (I_c). Fig. 3.11 shows an overview of our approach to building the parameter degradation models. The proposed diagnosis system extracts and stores battery parameters with the corresponding operating conditions. The prognosis system uses the stored data to construct the battery degradation model. The system, first, applies a symbolic regression to construct the generic model form of parameter degradation profiles. Then, the coefficients (D_S) of the generic model are fitted for adaptive degradation model construction (f_S). The constructed model enables prediction of battery EOL, which will be detailed later. Coefficients (D_S) will be regressed with the operating conditions ($\mathbf{x}$) to account for their impact on the parameter degradation rates, as we will elaborate later.

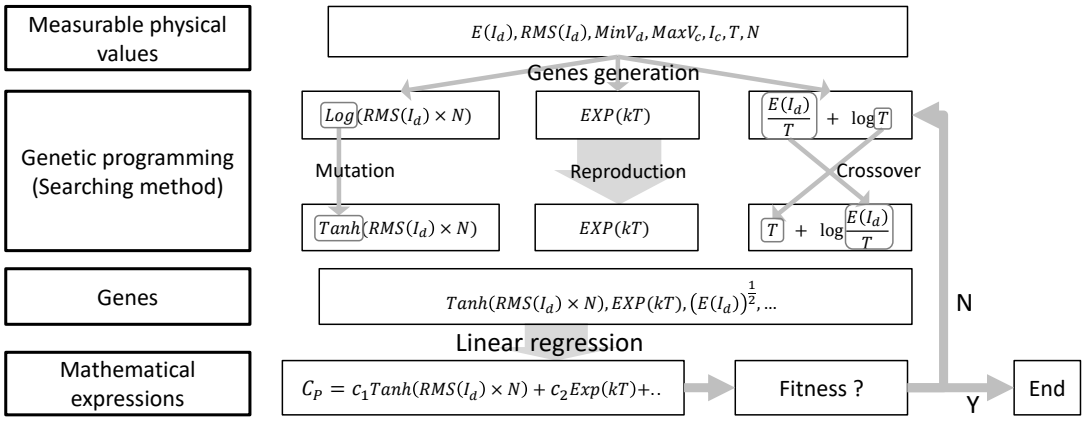

Figure 3.12: An example paramater function regression

Generic model-form of parameter degradation

Fig. 3.10 shows battery parameters with degradation patterns. We first explore mathematical degradation functions for describing the degradation of battery parameters. Note that some mathematical functions are commonly used in electrochemical behavior modeling. For example, exponential and logarithmic functions are utilized

in modeling various chemical reaction processes [39, 141, 143, 125]. Polynomial, hyperbolic functions are also exploited to describe the trend of physical quantities related to electrochemical reactions. Battery performance degradation is mainly due to chemical reactions, and hence a combination of these functions has been used to describe the performance degradation patterns.

The symbolic regression with polynomial, exponential, logarithmic and hyperbolic functions is performed to find a generic model-form of degradation based on many degradation profiles of batteries stored in a server. We initially selected a linear parameter model which is then evaluated in terms of its fitness with the collected data. If the fitness is not met, other models are explored in the search space. A more effective model is searched for via genetic programming, which is based on an evolutionary algorithm [75, 128, 11]. In genetic programming, candidate models are created for the next generation via a mutation and a crossover based on the parents' models with low weights. We reproduced models with large weights to leave the genes that are likely to critically affect the model. The system evaluates its fitness and repeatedly generates new generations until the fitness is satisfied.

Regression of parameter degradation rate

Battery degradation depends on the operating condition, such as temperature, dis/charge current and operating voltage range. To customize the parameter degradation model-form while considering the operating conditions, BMS must regress the parameters related to degradation rate over the operating conditions. Based on such a degradation rate under the corresponding operating conditions, we can find a degradation model function that represents the impact of the operating conditions on parameter degradation. To regress the parameters of the degradation rate model, neural network regression and support vector regression with Gaussian, polynomial

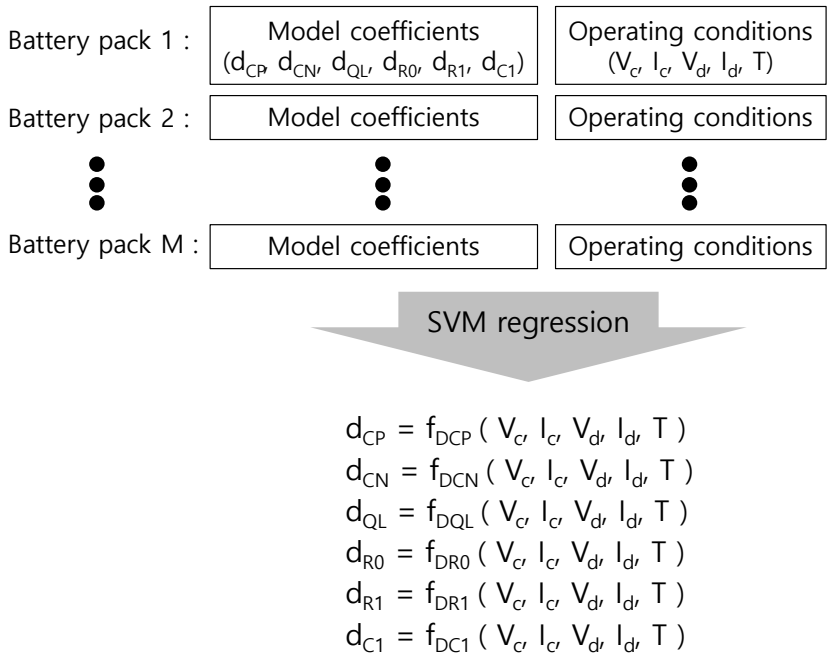

Figure 3.13: Development of the parameter degradation rate function based on parameter degradation and operating condition profiles

and linear functions can be used on the recored battery degradation data.

3.5.2 Battery capacity degradation and end-of-life prediction

Described below is how battery performance degradation can be estimated based on the parameter degradation trends and operating conditions. Then, we can identify when the battery capacity drop below the EOL capacity (70% of of their initial capacity) as shown in Fig. 3.14.

Performance estimation based on parameter degradation estimation

Based on the parameter degradation models, the performance degradation over cycles can be estimated. Energy capacity is the most important metric, and is defined as the available amount of energy while maintaining voltage within an applicable range. Hence, the energy capacity can be assessed based on the OCV curve and the current level for the underlying application. Fig. 3.15 shows an example of

energy capacity estimation. A decreased energy capacity causes battery to reach the voltage limit more quickly even with the same current. The internal resistance also accelerates the decrease of energy capacity because a larger resistance may incur a larger voltage drop, thereby causing an earlier voltage drop (or rise) below the minimum (or above the maximum) required value. The energy capacity can be assessed based on the total charged capacity by integrating the current over time in the test profiles.

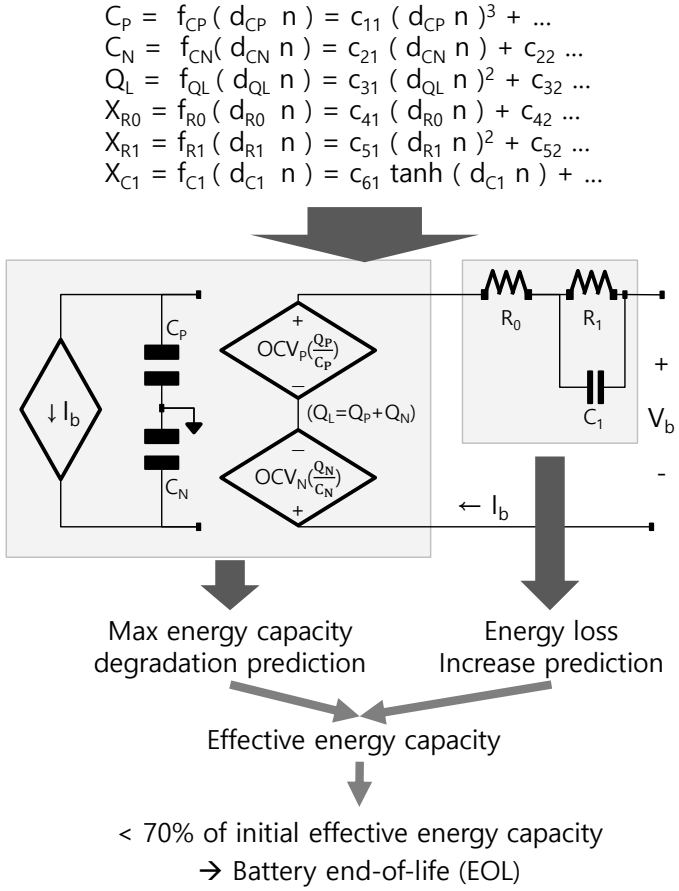

Figure 3.14: Battery EOL prediction based on the battery model and the model parameter degradation function

EOL prediction

Fig. 3.14 shows the algorithm for prediction of battery EOL. First, the degradation of model parameters over cycles can be predicted by using the degradation model.

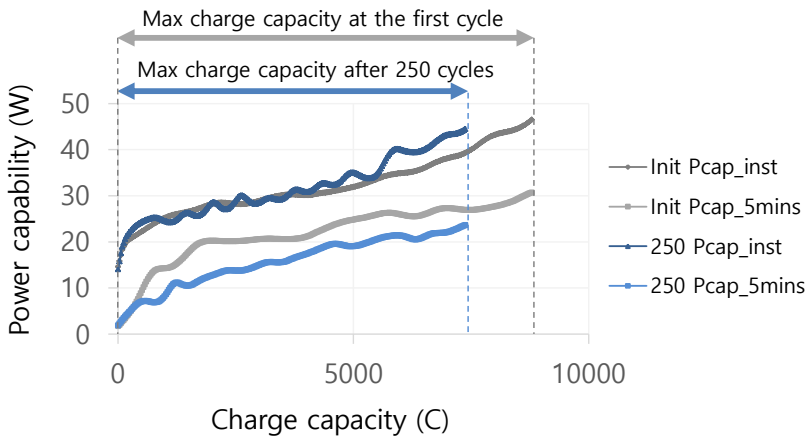

Figure 3.15: Example total capacity and power capability degradations. Grey lines represent an instantaneous power and power capabilities over 5 minutes during the first cycle. Blue lines show an instantaneous power and power capabilities over 5 minutes after 250 cycles. After 250 cycles, the battery's energy capacity and power capability over 5 minutes decrease.

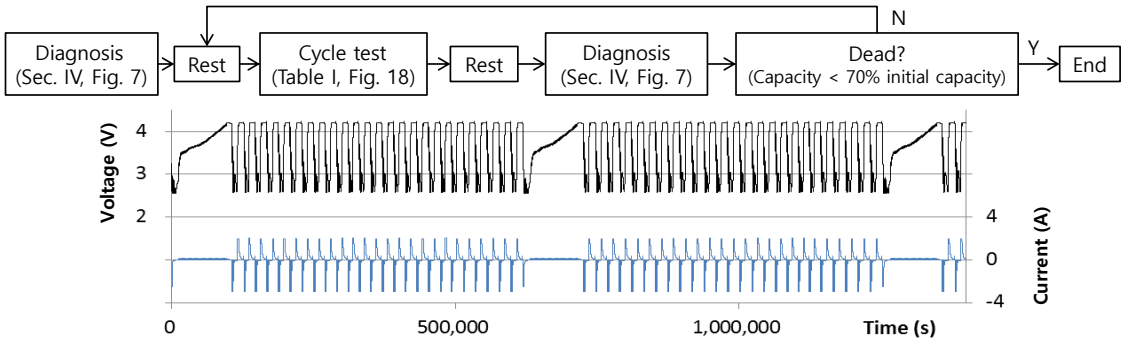

Figure 3.16: Test procedure.

Then, we can estimate energy capacity degradation and internal resistance increase based on the battery model and parameter degradation estimations. Note that, in most applications, battery EOL is defined as the point at which the a battery will hold only a pre-set percentage (70%) of its original storage capacity. Therefore, we can search for battery EOL by identifying the number of cycles where the energy capacity is estimated to drop below the 70% of its initial capacity.

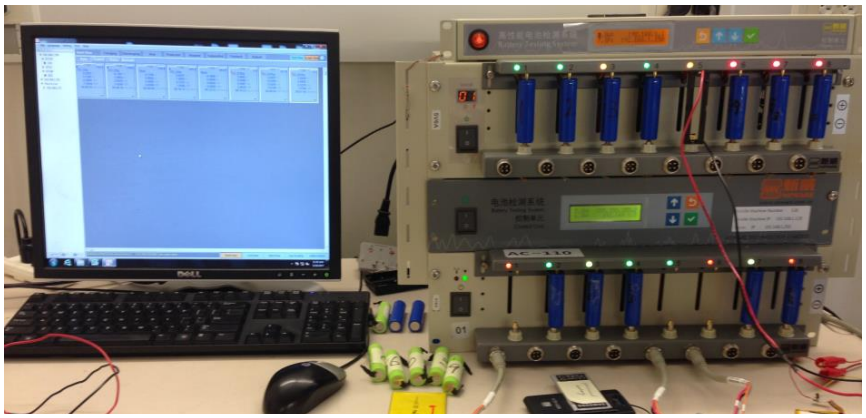

Figure 3.17: Neware battery tester.

Determination of operating condition bounds

The parameter degradation models tell not only the total capacity degradation under current operating conditions, but also the relationship between operating conditions and the parameter degradation rate. Therefore, the model can be used to optimize the operating condition bounds to guarantee the battery warranty while providing the required power capability and energy capacity. For example, if the estimated battery EOL is shorter than the warranty period, the operating condition bounds must be regulated to decelerate battery degradation at the expense of the battery's effective capacity. *Effective charge capacity*, Q_{eff}, can be calculated by considering the total charge capacity (C_Q) and charge loss ($Q_{loss}^{I_d}, Q_{loss}^{T}$) due to the regulation of operating conditions ($Q_{eff} = C_Q - Q_{loss}^{I_d} - Q_{loss}^{T}$). To regulate $RMS(I_d)$, an energy buffer is required to move charges to the energy buffer temporarily through a DC/DC converter, leading to the loss of available charge as:

$$Q_{loss}^{I_d} = (1 - \eta_d)(1 - \eta_c)(RMS(I_d^{init}) - RMS(I_d))\ t_{op},$$

where t_{op} is the operation time, η_d and η_c are charge transfer efficiencies, $RMS(I_d^{init})$ and $RMS(I_d)$ are initial and target discharge stresses. Thermal control also con-

sumes energy as:

$$Q_{loss}^{T} = \frac{1}{\eta_{th}}(T_{ext} - T)\ t_{op},$$

where η_{th} is a thermal efficiency, and T_{ext} is an external temperature. With the above system model, assumptions and notations, our problem can be stated formally as:

$$\begin{aligned} \underset{\mathbf{x}}{\text{maximize}} \quad & \alpha Q_{eff}(\mathbf{x}) + \beta S_{chg}(\mathbf{x}) \\ \text{subject to} \quad & \text{EOL}_{margin} + \text{EOL}_{req} < \text{EOL}_{model}(\mathbf{x}) \end{aligned}$$

where $\mathbf{x}$ is $\{RMS(I_d), I_c, V_c, V_d, T)\}$, S_{chg} is the charging time, EOL_{model} and EOL are estimated by the degradation model, EOL_{req} and EOL_{margin} are the required period of EOL and its margin. α and β are the weight of effective charge capacity and the required charge time, respectively. The charging speed can be assessed by total capacity (C_Q) and charge current (I_c) as:

$$S_{chg} = \frac{C_Q}{I_c}.$$

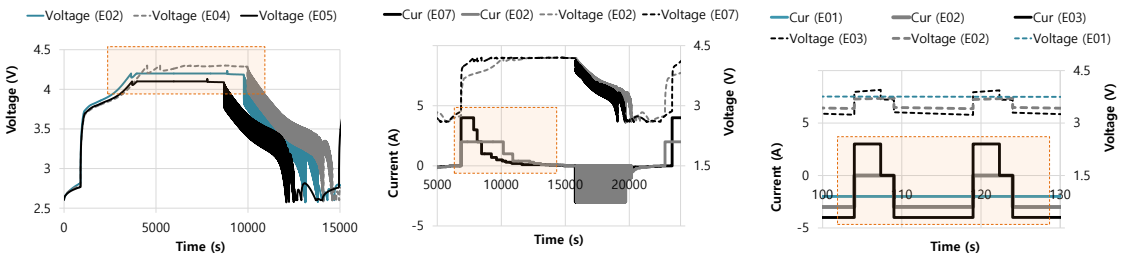

(a) Charge voltage (V_c) (b) Charge current (I_c) (d) Discharge current ($RMS(I_d)$)

Figure 3.18: Test profiles with different charge/discharge currents and voltages.

3.6 Evaluation

We have evaluated the proposed battery model construction, EOL prediction, and operation conditions optimization via extensive experiments, lasting 8 months cumulatively.

3.6.1 Methodologies and settings

Fig. 3.16 shows our testing procedure, which is implemented with the Neware's battery tester as shown in Fig. 3.17 and Li-ion batteries (18650, 2200 mAh) [135]. The battery discharge/charge current and output voltage are logged at 10Hz during the tests, based on which the proposed model construction is evaluated. We intermittently diagnosed batteries to extract their characteristics, and saved the diagnostic results with the corresponding cycle and operating conditions. This procedure is repeated until the batteries reach their EOLs. We collected battery degradation data under a wide range of operating conditions in terms of temperature (T: 23–40^{o}C), discharge stress ($RMS(I_d)$: 2–4A), charge voltage (V_c: 4.1–4.3V) and current (I_c: 1–4A), as summarized in Table 3.1 and Fig. 3.18.

Table 3.1: Profiles in battery testing.

	T (°C)	$V_d(V)$	RMS$(I_d)(A)$	$V_c(V)$	$I_c(A)$
Test-1	23	2.6	2.00	4.2	2
Test-2	23	2.6	2.45	4.2	2
Test-3	23	2.6	3.65	4.2	2
Test-4	23	2.6	2.45	4.3	2
Test-5	23	2.6	2.45	4.1	2
Test-6	40	2.6	2.45	4.2	2
Test-7	23	2.6	2.45	4.2	4
Test-8	23	2.6	4.00	4.2	2
Test-9	23	2.6	3.65	4.2	2
Test-10	40	2.6	2.45	4.2	2
Test-11	23	2.6	2.45	4.2	3
Test-12	23	2.6	2.45	4.1	2
Test-13	40	2.6	3.65	4.2	2
Test-14	23	2.6	2.45	4.3	1
Test-15	40	2.6	2.45	4.2	1
Test-16	23	2.6	2.85	4.2	2

3.6.2 Results

Degradation patterns and model

We evaluate the following three schemes for modeling battery degradation:

- EXP2-Const: the capacity degradation model based on two exponential func-

tions [39, 141],

- EXP-PW: the capacity degradation model via exponential and power functions [143, 125], and
- SYMR: our capacity degradation model using the symbolic regression described in Section 3.5.1.

The batteries' initial capacities are about 8500C. So, their EOLs are reached when their capacities reduce to $8500 \times 70\% \simeq 6000$C. Fig. 3.19 plots the prediction of capacity degradation at 80% and 90% SOH with the above three schemes, respectively. The EOL is also predicted when the battery is of 95%, 85%, and 75% remaining energy capacity, as summarized in Table 3.2. All three schemes predict EOL more accurately at later cycles, and SYMR achieves the best accuracy in all cases.

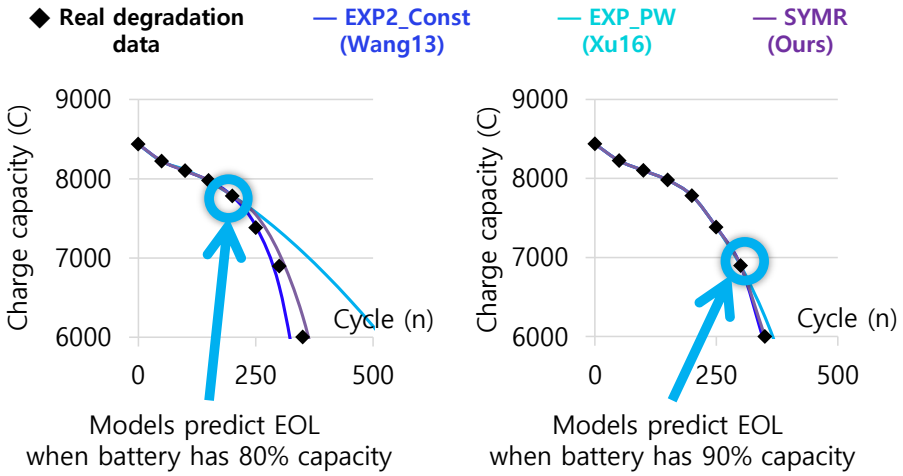

Figure 3.19: Examples of battery EOL prediction at different SOH levels.

Table 3.2: Errors in predicting battery EOL.

EOL prediction time	EOL prediction error (%)		
Remaining capacity (SOH)	EXP2-Const	EXP-PW	SYMR
95%	43.8	251.2	26.1
90%	40.6	73.9	16.5
85%	19.9	17.5	5.5
80%	9.4	10.4	5.4
75%	10.8	8.4	2.2

Parameter degradation rate

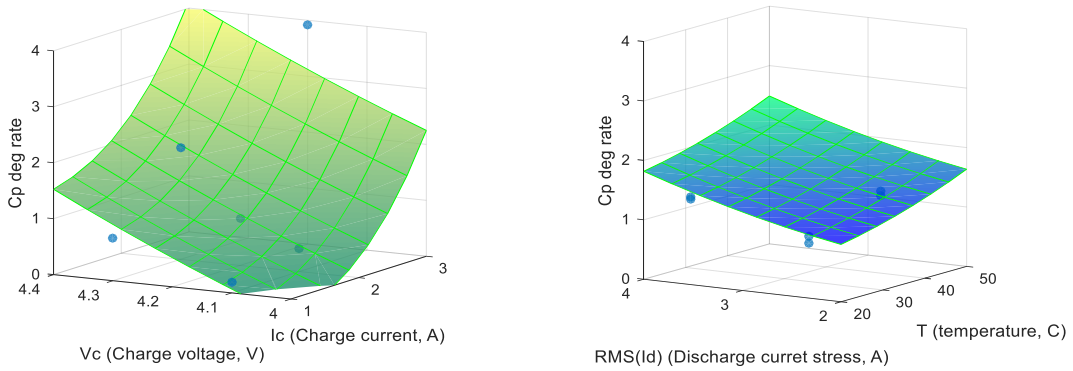

Figure 3.20: Degradation rate with respect to the operating conditions

Fig. 3.20 shows an example degradation parameter function (D_{CP}) with respect to the operating conditions. Fig. 3.20(a) shows the impact of the charge current (I_c) and charge voltage (V_c) on degradation coefficients in the model while keeping other conditions intact, and Fig. 3.20(b) shows the impact of temperature (T) and discharge/charge stress ($RMS(I_d)$) on the coefficient. Based on the degradation rate function, we can determine the impact of the operating conditions on the parameter degradation rate. This parameter degradation model will be used to schedule the target operating conditions to achieve our goal.

Determination of operation bounds

Using the battery parameter degradation model, we optimized the battery operation conditions. We set EOL_{mg} and EOL_{rq} to 100 and 500 cycles, respectively. The optimization result of controllable operation condition vector $[RMS(I_d), V_c, I_c, T] = [1.67, 4.29, 1.00, 23.22]$. That is, to use the battery over 500 cycles while maximizing the user's satisfaction in terms of effective charge capacity and charge speed, we have to maintain the battery temperature at 23.22^oC and limit the discharge stress

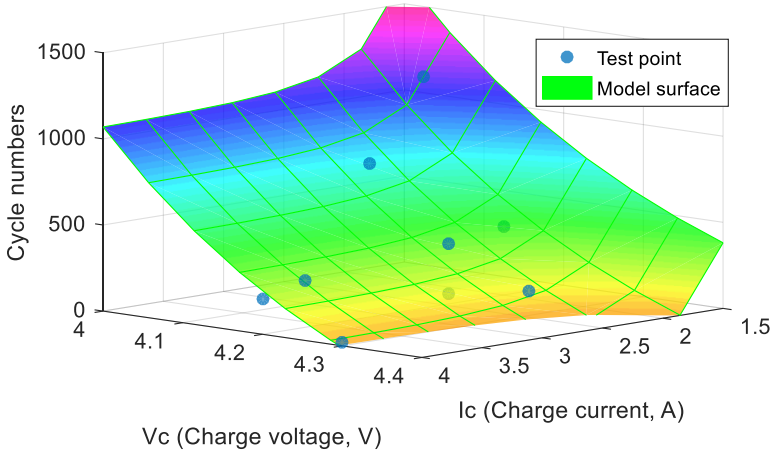

Figure 3.21: EOL predictions under different charge voltage and current conditions

to 1.67A, charge voltage to 4.29V and charge current to 1.00A, respectively. α and β are set to 0.85 and 0.15. Determination of weighing factors should be explored further to maximize the user's satisfaction which is part of our future work.

3.7 Conclusion

To diagnose and prognose batteries for their effective control, we have analyzed battery diagnostic data, predicted battery degradation, and optimized battery operation conditions. For battery prognosis, we have developed a degradation model based on the parametric OCV model and an equivalent circuit model. The thus-developed battery degradation model was used to predict battery EOL cycle and optimize battery operation conditions to guarantee the EOL warranty while maximizing battery utilization. Our evaluation with real battery data has shown the proposed schemes to yield an accurate battery degradation model.

CHAPTER IV

Modeling and Real-time Scheduling of Large-Scale Batteries for Maximizing Performance

4.1 Introduction

The methods of controlling discharge-rate and temperature are considered for deployment in EVs, since they are known to improve the battery capacity and lifetime. However, there are several obstacles to overcome in order to optimize and deploy solutions in real vehicles. First, an accurate estimation of battery behavior related to the battery performance and its degradation is very complicated. While the battery behavior varies non-linearly with temperature, the required discharge-rate, charge strategy and operating SOC range, their prediction requires the understanding of the entire battery electrochemical processes. This difficulty of accurate prediction makes it harder to choose/control the discharge-rate, temperature and operating SOC range of batteries. Moreover, the behavior and performance of batteries in a pack are not homogeneous; battery packs' performance and behavior are not expected to be the same even during the manufacturing stage. Enhancing one aspect of the performance (e.g., battery lifetime) may also affect the other aspect (e.g., capacity). For example, battery capacity improves temporarily at "instant high temperature" due to the increased chemical reaction rate and ion mobility. However, the "cumulative exposure to high temperature" causes the permanent lifetime to decline because of its accel-

eration of irreversible side reaction. Also, we should consider the timely scheduling of charge/discharge as well as thermal control, because batteries would otherwise be over-heated or over charged, potentially leading to catastrophic accidents. This requires determination of deadlines to protect the batteries from significant loss of performance and/or reliability. These obstacles call for an integrated *cyber-physical system* (CPS) in which batteries and energy management devices are physical components. We should thus take all the entities into account, and achieve the effective and timely control to improve the battery performance based on physical properties of the system components.

To this end, this chapter proposes a prognosis scheme and a real-time scheduling algorithm for controlling the discharge/charge current, temperature and operating SOC range to extend battery *operation-time* within its warranty period. The operation-time is defined as the "cumulative time for batteries to provide the required power after a full charge" [72]; with a longer operation time, we can drive farther or longer with the same amount of batteries. Note that battery effective capacity monotonically decreases over time, because the performance of batteries degrades over cycle/time. Therefore, the battery capacity at any time during the warranty period is at least as much as that at the end of warranty period. That is, an efficient BMS must provide the required power for an extended operation time even at the end of warranty period.

To control the battery operating SOC window, discharge/charge current and temperature efficiently to maximize the battery operation-time, we must first characterize the impact of them on battery behaviors that affect the operation time and its degradation. To construct an accurate battery behavior model, we use two regression schemes: a symbolic regression for a generic model form of battery behavior,

and a support vector regression for adaptively tuning the generic model. Based on the behavior model, we can schedule the SOC operating window, discharge/charge and temperature of batteries to maximize operation-time (t_o) within the warranty period. An analysis of the optimal solution allows us to derive an efficient real-time scheduling policy for controlling the discharge-rate and temperature of batteries so as to achieve our goal.

The main contributions of this chapter are to:

- develop a prognosis system that constructs the model form and its coefficients using *symbolic regression*;
- design a real-time scheduling framework to determine both battery discharge/charge rate and temperature to maximize battery operation-time during the warranty period based on the model construction; and
- demonstrate the efficiency of the proposed system via an in-depth, realistic evaluation.

The chapter is organized as follows. Section 4.2 provides the background of battery performance and our target BMS architecture. Section 8.3 formally states the problem from a cyber-physical perspective. Section 4.4 describes how we construct battery behavior models for predicting batteries' future states, and Section 4.5 details how to schedule discharge/charge current and battery temperature for improving battery performance based on the battery behavior models. Section 4.6 evaluates the proposed battery behavior prediction using our behavior models, and performance optimization. Finally, the chapter concludes with Section 4.7.

4.2 Target BMS Architecture

This section introduces our target BMS architecture for operation condition controls. We first describe the requirements of a good BMS for electric vehicles as shown in Fig. 4.1, and then our target BMS architecture.

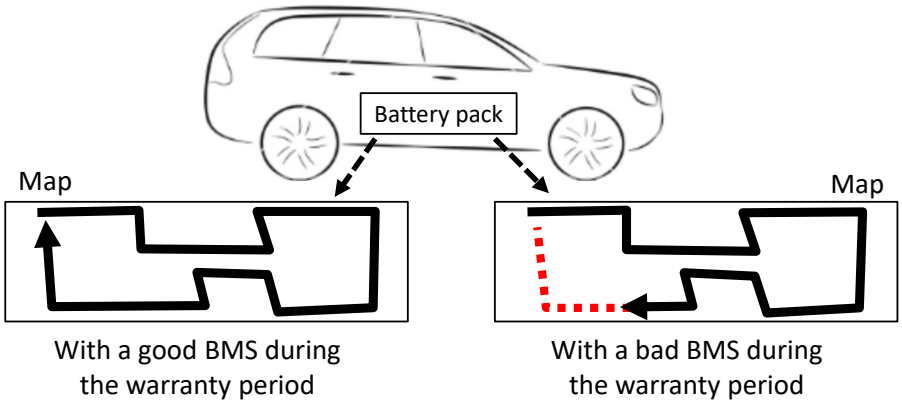

Figure 4.1: A good BMS allows electric vehicles (EVs) to drive longer distance and time (longer operation-time) for given batteries.

4.2.1 What is a good BMS ?

A battery pack in EVs supplies DC power to an inverter which operates the electric motors in EVs. To operate motors, a power inverter needs an applicable input voltage during the vehicle's operation. Therefore, a good BMS enables drivers to use their vehicles for a long operation-time by maintaining the output voltage no less than the applicable motor input voltage as shown in Fig. 4.1. The operation-time should also be kept long enough during the battery warranty period; otherwise, the vehicle requires a larger battery pack and/or more batteries must be recharged more frequently. Therefore, we must consider battery degradation to meet the specified warranty.

However, current battery systems still cannot achieve the required performance and replace the internal combustion engines mainly because they do not utilize bat-

teries' full capacity and capability in real vehicle applications. The power requirement of an EV is high and changes abruptly [130, 78, 68], because drivers frequently accelerate/decelerate their vehicles that weigh at least one ton during driving. It can also cause inefficiency and/or damage to battery, potentially leading to large energy losses and fast voltage drop within the warranty period. Therefore, a battery management system (BMS) in an EV is responsible for providing motors with the required power while protecting the battery cells from damage, excessive energy loss and life reduction caused by short bursts of power transfer. To achieve such functions, a BMS is often comprised of (i) a large number of battery cells that can supply the high current (hundreds of amperes) with the high output voltage (tens or hundreds of volts), and (ii) an auxiliary system to mitigate thermal and discharge stresses.

4.2.2 Target BMS architecture

We consider a BMS architecture which consists of a *regenerative braking system*, a *discharge-rate management system*, and a *thermal management system* as shown in Fig. 4.2. Although the architecture is relatively simple, it is equipped with essential functions and structures for efficient battery management, and each component is widely studied in battery and automotive industries. It allows batteries to save energy generated from a braking system, mitigate the discharge/charge stress via an energy buffer, and regulate the thermal condition for the efficient battery operation, which are detailed next.

Regenerative braking system (RBS)

To reuse the energy dissipated in their braking system, most EVs are equipped with a regenerative breaking system (RBS) in order to increase operation-time. Dur-

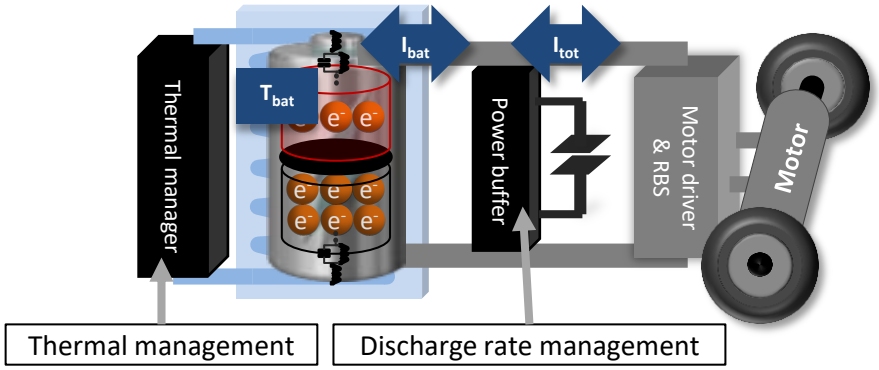

Figure 4.2: A target battery management architecture for EVs: a regenerative braking system (RBS) enables a battery system to store dissipated energy from the braking system, and discharge-rate and thermal management reduce energy loss while mitigating the stress of batteries.

ing braking, the RBS converts the vehicle's kinetic energy into electrical energy that can be stored in batteries for reuse to power the vehicle. Its effectiveness has been substantiated in terms of fuel economy [90, 52, 53]. Although the RBS improves the utilization of energy, the high recharging current for a very short period of time has a negative impact on the battery's health. Therefore, researchers introduced an auxiliary system as described next.

Discharge-rate management

Battery health and performance are damaged by short bursts of discharging current supplied to motors and recharging current generated from the RBS. To remedy this problem, researchers proposed deployment of ultra-capacitors (UCs); a BMS equipped with UCs and batteries is called a *hybrid energy storage system* (HESS). In a HESS, UCs are used as an energy buffer to smooth rapid power fluctuations in and out of the battery of an EV [114, 74, 25, 65]. Therefore, a HESS enables batteries to supply the average power required for operating vehicles, while UCs provide the sudden power surges required for acceleration and also accommodate instantaneous regenerative energy from the RBS.

Thermal management

Along with discharge-rate management, thermal management is one of the most important factors for a reliable BMS, and existing BMSes have thus employed thermal management policies so as to prevent battery cells from very high and low temperatures which may likely cause explosion and malfunction, respectively. Basically, the BMS monitors the temperature of battery cells, and triggers the thermal control when the temperature deviates from the normal operational range through "thermal fins", "air cooling system", or "liquid coolant system" [116, 70, 35, 99]. This control includes both cooling and heating, and existing controls are all or nothing, i.e., they cool/heat all the battery cells connected in parallel. Active fine-grained thermal control has also been proposed to reduce the safety margin, and then enhance the system performance based on its thermo-physical characteristics [69]. In principle, we increase the battery temperature for accelerating its chemical reaction if a large amount of power is required, and decrease the temperature when the battery needs to rest.

4.3 Problem Formulation and Solution

Thus far, we have discussed the requirements of a good BMS and our target BMS architecture meeting the requirements. To develop a good BMS, we should extend operation-time during the warranty period by maintaining the operating SOC, discharge-rate and temperature of battery within an efficient operational range. Presented below are a formal statement of our BMS problem and and an overview of our solution approach.

4.3.1 Problem statement

We have already introduced the target BMS architecture that can regulate battery temperature and discharge-rate for efficient use of batteries. The operating SOC range can be easily regulated. Specifically, the architecture regulates the temperature and discharge rate during every time interval, as described in Fig. 4.2 and the following matrix:

$$X = \begin{pmatrix} (I_{\text{bat}}, T_{\text{bat}})^{11} & \dots & (I_{\text{bat}}, T_{\text{bat}})^{1n} \\ \dots & \dots & \dots \\ (I_{\text{bat}}, T_{\text{bat}})^{m1} & \dots & (I_{\text{bat}}, T_{\text{bat}})^{mn} \end{pmatrix},$$

where $(I_{\text{bat}}, T_{\text{bat}})^{ij}$ are the battery discharge current and temperature during the j^{th} time interval of cycle i. A row vector consists of inputs $(I_{\text{bat}}, T_{\text{bat}})$ at every time interval from the start to the end of the battery operation (consisting of n intervals) in a cycle. Note that a charge/discharge cycle is defined as the process of fully charging a rechargeable battery and discharging it to a load. We need m input vectors for every cycle in the warranty period (consisting of m cycles). Therefore, battery temperature and discharge rate are the control knobs that can be scheduled at every time interval to improve the system performance in EVs as seen in Fig. 4.3. For instance, if we scheduled to store much energy into UCs from batteries and an RBS when the vehicle decelerates, we can supply more power when it accelerates while maintaining the battery discharge rate within an efficient operational range. Our goal is to maximize system performance by making the battery supply the required power to EV as long as possible by selecting the control knob matrix X. To evaluate the system performance, we introduced the operation-time (t_{o}) which measures how long the battery provides the EV the required power ($P_{\text{req}}(t)$). To increase the operation-time of battery, we should maintain battery output voltage

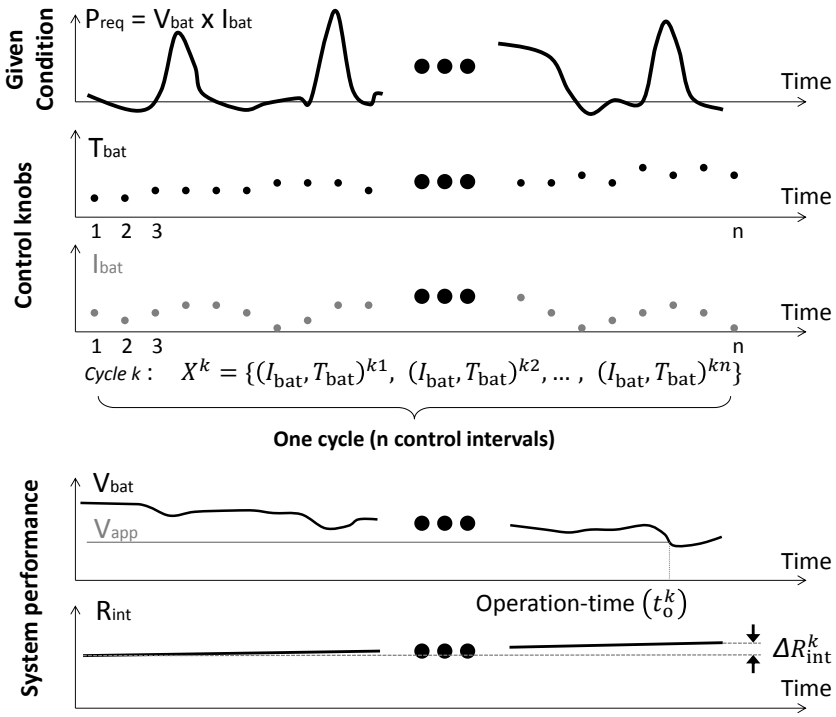

Figure 4.3: An example of discharge current (I_{bat}) and temperature (T_{bat}) controls under a given power requirement ($P_{\mathrm{req}}(t)$)

(V_{o}) above the applicable voltage (V_{app}) of motors as long as possible because it is the minimum required voltage for operating electric motors as shown in the last graph of Fig. 4.3. We also study the performance degradation of a battery, since it affects the operation-time (t_{o}) at later cycles in the warranty period. We estimate an internal resistance (R_{int}) at the first interval of each cycle to see the changes in the degradation. Note that the degradation depends on how the battery is used in previous cycles. Therefore, we should consider how battery degradation would change due to the control knob matrix X. Fig. 4.3 shows an example of their discharge-rate and temperature control over time (control interval) within a cycle for the given power requirement. The operation-time ends when the output voltage of battery reaches a certain pre-determined voltage value (which is dependent on the motors in EVs). During the cycle, battery degrades by ΔR_{int}.

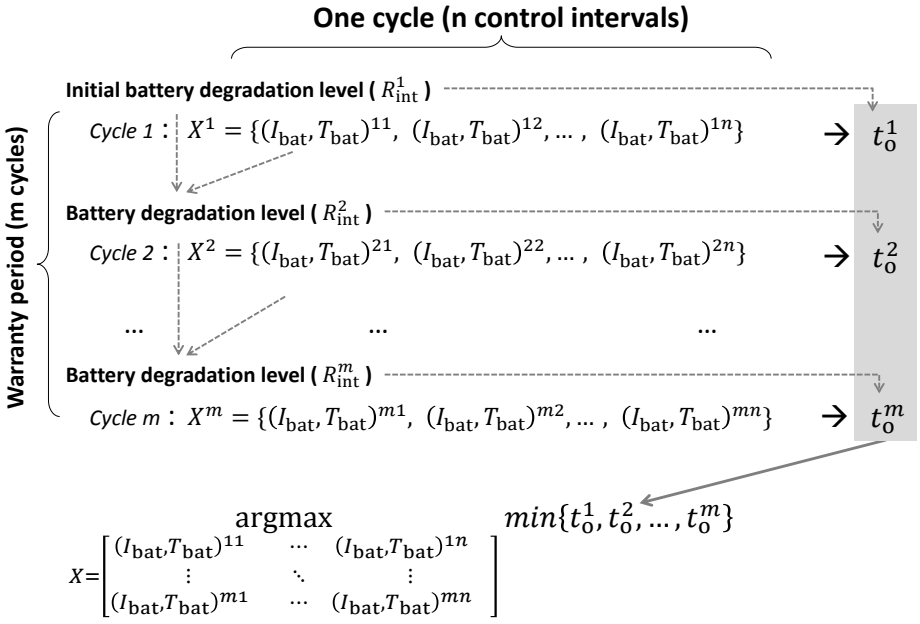

Figure 4.4: The k^{th} row of the control knob matrix X and the battery degradation level (R_{int}^k) at the k^{th} cycle affect battery operation-time at the k^{th} cycle. Our purpose is to find the control knob matrix X that maximizes the minimum operation-time.

With the above system model, assumptions and notations, Fig. 4.4 depicts our problem, which can be formally stated as:

Given power requirement $\{P_{\text{req}}(t)\}_{0<t<t_{\max}}$, n maximum control intervals, m warranty cycles, battery temperature upper bound (T_{ub}) and lower bound (T_{lb}), and battery discharge current upper bound (I_{ub}) and lower bound (I_{lb}),

determine the control knob matrix $X = \{X^1, \dots, X^m\}^T$ consisting of scheduling vectors $X^i = \{(I_{\text{bat}}, T_{\text{bat}})^{i1}, \dots, (I_{\text{bat}}, T_{\text{bat}})^{in}\}$ of battery discharge current (I_{bat}^{ij}) and temperature (T_{bat}^{ij}) at each control interval $j \in \{1, \dots, n\}$ for each cycle $i \in \{1, \dots, m\}$ so as to maximize the minimum operation-time $min\{t_{\text{o}}^1, \dots, t_{\text{o}}^m\}$ within the warranty cycles (m). The objective function of this optimization can then be defined as

$$\begin{aligned} &\underset{X}{\text{argmax}} && min\{t_{\text{o}}^1, \dots, t_{\text{o}}^m\}, \\ &\text{subject to} && T_{\text{lb}} < T_{\text{bat}}^{ij} < T_{\text{ub}}, \\ & && I_{\text{lb}} < I_{\text{bat}}^{ij} < I_{\text{ub}}. \end{aligned}$$

The reason for our focus on the minimum operation-time is that we want to maximize the EV's drivability during the entire warranty period. By finding the minimum operation-time, we can guarantee that the BMS is able to supply energy for the operation-time at any cycle within the warranty period. We also assume that the degradation in a cycle does not affect the operation-time in that cycle to simplify the problem. This assumption is reasonable because battery degrades very slowly and its change has a negligible influence on battery capacity within a cycle as seen in the supplementary file [66]. This assumption allows us to consider the control knob's impact on the operation-time and battery degradation separately.

We exploit both discharge-rate and thermal management to prevent the battery from a large voltage drop caused by high required current. By pre-charging UCs and transferring charges when the battery is required to supply large current, discharge-rate management can relieve the battery from discharge stresses while providing the required current to the electric load. Also, we can increase battery output voltage temporarily by increasing battery temperature, because it decreases battery internal resistance [69]. Boosting the output voltage via the discharge current and thermal management requires power, which may reduce the available energy from the battery for future usage. That is, we have to maintain battery output voltage while consuming the least amount of energy (E_{total}), since the output voltage is approximately proportional to the amount of the remaining energy in the battery. Therefore, to efficiently maintain battery output voltage, we have to consider the energy consumption as well.

4.3.2 Solution Approach from a CPS Perspective

Battery management requires understanding of chemical reactions since generating electricity entails complex chemical processes related to various physical con-

ditions. Battery output voltage is also affected by the physical conditions such as battery temperature, the discharge-rate and battery states. Therefore, we should figure out the relationship between the output voltage and controllable physical conditions (control knobs) and battery states (SOC, SOH). However, it is difficult to understand the electrochemical processes to capture the relationship between them. Also, each type of a battery has its own chemical reaction mechanism that generates energy. To make matters worse, battery behaviors and its performance are not the same even for the same type of batteries. To meet these challenges, we construct battery behavior models adaptively.

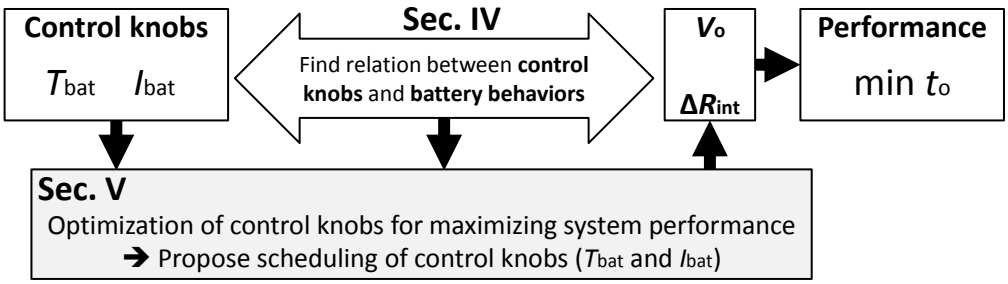

Figure 4.5: Approach overview: Section 4.4 describes how to refine a battery behavior model, and Section 4.5 propose how to determine control knobs (I_{bat} and T_{bat}) to maximize the performance based on the refined battery behavior model.

Fig. 4.5 depicts our CPS-perspective approach. Instead of using a pre-defined model, we first build a generic model that captures the battery behaviors related to measurable physical quantities. To adaptively construct its generic model, we employ an efficient regression scheme utilizing experimental data to distill online physical parameters that affect the battery behavior significantly. The generic model is then "customized" for each battery pack because each pack in different vehicles has different characteristics and works at different operation conditions. By using the model constructed above, we solve the problems and choose efficient control knobs for the effective operation conditions while considering its performance. Finally,

we propose a real-time scheduling policy that determines the discharge-rate and temperature of battery via an analysis of the solution.

4.4 Construction of Models for Battery Prognosis

As discussed in Section 4.3.2, we should characterize the impact of the control knobs on battery behaviors (V_o, R_{int}) and system performance ($min\{t_o\}$). To this end, we first explore measurable physical quantities that impact the system performance, and then describe how to extract effective physical quantities and/or their combinations. Finally, we construct battery behavior models based on these effective physical quantities for prognosis of batteries as shown in Fig. 4.6.

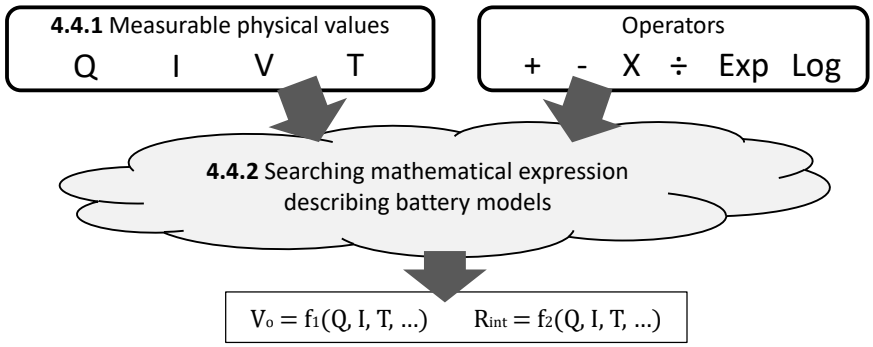

Figure 4.6: Building battery behavior models (output voltage and degradation model) for prognosis of batteries

4.4.1 Candidate physical quantities

Operation-time is the most important performance metric as it represents how long batteries can supply the required power, while *degradation rate* captures how quickly the operation-time deteriorates. So, we should figure out physical quantities affecting the battery behaviors and performance (operation-time and degradation rate) to prognose the batteries. Based on existing studies, we have identified candidate physical quantities affecting the battery operation-time and degradation as summarized in Table 4.1.

Physical quantities affecting operation-time

We identified three physical quantities that greatly affect battery operation-times: battery discharge/charge current ($I_{\mathrm{bat}}(t)$), the amount of discharges ($Q_{\mathrm{d}}(t)$), and battery temperature ($T_{\mathrm{bat}}(t)$).

The discharge/charge current ($I_{\mathrm{bat}}(t)$) is the most important physical quantity influencing the system performance in various ways [17, 34, 72]. A high discharge current reduces battery operation-time because such a high discharge current causes its output voltage to drop, and the battery to provide less energy than the battery with a lower discharge current, called the *rate-capacity* effect. On the other hand, during periods of low or no discharge current, the battery voltage can recover to a certain extent, which is termed the *recovery* effect. For instance, a high load causes a temporary voltage drop, and then a part of the cell voltage is recovered after a certain period of rest as shown in Fig. 4.7. The figure also shows that battery output voltage is dependent on the remaining charge in the battery, or *State-of-Charge* (SoC) $= 1 - \frac{Q_{\mathrm{d}}(t)}{Q_{\max}}$ [76]. Note that we can estimate the SoC based on the amount of discharge current ($Q_{\mathrm{d}}(t) = \int_0^t I_{\mathrm{bat}}(\tau) d\tau$). Meanwhile, battery temperature ($T_{\mathrm{bat}}(t)$) affects its operation-time. A higher temperature stimulates the mobility of electron or ion, temporarily increasing its capacity [110] with a reduced internal resistance.

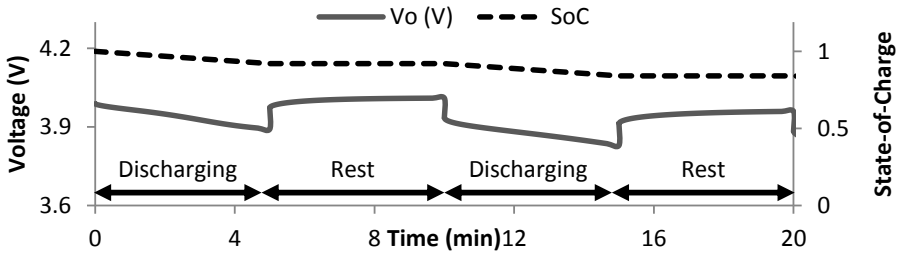

Figure 4.7: The output voltage (V_{bat}) and state-of-charge (SoC) when a battery is discharged at 23 A/m^2 of current and rested at 0 A/m^2 repeatedly. The results are extracted from evaluation tools/settings to be described in Section 4.6.

System performance	Physical quantity	Description
Operation-time (t_{o})	$I_{\mathrm{bat}}(t)$	Battery discharge/charge current
	$\frac{dI_{\mathrm{bat}}}{dt}(t)$	The rate change of battery discharge/charge current
	$\frac{dV_{\mathrm{bat}}}{dt}(t)$	The rate change of battery voltage
	$Q_{\mathrm{d}}(t) = \int_0^t I_{\mathrm{bat}}(\tau)d\tau$	The amount of discharged charge
	$T_{\mathrm{bat}}(t)$	Battery temperature
Degradation rate at k^{th} cycle ($\Delta R_{\mathrm{int}}^k$)	$\frac{1}{t_{\mathrm{o}}^k}\int_0^{t_{\mathrm{o}}^k} \lvert I_{\mathrm{bat}}(t)\rvert dt$	The average amount of battery discharge/charge current
	$Q_{\mathrm{d}}^k = \int_0^{t_{\mathrm{o}}^k} I_{\mathrm{bat}}(t)dt$	The amount of discharged charge
	$\int_0^{t_{\mathrm{o}}^k} T_{\mathrm{bat}}(t)dt$	Accumulative temperature exposure

Table 4.1: Physical quantities affecting system performance (operation-time (t_{o}) and battery degradation (ΔR_{int}))

Physical quantities affecting battery degradation

During the warranty period, the operation-time keeps on decreasing due to battery degradation (ΔR_{int}), and depends on the average amount of discharge/charge current ($\frac{1}{t_{\mathrm{o}}^k}\int_0^{t_{\mathrm{o}}^k} |I_{\mathrm{bat}}(t)|dt$), the amount of emitted charges (Q_{d}^k), and cumulative temperature exposure ($\int_0^{t_{\mathrm{o}}^k} T_{\mathrm{bat}}(t)dt$) at the k^{th} cycle as shown in Table 4.1. The average charge/discharge current ($\frac{1}{t_{\mathrm{o}}}\int_0^{t_{\mathrm{o}}} |I_{\mathrm{bat}}|dt$) affects the degradation rate of a battery. The battery degradation is known to accelerate exponentially with an increase of the discharge current density [92]. Also, performance degradation rate is closely related to how much energy is discharged in a cycle (Depth-of-Discharge, DoD) [103], which can be measured by SoC ($|SoC|_{t=t_{\mathrm{o}}}$) at the end of the cycle. On the other hand, the cumulative temperature exposure ($\int_0^{t_{\mathrm{o}}} T_{\mathrm{bat}}dt$) affects the degradation rate as explained next. The level of battery performance degradation depends on the time and thermal stresses to which the battery has been exposed, and it can be represented by a rise of battery internal resistance [137].

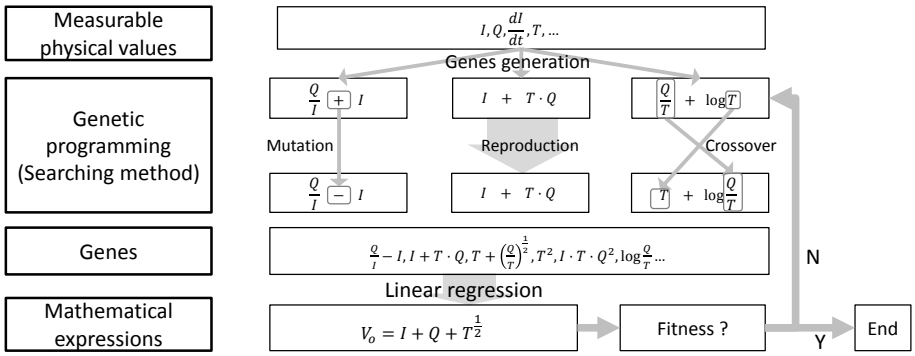

Step 1 : Generate random genes;
Step 2 : Generate genes for next generation via reproduction, mutation, and crossover of parent genes;
Step 3 : Execute ordinary least squares to regression to find weights of genes;
Step 4 : Check its fitness and jump to Step 2 if the fitness is not satisfied.

Figure 4.8: Symbolic regression process

4.4.2 Construction of a battery behavior model via symbolic regression with genetic programming

We have investigated physical quantities affecting battery output voltage and degradation. Here we discuss a systematic way to extract physical quantities and construct battery behavior models describing how they affect the output voltage and the rate of degradation from data. We first introduce symbolic regression with genetic programming for constructing battery behavior models. Then, we present the process of building a battery behavior model via the symbolic regression while addressing the issues in exploiting the regression scheme.

Symbolic regression with genetic programming

Symbolic regression is a type of regression analysis. This regression searches the space of mathematical expressions to find the model that best fits a given data set, both in terms of accuracy and simplicity [128, 11]. Unlike traditional linear and nonlinear regression methods that fit parameters to an equation of a given form,

symbolic regression searches both parameters and form of equations simultaneously. Searching for effective genes is done by *genetic programming*, which is an evolutionary algorithm-based method (inspired by biological evolution) to find the best mathematical expression as shown in Fig. 4.8 [75]. The symbolic regression with genetic programming has already been substantiated as its effectiveness for automated processes distilling the data into natural law model in the form of analytic mathematical expression [127]. Therefore, we exploit this regression scheme to construct accurate battery models, because chemical reactions occurring in batteries follow physical laws.

Battery behavior model construction process

Fig. 4.8 shows an example of the symbolic regression process to generate the battery behavior model. For the first generation, we generated genes ($\frac{Q}{I} + I$, $I + T \cdot Q$, $\frac{Q}{T} + \log\ T$) in a random way based on measurable physical quantities and mathematical operations. Then, we constructed the first battery behavior model consisting of the random genes with their weights. The model is tested in terms of its fitness, and then, if the fitness is not satisfied, we should explore other models to find a better one in a search space. In such a case, we generate genes for the next generation via a *mutation* ($\frac{Q}{I} + I \rightarrow \frac{Q}{I} - I$) and a *crossover* ($\frac{Q}{T} + \log T \rightarrow T + \log \frac{Q}{T}$) based on the parents' genes that have low weights. We execute a *reproduction* ($I + T \cdot Q$) of genes with large weights to leave the genes that are likely to critically affect the model. We check its fitness and repeatedly generate new generations until the fitness is satisfied.

In applications exploiting the symbolic regression, the identification of nontrivial relations is a major challenge. For example, $x^{\frac{1}{100}}$ can be selected for the gene because it may improve its fitness even if it would not affect the results much. Our key

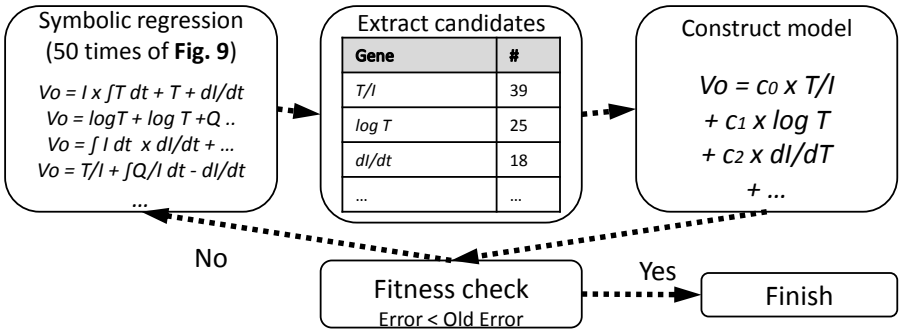

Step 1 : Execute symbolic regression 50 times and store the generated genes from the regression;
Step 2 : Sort the generated genes in order of occurrence and select genes that frequently occurs;
Step 3 : Construct generic behavior models based on the selected genes;
Step 4 : Check its fitness.

Figure 4.9: Algorithm for constructing a battery behavior model

insight into identifying nontrivial genes is that nontrivial genes would appear more than trivial genes. To find the most effective nontrivial genes for modeling battery behavior, we iterate the symbolic regression many times. Then, we sort the genes in the order of occurrence, and select the frequently appeared genes. For instance, at step 1, we executed 50 symbolic regressions and stored the generated genes. We select $\frac{dI}{dt}$, $\frac{T}{I}$, $\log T$ and so on, because it was generated frequently and thus likely to be nontrivial genes. Based on the extracted nontrivial genes, we construct the battery behavior model and repeat this process until the fitness is good enough to use them. Fig. 4.9 shows the entire process for constructing a battery behavior model.

4.5 Online scheduling of battery temperature and discharge/charge current

So far, we have built the battery behavior model affecting its operation-time and degradation rate. We now systematically schedule target operating conditions over cycles for solving the problem described in Section 4.3.1. Before presenting a scheduling policy, we first determine the relationship between performance metrics

(t_{o} and ΔR_{int}) and operating conditions (I_{bat} and T_{bat}) to get an insight into efficient schedulings of the operating conditions.

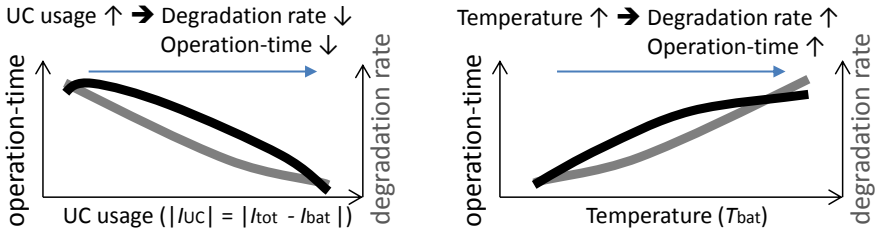

Figure 4.10: The effects of the thermal and discharge-rate control on the system performance.

4.5.1 Relationship between operation-time and degradation rate

Battery operation-time, degradation rate, and operating conditions are all closely related to each other. For example, old batteries whose internal resistances are high, cannot operate longer to power EVs than new batteries, recorded as follows:

- $R^i_{\mathrm{int}} \uparrow (\downarrow) \Longrightarrow t^i_{\mathrm{o}} \downarrow (\uparrow)$.

Also, the degradation rate depends on how the battery is used. Fig. 4.10 presents a general trend of operation-time and degradation rate related to the temperature and discharge/charge current. For instance, excessive use of UCs degrades its effectiveness because storing/extracting charge to/from UCs causes additional energy dissipation due to their internal resistance. In contrast, increasing use of UCs decelerates battery degradation since it can reduce battery discharge/recharge stress. Meanwhile, high temperature increases battery capacity by reducing battery internal resistance during an operation cycle. Unfortunately, continuous/frequent exposure to high temperature accelerates battery degradations. In summary, the following relation holds:

- $t^i_{\mathrm{o}} \downarrow (\uparrow) \Longleftrightarrow \Delta R^i_{\mathrm{int}} \downarrow (\uparrow)$.

These trends are used to maximize the minimum operation-time during the warranty

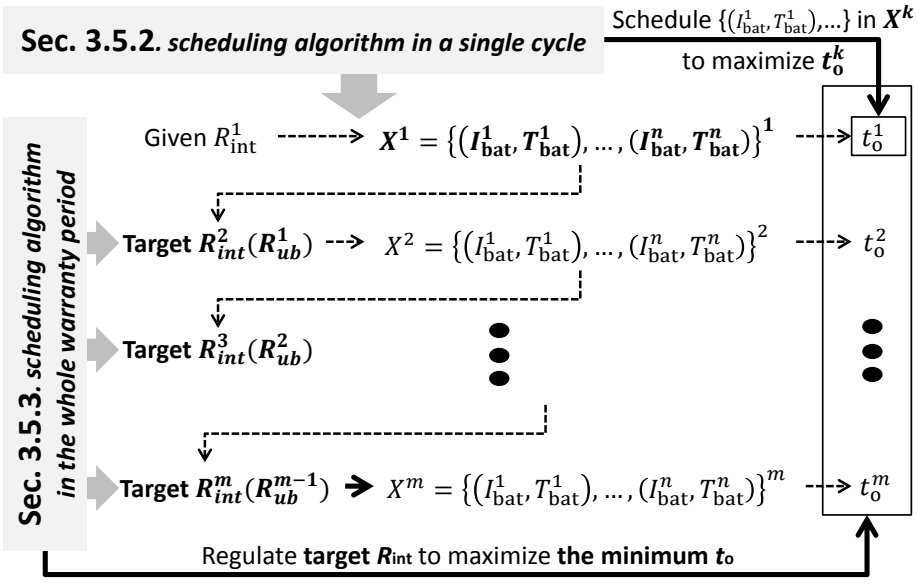

Figure 4.11: The entire scheduling process. Section 3.5.2 presents an algorithm determining a operating condition vector (X^{k}) for maximizing the operation-time (t^k_{o}) in a single cycle. Section 3.5.3 provides an algorithm of searching for the target degradation levels (R_{ub}) of each cycle for maximizing the minimum operation-time ($min\{t^1_{\mathrm{o}}, \dots, t^m_{\mathrm{o}}\}$).

period. Basically, we use a different control policy for a different cycle during the warranty period. For example, during very early cycles, we increase use of UCs at low temperature for future use of battery. In contrast, during late cycles of the warranty period, we focus only on its operation-time, rather than the degradation rate, because we do not have to consider the degradation level after the warranty period.

4.5.2 Scheduling algorithm in a single operation cycle

Fig. 4.11 shows the entire process of determining the operating condition matrix X. We first represent a scheduling policy to maximize operation-time (t_{o}) for the target degradation level (R_{int}) in a single cycle. Note that the target degradation level (R^{k+1}_{int}) is key in regulating the operation-time (t_{o}) of each cycle so as to maximize the minimum operation-time. Section 4.5.3 details how to determine the target degradation levels (R^{k+1}_{int}) to maximize the minimum operation-time during the entire

Algorithm 1 Algorithm for optimization in a cycle

1: **procedure** PROC1($R_{\rm ub}$,$R_{\rm int}$,$P_{\rm req}$)
2: $X_{\rm k} \leftarrow X_{\rm k}$ that has no additional power for the auxiliary devices;
3: /* Reduce $\Delta R_{\rm int}$ via $X_{\rm k}$ control if it is larger than the target $\Delta R_{\rm int}$ */
4: **while** $R_{\rm ub} < R_{\rm int}$ **do**
5: Set a target accumulative physical quantities that reduce $\Delta R_{\rm int}$
6: **end while**
7: $X_{\rm k} \leftarrow$ Search $X_{\rm k}$ maximizing $t_{\rm o}$ at $P_{\rm req}$ and maintaining the target cumulative physical quantities via the discharge current and temperature scheduling (Supplement file)
8: /* We can estimate $t_{\rm o}$ and $\Delta R_{\rm int}$ at X^k for supplying $P_{\rm req}$ via the behavior models constructed in Section 3.4*/
9: **return** $[t_{\rm o}, R_{\rm int}, X_{\rm k}]$;
10: **end procedure**

warranty cycle.

Scheduling requirement in one operation cycle

To maximize the operation-time in a cycle, we should maximize the time duration during which battery output voltage is within an applicable range for motors' operation while supplying the required energy. In the example in Fig. 4.12(a), the battery cannot supply the required power with an applicable voltage after initial $t_{\rm o}$, the operation-time of this scheduling, potentially stopping the motor operation. To increase operation-time, we have to compensate the voltage shortage by relieving the discharging stress or helping chemical reactions in the battery via discharge current and/or temperature control. In the meantime, we have to maintain the battery degradation level ($R_{\rm int}$) within the required range ($< R_{\rm ub}$) for its future usability. The next subsection provides a detailed algorithm for extending operation-time while keeping the degradation rate below the specified level.

Algorithm for a single cycle

Algorithm 1 describes how to determine vectors of ($I^i_{\rm bat}$, $T^i_{\rm bat}$) in a single cycle. Initially, the minimum use of the thermal fins or energy buffers is set (Line 2). It would not be the best solution because the required degradation rate may not be

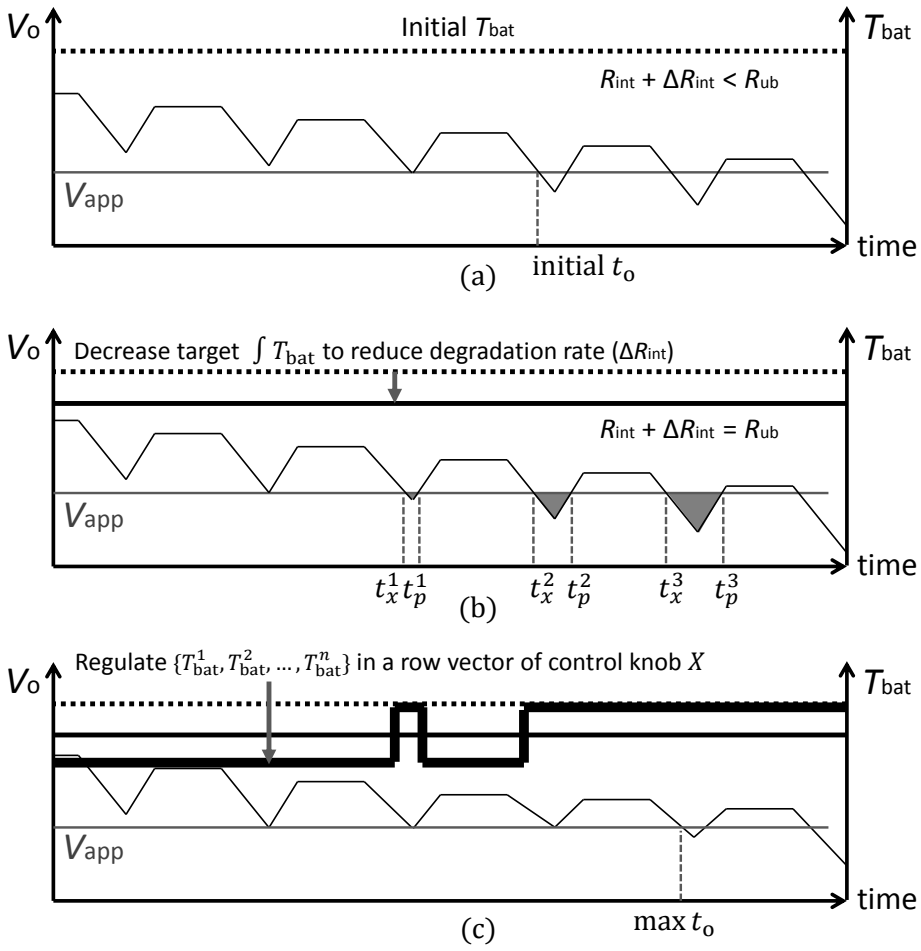

Figure 4.12: An example of the temperature scheduling in a cycle

satisfied and/or the output voltage of battery could be dropped quickly as shown in Fig. 4.12 (a). First, to meet the required degradation rate at the k^{th} cycle, steps (Line 4–6, Fig. 4.12 (b)) determine the target cumulative physical quantities affecting the degradation. The final step (Line 7, Fig. 4.12 (c)) determines a pair of (I^i_{bat}, T^i_{bat}) of each control interval to compensate as many voltage drop periods as possible while maintaining the required cumulative physical quantities. A detailed algorithm for Line 7 is presented in the supplementary file [66].

Algorithm 2 Algorithm for optimization within a whole period

1: **procedure** PROC2($N_{\mathrm{w}}, R_{\mathrm{ub}}, R^1_{\mathrm{int}}, P_{\mathrm{req}}$)
2: $[t^1_{\mathrm{o}}, R^2_{\mathrm{int}}, X^1] \leftarrow$ PROC1(∞, R^1_{int}, P_{req});
3: **for** $i = 2; i \leq N_{\mathrm{w}}; i{+}{+}$ **do**
4: $[t^i_{\mathrm{o}}, R^{i+1}_{\mathrm{int}}, X^i] \leftarrow$ PROC1(∞, R^i_{int}, P_{req});
5: $R^{i-1}_{\mathrm{UB}} \leftarrow R^i_{\mathrm{int}}$
6: **while** $t^i_{\mathrm{o}} \neq t^{i-1}_{\mathrm{o}}$ **do**
7: // To increase t_{o}, decrease R_{int}
8: $R^{i-1}_{\mathrm{ub}} \leftarrow R^{i-1}_{\mathrm{ub}} - 0.01$;
9: $[t^{i-1}_{\mathrm{o}}, R^i_{\mathrm{int}}, X^{i-1}] \leftarrow$ PROC1(R^{i-1}_{ub}, R^{i-1}_{int}, P_{req});
10: $[t^i_{\mathrm{o}}, R^{i+1}_{\mathrm{int}}, X^i] \leftarrow$ PROC1(R^i_{ub}, R^i_{int}, P_{req});
11: **end while**
12: **end for**
13: **return** $[t_{\mathrm{o}}, X]$;
14: **end procedure**

4.5.3 Scheduling algorithm during the whole warranty period

So far, we proposed a scheduling algorithm for maximizing operation-time in a cycle while satisfying the required degradation rate (ΔR_{int}). We now expand the algorithm for the whole warranty period to maximize the minimum operation-time (min $\{t_{\mathrm{o}}\}$) based on the impact of battery thermal and discharge-rate control on the operation-time and degradation rate.

Optimization within warranty period

Algorithm 2 determines the target degradation rate (R_{ub}) for each cycle to maximize the minimum operation-time. At the first step (Line 2), the temperature and discharge current are scheduled without considering the battery degradation rate as shown in Fig. 4.13 (a). The battery temperature would be set only for its safety, and therefore UCs are used as little as possible to save additional energy consumption by the auxiliary devices. Next, the target degradation level is regulated for the present cycle (Line 8) to increase the operation-time during the next cycle. Even if it may cause inefficiency in terms of the operation-time of the present cycle, we can improve the overall system performance by increasing the worst-case operation-time during

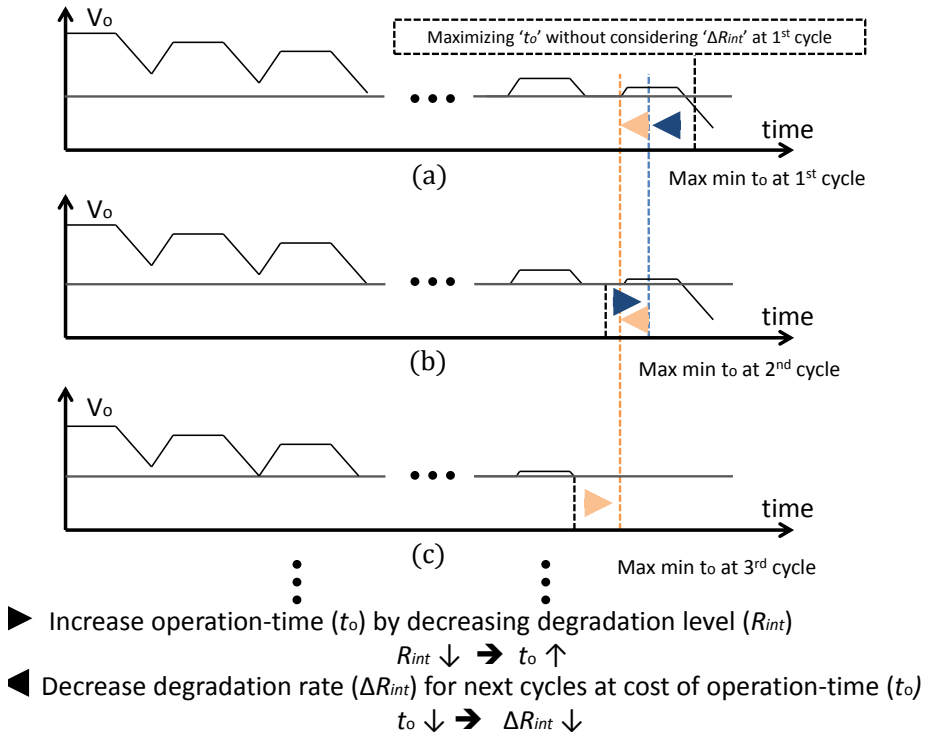

Figure 4.13: Determination of each target R_{int} to maximize the minimum operation-time

the warranty period. We iterate this process until all the operation-times become similar as shown in Figs. 4.13 (b) and (c).

4.5.4 Real-time scheduling algorithm

To schedule the temperature and discharge current needed to achieve our goal, we first solve the scheduling problem for a given power requirement. Typically, the future power requirement is unknown, because it depends on a number of variables, including, but not limited to, driving conditions, vehicle type, and road conditions. But, solving for a given power requirement allows for the creation of an implementable schedule. Using past power requirement patterns, we can determine the amount of power needed for a few seconds of battery usage [68]. Based on these patterns, we can adopt a power requirement predictor and determine the discharge current and temperature in real time based on the prediction as shown in Fig. 4.14. We should

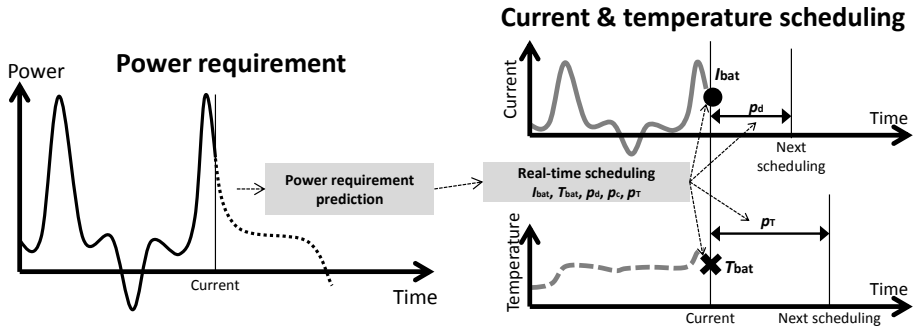

Figure 4.14: Real-time prediction and scheduling for battery discharge current and temperature

also determine the frequency at which discharge current and temperature must be determined (scheduling period). This scheduling period is used to preclude batteries from inefficient usage.

Algorithm 3 Algorithm for real-time discharge current scheduling

```
1: procedure PROC3(I_tot, I*_bat)
2:     while Driving do
3:         if Recharge then
4:             I_bat = 0;
5:             Sleep(p_c);
6:         else if I_bat < I*_bat then
7:             I_bat = I_tot;
8:         else
9:             I_bat = I*_bat;
10:            Sleep(p_d);
11:        end if
12:    end while
13: end procedure
```

The scheduling results shown in Fig. 4.18 give insight into the real-time scheduling of the discharge current. The UCs should be fully recharged when the braking system generates energy. They can then supply some of the stored charge to the motor, based on the target degradation rate. Algorithm 3 schedules discharge current in real time. It requires both the present total discharge current (I_{tot}) and the target battery discharge current (I^*_{bat}) needed to control the degradation rate. First, when the power is recharged from the braking system, the battery current is set to 0 to charge the UC. Then, the discharge current is rescheduled after p_{c}. If the battery is discharged

to the electric load, the target battery discharge current is determined based on its amount. If it is in the normal discharge range ($I_{\text{bat}} < I^*_{\text{bat}}$), the battery is allowed to supply charges to the load ($I_{\text{bat}} = I_{\text{tot}}$). If it is outside of the normal range, the UC provides charges to maintain the battery discharge current ($I_{\text{bat}} = I^*_{\text{bat}}$). Later, the discharge current is scheduled (p_{d}). The scheduling period (p_{d} and p_{c}) must be determined carefully for real-time scheduling. Otherwise, it may lead to additional power consumption. For instance, if the discharge current is not rescheduled in time, the battery discharges energy to the UC, even though the UC does not require power. From the power requirement prediction, the length of the discharge/charge period can be estimated (p^*_{d} / p^*_{c}). We set p_{d} (p_{c}) to p^*_{d} (p^*_{c}) over 10. Real-time temperature scheduling is similar to the discharge current scheduling, and thus we omitted the result.

4.6 Evaluation

We now evaluate the proposed battery model construction and scheduling of battery temperature and discharge/charge current. We first describe tools and setups for the evaluation, and then demonstrate the accuracy of battery behavior predictions and performance improvement by our scheduling system.

4.6.1 Evaluation settings

To test the proposed model construction, we exploit real data including battery discharge/charge current (I_{bat}), temperature (T_{bat}), and output voltage (V_{o}) by using Neware's battery tester [101]. We measure the performance improvement of the proposed temperature and current scheduling by using commonly-used vehicle (*Advisor 2.0*) [106] and battery simulator (*Dualfoil5*) [40]. To make the simulation more realistic, we obtained real driving data from "The US Environmental Protection Agency

(EPA)" and "California Air Resources Board" such as ARB02, SC03 and LA92.

4.6.2 Evaluation results

Our goal is to maximize the minimum battery operation-time during the warranty period by determining efficient battery temperature and discharge/charge current. For effective temperature and current schedules, we constructed a battery behavior model. We evaluate the following schemes for modeling battery voltage and degradation rate:

- V-LR: battery voltage model via linear regression with a circuit-based battery model;
- V-SVR: battery voltage model via support vector regression;
- V-SR: our battery voltage model via symbolic regression described in Section 4.4;
- R-LR : battery degradation rate model via linear regression with temperature (*likewise* discharge current) linear degradation model;
- R-SVR : battery degradation rate model via support vector regression;
- R-SR: battery degradation rate model via symbolic regression with described in Section 4.4.

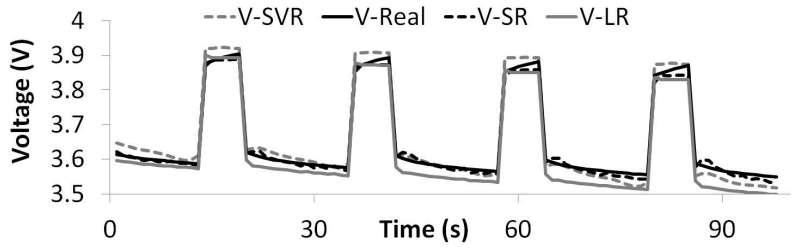

Figure 4.15: An example of battery output voltage predictions.

Table 4.2 shows the error of the constructed model of V-SR, V-SVR and V-LR for battery output voltage prediction, and Fig. 4.15 plots their predictions. Root-mean-square error (RMSE) is used to measure the prediction accuracy. As shown

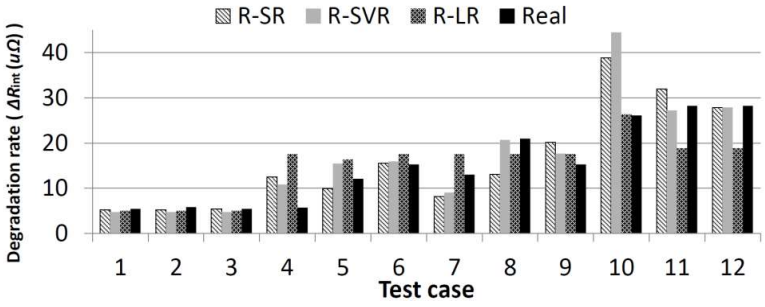

Figure 4.16: Degradation rate predictions. We use 12 degradation patterns from the battery tester. We select 10 degradation patterns to build a degradation model and validate the model with 2 remaining degradation cases. The validation process is then repeated 6 times (6-fold cross-validation).

in this table, V-SR improves the accuracy of the model by up to 67.9% (49.8%), compared to V-LR (V-SVR). The basis form of V-LR is a circuit-based battery model whose internal resistance depends on temperature exponentially [69]. However, at low temperature, the accuracy of the model is lower than that of V-SR, because the exponential internal resistance model is correct only for a specific range of temperature. So, while V-SVR predicts the output voltage more accurately than V-LR, V-SR has the best overall prediction accuracy of the three output voltage models. Table 4.3 and Fig. 4.16 show the errors of degradation predictions. R-SR shows improvements of prediction accuracy by 5.6% and 8.0% over R-LR and R-SVR, respectively. That is, the degradation rate model constructed based on various physical quantities yields an accurate behavior model to predict the battery's states.

Prediction methods	prediction error $E(V_o)$
V-LR	0.00336
V-SVR	0.00215
V-SR	0.00108

Table 4.2: Average error of battery output voltage prediction

Performance of the proposed scheduling policy

We have evaluated the following three discharge/charge current and temperature scheduling schemes:

Prediction methods	prediction error E(R_{int})
R-LR	1.626
R-SVR	1.668
R-SR	1.535

Table 4.3: Average error of battery degradation prediction (R_{int})

- Const-TI: fixed operational temperature and discharge-rate;
- Opt-TI: our scheduling scheme described in Section 4.4;
- RT-TI: our real-time scheduling scheme described in Section 4.4.

	Minimum operation-time (t_o) (s)		
Prediction methods	ARB02	LA92	SC03
Const-TI	407	331	321
Opt-TI	451	396	595
RT-TI	407	368	554

Table 4.4: Minimum operation-times

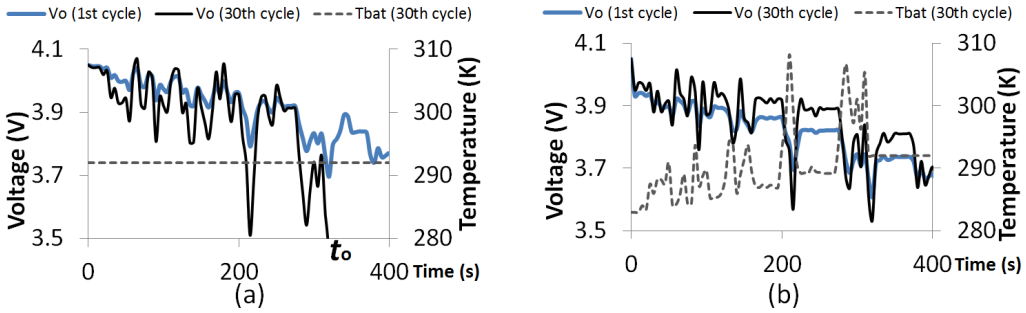

Figure 4.17: Voltage profiles during the first cycle and the last cycle (30) for SC03 driving under Opt-TI scheduling. Compared to Const-TI, the voltage drop was tolerable due to pre-heating the battery and lower degradation level.

We ran simulation and extracted operation-times during the warranty period of each scheme under various electric loads. The minimum operation-times are then extracted to evaluate the schemes. As shown in Table 4.4, Opt-TI improves the minimum operation-time by up to 10.8% at ARB02, 19.6% at LA92 and 85.3% at SC03, respectively, over Const-TI. Figs. 4.17 (a) and 4.18 present examples of battery voltage and scheduled temperature (T_{bat}) and battery discharge/charge current (I_{bat}) under Opt-TI during the first and the last cycles. The algorithm pre-heats

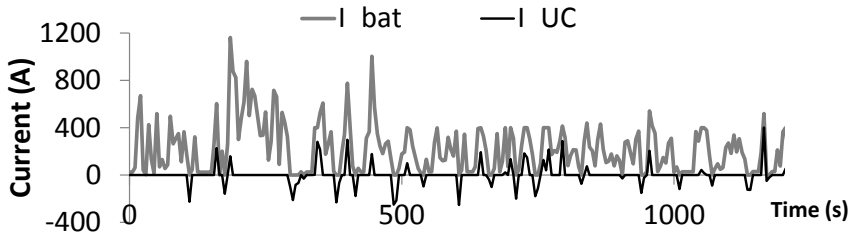

Figure 4.18: UC current (I_{UC}) profile for SC03 under Opt-TI. I_{UC} helps the battery when it is required to supply high power by mitigating the discharge/charge stress to the battery.

batteries and pre-charges UCs to preclude the batteries from a fast voltage drop. By comparing Figs. 4.17 (a) and (b), we can see the differences between Const-TI and Opt-TI during early cycles and late cycles. As we discussed in Section 4.5.3, Opt-TI utilizes the thermal and discharge/charge current management much at early cycles to decelerate the battery degradation. Then, it maximizes operation-time without considering its degradation during late cycles. Therefore, although battery output voltage during early cycles of Opt-TI (in Fig. 4.17 (b)) is lower than that of Const-TI (in Fig. 4.17 (a)), Opt-TI could maintain the output voltage within the applicable range longer than Const-TI during the last cycle, because Opt-TI decelerated the battery degradation during early cycles. The battery behavior models constructed in Section 4.4 enable our BMS to determine a pair of $(I_{\mathrm{bat}}, T_{\mathrm{bat}})$ at each control interval under Opt-TI, because they allow the BMS to predict battery operation-time and degradation rate with respect to $(I_{\mathrm{bat}}, T_{\mathrm{bat}})$ schedules. The derived real-time prediction model, RT-TI, determines the temperature and discharge current of a given cycle, while the target degradation rate is calculated by the model Opt-TI. The simulation shows that the minimum battery operation-time of RT-TI is generally similar to the LA92 and SC03 cases of the Opt-TI model. However, certain conditions, like highly variable driving patterns in one case (ARB02), reduced the operation-time of the RT-TI model. In extreme cases, like ARB02, the minimum battery operation-time

is similar to the Const-TI.

4.7 Conclusion

In this chapter, we have proposed a new integrated BMS that schedules the amount of energy pre-charged into UCs and battery temperature at each control interval based on the analysis of their impact on the battery capacity and degradation. We have also proposed a battery prognosis scheme, which is able to predict when the battery cannot provide the required power. Our evaluation with real battery data and realistic driving simulation shows that the proposed schemes make a significant improvement in BMS's efficiency over a simple method used in the existing BMSes for EVs.

In future we would like to improve the BMS using the proposed architecture. Primarily, the accuracy of the prognosis scheme and power requirement predictions should be enhanced for efficient discharge/charge current and temperature schedule. This could be achieved by increasing the accuracy of the battery behavior and power requirement models. For this, we have to process the model construction after acquiring lots of battery behavior and driving data under various conditions via a remote prognosis system. Our framework can also be used for other types of batteries including fuel cells which have their own power and energy densities, because battery behavior models are extracted by using behavior data of the batteries installed in the system, and scheduling discharge/charge current and temperature of the batteries based on the constructed behavior model.

CHAPTER V

Real-Time Battery Thermal Management for Electric Vehicles

5.1 Introduction

As many researchers pointed out [13, 32, 63, 85], temperature is one of the most critical factors in designing and operating EVs. For example, an extremely high temperature may lead to malfunction or performance degradation of battery cells. In contrast, a battery system operating at a very low temperature might be dysfunctional or have a low capacity due to low reaction rates with freezing electrolytes. In addition, the discharge rate of cells varies with temperature, altering their capacity.

To address the challenges related to temperature, most automotive manufacturers have developed their own thermal management systems for their EVs [35, 99]. That is, a BMS (Battery Management System) monitors the temperature of battery cells, and triggers the thermal control when temperature deviates from the normal operational range. This control includes both cooling and heating, and existing controls are all or nothing—whether or not they cool/heat *all* the battery cells connected in parallel. However, such coarse-grained controls result in a large safety margin and hence inefficiency. More importantly, they do not exploit temperature for more efficient management, in that more sophisticated controls of temperature even within the normal operational range may yield better battery performance.

The goal of this chapter is to develop thermal management for an efficient and reliable BMS. Efficiency is defined by "the ratio of the useful energy delivered by a dynamic system to the energy supplied to it" [96]; we achieve efficiency by maximizing *operation-time* [72], or the cumulative time for a BMS to provide the required power after a full charge. We achieve reliability by guaranteeing that a BMS provides the required power throughout the given battery warranty period without an explosion or malfunction, while letting its cells undergo charge-and-discharge cycles.

To improve efficiency without compromising reliability, we need a *cyber-physical perspective* of battery thermal management, integrating and coordinating between cyber and physical parts. For physical parts, we should understand thermo-physical characteristics of battery cells and external thermal stress conditions, as they have significant impact on battery performance. By carefully accounting for these non-linear physical properties and abstracting the characteristics in the cyber space as shown in Fig. 5.1, we can develop desirable thermal management that reduces the safety margin, thereby increasing the efficiency of the entire battery system in EVs.

To achieve this goal, we use temperature as a control knob; beyond a simple temperature control only for the normal operational range, we design a battery thermal management system, which actively controls temperature for more efficient and reliable operations. This requires understanding the thermal and general issues of batteries that affect the efficiency and reliability. Therefore, we analyze the issues based on battery thermo-physical characteristics and their impact on the electrical state of battery cells. Based on this analysis, we derive strategies in achieving the goal, and then propose a battery thermal management system with cell-level thermal controls. Our policy boosts the performance of cells temporarily when high power is required, while resting cells otherwise to reduce stresses; we will present details of

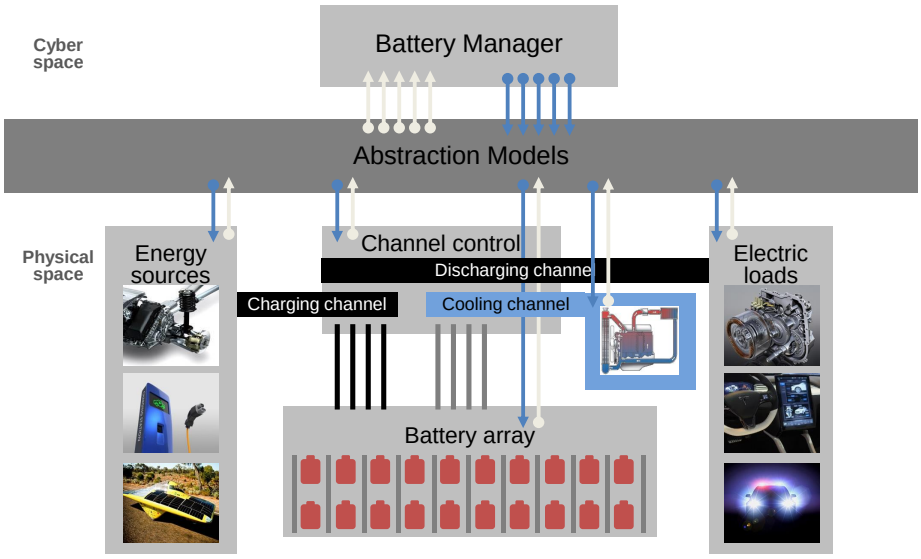

Figure 5.1: Cyber-physical perspective for a BMS

our policy along with their underlying principles. To evaluate the proposed BMS, we adopt realistic workloads based on real driving patterns, and simulate them with a widely-used battery simulator. Our simulation results demonstrate the effectiveness of the proposed battery thermal management, improving the operation-time up to 58.4%, without sacrificing reliability, over the existing BMS.

This chapter makes the following three main contributions:

- Abstraction of thermo-physical characteristics in the cyber-space to address the issues associated with efficient and reliable thermal management;
- Design of a battery thermal management system with a new architecture, which is, to our best knowledge, the first comprehensive study to exploit temperature as a control knob for BMSes; and
- In-depth evaluation of the proposed thermal management, demonstrating its significant improvement of efficiency without compromising reliability.

The chapter is organized as follows. Section 5.2 presents general and thermal management approaches in existing BMSes, and Section 5.3 formally states the problem

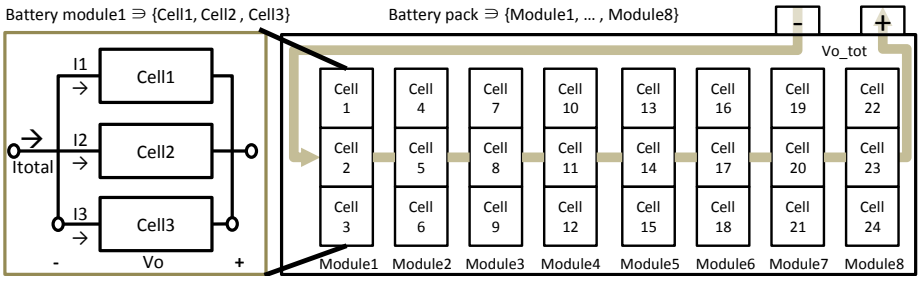

Figure 5.2: A battery pack with modules and cells

we want to solve via thermal management. Section 5.4 describes physical characteristics related to thermal and general issues of large-scale battery systems, and Section 5.5 presents our battery thermal management system. Section 5.6 evaluates our system via realistic simulations, and finally, Section 5.7 concludes the chapter.

5.2 Background

As illustrated in Fig. 5.2, a battery pack consists of some interfaces (e.g., electrodes) and several battery modules, each of which is composed of several battery cells. In a battery module, all the battery cells are connected in parallel, reducing the possibility of battery failure caused by a cell-level failure. The modules in a pack are usually connected in series, enabling the battery pack to provide a high voltage and power.

A BMS is responsible for powering EVs while protecting hundreds/thousands of battery cells from damage and keeping them in an operational condition. For a BMS to perform these functions, battery cells should be properly controlled because their safety and performance depend on stress conditions around them. In this section, we discuss the battery properties and the related work thereof.

5.2.1 Battery Scheduling for Efficient Battery Management

Rate-capacity and recovery effects are the most prominent physical properties for efficient battery management. The rate-capacity effect means that the higher the discharge rate, the lower the deliverable capacity. The recovery effect means that a rest restores the output voltage temporarily dropped by large discharge current. Therefore, we can increase the capacity of batteries, by minimizing the discharge rate per cell and resting battery cells.

State-of-Charge (SoC) represents percentage of deliverable charge, from 0% with no charge, to 100% with full, and balancing SoC is one of the most critical issues affecting the performance of large-scale battery systems because the performance of a large battery pack depends on the electrical state of the most worn battery cell in the pack.

To achieve better battery performance, a line of work has focused on *battery scheduling* that equalizes SoC and/or reduces the discharge rate [17, 55, 59, 71, 72]. They control switches to draw energy from battery cells at a proper discharge rate. For example, when an electric motor needs high power, a battery manager connects all the cells to the electric load to improve battery efficiency. In contrast, when the motor demands low power from the battery, the battery manager disconnects some cells with low SoC, achieving recovery of the output voltage and equalization of SoC.

5.2.2 Thermal Management of Large-scale Batteries

Besides discharge behaviors and SoC balancing, battery thermal characteristics are also important to their efficiency, operation and safety. Of many characteristics, we will focus on the following two major characteristics. First, battery efficiency improves temporarily at "instant high temperature" due to the increased chemical reac-

tion rate and ion mobility. However, the "cumulative exposure to high temperature" causes the permanent lifetime to decline because of its acceleration of irreversible side reaction. Therefore, most BMSes are required to restrict each cell within a certain temperature range to achieve reasonable performance. Every EV must thus be equipped with a thermal management system that keeps cell temperature within the operational range, requiring both cooling and heating. Whenever the temperature of a battery pack deviates from an operational temperature range, thermal management is activated to guarantee thermal stability of batteries [35, 99, 70, 115, 116].

For cooling, the radiator transfers heat from the fluid inside to the air outside, thereby cooling the fluid, which in turn cools batteries. Heating is also required for driving at extremely cold temperature. For example, GM Chevy Volt [99] uses 144 thermal fins to actively cool/heat 288 battery cells with a coolant flow valve controlling cooled/heated coolant flows. Ford Focus [35] is also equipped with an active liquid-cooling and heating system for thermal management of its lithium-ion battery packs.

So far, this simple approach has been effective for the normal operation of battery cells during a vehicle warranty period; a warranty can be made by thoroughly testing battery cells' performance in thermal experiment chambers. However, such a passive, coarse-grained thermal control does not take full advantage of thermal management systems. By understanding battery thermal characteristics and controlling temperature, we can improve battery's capacity without compromising the lifetime of battery cells. This is because heating the cell increases the battery performance instantaneously, while cooling the cell for the situation of requiring low power can delay the drop of lifetime. To regulate cell temperature systematically, we analyze battery dynamics and propose active and cell-level thermal management for more

efficient and reliable BMSes.

5.3 Problem Statement

In this chapter, we would like to develop "good" thermal management for more efficient and reliable battery systems. For this, we state the problem of thermal management for which we first introduce relevant terms.

A battery pack in EVs supplies DC power to an inverter which operates the electric motors in EVs. To operate motors, a power inverter needs an applicable input voltage (V_{app}) during the vehicle's operation. Then, the *operation-time* (ℓ_{op}) is defined as the cumulative time for a battery pack to provide the required power with applicable output voltage range after a full charge [72].

Therefore, a BMS should enable its battery pack to supply the required power ($P_{req}(t)$) to electric motors while maintaining output voltage no less than the applicable input voltage for a long operation-time. Meanwhile, the operation-time should be kept long during the battery warranty period; otherwise, the vehicle requires a larger battery pack and/or batteries must be recharged more frequently.

In this chapter, we want to develop a BMS that yields a long operation-time during the warranty period by controlling the temperature of battery cells. We can control battery temperature by selecting the coolant type in each thermal fin at each time instant to be cooled or heated, which will be detailed in Section 5.5.3. That is, the coolant type is used as a control knob for our BMS. Our goal is then to determine the coolant type at each time instant ($C_{fin}(t)$) such that the operation-time (ℓ_{op}) is maximized during the warranty period without any malfunction or explosion, which is formally expressed as:

Given stress conditions $\{P_{req}(t), T_{ext}(t)\}_{0<t<t_{warr}}$, determine $\{C_{fin}(t)\}_{0<t<t_{warr}}$, such

that ℓ_{op} is maximized at t_{warr} without any malfunction or explosion in [0, t_{warr}], where $T_{ext}(t)$ is temperature outside the battery pack, and 0 and t_{warr} are the time at the beginning and end of the battery warranty period, respectively. Note that the stress conditions and the control of $C_{fin}(t)$ are valid/necessary only during operation of the EV in [0, t_{warr}].

Note that ℓ_{op} monotonically decreases over time, because the performance of a battery keeps on degrading over time and never recovering. Therefore, ℓ_{op} at any time during the warranty is at least as much as that at t_{warr}.

5.4 Abstraction of Physical Dynamics of Batteries

Several battery dynamics under stress conditions affect the performance and safety of battery systems. For example, uncontrolled high temperature may cause explosion, while an extremely low temperature reduces the battery's performance, potentially leading to failure to power the electric vehicle. Therefore, the impacts and dependencies of control knobs and external conditions on battery dynamics should be analyzed to improve the safety and performance of a battery system.

To this end, we will first identify the factors that affect the performance by bridging different abstraction models for battery physical dynamics. Then, based on the unified abstraction model, we will address how a change in temperature affects battery physical dynamics, which will be a basis for our battery thermal management to be described in Section 7.5.

5.4.1 Abstraction of Battery Characteristics

By analyzing the dependency on thermal conditions and the impacts on states of batteries, we can figure out how controllable thermal conditions affect the output voltage of the entire battery system and each cell's temperature.

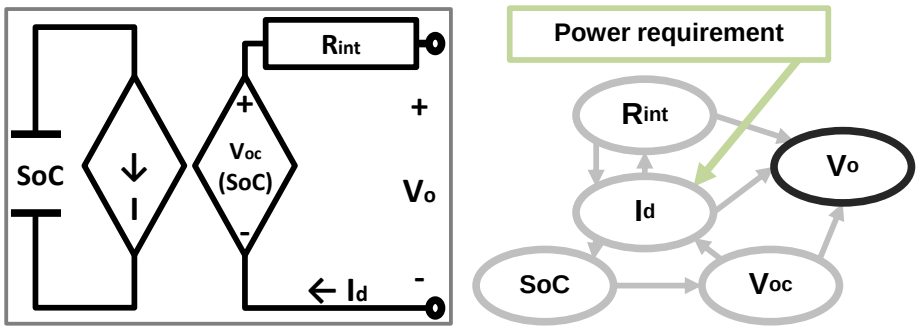

Figure 5.3: Circuit-based battery model

Circuit-Based Battery Model ($V_o = f(R_{int}, I_d, SoC)$)

Output voltage (V_o) dictates the operation-time of a battery system, and the output voltage is greatly affected by battery cells' internal states. A circuit-based battery model uses fundamental electric elements, such as internal resistance (R_{int}), discharge current (I_d), and open-circuit voltage (V_{oc}) to represent the cell's internal states, and explains the output voltage by basic circuit theory as described in Fig. 5.3 and Eq. (5.1).

When the cell is connected to an external load, an electron flow (I_d) occurs from the anode to the cathode through the external load. Open-circuit voltage (V_{oc}) is the difference of electrical potential between two terminals of the cell when disconnected from any circuit, and it largely depends on deliverable charges (SoC) in battery cells. The internal resistance (R_{int}) represents all the factors causing voltage drop between open-circuit voltage (V_{oc}) and output voltage (V_o) when the power source delivers current. In addition, large capacitors are adopted to represent states of deliverable charge (SoC) of cells. Then, the output voltage is expressed as [85]:

$$V_o = V_{oc} - I_d R_{int} = f(SoC) - I_d R_{int}, \tag{5.1}$$

which says that a change in internal resistance affects output voltage as follows:

P1. Internal resistance $\Rightarrow$ Output voltage ($R \uparrow \rightarrow V_o \downarrow$): As the internal resistance

gets higher, the output voltage decreases.

Supplying the required power (P_{req}) to the electric load induces power dissipation (P_d) in a battery pack. That is, total power consumption (P_{bat}) in a battery pack (P_{bat}) consists of the two power consumption parameters (P_{req} and P_d) as shown in the following equation [85]:

$$\begin{aligned} V_{oc} = V_o + I_d R_{int} \;&\Rightarrow\; V_{oc} I_d = V_o I_d + I_d^2 R_{int} \\ &\Rightarrow\; P_{bat} = P_{req} + P_d. \end{aligned} \tag{5.2}$$

Therefore, to use batteries efficiently and increase the operation-time of a battery pack, a BMS should reduce power dissipation (P_d) during operation, which is recorded as follows.

P2. Internal resistance ⇒ Power dissipation ($R\uparrow \rightarrow P_d\uparrow$): As internal resistance gets higher, power dissipation increases.

Since the output voltages of the cells connected in parallel should be the same and the variation of open-circuit voltage is small, discharge current depends on internal resistance according to Eq. (5.1). Then, the discharge current of a cell with larger internal resistance is lower than that of the other cells in the module, as recorded in the following statement:

P3. Internal resistance ⇒ Discharge rate ($R\uparrow \rightarrow I_d\downarrow$): As internal resistance gets higher, the discharge rate per cell decreases in a module.

Relation between Internal Resistance and Cell Temperature ($R_{int} = f(T_{cell}, t)$)

As shown in P1 and P2, internal resistance is an important parameter that affects batteries' performance. Therefore, we describe how internal resistance varies with thermal stresses during operation.

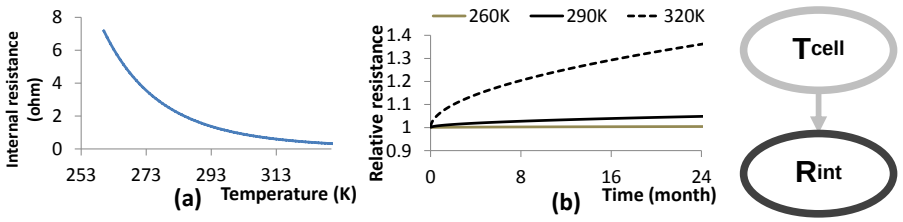

Figure 5.4: Internal resistance increases as temperature decreases, and relative internal resistance increases as time to expose to high temperature increases; both graphs are obtained with evaluation tools/settings to be described in Section 5.6.

Before presenting the effect of temperature on internal resistance, we define two terms related to time interval. An *operation cycle* represents a cycle of a battery cell's operation from its full charge to no charge. A *calendar life* is a duration from a battery cell's production to its warranty period (e.g., 5 years). We describe how temperature affects internal resistance, when a given temperature lasts during (i) an operation cycle, and (ii) a calendar life.

Regarding (i), a higher temperature stimulates the mobility of electron or ion, temporarily reducing the cell's internal resistance and increasing its capacity (by P2). For example, as shown in Fig. 5.4(a), resistance with 320K is smaller than that with 290K. Therefore, during an operation cycle, the following relation holds:

P4. Temperature $\Rightarrow$ Internal resistance ($T\uparrow \rightarrow R\downarrow$ (operation cycle)): As temperature during an operation cycle increases, internal resistance decreases.

In literature, relation between internal resistance and cell temperature is well-described by a polynomial model, and experimental results substantiate its effectiveness [110]:

$$R_{int} = c_3 T_{cell}^3 + c_2 T_{cell}^2 + c_1 T_{cell} + c_0. \tag{5.3}$$

This model dictates cell temperature (T_{cell}) for the required internal resistance (R_{int}).

On the other hand, a long-term temperature exposure affects internal resistance the other way around, as explained next. Battery performance deteriorates over time, regardless of whether the battery is used or not, which is known as "calendar fade",

and it can be represented by a rise of internal resistance as shown in Fig. 5.4(b). There are two key factors influencing the calendar life, namely temperature (T) and time (t), and empirical evidences show that these effects can be represented by two relatively simple mathematical dependencies (t and T). The extent of deterioration can be assessed by relative resistance (μ), which is expressed as [136, 137]:

$$\mu(T;t) = 1 + exp(\beta_0 + \beta_1 \cdot \frac{1}{T}) \cdot t^{\rho}, \tag{5.4}$$

where β_0, β_1, and ρ represent the model parameters. According to Eq. (5.4), the following statement holds:

P5. Temperature over time $\Rightarrow$ Resistance ($t\uparrow, T\uparrow \rightarrow R\uparrow$ (calendar life)): As time to high temperature exposure increases during a calendar life, internal resistance increases.

Thermal Behavior Model ($T_{cell} = f(T_{amb}, R_{int}, I_d)$)

While internal resistance depends on cell temperature (P4 and P5), cell temperature, in turn, varies with a battery internal state and external stress.

Any battery operation generates heat due to internal resistance when the cell delivers power to electric loads, which is also known as *joule heating* ($I_d^2 R_{int}$ loss). Some part of generated heat (Q_d) would be released on the surface of cells (Q_t), and the remaining heat is absorbed into cell materials (Q_s), which can be calculated by [18]:

$$Q_d = I_d^2 R_{int}, Q_s = C_{cell} \frac{dT_{cell}}{dt},$$
$$Q_t = Ah(T_{cell} - T_{amb}),$$

where A is the surface area, h the heat transfer coefficient, T_{amb} temperature around the cell, and C_{cell} heat capacity, respectively. Note that ambient temperature (T_{amb}) is affected by external temperature (T_{ext}) and temperature of thermal fins (T_{fin}).

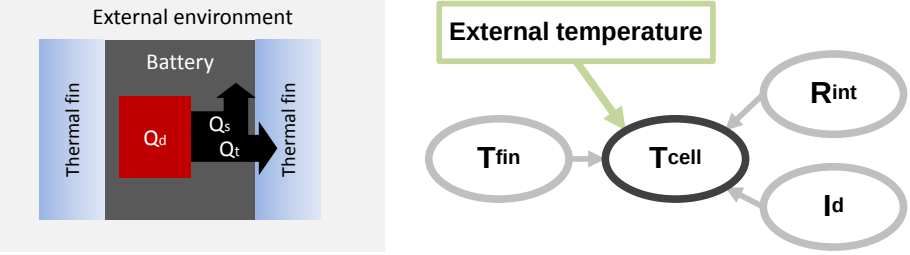

Figure 5.5: Battery thermal dynamics

Eq. (5.5) shows Bernardi's energy balance [18], and it can explain cell temperature (T_{cell}) variation by heat generation (Q_d) as shown in Fig. 5.5. Then, Eq. (5.5) can be solved by Eq. (5.6) as follows.

$$Q_d = Q_t + Q_s, \tag{5.5}$$

$$T_{cell}(t + \Delta t) = T_{cell}(t) + \Delta t[c_1(T_{cell} - T_{amb}) + c_0 I_d^2 R_{int}], \tag{5.6}$$

where t is the current time and Δt the time interval. Based on the equation, the following statement holds.

P6. Discharge current ⇒ Heat generation ($I_d\uparrow \rightarrow T\uparrow$): As discharge current increases, heat generation increases.

If we bridge all the battery characteristics discussed in P1–P6, we have an abstract layer from the temperature of thermal fins (T_{fin}) to operation-time, as described in Fig. 5.6.

5.4.2 Battery Physical Dynamics According to a Thermal Change

Our goal is to develop thermal management so as to increase battery operation-time during its warranty period without explosion and malfunction. To figure out battery dynamics affecting the operation-time and safety, we constructed an abstraction layer by accumulating several physical dependencies as shown in Fig. 5.6. We revisit the physical dependencies (P1–P6) on the abstraction to analyze the battery

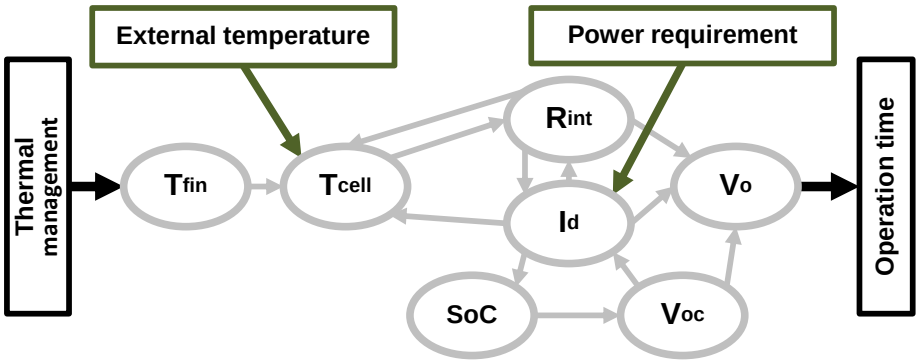

Figure 5.6: Abstraction of battery dynamics

physical dynamics, which will be a basis for our thermal management to be presented in Section 7.5.

Thermal runaway (P3, P4 and P6)

Thermal runaway is one of the most serious thermal issues affecting safety of a battery cell, and results in extremely high temperature and current. A rise in the temperature of a battery cell decreases its internal resistance (by P4) and increases its current (by P3) in a parallel connection, which, in turn, raises its temperature (by P6); this process may repeat, as illustrated in Fig. 5.7. Since extremely high temperature (above around $80°C$) may cause an explosion due to decomposition of materials [85, 63], the thermal stability of battery cells should be maintained.

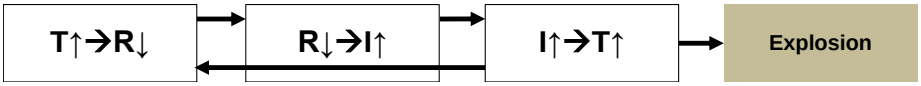

Figure 5.7: Increase in temperature of a cell causes a further increase in the temperature, potentially resulting in explosions of the battery cells because of material decomposition inside the cells.

Malfunction at low temperature (P1 and P4)

Each BMS has a specification of applicable output voltage (V_{app}). The BMS should guarantee delivery of the required power within V_{app} range. However, a decrease in temperature increases internal resistance (by P4), and it may cause a higher voltage

drop (by P1) in order to supply the same current. Output voltage (V_o) drops below the applicable voltage (V_{app}) making a power inverter unable to operate in a specified condition, and hence failing to provide the required power to the vehicle's electric motors. Fig. 5.8 illustrates how a low temperature causes malfunction.

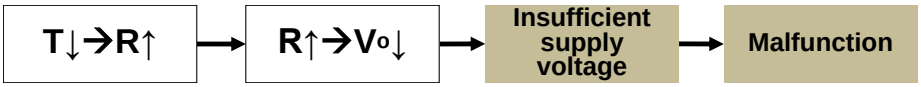

Figure 5.8: Low temperature leads to high internal resistance and voltage drop.

Short operation-time at lower temperature (P2 and P4)

A decrease in temperature reduces the mobility of charges and chemical reaction in cells, which can be represented by the increased internal resistance (by P4). This increased internal resistance implies a larger power dissipation during operation (by P2), which reduces operation-time as shown in Fig. 5.9. For example, it is reported that a drop of just 20 Celsius degrees can drain 10 – 20% of a battery's charge [45].

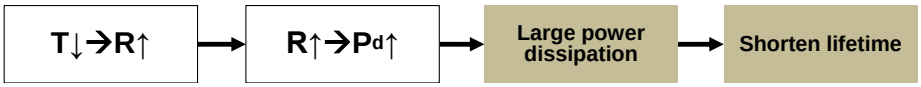

Figure 5.9: Low temperature leads to higher internal resistance and power dissipation.

Performance degradation due to continuous exposure to high temperature (P1, P2 and P5)

Operating under continuous exposure to high temperature induces a rapid increase in internal resistance (by P5) due to the acceleration of irreversible side reactions [85]. The increase in internal resistance causes energy dissipation of cells, shortening their operation-time. Faster performance degradation may also cause battery malfunction even during its warranty period (by P1 and P2), potentially leading to tragic accidents or financial loss. Figs. 5.8 and 5.9 illustrate what we explained so far.

Unbalanced SoC (P4, P5 and P3)

Uneven temperature distribution causes different resistances between battery cells in a battery pack (by P4 and P5). Since the discharge rate depends on internal resistance (by P3), the discharge rates available for different cells are uneven, leading to unbalanced SoC among the cells in a battery pack as shown in Fig. 5.10.

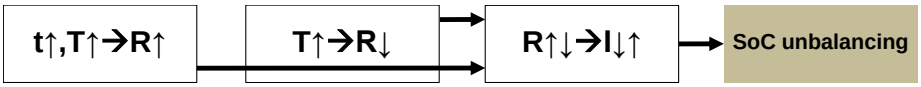

Figure 5.10: Uneven degradation and temperature of cells cause different internal resistances of battery cells, leading to different discharge current and SoCes.

Rate-capacity effect and recovery effect (P4, P5, P3 and P6)

A higher discharge rate causes more capacity loss yielding larger voltage drop due to heat loss (by P5), called *rate-capacity effect* explained in Section 5.2.1. In case of a very low (or zero) discharge rate, the battery can recover its capacity loss to some extent during high-rate of discharge, called *recovery effect*, also discussed in Section 5.2.1. Uneven temperature distribution may cause more unexpected discharge current (by P3, P4, P5), leading to more rate-capacity effect in some cells as shown in Fig. 5.11. Also, uneven discharge rates cause different amounts of heat loss (by P6), causing unbalanced SoC of cells in a battery pack.

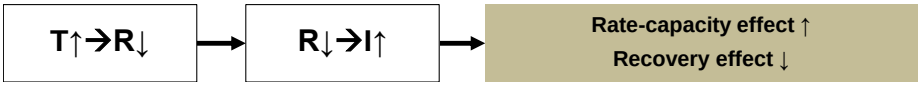

Figure 5.11: Uneven states of cells yield different rate-capacity/recovery effects, leading to unbalanced electrical states.

5.5 The Proposed Battery Thermal Management

So far, we have investigated and abstracted the physical characteristics of batteries. We have then uncovered their effects on thermal dynamics that dictate the performance of a large-scale battery system. Based on these, we now identify the

thermal requirements considering the thermal dynamics, and then develop a battery thermal management policy which can satisfy the requirements based on the abstraction.

5.5.1 Requirements for efficient and reliable BMSes

To enhance the battery's operation-time, we need to control the physical dynamics we discussed thus far. To protect battery cells from thermal runaway (Section 5.4.2) and malfunction at low temperature (Section 5.4.2), the operation temperature (T_{cell}) should lie between its upper (T_{up}) and lower (T_{low}) bounds as follows.

R1. $T_{low} < T_{cell} < T_{up}$.

According to P3, delivering power with high temperature reduces internal resistance and improves the capacity of a battery cell during an operation cycle. Unfortunately, continuous/frequent exposure to high temperature also accelerates the degradation of battery cells during a calendar life (as shown in P4 and Section 5.4.2). According to these two characteristics, to improve capacity of cells while increasing lifetime, we should

R2'. Maximize $\Big[T_{cell}(t)\Big]$ for $0 < t < t_{warr} \in \mathsf{OPERATION}$, and

R3'. Minimize $\Big[\int_0^{t_{warr}} T_{cell}(t)dt | t \in \mathsf{OPERATION}\Big]$,

where $\mathsf{OPERATION}$ is a set of time intervals in which an EV operates.

However, we cannot achieve R2' and R3' at the same time, because maximizing cell temperature will increase cumulative cell temperature. Therefore, existing studies on battery thermal management attempted to determine a static operation temperature range [94, 37], rather than dynamic thermal control, and therefore they cannot fully address the two requirements.

To achieve R2' and R3' together, we should focus on a property: EVs require

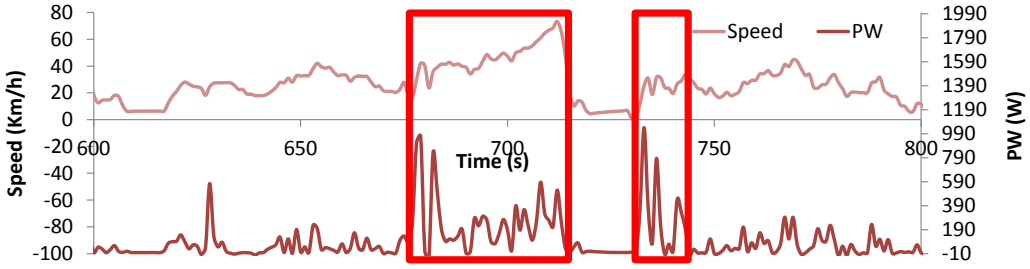

Figure 5.12: Driving pattern and power requirements, generated by a vehicle simulator with real driving records

power intermittently, rather than continuously. For example, requiring high power for rapid accelerations consumes most energy as shown in Fig. 5.12. This means, we do not have to heat cells all the time for reduction of energy dissipation, because heating the cells only during the period of high power requirement can reduce energy dissipation mostly. Therefore, separating the management period based on the power requirement can greatly reduce energy dissipation without losing potential performance improvement much. That is, we divide OPERATION into two: WORK and REST, which denote a set of time intervals in OPERATION in which a battery cell should provide a high power, and a lower power (or no power) is required, respectively; by definition, OPERATION = WORK $\cup$ REST. Then, we modify R2' and R3' such that it is possible to achieve them together by scheduling heating/cooling based on their working/resting status: maximizing working cell temperature ($T_{cell} \uparrow$, if $t \in$ WORK) and minimizing cumulative resting cells temperature ($T_{cell} \downarrow$, if $t \in$ REST), as recorded below.

R2. Maximize $\left[T_{cell}(t)\right]$ for $0 < t < t_{warr} \in$ WORK, and

R3. Minimize $\left[\int_0^{t_{warr}} T_{cell}(t)dt | t \in \text{REST}\right]$,

Also, we should take into account issues that previous work focused on. First, we have to equalize the SoC of cells during operation-time (as mentioned in Section 5.4.2), because just one deep discharged battery cell can lead to significant reduction

of capacity of the entire battery pack. Therefore, we enforce

R4. Minimize deviation $\left[\text{SoCes}\right]$.

By *rate-capacity effect*, a higher discharge rate causes inefficiency of a battery. To reduce inefficient energy loss by excessive high discharge rates, we set a discharge current limit (I_{dlim}) where the rate-capacity effect does not have much impact on the cell's capacity, and enforce cells to operate within the tolerable discharge rate range ($\leq I_{dlim}$), if possible, as follows.

R5. $I_d \leq I_{dlim}$ if possible.

Meeting R1–R5 will reduce energy dissipation and protect cells from unbalanced SoC, explosion, and malfunction. By controlling the temperature of each cell, we can directly meet R1–R3 and also alter discharge rate, addressing R4 and R5. That is, by P3 and P4, we can decrease (increase) discharge rate by lowering (raising) temperature. To realize such a control, we need a battery thermal management system and a cell-level thermal management architecture, which are detailed next.

5.5.2 Main thermal management: after starting a vehicle

We now propose a battery thermal management system (TMS) that meets R1–R5. Its basic principle is to heat (cool) cells to be high-discharged (rested or low-discharged). Based on each cell's SoC and the required power, our TMS determines the type of coolant for each cell to realize the principle and achieve our goal. Algorithm 4 describes how the proposed TMS operates.

Update states of cells (Lines 2–6)

We update all the states of battery cells in a pack to support the following steps. We can directly measure each cell's output voltage and current via sensors, and then estimate the cell's SoC, R_{int}, and V_{oc} based on the measured values [118, 77, 33, 82].

Algorithm 4 Algorithm for thermal management after starting operation

```
1:  for Each module do
2:      measure V_o
3:      for Each cell X (the n-th cell) in the module do
4:          measure I_d[n] and T_cell[n];
5:          estimate SoC[n], V_oc[n] and R_int[n];
6:      end for
7:      if High power is required then
8:          increase V_o;
9:      else
10:         decrease V_o;
11:     end if
12:     for Each cell X (the n-th cell) in the module do
13:         choose efficient I_d[n];
14:         choose R_int[n] from Eq. (5.1);
15:         choose T_cell[n] from Eq. (5.3);
16:         choose T_fin[n] from Eq. (5.6) and thermal distribution in a pack;
17:         if T_fin[n] ≥ previous T_fin[n] then
18:             HeatingSet ← HeatingSet ∪ {X};
19:         else
20:             CoolingSet ← CoolingSet ∪ {X};
21:         end if
22:         if T_cell[n] ≥ T_up then
23:             CoolingSet ← CoolingSet ∪ {X};
24:             HeatingSet ← HeatingSet \ {X};
25:         end if
26:     end for
27: end for
```

Set target output voltage (Lines 7–11)

This step regulates the target output voltage (V_o) based on the power requirements. Increasing V_o helps power the vehicle because the following steps heat the battery cells to reduce internal resistance in order to supply the target output voltage. Unfortunately, the power requirement may change abruptly (e.g., due to sudden acceleration or deceleration of the vehicle) and thermal control takes time. Therefore, we predict the power requirement by analyzing the driving patterns [144, 68] before segmenting the driving path for effective management in the subsequent steps.

Calculate the target discharge current (Line 13)

This calculates efficient discharge current (I_d) of cells for small heat dissipation and SoC balancing. As discussed in R5, we need to make each cell's discharge rate no

larger than I_{dlim} for reduction of inefficient energy dissipation. Suppose $I_{dlim} \leq \frac{P_{req}}{N \cdot V_{tot}}$ holds, where P_{req} is the required power, N is the number of parallel-connected cells, and V_{tot} is the total output voltage. Then, by making each cell discharged at $\frac{I_{tot}}{N}$, we can supply the required power without excessive heat dissipation, where I_{tot} is total discharge current. To meet R4, we set I_d based on the SoC when the level of power requirement (P_{req}) is satisfied; cells with higher SoC should work more. Therefore, the discharge current (I_d) is set to $\frac{I_{tot}}{N}$ if $I_{dlim} \leq \frac{P_{req}}{N \cdot V_{tot}}$ holds, and $I_{tot}\frac{SoC}{\Sigma SoC}$ otherwise, which is recorded as:

$$I_d = \begin{cases} \frac{I_{tot}}{N}, & \text{if } I_{dlim} \leq \frac{P_{req}}{N \cdot V_{tot}}, \\ I_{tot}\frac{SoC}{\Sigma SoC}, & \text{otherwise.} \end{cases}$$

Calculate the required thermal fins' temperature (Lines 14–16)

After setting I_d and V_o, we can calculate the required R_{int} and T_{cell} from Eqs. (5.1) and (5.3) as:

$$c_3 T_{cell}^3 + c_2 T_{cell}^2 + c_1 T_{cell} + c_0 = R_{int} = \frac{V_{oc} - V_o}{I_d},$$

while Eq. (5.6) calculates the desirable ambient temperature (T_{amb}).

Cell temperature depends on ambient temperature including the temperature of thermal fins, and the ambient temperature can be estimated by updating temperature distribution in a battery pack as shown in Fig. 5.13. Note that the temperature distribution can be calculated based on temperatures measured by sensors in a pack. Based on the temperature distribution, we can obtain thermal fins' temperatures that achieve the target ambient temperature.

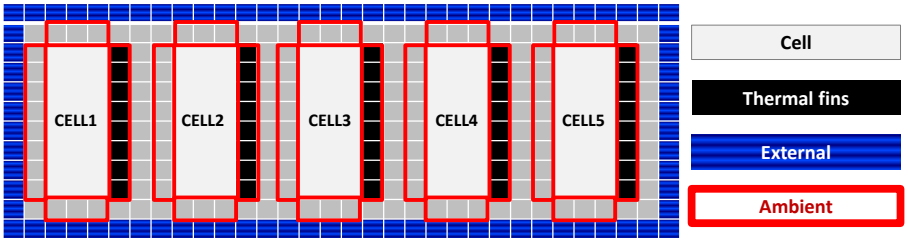

Figure 5.13: Temperature distribution and ambient temperature of cells in a battery pack

Select the coolant type for thermal fins (Lines 17–25)

Lines 17–21 determine the coolant type (heated or cooled) for cells based on current and required fin temperatures. In Lines 22–25, we choose the cells whose temperature is higher than the upper limit, and move them from HeatingSet to maintain thermal stability.

As discussed earlier, the way of calculating I_d addresses R4 and R5. Then, all the steps will meet R2 and R3, since cells are heated (cooled) when they need high power (otherwise). The final step (Lines 22–25) guarantees R1. So, Algorithm 4 meets R1–R5.

5.5.3 Thermal Management Architecture

R1–R3 can be met by the existing thermal architecture, since it can regulate the temperature of battery cells in a timely manner. To satisfy R4 and R5, we need a new architecture which can cool/heat each cell selectively as shown in Fig. 5.14. The new architecture is not much different from existing architectures. While existing BMSes are already been equipped with the heating/cooling capability (e.g., [99, 35]), we need to add more coolant flow valves between the heating/cooling channel and thermal fins for each cell, as shown in the figure. Each coolant control valve should be able to select the type (either heating or cooling) of coolant for cells.

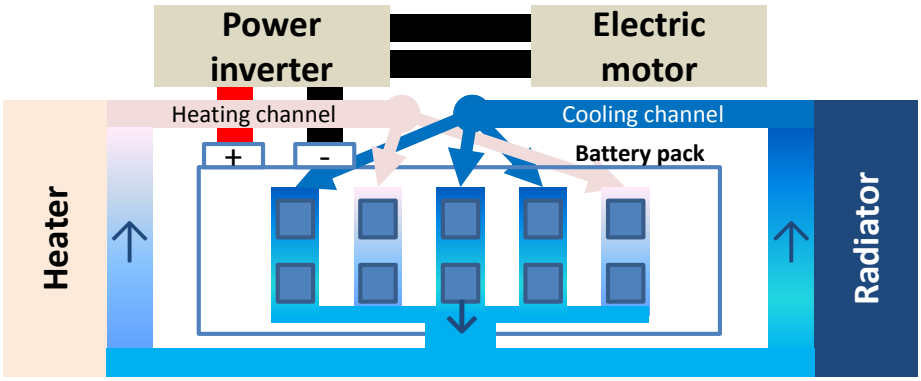

Figure 5.14: Thermal management for battery packs

5.6 Evaluation

We now evaluate the performance improvement by the proposed TMS, focusing on whether or not the goal stated in Section 5.3 is met. We first introduce the performance metrics and evaluation tools/settings to be used. We then present the evaluation results, and finally make remarks on the TMS implementation.

5.6.1 Evaluation metrics

To evaluate the performance of the proposed TMS, we conducted various simulations, and recorded relevant internal battery states. To check if the goal is achieved or not, we extracted the information of battery operation-time. Also, for the analysis of the simulation results, we use (i) *energy dissipation* to show how fast battery energy is depleted, and (ii) *internal resistance* to assess the degradation rate of batteries.

5.6.2 Evaluation tools and settings

To study battery behavior under the proposed TMS, we designed a comprehensive simulator which can calculate each cell's internal states under realistic situations. Also, to obtain realistic thermal stress values for each cell, we selected three US cities representing cold, medium, and hot regions: Anchorage, AK; Ann Arbor, MI; and Phoenix, AZ, denoted by AC, AA and PH, respectively. Fig. 5.15 provides an

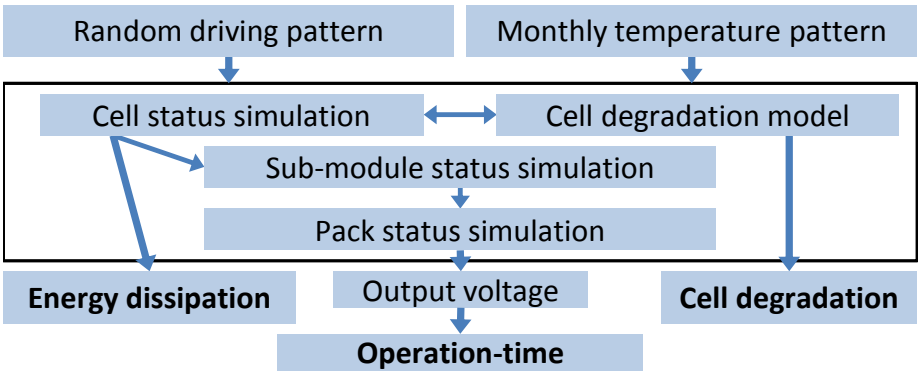

Figure 5.15: Evaluation tools

overview, components of which are described next.

Dualfoil5 (cell-level battery simulator)

Dualfoil5 is a popular battery simulator written in Fortran, and can simulate various types of batteries including the lithium-metal, lithium-ion, and sodium-ion batteries [40]. The program reads the load profile as a sequence of constant current steps, and the battery lifetime is obtained from the output by reading off the time at which the cell potential drops below the cutoff voltage. The equations and methods used in the program rely on an electrochemical model that describes the charge and discharge of a lithium ion battery developed by Marc Doyle *et al.* [40].

CarSim with driving patterns (power requirement)

To acquire realistic power requirements, we exploit US driving patterns [7], a daily driving pattern model [130, 78], and CarSim [4]. CarSim is a well-known and widely-used vehicle modeling tool, simulating the dynamic behavior of vehicles under specified driving conditions, and calculating the required power during driving. We obtain the power requirement profile as follows. First, a daily driving pattern model with a set of US real driving patterns yields daily driving patterns. These daily driving patterns are then fed to CarSim to generate the power requirement. Fig. 5.16

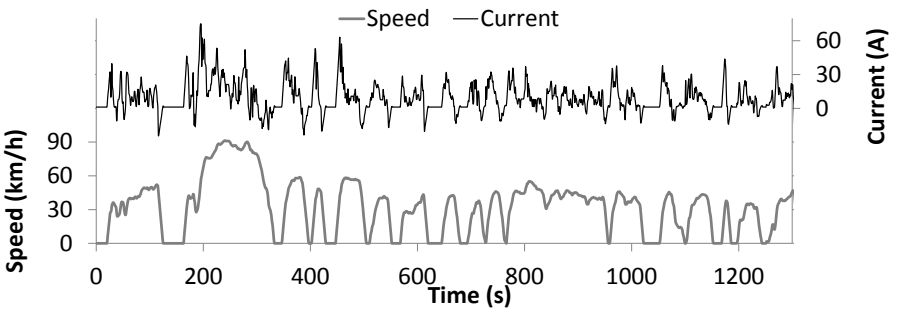

Figure 5.16: Speed and power requirement profiles

shows a set of speed and power requirement profiles generated by this process.

5.6.3 Evaluation results

We evaluate the following three thermal management schemes:

- BASE: no thermal management;
- EX: existing approaches described in Section 5.2 (pack-level cooling/heating only for thermal stability); and
- MSC: our thermal management described in Section 5.5 (active cell-level cooling/heating for efficient BMSes).

For these evaluations, we generated realistic driving and external temperature profiles before simulating the behavior of a battery system with the above three schemes. The three metrics described in Section 5.6.1 are then extracted from the simulation results.

Operation-times after one-year operation

We ran simulation and extracted operation-times of each scheme under various stress conditions. Average operation-times are then calculated to show the overall performance of each scheme. Table 5.1 shows the ratio of the average operation-time of MSC (and EX), to that of BASE. As shown in the table, MSC improves the operation-time by up to 204% and 58.4%, respectively over BASE and EX. Also, MSC

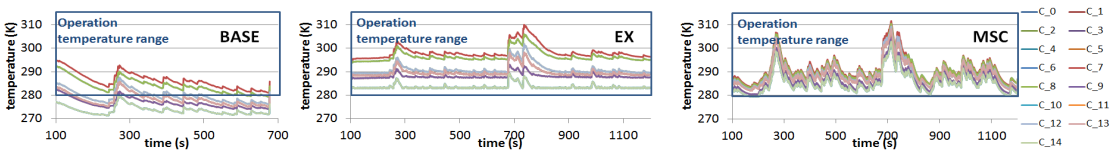

Figure 5.17: Example of thermal management in AC; C_x means Cell x

keeps all the batteries within a tolerable temperature range to prevent explosion or malfunction as shown in Fig. 5.17; in AC, some batteries operate at extremely cold temperature under BASE, potentially leading to malfunction or inefficient usage of the battery pack, whereas all the cells in a pack operate within a tolerable temperature range under MSC and EX.

	Average ℓ_{op} (Sec)		
City, Month	AC	AA	PH
EX/BASE	1.92	0.92	1.03
MSC/BASE	3.04	1.40	1.62

Table 5.1: Average operation-time

From Table 5.1, we can observe that MSC's improvement in AC is more pronounced than that in AA and PH, because there is more room for performance improvement in colder areas, which we will elaborate in Section 5.6.3. As shown in Table 5.1, MSC effectively exploits such room for improvement. For a more detailed analysis for the improvement of MSC, we investigate energy dissipation and performance degradation in the following subsections.

Energy dissipation

Our TMS in Section 5.5 includes several methods to decrease energy dissipation. They actually contribute to the extension of operation-time, since reducing energy dissipation increases available energy in the cells, which, in turn, extends the operation-time.

We compare the energy dissipation of the three thermal management schemes

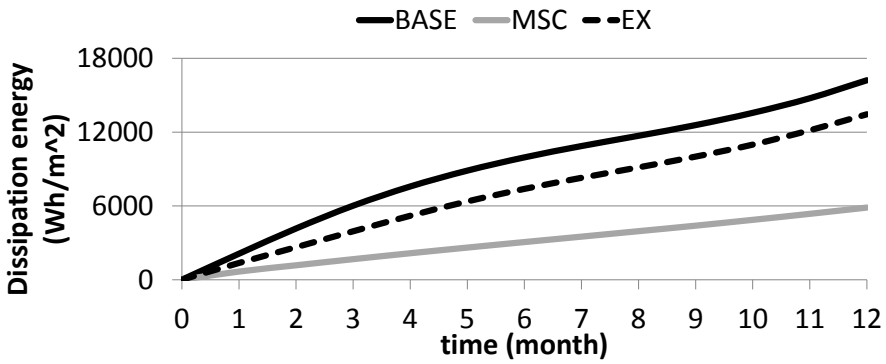

Figure 5.18: Cumulative energy dissipation for one-year operation in AA

when the car operates in AC, AA and PH. Table 8.3 shows energy dissipation when drivers operate their cars repeating the same driving pattern every day for a year. Fig. 5.18 shows an example energy dissipation of each management scheme. Compared to BASE, MSC reduces energy dissipation by 70.6% in AC, 63.8% in AA, and 48.4% in PH. MSC is even better than EX in that it can reduce more energy dissipation by up to 58.6% than EX. This reduction of energy dissipation extends the operation-time under MSC.

	Cumulative energy dissipation (Wh/m^2)		
City	AC	AA	PH
BASE	20978	16216	10474
EX	14910	13450	9976.5
MSC	6167.5	5864.6	5403.5

Table 5.2: Energy dissipation after one year of operation

An interesting point to note is that the difference between energy dissipation of MSC (or EX) and that of BASE is significant in AC. This can be reasoned as follows. In a hotter area, the efficiency is higher (or smaller energy dissipation) even without any thermal management (i.e., BASE), because high temperature increases the chemical reaction rate in a battery. So, in AC where temperature is extremely low in winter, MSC and EX heat the cells to attain effective operation temperature; we observe from Fig. 5.17 that EX and MSC yield a tolerable temperature range for

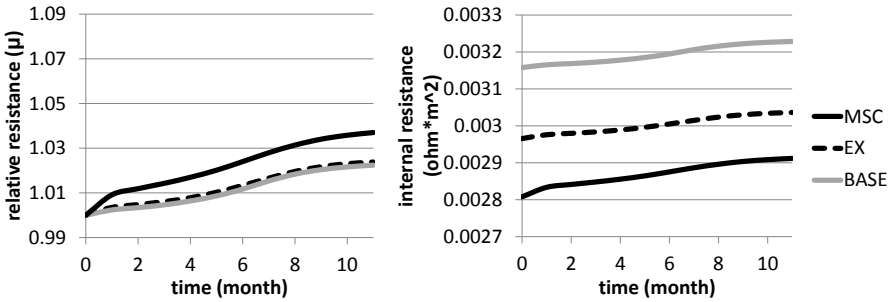

Figure 5.19: Relative resistance and internal resistance in AA

battery cells. This reduces energy dissipation.

MSC reduces energy dissipation significantly more than EX, since it not only timely cools/heats the cells in order to reduce energy dissipation, but also selectively cools/heats the cells for SoC equalization. Therefore, each cell operates more efficiently under MSC, by reducing temperature differences between cells. The reduction of energy dissipation is one of the dominant reasons for improving the operation-time.

Degradation of battery performance

The degree of battery performance degradation depends on its cumulative exposure to high temperature. To evaluate the performance degradation, we compare cells' degradation levels, which are represented by relative resistance and the absolute value of internal resistance, under each thermal management scheme in AC, AA and PH during a 1-year period. Of these three locations, we chose AA, since the results for other locations exhibit a similar or same trend.

Figs. 5.19(a) and (b) plot relative resistance and the absolute value of internal resistance, respectively. As shown in Fig. 5.19(a), MSC leads to a little bit faster degradation than the other schemes, because MSC actively cools/heats each cell. However, such active control reduces the absolute value of internal resistance; as shown in Fig. 5.19(b), internal resistance after one-year usage under MSC is smaller than that under other schemes. This implies that MSC, despite higher relative re-

sistance, is still more efficient for up to one year. These results validate an increase of operation-time discussed in Section 5.6.3, i.e., MSC is efficient in using a battery pack.

5.6.4 Remarks on implementation

We can build the TMS based on the existing approaches for cooling and heating engines and batteries in the current vehicles on the market. To implement the BMS that accommodates the proposed TMS, some additional hardware should be installed in each battery pack. Measuring the output voltage and discharge current of cells requires sensors, just as other BMSes [60, 73, 55] do. Additional control flow valves are also required for cell-level thermal controls; their performance and reliability should be considered since they directly affect the effectiveness of battery management. It would be interesting to design a BMS with efficient and reliable management of hardware sensors and actuators by considering their physical characteristics along with battery dynamics. This is part of our future work.

5.7 Conclusion

To resolve increasing demand to make EVs less expensive and safer, BMSes should cope with thermal and general issues that affect efficiency and reliability of BMSes. A thermal management is the key to addressing these issues, since temperature has significant impact on electrical states of BMSes. In this chapter, we presented how to achieve efficient and reliable BMSes using thermal controls. We proposed a battery thermal management scheme that cools/heats battery cells timely and selectively based on the analysis for impacts of power requirements and temperature variation on electrical states of battery cells. To support this scheme, we also proposed thermal management architecture, which is able to cool/heat battery cells selectively.

Our evaluation with realistic simulation showed that our approach makes a significant improvement in BMSes' efficiency without compromising their reliability, over a simple method often seen in the existing BMSes.

It would be interesting to explore ways of improving thermal management based on the proposed architecture. We may be able to improve performance with a more accurate and adaptive abstraction model instead of the basic model used in this chapter. We can also improve the BMS efficiency by heating/cooling cells in advance with more accurate power requirement prediction [144, 68].

CHAPTER VI

Optimal Design and Discharge/Charge Rate Management for Hybrid Energy Storage

6.1 Introduction

An electric vehicle (EV) requires a high rate of voltage and current since its powertrain must drive large motors in order to move its heavy vehicle body. To supply a high rate of current, tens/hundreds of small cylindrical battery cells or a few of large battery pouches are connected in parallel. To drive large motors, tens/hundreds of battery cells are connected/stacked in series, forming a high-voltage source.

EVs' batteries must support high peak discharge (charge) currents to (from) electric loads needed during acceleration and/or hill climbing, and accommodate momentary power generated during regenerative breaking. The resulting current surges in and out of the batteries tend to dissipate an extensive amount of energy and accelerate the capacity degradation due to high voltages, large discharge/charge currents, and frequent changes of their volume of electrodes. To mitigate these "harmful" discharge/charge surges, researchers proposed hierarchical energy-storage systems consisting of an energy buffer with high power-density and a main energy storage (battery pack) with high energy-density [28, 60, 111]. The energy-dense battery pack extends the driving range, while the power-dense energy buffer enables good acceler-

ation and accommodates momentary power generated during regenerative braking. Such a battery pack need not be oversized or designed to accommodate the peak power discharge/charge demands, thus reducing the battery-pack cost while delivering the required power.

Another important issue of a large-scale battery pack is the imbalance of its constituent cells' State-of-Charge (SoC). In a pack with series-connected battery cells, the same current flows through each battery stack even if its energy capacity and SoC are different from others'. It may cause incomplete charging of the battery pack or incomplete use of the pack's energy to protect the battery cells in the pack from over-charging and/or deep-depth of discharge. Various cell-balancing techniques have been proposed to maintain energy evenly among the battery cells [98]. *Passive balancing* dissipates the energy of cells with high SoC in the form of heat, until their SoC becomes equal to the lowest one in the stack. It allows all cells to have the same SoC using a simple method, but does not improve the run-time performance of a vehicle. *Active cell balancing* overcomes the energy loss of the passive balancing by delivering energy to where it is needed most, using an inductive or capacitive energy storage.

A large-scale battery pack must be managed effectively to handle its battery cells' imbalance and peak discharge/charge currents. Its battery management system (BMS) must transfer energy not only among the battery cells to balance their SoC, but also between the battery pack and the energy buffer to reduce peak discharge/charge current surges. While hardware architectures and control algorithms have been proposed to efficiently transfer charges for balancing cells and reducing the peak power requirement, little has been done on how they can be optimized and effectively applied in real operating environments.

To fill this gap, we propose the design and management of a *hybrid energy storage system* (HESS) that takes into account the above issues. We first address the problem of sizing energy-dense main battery and power-dense energy buffer for effectively peak power reduction and SoC balancing. Then, we determine the target discharge/charge current of the battery pack and the energy buffer. The target current must be determined adaptively based on the power requirement history and the SoC of energy components so as to effectively maintain battery discharge/charge current within the required operating range, while balancing battery cells' SoC.

The paper is organized as follows. Section 8.2 describes the backgrounds and our overall approach. Sections 6.3 and 6.4 describe the proposed HESS design and algorithm for determining discharge/charge currents, respectively. Section 8.7 implements our solutions on a prototype and evaluates their performance. Finally, the paper concludes with Section 8.8.

6.2 System Model and Problem Statement

This section describes our target architecture for power management. Figs. 6.1 and 6.2 show a hybrid energy storage system including multiple energy storage components with the DC/DC converters, and circuit models of a battery and an ultra-capacitor. The proposed algorithms with these models determine the desired discharge/charge current to enable effective control of the DC/DC converter input switches.

6.2.1 Li-ion battery and ultra-capacitor model

According to the equivalent battery circuit models, the terminal battery voltage (V_b) depends on open circuit voltage (V_{oc}), current through the battery (I_b), and

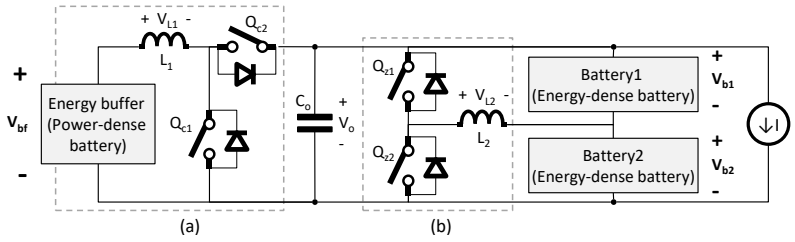

Figure 6.1: BMS architecture consisting of (a) an energy buffer for peak power reduction and (b) an SoC-balancing circuit

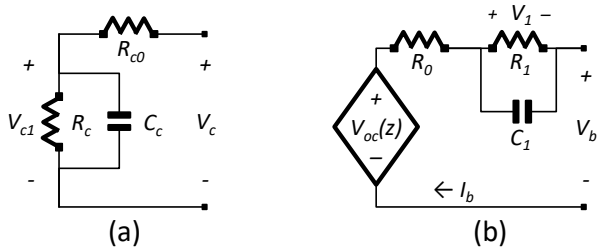

Figure 6.2: (a) Ultra-capacitor (energy buffer) model with open circuit voltage (V_{c_1}), its capacitance (C_c), internal resistance (R_{c_0}), and resistance for self discharge (R_c) (b) Battery model consisting of open circuit voltage (V_{oc}), internal resistance (R_0, R_1) and capacitance (C_1)

internal parameters (V_1, R_0):

$$V_b = V_{oc} - V_1 - R_0 I_b, \tag{6.1}$$

where V_1 represents the dynamic voltage behaviors due to Lithium-ion diffusion and charge transfer. The dynamic voltage is modeled by an RC circuit:

$$\dot{V}_1 = \frac{-1}{R_1 C_1} V_1 + \frac{1}{C_1} I_b, \tag{6.2}$$

and this is reformulated as a discrete time model of Li-ion batteries:

$$V_1[k+1] = e^{\frac{-\Delta t}{R_1 C_1}} V_1[k] + R_1(1 - e^{\frac{-\Delta t}{R_1 C_1}}) I_b[k], \tag{6.3}$$

where Δt is a control time interval. The battery's open circuit voltage (V_{oc}) depends on the battery's SoC (z), and its changes can be estimated based on the battery current (I_b) and the total charge capacity (C_{bat}):

$$V_{oc}[k] = f(z[k]),\ z[k+1] = z[k] - \frac{1}{C_{bat}} I_b[k],$$

where f is a V_{oc} function of SoC. This model is used for estimating V_{oc} and SoC based on battery voltage (V_o) and current measurements (I_b).

Similarly, the ultra-capacitor voltage (V_c) depends on the internal parameters (R_c, R_{c_0}, C_c) and current (I_L) via

$$\begin{aligned} V_c &= V_{c_1} - R_{c_0} I_{L_1}, \\ \dot{V}_{c_1} &= \frac{1}{R_c C_c} V_1 - \frac{1}{C_c} I_{L_1}, \end{aligned} \tag{6.4}$$

where R_{c_0} is the internal resistance, R_c is the resistance of self-discharge, and C_c is the capacitance of ultra-capacitor, respectively. With these battery and buffer models, the discharge/charge current dynamics from energy storage components (I_{L_1}, I_{L_2}) can be described when the converter switches are turned on ($I^o_{L_1}$) and off ($I^f_{L_1}$) as:

$$\begin{aligned} \dot{I}^o_{L_1} &= \frac{-R_{c_0}}{L_1} I_{L_1} + \frac{1}{L_1} V_c = \frac{-R_{c_0}}{L_1} I_{L_1} + \frac{1}{L_1}(V_{c_1} - R_{c_0} I_{L_1}), \\ \dot{I}^f_{L_1} &= \frac{-R_{c_0}}{L_1} I_{L_1} + \frac{1}{L_1} V_c = \frac{-R_{c_0}}{L_1} I_{L_1} + \frac{1}{L_1}(V_{c_1} - R_{c_0} I_{L_1} - V_o), \end{aligned} \tag{6.5}$$

where $\dot{I}^o_{L_1}$ and $\dot{I}^f_{L_1}$ are the rate changes of inductor currents when the converter switch is turned on and off, respectively. It depends on the system parameters and the SoC of energy storage components. Hence, the current dynamics determine the desired switch duty cycles, the ratio of time when switch is on to that when the switch is off.

6.2.2 Problem statement

We now formally state the problem to be solved based on the system models as:

Given power requirement (I_{rq}), a set of battery SoCs and performance parameters of energy storage components,

Determine the duty cycles $\{Q_{c_1}[k],\ Q_{c_2}[k],\ Q_{z_1}[k],\ Q_{z_2}[k]\}_{0<k<k_e}$ that minimize the following objective function during the operation ($0 < k < k_e$).

$$\begin{aligned} &\textsf{Minimize (S0) Dischage/charge stress} = \frac{1}{T_{op}} \int I_b^2 \, dt \\ &\textsf{Subject to (S1)} \; I_{rq} = I_{L_1} + I_{L_2} + I_b \\ &\qquad\qquad\qquad\quad \textsf{(S2)} \; z_1[k_e] = z_2[k_e]. \end{aligned} \tag{6.6}$$

The energy system must supply the required power with current (I_{rq}) to the electric load. The sum of current supplies from energy storage components (I_{L_1}, I_{L_2}, I_b) must be the power requirement for all $k \in [0, k_e)$ (**S1**). While providing the required power to the load, the power supplies from the energy storage components must be limited within specific ranges for efficient operations. Also, the current between batteries must be controlled to balance the battery SoC (**S2**). The control knobs are the duty cycles of the converter switches (Q_{c_1}, Q_{c_2}, Q_{z_1}, Q_{z_2}), dictating the converter current (I_{L_1}, I_{L_2}). The objective function in **S0** represents the amount of discharge/charge stress during operation period (T_{op}). Note that large discharge/charge currents harm the batteries more than moderate amounts of current. Therefore, we assess discharge/charge stress as square of discharge/charge current in this chapter.

6.2.3 Overall solution approach

Fig. 6.3 shows the proposed overall control system. Here we are focusing on the determination and control of discharge/charge currents of batteries and an energy buffer. We first determine the target discharge/charge current for SoC balancing and peak power reduction. The current determination algorithm (denoted by 1)) considers SoCs in the batteries and the buffer, and analyzes the current requirement pattern to determine effective discharge/charge currents. The converter controller (denoted by 2)) regulates the duty cycles of the converter switch input to achieve the determined target current.

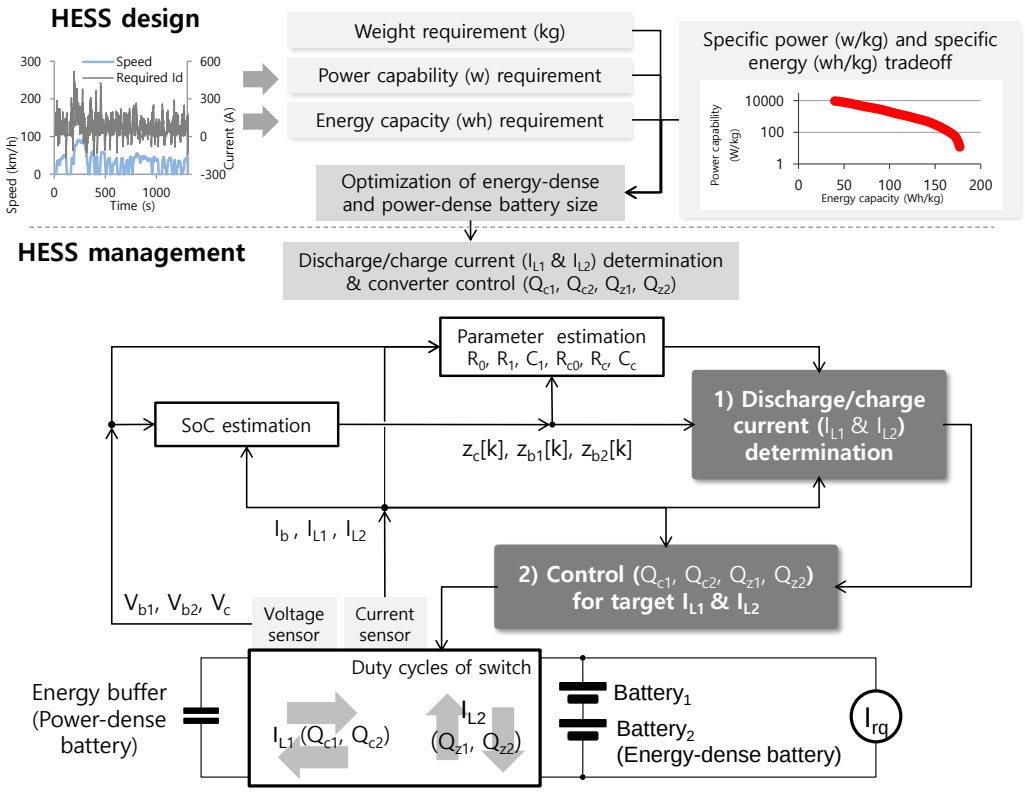

Figure 6.3: Overall discharge/charge current management

6.3 Problem of Designing a HESS with Power- and Energy-Dense Batteries

We first analyze the power demand to identify the HESS design requirements, such as power capability and energy capacity to support the power demand profiles. Then, we make a formal statement of HESS design problem subject to these constraints.

6.3.1 Power requirement analysis and HESS requirements

The main advantage of a HESS is its capability of supplying peak power bursts using a small number of power-dense batteries so that the designer can use the energy-dense battery as the primary energy source, increasing the system's total energy capacity. Therefore, the energy-dense battery must be able to supply at least the average required power (P_{avg}) to the electric load, while the system has a sufficient capability for powering the vehicle. That is, the power-dense battery must be able

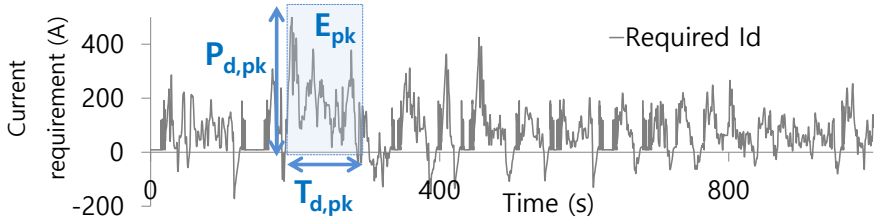

Figure 6.4: Peak power and energy

to accommodate the surplus energy and supply the energy to the electric load when the peak power is required. These requirements determine the energy capacity of the power-dense battery, which must be larger than the amount of energy that could be charged into the power-dense battery or discharged to the electric load during peak charge/discharge periods. We will identify the peak discharge/charge powers $(P_{d,pk}, P_{c,pk})$ and their time duration (T_{pk}) in the power demand profiles as shown in Fig. 6.4. These parameters allow the system designer to determine how much energy the power-dense battery should be able to store for effective energy accommodation (from RBS) and supply to the load:

$$E_{pk} = T_{pk} P_{d,pk}$$

6.3.2 The Problem of Designing a HESS for Power Requirement Analysis

With the above design requirements, assumptions and notations, our problem can be formally stated as:

Given the total weight requirement (m_{rq}), and a tradeoff function (f_{ep}) between the specific power (P^s) and energy (E^s),

Determine the HESS design parameters $\{E_e^s, m_e, E_p^s, m_p\}$ to

$$
\begin{aligned}
\textsf{maximize}\ & (\textsf{S0})\ \text{HESS Energy capacity} = E_e^s m_e + E_p^s m_p \\
\textsf{subject to}\ & (\textsf{S1})\ P_e^s m_e + P_p^s m_p \geq P_{pk} \\
& (\textsf{S2})\ E_p^s m_p \geq E_{pk} \\
& (\textsf{S3})\ P_e^s m_e \geq P_{avg} \\
& (\textsf{S4})\ m_e + m_p = m_{rq},
\end{aligned} \tag{6.7}
$$

where E_e^s is the specific energy of the energy-dense battery, m_e the weight of the energy-dense battery, E_p^s the specific energy of the power-dense battery, m_p the weight of the power-dense battery, and m_{rq} total maximum weight requirement, respectively. P_e^s and P_p^s are the specific powers of the energy-dense battery and power-dense battery, respectively, and they can be determined by their specific energy ($P_e^s = f_{ep}(E_e^s), P_p^s = f_{ep}(E_p^s)$). To make the problem analytically solvable, we assume that the system cost depends only on the system weight, and approximated the tradeoff between Li-ion battery power capability and energy capacity ($P^s = f_{ep}(E^s)$) based on the recent result reported in [134]. The objective function in **S0** represents the total energy capacity of the HESS, and must be maximized while the battery system must be able to supply the peak power (**S1**). To support the system's peak power, the power-dense battery must have a sufficient energy capacity to be able to supply the peak power (**S2**). Since the energy-dense battery is the primary energy source, it must be able to provide the average required power to the load (**S3**). The sum of weights of energy storage components ($m_e + m_p$) must be lower than the total weight limit (m_{rq}) (**S4**).

6.4 Effective Discharge/Charge for Peak Power Reduction and SoC-Balancing

We develop a decision algorithm for effective discharge/charge currents from/to the batteries and the energy buffer by considering the current requirement patterns (I_{rq}) and the SoC (z) of energy storage components. Algorithm 5 describes the overall discharge/charge current management for peak power reduction and SoC-balancing. Algorithm 6 periodically calculates the effective current bounds that Algorithm 5 needs.

6.4.1 The overall algorithm

Algorithm 5 Target current decision (I_{L_1}, I_{L_2})

```
1:  while 1 do
2:      /* Target current for peak current reduction */
3:      if  I_{b,ub} < I_{rq,n}  then
4:          I_{L_1} ← I_{rq} − I_{b,ub}
5:      else if  I_{b,lb} > I_{rq,n}  then
6:          I_{L_1} ← I_{rq} − I_{b,lb}
7:      else
8:          I_{L_1} ← 0
9:      end if
10:     /* Target current for SoC balancing */
11:     if Δz > Δz_{st} then
12:         while Δz > Δz_{end} do
13:             if  I_{z,ub} > I_{rq,n} > I_{z,lb}  then
14:                 I_{L_2} ← min(I_{z,ub} − I_{rq}, I_{rq} − I_{z,lb})
15:                 if z_1 > z_2 then
16:                     I_{L_2} ← −I_{L_2}
17:                 end if
18:             else
19:                 I_{L_2} ← 0
20:             end if
21:         end while
22:     else
23:         I_{L_2} ← 0
24:     end if
25: end while
```

Lines 3–9 of Algorithm 5 determine the discharge current from the buffer (I_{L_1}) in order to meet the high discharge/charge current requirement (I_{rq}). When I_{rq} is larger than its upper bound ($I_{b,ub}$), the energy buffer provides energy to reduce the battery

discharge current (lines 3–4). When I_{rq} is less than its lower bound ($I_{b,lb}$), the buffer takes in the generated current to protect batteries from over-recharge current (lines 5–6). The algorithm also determines the target current between batteries (I_{L_2}) based on SoC-balancing in batteries (lines 11–24). If the SoC difference (Δz) is larger than its threshold (Δz_{st}), the SoC-balancing operation kicks in until the SoC difference (Δz) reaches the termination condition (Δz_{end}). The balancing operation transfers the charge in a battery with higher SoC to the one with lower SoC (lines 15–16), and the amount of current to be transferred is limited to protect batteries from over-dis/recharge current (lines 13–14). Figs. 6.5 and 6.6 show examples of power reduction and SoC-balancing with the proposed current management. Determination of the current bound for power buffering and SoC-balancing will be detailed next.

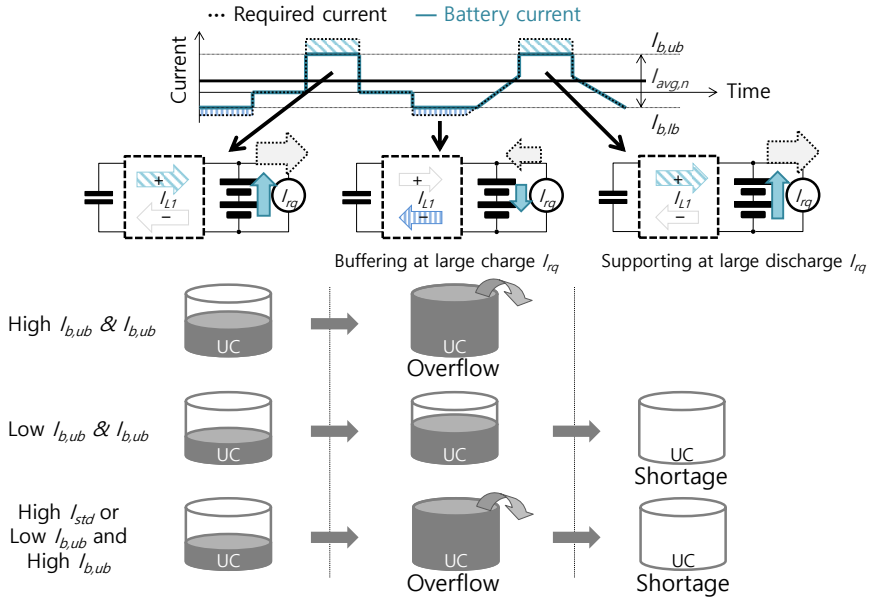

Figure 6.5: Power buffering for peak power reduction.

6.4.2 Determination of current bound

Battery discharge/charge currents must be controlled within a proper range since the peak discharge/charge current significantly affects battery performance degrada-

tion. Thus, Algorithm 6 determines the current bounds ($I_{b,ub}$, $I_{b,lb}$, $I_{b,ub}$ and $I_{b,lb}$) to minimize the discharge/charge stress.

Algorithm 6 Determination of the current bound for peak current reduction and SoC-balancing

1: $E_c \leftarrow \frac{1}{2} C_c V_{c,rated}^2$
2: **while** 1 **do**
3: $T_c \leftarrow$ DisChargeCycleTimeUpdate()
4: $I_{avg}[k] \leftarrow \frac{k-1}{k} I_{avg}[k-1] + \frac{1}{k} I_{rq}$
5: $I_{std}[k] \leftarrow \{\frac{k-1}{k} I_{std}[k-1]^2 + \frac{1}{k}(I_{rq} - I_{avg}[k])^2\}^{\frac{1}{2}}$
6: $[I_{ub}, I_{lb}] \leftarrow$ FindBound$(T_c, E_c, I_{avg}[k], I_{std}[k])$
7: $I_{b,ub} \leftarrow I_{avg}[k] + (I_{ub} - I_{lb})(1 - (z_c[k] - z_c^{opt}))$
8: $I_{b,lb} \leftarrow I_{avg}[k] - (I_{ub} - I_{lb})(1 - (z_c^{opt} - z_c[k]))$
9: $E_z \leftarrow |E_{bat_1}(z_{b_1}) - E_{bat_2}(z_{b_2})|$
10: $T_z \leftarrow$ TargetBalanceTimeUpdate()
11: $[I_{z,ub}, I_{z,lb}] \leftarrow$ FindBoundSOC$(T_z, E_z, I_{avg}[k], I_{std}[k])$
12: Sleep()
13: **end while**

Power requirement pattern and UC energy capacity (lines 1–6)

Algorithm 6 represents the upper and lower current bounds to effectively limit the battery discharge/charge. The required amount of energy depends on the driving pattern, motor performance, and regenerative braking system (RBS). It creates the uncertainty in the required amount of discharge/charge current during driving. Therefore, we have to analyze the discharge/charge history to set the most effective current discharge/charge bound, protecting the battery without the buffer's energy overflow and shortage. Lines 4–5 calculate the average and standard deviation of the current requirement ($I_{avg}[k]$, $I_{std}[k]$). In this algorithm, the current bounds will be determined under the assumption that the required current would follow with a Gaussian normal distribution with average, I_{avg}, and standard deviation, I_{std}. When the average required current(I_{avg}) is high, the current bound I_{ub} and I_{lb} should be increased to effectively buffer recharging energy and supply the energy while limiting the battery discharge/charge current. The standard deviation of the required current (I_{std}) also affects the determination of I_{ub} and I_{lb}. A large standard deviation means

the transfer of a large amount of energy with a high peak current. In this case, I_{ub} should be increased and I_{lb} decreased to buffer the energy effectively without shortage of energy in the buffer as seen in Fig. 6.5.

Algorithm 7 describes how to determine I_{ub} and I_{lb} for peak power reduction. During the charging/recharging cycle (T_c), the UC receives power from electric load and supplies power to the load once. To maximize buffer utilization, when power is recharging, the buffer must be fully charged without overflow and use all the stored energy in the buffer without energy shortage in reducing discharging. Thus, we determine I_{ub} and I_{lb} to make the buffered energy in UC (E_{bf}) and an available UC energy capacity (E_c) equivalent. The energy stored in UC (E_c) can be calculated using the standard equation related to capacitor energy ($E_c = \frac{1}{2}C_c V_{c,rated}^2$), where $V_{c,rated}$ is UC-rated voltage and C_c UC capacitance. To estimate the amount of the buffered energy in UC (E_{bf}), we assume that current requirement patterns follow a Gaussian normal distribution with average (I_{avg}) and standard deviation (I_{std}) of the current requirement. We can then probabilistically calculate the amount of the buffered energy (E_{bf}) by integrating buffered current ($I_{bf} = i - I_{ub}$) as:

$$
\begin{aligned}
E_{bf}(I_{ub}) &= \int_0^{T_c} P_{bf}(t)dt = T_c \int_{I_{ub}}^{\infty} P_{bf}(i)\mathrm{PDF}(i)di \\
&= T_c \int_{I_{ub}}^{\infty} V_b I_{bf}(i)\mathrm{PDF}(i)di \\
&= T_c \int_{I_{ub}}^{\infty} V_b (i - I_{ub})\mathrm{PDF}(i)di \\
&= T_c V_o \Big[\int_{I_{ub}}^{\infty} i\mathrm{PDF}(i)di - I_{ub} \int_{I_{ub}}^{\infty} \mathrm{PDF}(i)di \Big] \\
&= T_c V_o \Big[\int_{I_{ub}}^{\infty} i\mathrm{PDF}(i)di - I_{ub}(1 - \mathrm{CDF}(I_{ub})) \Big] \\
&= T_c V_o \Big[I_{std}^2 \mathrm{PDF}(I_{ub}) + (I_{avg} - I_{ub})(1 - \mathrm{CDF}(I_{ub})) \Big], \qquad (6.8)
\end{aligned}
$$

Algorithm 7 FindBound

```
1: procedure [I_ub, I_lb] = FindBound(E_c, I_avg, I_std)
2:     for I_ub = I_avg; I_ub < I_avg + 2I_std; I_ub = I_ub + I_std/20 do
3:         if E_bf(I_ub) > E_c then
4:             Break;
5:         end if
6:     end for
7:     I_lb = I_avg − (I_ub − I_avg)
8:     return [I_ub, I_lb]
9: end procedure
```

where V_o is the battery output voltage, and P_{bf} is the buffered power.

Buffer state-of-charge (lines 7–8)

We assume that the power requirement follows a Gaussian normal distribution, but this assumption does not hold for the power requirement in every period. Lines 7–8 additionally adjust the current upper and lower bounds based on the SoC of the energy buffer, protecting the buffer in case the current requirement is larger than expected. When UC is fully charged ($z_c \approx 100\%$), it cannot be charged any more. Therefore, when z_c is high, we need to decrease I_{lb} to reduce the charging energy, and decrease I_{ub} to use more energy in UC to support loads. When UC is discharged fully ($z_c \approx 0\%$), it cannot be discharged any more. Therefore, when z_c is low, we need to increase I_{lb} and decrease I_{ub}.

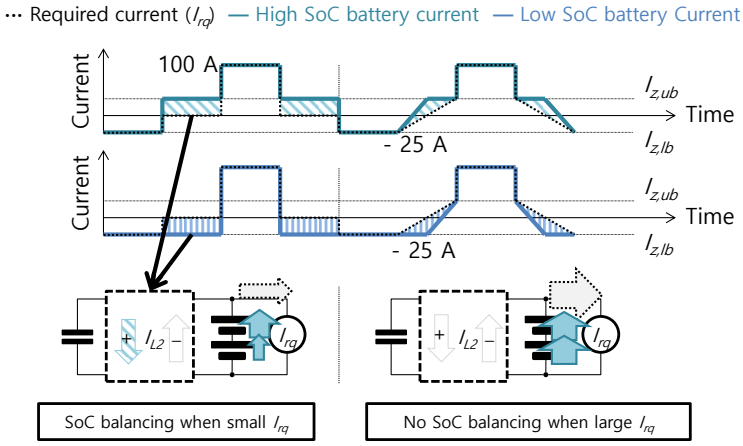

Figure 6.6: SoC-balancing

Algorithm 8 FindBound for SoC-balancing

1: **procedure** $[I_{z,ub}, I_{z,lb}]$ = FINDBOUNDSOC$(T_z, E_z, I_{avg}, I_{std})$
2: **for** $I_{z,ub} = 0; I_{z,ub} < I_{avg} + 2I_{std}; I_{z,ub} = I_{z,ub} + \frac{I_{std}}{20}$ **do**
3: $I_{z,lb} = -I_{z,ub}$
4: **if** $E_{tr}(T_z, I_{z,ub}, I_{z,lb}) < E_z$ **then**
5: Break;
6: **end if**
7: **end for**
8: **return** $[I_{ub}, I_{lb}]$
9: **end procedure**

Power requirement pattern and SoC balancing (lines 9–11)

Currents between batteries also have to be regulated for SoC-balancing based on the total current requirement (I_{rq}). When battery supplies large power to load or receive power from the load, additional current for SoC-balancing may harm the batteries due to the increased discharge/charge current from some batteries. Therefore, we determine an acceptable current requirement range for cell balancing to protect cells from over-discharge/charge currents. The current bounds for SoC operation ($I_{z,ub}, I_{z,lb}$) are determined based on the power requirement patterns and the SoC differences between batteries. E_z is the amount of energy transferred for SoC-balancing.

Algorithm 8 determines the current ranges for energy transfer to balance SoC considering the time period (T_z), the remaining energy difference (E_z), and the power requirement pattern (I_{avg}, I_{std}). We search for $I_{z,ub}$ to achieve the battery SoC-balancing ($E_{tr} = E_z$) within the required time period (T_z). Then, the amount of energy transferred between batteries that depends on the current ranges and the power requirement, and time period (T_z) can be calculated according to Eq. (6.9).

$$
\begin{aligned}
E_{tr} &= \int_0^{T_z} P_{bal}(t)dt \\
&= T_z \int_0^{I_{z,ub}} V_o(I_{z,ub} - i)\mathrm{PDF}(i)di \\
&+ T_z \int_{I_{z,lb}}^{0} V_o(i - I_{z,lb})\mathrm{PDF}(i)di \\
&= T_z V_o \Big[I_{z,ub} \int_0^{I_{z,ub}} \mathrm{PDF}(i)di - \int_0^{I_{z,ub}} i\mathrm{PDF}(i)di \\
&+ \int_{I_{z,lb}}^{0} i\mathrm{PDF}(i)di - I_{z,lb} \int_{I_{z,lb}}^{0} \mathrm{PDF}(i)di \Big] \\
&= T_z V_o \Big[I_{z,ub}[\mathrm{CDF}(I_{z,ub}) - \mathrm{CDF}(0)] \\
&- [I_{std}^2(\mathrm{PDF}(0) - \mathrm{PDF}(I_{z,ub})) + I_{avg}(\mathrm{CDF}(I_{z,ub}) - \mathrm{CDF}(0))] \\
&+ [I_{std}^2(\mathrm{PDF}(I_{z,lb}) - \mathrm{PDF}(0)) + I_{avg}(\mathrm{CDF}(0) - \mathrm{CDF}(I_{z,lb}))] \\
&- I_{z,lb}[\mathrm{CDF}(0) - \mathrm{CDF}(I_{z,lb})] \Big]
\end{aligned} \tag{6.9}
$$

6.5 Control system

This section represents a control system for the converters' input signals to buffer the discharge/charge current and transfer charge between batteries.

6.5.1 Converter operation for current control

Discharge/charge current from energy storage components (I_{L_1}, I_{L_2}) can be adjusted by duty-cycle controls of converter input switches ($Q_{c_1}, Q_{c_2}, Q_{z_1}, Q_{z_2}$). For example, when Q_{c_1} switch is turned on, charge flows from the buffer to ground storing energy in the form of current (I_{L_1}). Then, when Q_{c_1} switch is turned off, the inductor L_1 flows the charge from the buffer to the battery and the electric load even when V_c is lower than V_o because of the inductor's property. Note that an inductor tends to maintain current flow through it. It moves the energy until the current

dropps to 0. Turning on/off other switches (Q_{c_2}, Q_{z_1}, Q_{z_2}) does similar operations that move energy between energy storage components.

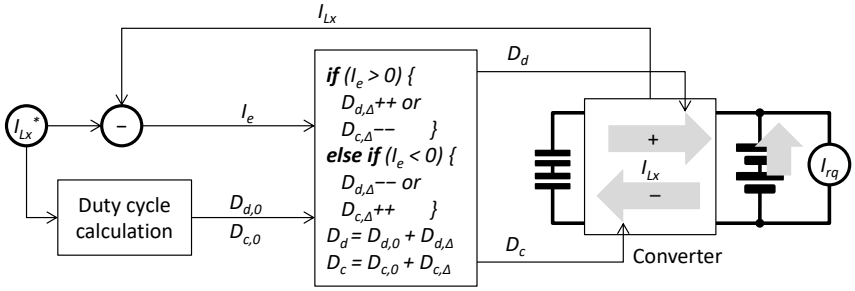

Figure 6.7: Control of duty cycles (D_c, D_d) for the target current

6.5.2 Selection of duty cycles ($D_{d,0}, D_{c,0}$) for regulating current (I_{L_1}, I_{L_2})

We can calculate the required duty cycles for the target current based on parameters including inductance, resistance and capacitance in our system. The fundamental principle is that the current increase ($\Delta I^o_{L_1}, \Delta I^o_{L_2}$) must be the same as the current decrease ($\Delta I^f_{L_1}, \Delta I^f_{L_2}$) at the target level to maintain the target current (I_{L_1}, I_{L_2}). Current increase and decrease can be described as:

$$\Delta I^o_{L_1} = \Delta I^f_{L1} \;\rightarrow\; t_o \dot{I}^o_{L_1} = t_f \dot{I}^f_{L_1}, \tag{6.10}$$

where t_o (t_f) and $\dot{I}^o_{L_1}$ ($\dot{I}^f_{L_1}$) are the time duration and the rate change of current when the switch is turned on (off), respectively. Using Eq. (6.10) and the definition of duty cycle, we can derive the desired duty cycle as a function of the target current (I_{L1}) as:

$$\begin{aligned} D_c &= \frac{t_o}{t_o + t_f} = (1 + \frac{t_f}{t_o})^{-1} = (1 + \frac{\dot{I}^o_{L1}}{\dot{I}^f_{L1}})^{-1} \\ \dot{I}^o_{L_1,k} &= (\frac{R_c}{L_1} - 1) I_{L_1,k} + \frac{1}{L_1} V_{c,k} \\ \dot{I}^f_{L_1,k} &= (\frac{R_c}{L_1} - 1) I_{L_1,k} + \frac{1}{L_1} V_{c,k} + \frac{1}{L_1} V_{o,k} + \frac{R_c}{L_1} I_o, \end{aligned} \tag{6.11}$$

where R_c, L_1 are system parameters, V_o battery voltage, and V_{uc} the energy buffer voltage. We can also calculate the duty cycles (D) for the current through other inductors.

6.5.3 Adaptively adjust duty cycles ($D_{d,\Delta}, D_{c,\Delta}$)

To compensate the current errors (I_e) due to measurement and model errors, the controller uses a feedback control loop. When the current is larger than the target current, it reduces the fraction of time duration when the switch stays on (t_o) to decrease the current and eliminate the error (I_e) as shown in Fig 6.7. Therefore, we finally determine the duty cycles based on the calculation from the current dynamics and the error between the target current and the present current as:

$$D_d = D_{d,0} + D_{d,\Delta}$$

$$D_c = D_{c,0} + D_{c,\Delta}.$$

One important consideration is that the discharge and charge switches must not be turned on at the same time. It causes the batteries to be short-circuited, destroying the converter and batteries. Therefore, the controller has to turn off the charge switch ($D = 0$) before turning on the discharge switch ($D \uparrow$) when the controller increases the discharge current.

6.6 Evaluation

We evaluate the proposed current management for peak discharge/charge reduction and SoC-balancing, with a focus on whether or not they meet the goals stated in Section 8.2.

6.6.1 Experimental setup

We have built a prototype which is equipped with wheels, wheel motors, stepper motors, coolers and an HESS, including a pack of lithium-ion batteries and a pack of UCs as shown in Fig. 6.8. The system is required to execute user applications, and allocate available resources for their execution. For realistic evaluations, we acquired driving profile/data from the Air Resources Board (ARB02) and US Environmental Protection Agency (UDDS, SC03, US06) [3]. We programmed the application to operate wheel motors to achieve these driving profiles.

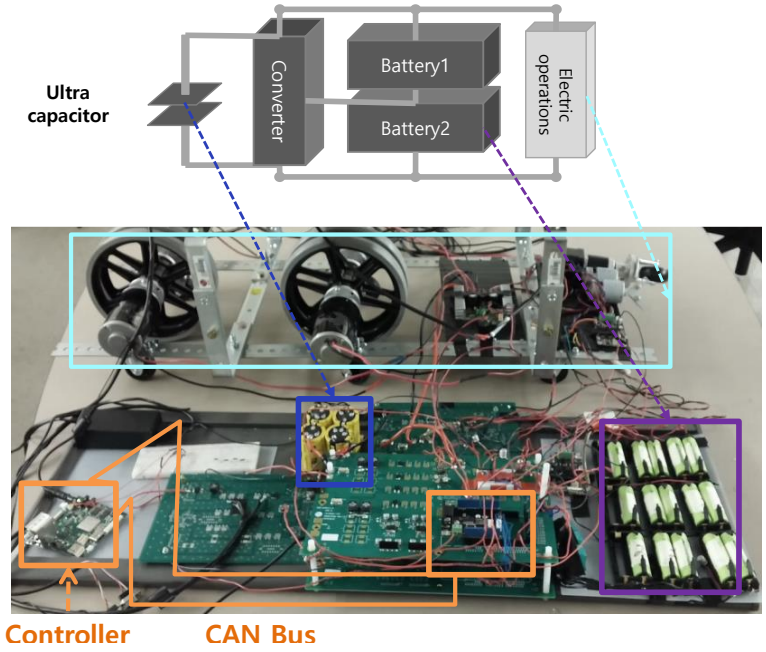

Figure 6.8: Prototype for evaluation

6.6.2 Results

Fig. 6.9 shows the current measurements resulting from the peak power reduction control. It shows the current requirements (I_{rq}) with a pattern (I_{avg}, I_{std}) and the discharge/charge current (I_b) from the battery with the determined bounds ($I_{b,ub}$, $I_{b,lb}$). Fig. 6.10 presents the results of an SoC-balancing example. When the SoC differences exceed over its threshold, the controller starts regulating the converter switches to

transfer charges for SoC-balancing. To protect batteries from large discharge/charge stresses due to SoC-balancing, charge transfer operations are executed only when the current requirements are within the current bounds ($I_{z,lb} < I_{rq} < I_{z,ub}$).

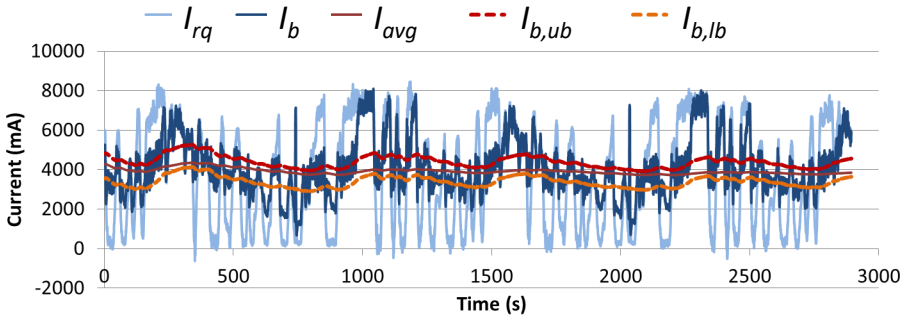

Figure 6.9: Example of the proposed power buffering for peak power reduction

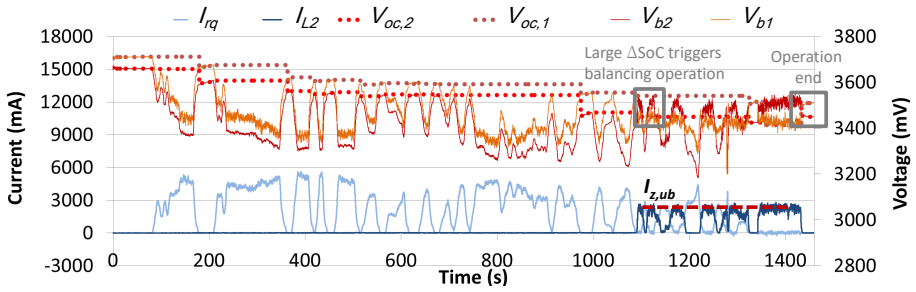

Figure 6.10: Example of the proposed SoC-balancing

Driving cycle	Baseline	Our control	Reduction ratio
UDDS	20.96 A^2	18.25 A^2	12.9 %
ARB02	10.81 A^2	8.67 A^2	19.8 %
SC03	13.60 A^2	12.37 A^2	9.0 %
US06	27.92 A^2	26.67 A^2	4.5 %

Table 6.1: Dis/charge stress ($\frac{1}{T}\int I_b^2 dt$) under the proposed peak power reduction and the baseline

Table 8.3 shows the discharge/charge current stresses ($\frac{1}{T}\int I_b^2 dt$) at different driving cycles. The proposed discharge/charge current management reduces the discharge/charge stress while reducing SoC imbalances at the end of cycle by up to 19.8%. In the US06 driving cycle case, a vehicle was driven at a high speed for a while, decreasing the utilization of energy buffer.

6.7 Conclusion

In this chapter, we have proposed a discharge/charge current management that minimizes the battery discharge/charge stress and ensures SoC balancing between batteries. To adaptively control the discharge/charge rate, we have proposed an algorithm for determining the discharge/charge rate while considering the current requirement pattern and the SoCs of energy storage components. We have also designed a control system to achieve the target current determined by this algorithm. We have validated the algorithm and control with an HESS-powered prototype system running realistic applications, demonstrating peak current reduction and SoC balance. In future, we would like to develop a design framework for general large-scale energy storage systems. We also plan to build a power/energy management system that balances not only the SoC of batteries, but also the SoH of energy storage components.

CHAPTER VII

Real-Time Discharge/Charge Rate Control for Hybrid Energy Storage in Electric Vehicles

7.1 Introduction

An effective battery management system (BMS) can reduce the required number of battery cells and extend the replacement period, hence reducing the battery cost. As part of our goal of designing such a BMS, we will in this chapter focus on extending batteries' life which has significant impact on the battery cost. *Battery life* is defined as the duration (measured in the number of cycles or elapsed time) of a rechargeable battery until it degrades irreversibly and cannot hold a useful capacity of the underlying applications [43]. That is, the battery capacity monotonically decreases with time, and will never be recovered. As a result, EVs must be equipped with enough batteries to maintain the required capacity throughout their warranty period. This capacity degradation may also require battery replacements, incurring an additional (maintenance) cost. It is therefore necessary for the BMS to slow down the capacity degradation of batteries in order to reduce the cost of purchasing and maintaining EVs.

Among the various reasons for battery capacity degradation, the discharge/charge rate is reported to be the most critical [85, 63]. For example, a continuous exposure to high discharge current leads to fast capacity degradation, thereby shortening the

battery life [92, 34], which is inevitable due to abrupt changes in the EVs' power requirement, such as acceleration. To extend the battery life, researchers focused on hybrid energy storage systems (HESSes) built with two or more types of energy storage devices [47, 122, 27, 138, 109]. The main principle for regulating the battery' discharge/charge rate in a HESS is to adjust the discharge/charge rate for each storage device.

The goal of this chapter is, therefore, to develop discharge/recharge rate management for an efficient HESS so as to reduce its initial deployment and maintenance costs. It requires not only comprehensive understanding of physical dynamics beneath the HESS, but also efficient management of the HESS based on this understanding. For example, in a HESS consisting of batteries, ultra-capacitors (UCs) and boost-buck DC/DC converters, the discharge/charge rate of each storage is dominated by a second-order differential equation, and we have to carefully regulate the parameters in the equation so as to minimize battery performance degradation. That is, we need to take a *cyber-physical perspective*, integrating and coordinating physical dynamics and adaptive controls as follows. First, we capture parameters affecting the discharge/charge rate in the HESS based on the circuit dynamics that represent the underlying discharge/charge operations. Second, we introduce three key control knobs that can manipulate the parameters, and develop management algorithms that manipulate control knobs to extend battery life using *adaptive* control schemes. Finally, we propose a *reconfigurable* architecture that realizes our management algorithms to regulate control knobs.

We evaluate the proposed battery discharge/charge rate management using workloads based on real driving patterns, and simulate them with a popular simulation tool. Our evaluation results demonstrate the effectiveness of the proposed battery

discharge/charge rate management. Compared to the existing simple management schemes, our system improves the battery life up to 37.7% without increasing initial cost.

The main contributions of this chapter are:

- Consideration of physical circuit dynamics to address the issues associated with battery life;
- Design of battery discharge/charge rate management with a new architecture; and
- In-depth, realistic evaluation of the HESS managements, demonstrating that the proposed system significantly increases the HESS efficiency without increasing initial cost.

The chapter is organized as follows. Section 7.2 examines the state-of-art BMSes, each consisting of a regenerative braking system, batteries and UCs. Section 7.3 states the problem from a cyber-physical perspective. Section 7.4 describes the physical dynamics related to the discharge/charge rate of batteries in a HESS. Section 7.5 presents our battery discharge/charge rate management algorithms, and Section 8.7.1 describes a HESS management architecture. Section 7.7 evaluates our system via simulation, and finally, the chapter concludes with Section 7.8.

7.2 State-of-Art Battery Management Systems

This section introduces the background of HESSes, including a brief review of existing BMSes. First, we describe the function and structure of a BMS shown in Fig. 7.1. Then, we introduce the part of a BMS that can supply power. Finally, we present an advanced architecture that can be incorporated into a BMS so as to overcome some disadvantages of existing simple BMSes; this architecture is the basis

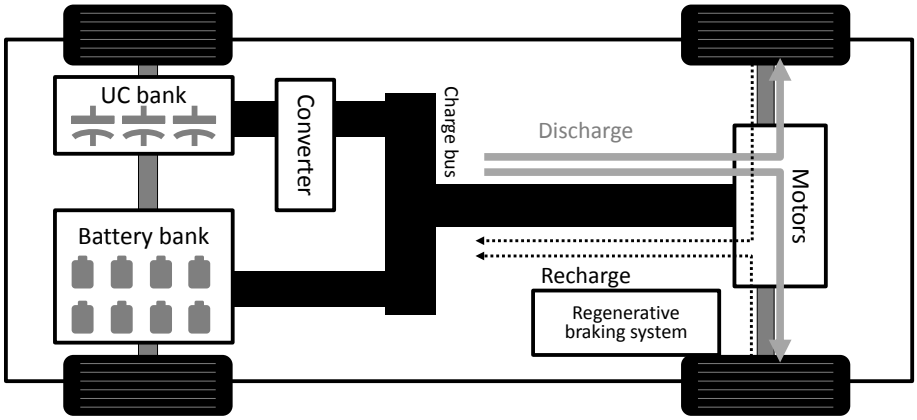

Figure 7.1: Energy storage system in EVs

for our approach described in the following sections.

7.2.1 Overview of BMS

As illustrated in Fig. 7.2, the power requirement of an EV is high and changes abruptly [28, 122, 68], because drivers frequently accelerate/decelerate their vehicles that weigh at least one ton during driving. Therefore, the battery management system (BMS) in an EV is responsible for providing motors with the required power while protecting batter cells from damage and life reduction caused by *short bursts of power transfer*. To perform such functions, a BMS is often comprised of two parts: (i) a large number of battery cells that can supply high current (hundreds of ampere) with high output voltage (tens or hundreds of volt), and (ii) an auxiliary system to mitigate the stress caused by large and abrupt power requirements from a regenerative braking system and motors.

7.2.2 Regenerative braking system (RBS)

To meet the requirements of a BMS, most EVs are equipped with a regenerative breaking system (RBS) to reuse the energy dissipated in their braking system. During braking, the RBS converts the vehicle's kinetic energy to electrical energy that can

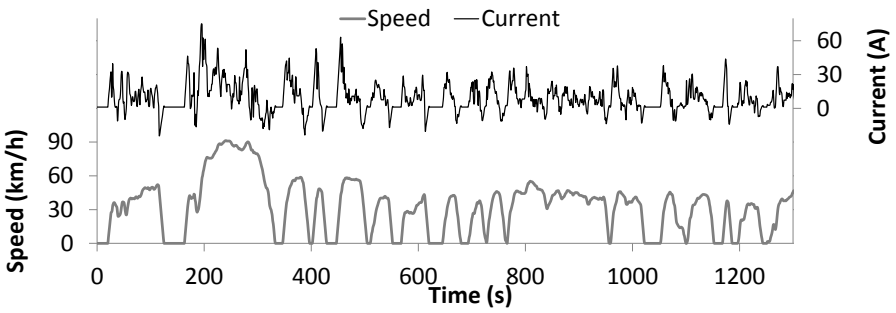

Figure 7.2: Variation of an EV's power requirement

be stored in batteries for reuse to power the vehicle. Its effectiveness has been substantiated in terms of fuel economy [52, 53, 49, 90]. Although the RBS improves the utilization of energy, high recharging current for a very short period of time has a negative impact on the battery's health. Therefore, researchers deployed an auxiliary system that will be introduced next.

7.2.3 Hybrid Energy Storage System (HESS)

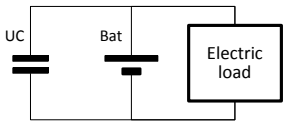

(a) Structure of a simple HESS

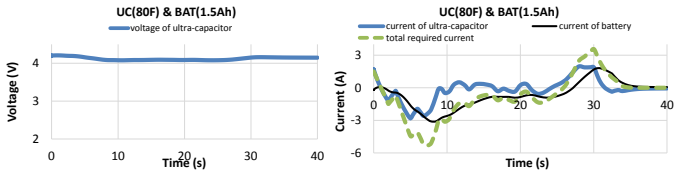

(b) Example of voltage and discharge currents of the battery and the ultra capacitor (UC)

Figure 7.3: A simple HESS

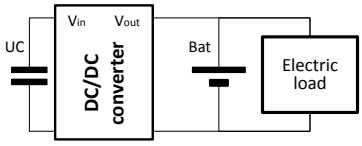

(a) Structure of a HESS including a converter

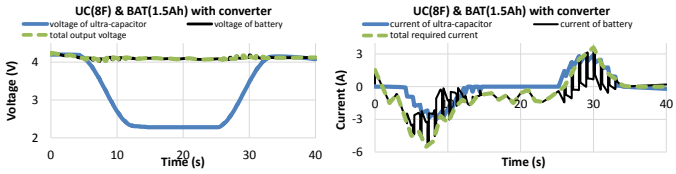

(b) Example of voltages and discharge currents of the battery and the UC

Figure 7.4: A HESS with a DC/DC converter

Battery health is damaged by short bursts of discharging current supplied to motors and recharging current generated from the RBS. To remedy this problem,

researchers deployed ultra-capacitors (UCs) in the BMS; a BMS with UCs as well as batteries is called a *hybrid energy storage system* (HESS). In a HESS, UCs are used as an energy buffer to smooth rapid power fluctuations in and out of the battery of an EV [74, 62, 25, 111]. HESSes effectively utilize the properties of batteries and UCs, called *power density* and *energy density*. That is, available power density of batteries is lower than UCs so that the higher the discharge rate, the less efficient the energy conversion, whereas UCs do not suffer such efficiency degradation. On the other hand, UCs have lower energy density and higher unit cost than batteries as shown in Table 7.1, implying that we should place a large number of UCs in an EV. Therefore, HESSes make batteries supply the average power required for operating vehicles, while UCs provide the sudden power surges required for acceleration and also accommodate instantaneous regenerative energy from the RBS.

Type	Ultra-capacitor	Lithium battery
Power density (W/kg)	100 - 10 K	80-2000
Energy density (WH/Kg)	1 - 10	60 - 150
Cost (USD/WH)	10.3	3.7

Table 7.1: Power density, energy density, and cost of energy storages [27]

Fig. 7.3 shows a simple HESS where an UC is connected directly to a battery, and the UC acts as a low pass filter so as to reduce the peak discharge current of the battery. Unfortunately, the HESS with this configuration requires a large number of UCs because the configuration cannot fully exploit UCs' capacity because of the same terminal voltages of the UC and the battery [62, 117]. To address this problem, many configurations of HESSes have been proposed [62, 25]. For example, Fig. 7.4 illustrates the most widely-studied configuration of HESS that includes a bi-directional DC/DC converter between a battery and an UC. This configuration allows voltage separation and an increase in utilization of the UC via the converter

so as to reduce the required capacitance (8F) of the UC in comparison with that (80F) of the simple HESS shown in Fig. 7.3.

7.2.4 Effective utilization of energy capacity for UCs in a HESS

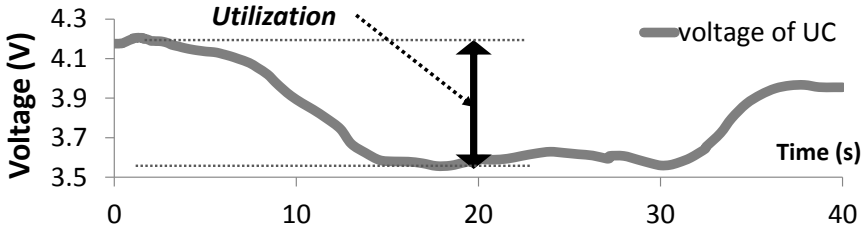

Figure 7.5: Capacity utilization of a HESS

The ability of effectively utilizing UCs is a main focus in evaluating HESS configurations. That is, if we capture as much redundant energy into the UC bank as possible and then use all of that energy when required, we can efficiently utilize UCs without wasting the UC banks' capacity and their deployment cost. We can evaluate the utilization based on the law of storage in a standard capacitor. Energy stored in an UC (E_{UC}) is affected by the voltage (V) and the size of capacitors (C) as:

$$E_{UC} = \frac{1}{2}CV^2.$$

Therefore, the utilization of UCs' capacity can be measured by the range of voltage swing as shown in Fig. 7.5. For example, when 50% of an UC's voltage variation within a tolerable voltage range is permitted, 75% of the UC's energy can be delivered, whereas we can use only 20% of the energy for a 10% variation range, decreasing the UC's effectiveness. The HESS with a DC/DC converter in Fig. 7.4 shows high utilization of UCs' energy capacity by separating the voltage between the UC and the battery, while the simple HESS in Fig. 7.3 could not effectively utilize the energy capacity of UCs because the voltage drop is only 20%. To enhance the UCs' capacity utilization, several feedback control schemes have been proposed

based on the UC-converter-battery architecture that regulates the discharge current adaptively [138, 47, 109, 62, 25].

Although a HESS can reduce the stresses and enhance the life of batteries, it still has not been used widely in commercial EVs, because UCs are not only expensive, but also required to endure high discharge current and high operating voltage. Furthermore, it takes a long time to find the optimal configuration for EVs, since it requires a number of tests in various environments. This is because discharge/charge current varies with driving conditions and behaviors which are related to a complex human decision-making process [68]. We will address these issues using adaptive control of converters and dynamic reconfiguration of UC banks.

7.3 Problem Statement and Solution Approach

We want to develop a "good" HESS using an efficient and reliable BMS. We first introduce relevant terms and design constraints, state the problem, and then briefly describe our solution approach.

7.3.1 Battery life

A long lifetime of batteries reduces their number and extends their replacement periods, reducing the cost of EVs. Therefore, most BMSes are required to maintain appropriate battery operational environments to avoid damage and fast capacity reduction [69]. The battery life is known to depend on the number of discharge/charge cycles, the amount of energy used at each cycle (depth of discharge), operational temperature, and discharge/charge current [145, 121, 102, 131, 104, 97, 92, 34]. Here we focus on the impact of discharge/charge current on the battery life, and propose a HESS that reduces stress of batteries, and doesn't affect the depth of discharge, operational temperature, and the number of cycles. Given the depth of discharge,

operation cycle and operational temperature, the battery life depends on discharge current the battery supply as [92, 34]:

$$L_{cycle} = \alpha e^{-\beta I_{bat}}, \tag{7.1}$$

where L_{cycle} is the cycle life, I_{bat} is the discharge current, α and β are positive coefficients. That is, a decrease in discharge/charge stress can extend the battery life exponentially.

7.3.2 Physical constraints and cost of components

To operate the electric motors satisfying vehicles' required drivability, a BMS is required to provide a large amount of charge in a few seconds. It should also maintain tolerable voltage and current for electric components during operation. The *rated voltage* (V_r) of an UC is the maximum voltage that the UC is designed for. That is, to use UCs without destruction, we should keep UCs to operate within the tolerable voltage range. Likewise, we have to maintain the rated current when we use the converter. *Rated current* (I_r) is defined as "the maximum amount of electrical current a device can carry before sustaining immediate or progressive deterioration" [1]. From the market [2], we can acquire a variety of capacitors and converters, and the price depends on their specifications. Obviously, the larger capacitance or rated voltage, the more expensive. For example, an UC with 5.4V of rated voltage and 5F capacitance costs \$15.3 while another UC with 5.4V and 1.5F costs only \$10.2. Therefore, we should consider the overall cost of the components as well as their specifications when a BMS is designed.

7.3.3 Problem Statement

In this chapter, we want to develop a BMS that enables its battery pack to supply the required power ($P_{req}(t)$) for a long time. Specifically, we would like to determine

the BMS operation at each time instant (t) so as to maximize the battery life (L_{cycle}) within tolerable voltage ($<= |V_r|$) and current range ($<= |I_r|$), which is formally expressed as:

Given the power requirements $\{P_{req}(t)\}_{0<t<t_{op}}$, determine the states of control knobs for the HESS, such that L_{cycle} is maximized subject to the fixed cost without causing over-voltage ($> |V_r|$) and over-current ($> |I_r|$), where 0 and t_{op} are the beginning and end time instants of the battery operation, respectively.

Note that the power requirements and the control knobs' states are valid/necessary only during the EV's operation in [0, t_{op}]. Available control knobs will be extracted by carefully considering the physical dynamics on the HESS in Section 7.4. Note that L_{cycle} monotonically decreases with the increase of the cumulative amount of current according to Eq. (7.1). Therefore, we focus on minimization of the cumulative current (I_{bat}) over time to maximize L_{cycle}.

7.3.4 Cyber-physical system perspective of the HESS

Various control schemes and architectures for HESS have been proposed and studied for efficient usage of batteries. However, they have not been adopted in EVs due to their high cost. Thus, we need to develop a more efficient HESS which addresses the cost problem via integrated management exploiting existing approaches. To this end, we build a cyber-physical system (CPS) for HESS by considering all the parameters that affect discharge/charge operation beneath the HESS. We first capture the physical dynamics of HESS, and identify the effective control knobs including new control knobs which have not been identified before. Then, we propose integrated management with a relevant architecture that enhances the life of the HESS by effectively regulating the control knobs.

In the rest of the chapter, we detail the cyber-physical system of HESS shown

in Fig. 7.6. In Section 7.4, we explore physical dynamics when UCs supply power through a DC/DC converter. Our careful exploration of the physical side enables extraction of effective control knobs that are able to regulate the physical operation and enhance the battery life. Section 7.5 develops the management algorithms that can determine desirable control knobs yielding a long battery life based on the understanding of physical dynamics detailed in Section 7.4. In Section 8.7.1, we construct not only the HESS architecture which is able to regulate the control knobs, but also a unified management algorithm that can be applied to the architecture.

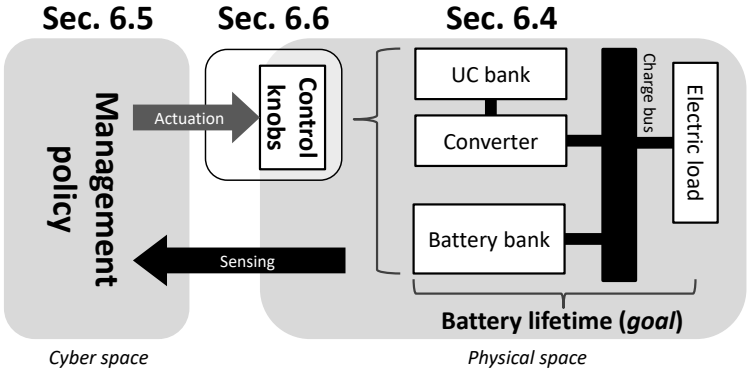

Figure 7.6: CPS perspective for the design/management of the HESS

7.4 Analysis of Discharge/Charge Rate of a HESS

Discharge/charge rate greatly affects the battery life, and should therefore be controlled properly. Unlike the conventional battery systems, the battery discharge/charge rate can be regulated in a HESS due to UCs' capability of controlling discharge/charge current. For example, an increase (decrease) in discharge current of UCs decreases (increases) discharge current of batteries while supplying the total required current to the electric load. In this section, we first describe how converters in the HESS operate and how they influence the discharge/charge rate of UCs. Second, we identify controllable parameters that affect the discharge/charge rate of UCs.

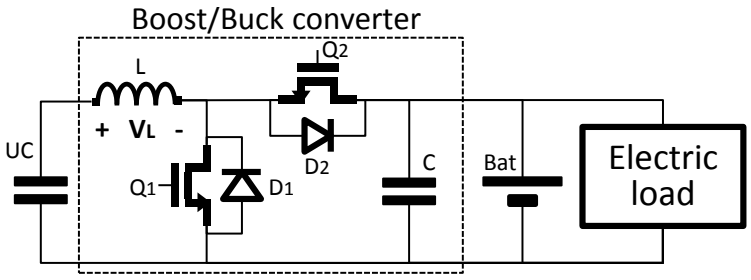

Figure 7.7: A basis for the proposed HESS

7.4.1 Circuit dynamics in the HESS

We investigate the physical dynamics of the UC-converter-battery unit shown in Fig 7.7 [114], because this will be the basis for our approach in the following sections. The main principle is that an inductor resists changes in current by developing a voltage (V_L) across it which is proportional to the rate of the current change as:

$$V_L = L\frac{dI}{dt}. \tag{7.2}$$

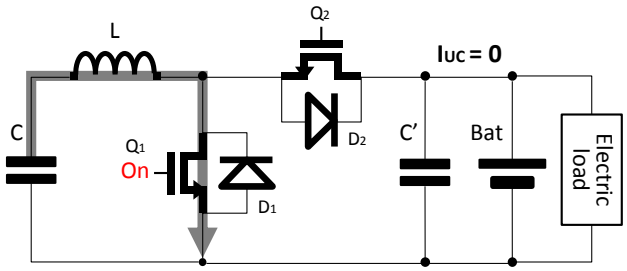

(a) Energy is accumulated in inductor when Q_1 is turned on

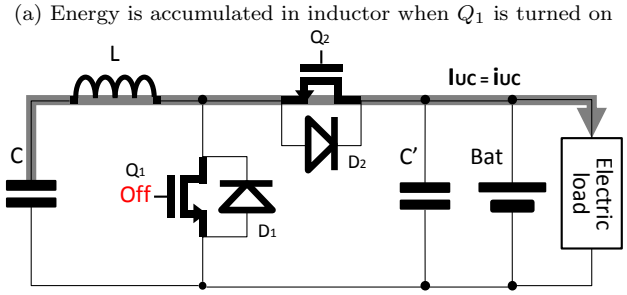

(b) Energy is transferred to the electric load when Q_1 is turned off

Figure 7.8: Physical dynamics of the UC-converter-battery unit

When switch Q_1 is closed, electron flow (I) occurs through the inductor (L) because output voltage of the UC drives current between terminals of the inductor.

According to Eq. (7.2), the inductor allows the current to slowly increase by decreasing its voltage drop, and energy is accumulated in the inductor. Then, when switch Q_1 is opened, current will be decreased slowly since the inductor fights abrupt changes in current. As a result, the inductor must act like a current source toward the electric load through diode D_2 for a few seconds. One can expect a similar effect during recharging through D_1 by controlling Q_2 switch. Therefore, the converter makes charge in UCs (likewise load) transfer to the load (likewise UCs) by repeatedly switching Q_1 (likewise Q_2).

During this process, the amounts of stored and transferred energy are affected by the size of the inductor (L) and the capacitor (C). When Q_1 is closed, the charge stored in the capacitor transfers to the inductor in the LC circuit. The differential equation of the LC circuit is

$$\frac{d^2 i_{UC}(t)}{dt^2} + \frac{1}{LC} i_{UC}(t) = 0,$$

and the solution of this differential equation is

$$i_{UC}(t) = I_p \sin(\frac{1}{\sqrt{LC}} t), \tag{7.3}$$

where I_p is the peak current. Note that the rate of energy transferred to the load is dominated by the size of L and/or C (from $\frac{1}{\sqrt{LC}}$ called the *resonance frequency*). Peak current (I_p) can be calculated based on the law of energy conservation as:

$$\begin{aligned} E_{tot} = E_C + E_L &= \frac{1}{2} L I^2 + \frac{1}{2} C V^2 \\ &= \frac{1}{2} L I_p^2 + 0 = 0 + \frac{1}{2} C V_0^2, \end{aligned} \tag{7.4}$$

where V_0 is the initial voltage difference through the inductor. Initially, all the energy in the system is stored in the UC ($\frac{1}{2} C V_0^2$) and no energy in the inductor. When Q_1 is closed, the energy in UCs starts to transfer to the inductor as a form of current

($\frac{1}{2}LI^2$). Because total energy in the LC circuit must be conserved, the energy and current in an inductor reach the peak current when all the energy accumulated in UCs transferred to the inductor. Eq. (7.4) can be modified as:

$$I_p = \sqrt{\frac{C}{L}} V_0.$$

Note that the large capacitance (C), initial voltage of the UC (V_{UC}) and small inductance (L) yield a high peak current (I_p). Finally, Eq. (7.3) can be re-written as:

$$i_{UC,on}(t) = \sqrt{\frac{C}{L}} V_{UC} \sin(\frac{1}{\sqrt{LC}} t). \tag{7.5}$$

We can also expect a similar effect when Q_1 is closed and write the discharge current as:

$$i_{UC,off}(t) = \sqrt{\frac{C}{L}} (V_{UC} - V_{bat}) \sin(\frac{1}{\sqrt{LC}} t), \tag{7.6}$$

where V_{bat} is the battery voltage.

7.4.2 Control knobs

Eq. (7.5) shows parameters that should be controlled for an efficient BMS. We now present the three control knobs affecting the parameters (t, L, C, and V_{UC}) in the equation, which are the keys to the development of our discharge/charge rate management to be presented in Section 7.5.

Duty cycle of signal for converter switches ($i_{UC}(t) = \sqrt{\frac{C}{L}} V_0 \sin(\frac{1}{\sqrt{LC}} \boxed{\mathbf{t}})$)

To operate the converters in the HESS, we need the switching signals for Q_1 and Q_2 switches. The duty cycle of the signal, the ratio between the pulse duration (T) and the period (P), should be controlled properly, because it determines the energy accumulation period (T) and the amount of charge moving to/from the electric load

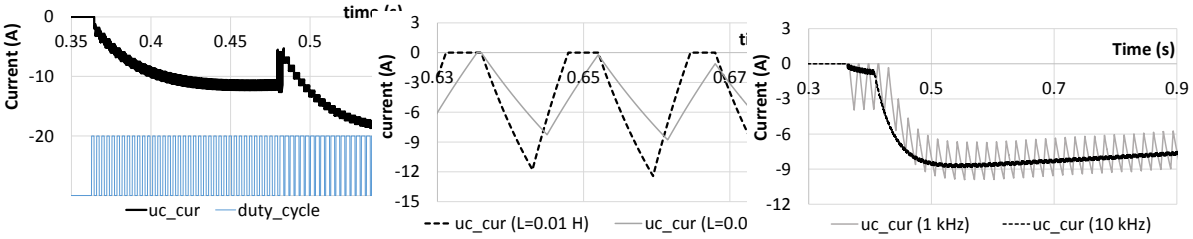

(a) Discharge current varies with the duty cycle of switch Q_1 in the converter

(b) Discharge current varies with the size of LC in the UC/converter

(c) Discharge current varies with switch Q_1's cycle in the converter

Figure 7.9: Three control knobs for discharge-rate management

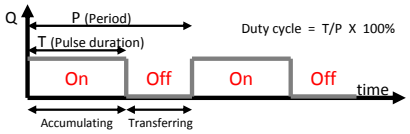

(a) Duty cycle of a rectangular waveform

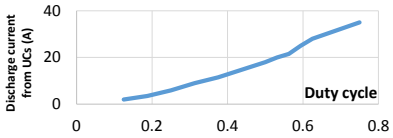

(b) Discharge current varies with the duty cycle of converter control signal

Figure 7.10: Duty cycle as a control knob

as illustrated in Fig. 7.9-(a). Fig. 7.10-(a) illustrates an example of duty cycle for the converter switches, and Fig. 7.10-(b) shows the discharge current variation with duty cycles. For example, when the converter accumulates more energy during each period due to an increase in the duty cycle, the system supplies more energy to the electric load.

LC Configuration of the UC-converter in the UC bank ($i_{UC}(t) = \sqrt{\frac{C}{L}} V_0 \sin(\frac{1}{\sqrt{LC}} t)$)

The LC configuration in the UC-converter dictates the UC's capacitance (C), the inductor's inductance (L) and the capacitor output voltage (V_0) as described in Fig. 7.11, and then affects the form of discharge/charge current according to Eq. (7.5). For example, a change in current through a larger inductor (high L) in the HESS tends to be slower as illustrated in Fig. 7.9-(b). Therefore, we can adaptively determine discharge/charge patterns by regulating V_0, L and C via reconfiguration

of LC circuit in the multiple UC-converters. For instance, when a UC bank's voltage (V_0) is too low to supply the required current, we can serialize UCs in the UC bank so as to increase output voltage of the UC bank.

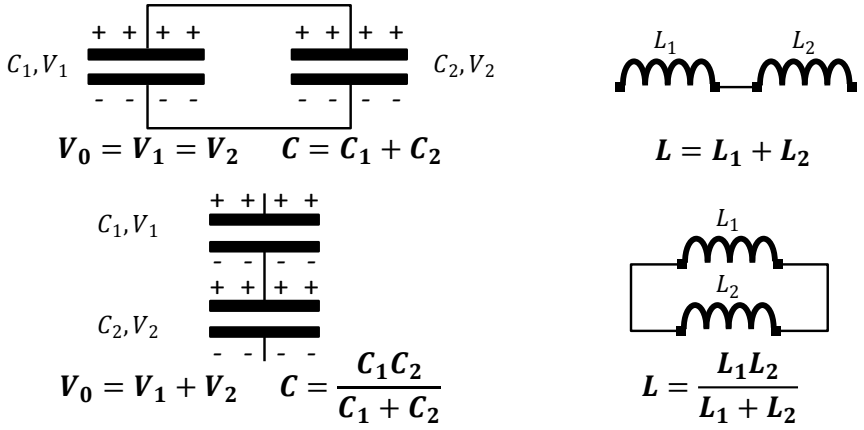

Figure 7.11: Voltage, capacitance and inductance vary with the configuration

Frequency of signal for converter switches

Discharge/charge current fluctuations in batteries may damage batteries. For example, as shown in Fig. 7.9-(c), discharge current changes greatly and peak-to-peak current gets up to 4A when it is operated by a 1 kHz switch signal, whereas discharge/charge current is stable at 10 kHz switch frequency. Therefore, the converter switches should be cycled fast enough to prevent the excessive discharge/charge current fluctuations. However, the required frequency for stable discharge/charge rate varies with *duty cycle* and *LC configuration* in the UC-converters, since the form of discharge/charge current depends on them. Based on the *duty cycle* and the *LC configuration*, we then adaptively regulate the frequency of the converter input switches to protect batteries from excessive discharge/charge current variations.

7.5 The Proposed Battery Discharge/charge-rate Management in the HESS

So far, we have examined circuit dynamics and control knobs that affect the discharge/charge current in the HESS. Based on them, we now develop battery discharge/charge rate management policies to extend the battery life. To extend the battery life, the BMS should mitigate the discharge/charge stress based on the power requirements and the battery degradation model, which is discussed in the previous chapter. This section states the requirements for extending the battery life when the information is not available, and then develop an overall management policy.

7.5.1 Requirements

To avoid fast performance degradation due to the stress, we should reduce peak discharge current ($\max(I_{bat(t)})$) and the amount of charge transferred to/from the electric motors as follows.

- Minimize $\Big[\int |I_{bat}(t)|dt\Big]$.
- Minimize $\Big[\max(I_{bat,discharge}(t))\Big]$.
- $\Big[I_{bat,recharge}(t) = 0\Big]$.

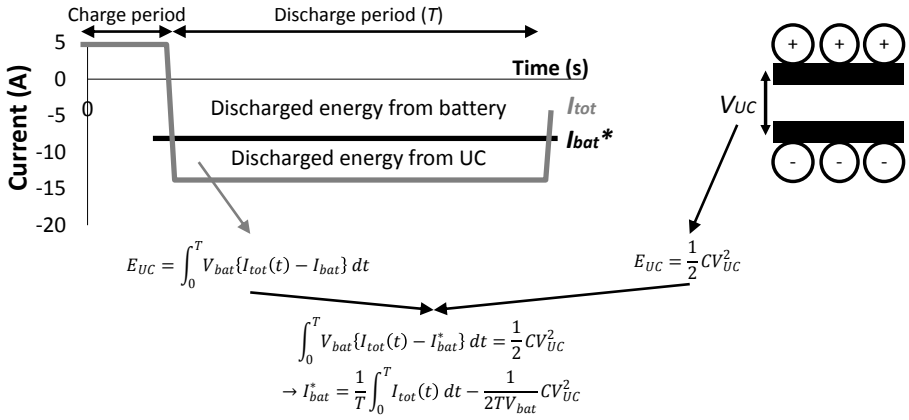

Figure 7.12: Calculation of target battery current (I_{bat}^*)

To satisfy the requirements of minimizing battery discharge/charge stress, all the energy in the UC ($E_{UC} = \frac{1}{2}CV^2$) should be discharged during the discharge period (T), and the UC accumulates the charge supplied by the RBS to reduce charge stress of battery as shown in Fig. 7.12. If total discharge current is known through a power requirement prediction, we can calculate constant target battery discharge current (I^*_{bat}) during the period (T) satisfying the requirements for reducing battery discharge/charge stress. The target discharge current (I^*_{bat}) is set to "0" if the braking system supplies charge to the battery ($I_{tot} > 0$), or "$\frac{1}{T}\int_0^T I_{tot}(t)dt - \frac{1}{2TV_{bat}}CV_{UC}^2$" otherwise. The following approaches in Sec. 7.5.2 are taken to make the battery current (I_{bat}) the target battery current (I^*_{bat}) as seen in Fig. 7.14.

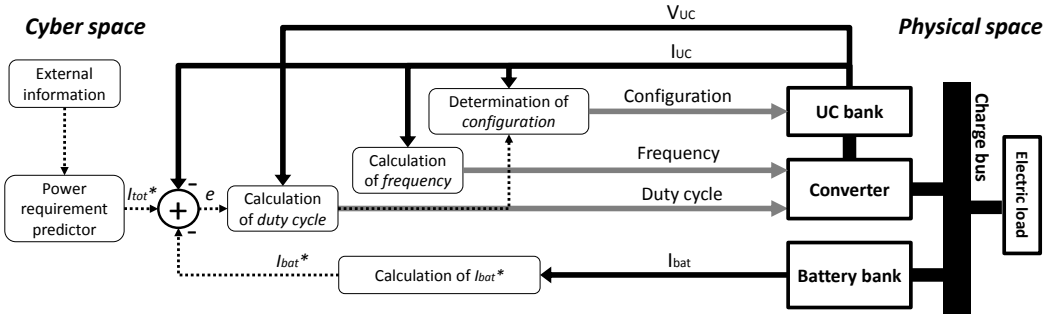

Figure 7.13: A schematic diagram of discharge/charge rate management: solid black lines, solid black arrows, solid grey arrows, and black dotted arrows indicate the current flows in the physical space, sensing flows, control for the physical space, and control flows in the cyber space, respectively; I^*_{tot}, I_{bat}, I^*_{bat} and I_{UC} denote the total predicted discharge/charge current, the discharge/charge current of a battery, the target discharge/charge current of a battery and a UC. Based on these values, the manager regulates the control knobs (i.e., *control frequency*, *duty cycles* and *configuration* of UC-converters)

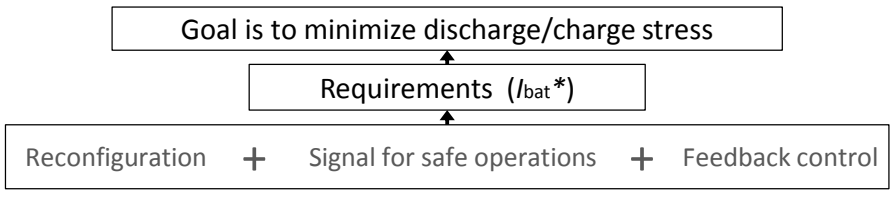

Figure 7.14: Requirements and approaches

7.5.2 Overall Management

By satisfying the requirements, we can design an efficient discharge/charge rate manager achieving a long life as seen in Fig. 7.14. To this end, we propose an integrated management algorithm for *duty cycle*, *frequency*, and *configuration* as illustrated in Fig. 7.13. Our management algorithm determines the *duty cycle* of converter switches that make target battery current (I^*_{bat}), and *configuration* of UC-converters (V_{UC}, L and C) which enables the HESS to achieve the target battery discharge/charge rate (I^*_{bat}). Meanwhile, the *frequency* for converter switches should be chosen carefully for the stable transfer of charge.

Dynamic regulation of duty cycle

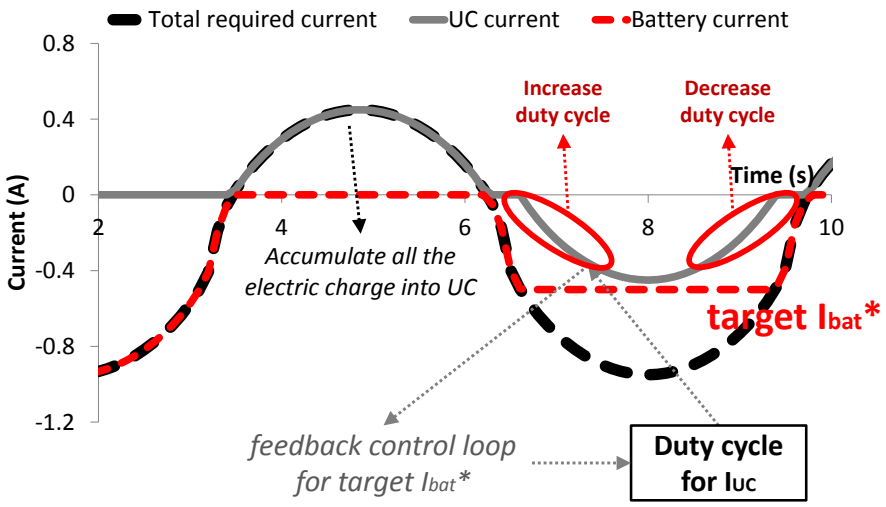

Figure 7.15: Duty cycle selection

To satisfy the requirements for achieving high UC utilization and moderate stress on the batteries, we set the target battery and UC current (I^*_{bat} and I^*_{UC}). We achieve the target discharge current by regulating the discharge rate of UCs (I_{UC}) through adaptive selection of duty cycle (D) as follows.

In Section 7.4.1, we explored the discharge current when a switch is repeatedly

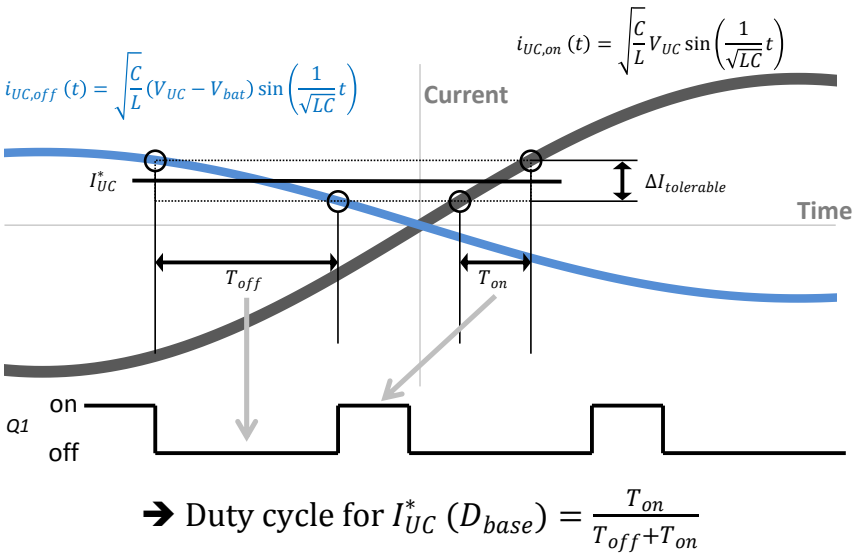

Figure 7.16: Base duty-cycle calculation

turned "on" and "off" ($i_{UC,on}$ and $i_{UC,off}$). By comparing the change rates of these discharge currents ($i_{UC,on}$ and $i_{UC,off}$), we can calculate the base duty cycle (D_{base}) that can maintain the required discharge current (I^*_{UC}). Fig. 7.16 and the following equation show how to calculate the base duty cycle for the target discharge current.

$$D_{base} = \frac{T_{on}}{T_{on} + T_{off}},$$

where T_{on} (likewise T_{off}) is the time duration the UC's current $i_{UC,on}$ (likewise $i_{UC,off}$) changes up to tolerable variation ($\Delta I_{tolerable}$) when the UC supplies the target current (I^*_{UC}).

To reduce the error due to inaccuracy in voltage measurements (V_{UC}, V_{bat}) or element sizes (L, C), we also adopt a *PD controller* handling the difference (u) between the target battery current ($I_{bat}*$) and the present battery current (I_{bat}) as seen in steps 3–5 of Algorithm 9. Finally, we select the duty cycle (D) to make the batteries supply the target discharge current (I^*_{bat}) based on the base duty cycle (D_{base}) and the estimation of difference (u) between the target and actual discharge rate.

Algorithm 9 Algorithm for dynamic regulation of duty cycle (DUTY)

1: $I^*_{bat} \leftarrow \text{target}(I_{bat}, C, V_{UC}, V_{bat}, T, I^*_{tot}(t))$;
2: $D_{base} \leftarrow (L, C, V_{UC}, V_{bat})$
3: $e \leftarrow I^*_{bat} - I_{bat}$;
4: $e_d \leftarrow \frac{(e - e_{prev})}{\Delta t}$;
5: $u \leftarrow k_p \cdot e + k_d \cdot e_d$; // k_p and k_d are tuning parameters
6: $D \leftarrow D_{base} + u$;

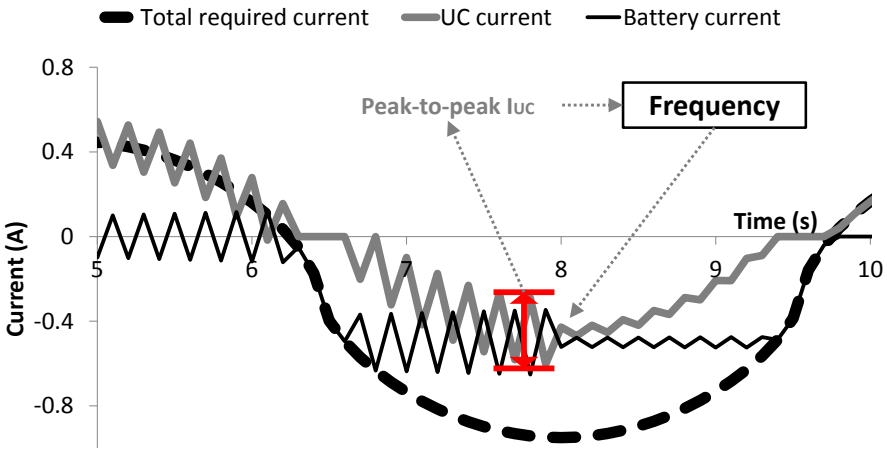

Figure 7.17: Selection of frequencies for converters

Dynamic regulation of switching frequencies for converters

To protect the batteries from current surges due to a periodically controlled converter, we control the frequencies ($f = \frac{1}{T}$) of the signal for the converter switches. We repeatedly capture the peak-to-peak discharge current of UCs (peak-to-peak I_{UC}), and regulate the frequency, achieving the moderate discharge rate of UCs and batteries as illustrated in Fig. 7.17 and Algorithm 10.

Reconfiguration

To increase the voltage swing range of UC banks while maintaining the capacity of the bank, we reconfigure UC-converter dynamically. When the UC bank is already charged or supposed to be recharged from the RBS soon, we parallelize the UCs in the bank to store the charge in UCs efficiently. However, the charge would be transferred to the electric load for operating EVs, and the capacitor voltage (V_0) would be

Algorithm 10 Algorithm for dynamic frequency regulation (FREQ)

```
if |peak-to-peak I_UC| ≥ margin then
    f ↑
else
    f ↓
end if
```

dropped over time. Then, UC banks cannot supply required current ($u \geq margin$) effectively due to lack of peak discharge current (I_p in Eq. (7.3)) even if the duty cycle (D) is maximum. In this case, we restore the output voltage of UC banks to increase peak current (I_p) by serializing the UCs. This reconfiguration enables the bank to supply the charge to the load, leading to larger voltage swing and energy capacity utilization as shown in Fig. 7.18. Algorithm 11 shows this process for determining whether to serialize or parallelize configuration (CFG) of the UC-converter in the HESS based on the current duty cycle (D) and the difference between the target and actual currents (u).

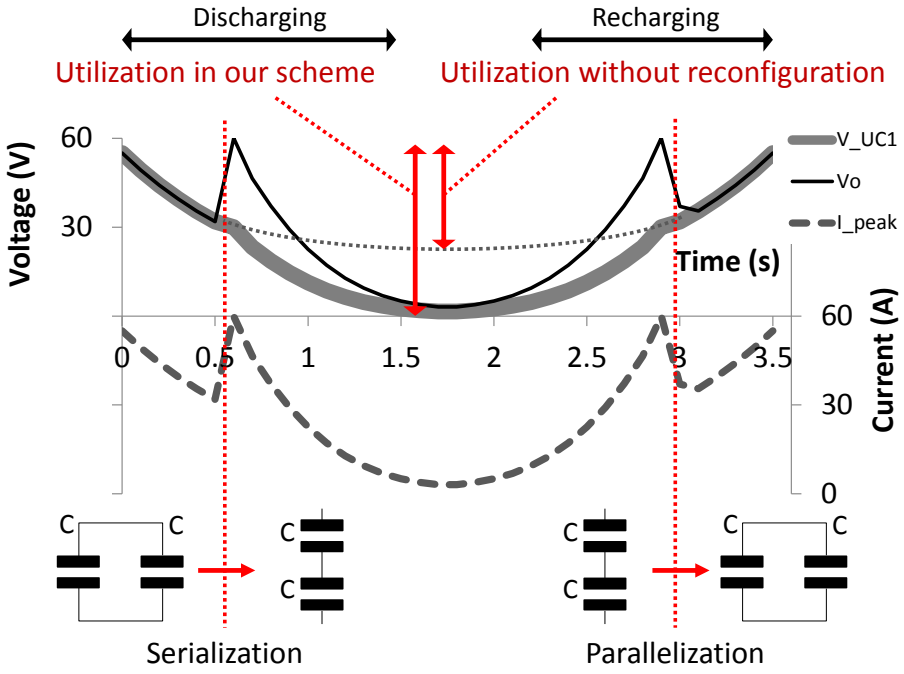

Figure 7.18: Selection of HESS configuration

Algorithm 11 Algorithm for selection of the HESS configuration (CFG)

```
if D = max(D) & u ≥ margin then
    CFG ← Series;
else if I_bat ≤ 0 then
    CFG ← Parallel;
else
    NO ACTION
end if
```

7.6 Implementation

So far, we have examined the circuit dynamics underlying HESSes and relevant management policies for efficient usage of UC banks. This section describes our implementation of a HESS architecture that supports the management algorithms discussed in Section 7.5.

7.6.1 Basic HESS architecture

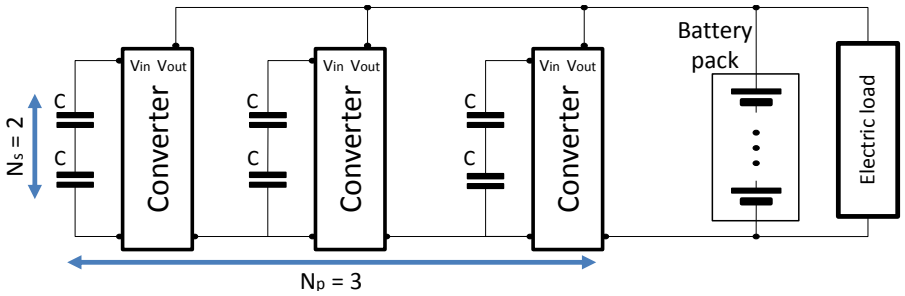

Figure 7.19: Basic architecture for a HESS

Fig. 7.19 shows a basic HESS architecture. Let N_p and N_s denote the number of UCs connected in parallel and series, respectively, and they are determined based on the components' physical constraints as discussed in Section 7.3.2. For example, if an UC pack should operate at high voltage, we have to deploy a large number of UCs in series (N_s).

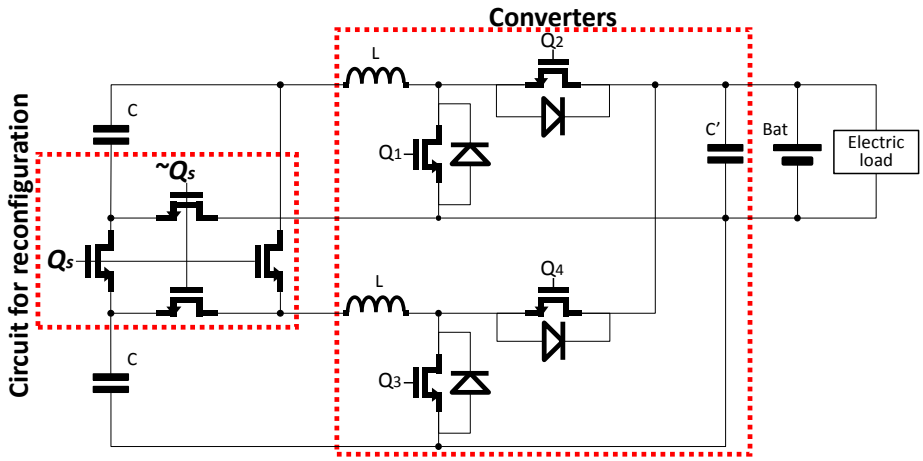

Figure 7.20: Reconfigurable architecture for a HESS

7.6.2 Reconfigurable architecture

The discharge/charge rate of the battery and UCs is strongly coupled with the HESS topology as seen in Section 7.4.2. Also, Section 7.2.1 shows the required discharge/charge rate (I_{tot}) in a modern energy storage varies widely, necessitating various HESS configurations. An optimal topology of the UC-converter depends on states of charge in UCs and/or the required discharge/charge current, necessitating a reconfigurable HESS. Therefore, we add reconfigurability with a few additional switches on the basic architecture of a HESS as illustrated in Fig. 7.20.

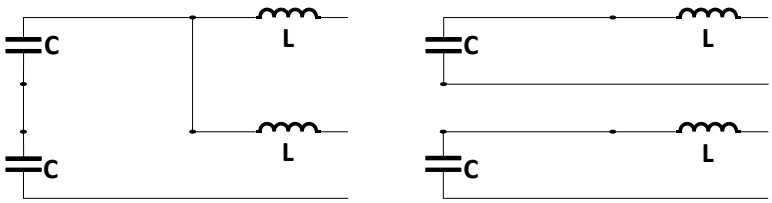

Figure 7.21: Two available configurations; the left configuration is set when Q_s is turned on and the right configuration when the switch is turned off

An input of switch Q_s determines the topology as seen in Fig. 7.21. For example, if Q_s is opened, we can use two UC-converter units which have C capacitance and L inductance, allowing for storing a large amount of charge. When the switch Q_s is

Algorithm 12 Algorithm for Discharge/Charge Rate Management

1: **while** 1 **do**
2: $[I_{bat}, I_{UC}] \leftarrow$ current sensors;
3: $I^*_{tot} \leftarrow$ Power requirement prediction;
4: $[D_{Q_1,Q_2,Q_3,Q_4}, u] \leftarrow \text{DUTY}(I^*_{tot}, I_{UC}, I_{bat})$;
5: $f_{Q_1,Q_2,Q_3,Q_4} \leftarrow \text{FREQ}(I_{UC})$;
6: $\text{CFG} \leftarrow \text{CFG}(D, u)$;
7: **if** $\text{CFG} = Series$ **then**
8: $Q_s \leftarrow 1$;
9: **else**
10: $Q_s \leftarrow 0$;
11: **end if**
12: $\text{delay}(\Delta t_{control})$;
13: **end while**

closed, UCs are serialized while inductors are parallelized, leading to decrease in not only capacitance of the UC bank ($2C \rightarrow \frac{1}{2}C$) but also inductance of the inductor in the converter ($2L \rightarrow \frac{1}{2}L$). Serialization of UCs can increase peak current (I_p) due to the increased voltage (V_0), enabling the BMS to effectively exploit UCs.

7.6.3 Management algorithm

The cyber part should be able to select inputs of switches (Q_s, Q_1, Q_2, Q_3 and Q_4) to satisfy the target discharge/recharge rate of batteries and UCs. Algorithm 12 describes our management policy. The main principle of our approach is to capture the charge in the UC bank temporarily and supply them to the electric load in order to reduce the battery stress. Steps 2–3 pre-process; we measure the current of UCs and battery banks, and calculate the discharge current of the next step. Steps 4–5 determine the form of cycled signal for converter switches. Algorithm 9 regulates duty cycle (D_{Q_1,Q_2,Q_3,Q_4}) of switch signals to yield the desirable battery current for longer lifetime, and Algorithm 10 chooses the frequency (f_{Q_1,Q_2,Q_3,Q_4}) of the signals for protecting cells from excessive current variations caused by periodically controlled ($\Delta t_{control}$) converters. Steps 6–11 decide on the configuration of UC-converters (CFG) according to Algorithm 11.

7.7 Evaluation

We now evaluate the proposed HESS. We first introduce performance metrics for the HESS and then describe the tools and settings used for the performance evaluation. Finally, we present the evaluation results. Fig. 7.22 describes our evaluation process.

7.7.1 Evaluation metrics: battery lifetime

Lifetime is an important metric in evaluating large-scale battery systems, because it significantly affects the cost of EVs. To evaluate the battery lifetime in the proposed HESS, we conducted extensive simulations, and recorded discharge/charge stresses. Then, we computed the battery lifetime by feeding the stress measurements into the lifetime model introduced in Section 7.3.1. We evaluated the lifetimes of multiple systems built at the same materials cost for a fair comparison.

7.7.2 Evaluation tools and settings

We built the several energy storage architectures by programming the control blocks and loading electric component models in a simulation tool. We then simulated different HESSes with a given electrical load using MATLAB, which is widely used for the verification of control systems [93]. During simulations, we recorded the interesting physical states to evaluate the HESSes.

Electric load

The US Environmental Protection Agency (EPA) provides "Dynamometer Drive Schedules" for standard emissions testing of driving. We used the dynamometer drive schedules as the *electric load* of an EV's powertrain.

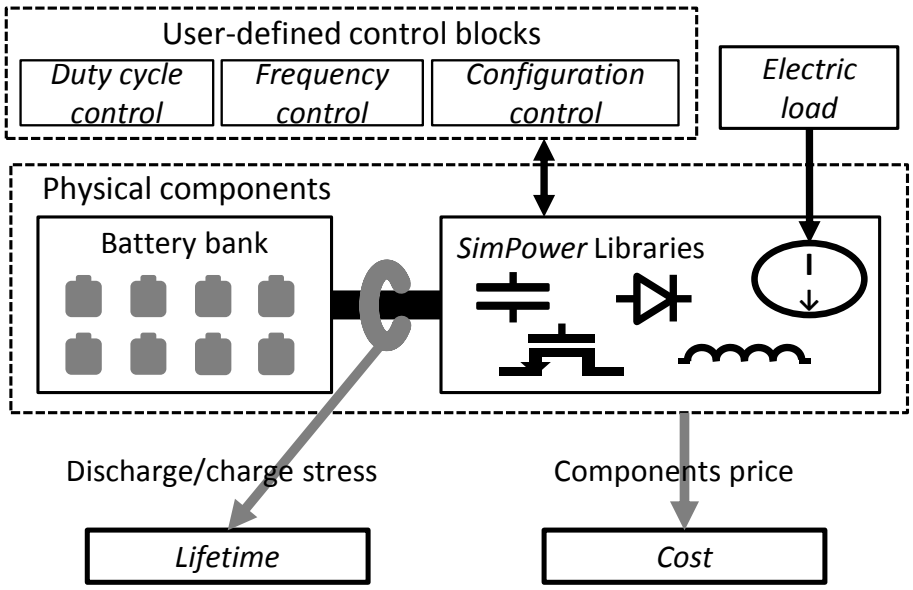

Figure 7.22: Evaluation process

Physical space simulation

MATLAB is a high-level language with a numerical computing environment, developed by MathWorks. *SimPowerSystems* library in MATLAB provides electric component models and tools for modeling and simulating electrical power systems. We used the component models to implement our reconfigurable HESS architecture in Section 8.7.1. We filled in the internal parameters of the components library by using the specification of components in the website [2] for realistic simulations.

Cyber space implementation

We also implemented control blocks describing our management algorithms. We specified the inputs of the control blocks and made the blocks determine outputs via the proposed algorithms such as *duty cycle control*, *frequency control* and *configuration control*. The algorithms monitor the states of the HESS and regulate the control knobs based on the states so as to reduce the discharge/charge stress of batteries.

7.7.3 Evaluation results

We have evaluated the following three HESS schemes:

- BASE: no ultra-capacitors;
- EX: existing HESSes introduced in Section 7.2 (the HESS with DC/DC converters);
- DRF: our HESS described in Section 7.5 (adaptive discharge/charge rate management with a reconfigurable architecture).

Lifetime

We ran simulation and extracted the discharge/charge stress of batteries for each scheme. Then, we estimated their lifetime based on the lifetime model. Table 7.2 shows the ratio of the average lifetime of DRF (and EX), to that of BASE. As shown in this table, DRF improves the lifetime by up to 153% and 37.7% over BASE and EX, respectively. We compared the discharge/charge stress to batteries under the three schemes by using the following equation.

- $\frac{1}{T}\Big[\int_0^T |I_{bat}(t)|dt\Big]$,

where T is an operation period. Table 7.3 shows the battery stresses under the same workload. Compared to BASE, DRF reduces the stress by 15.9%. DRF is even better than EX in that it can reduce the discharge/charge stress by up to 5.4% than EX. This reduction of discharge/charge stress extends the lifetime under DRF.

Type	EX/BASE	DRF/BASE
Lifetime (N_{cycle})	1.83	2.53

Table 7.2: Lifetime of energy storage systems

Type	BASE	EX	DRF
Stress of Battery	149.42	135.67	128.43

Table 7.3: Discharge/charge stress of energy storage systems

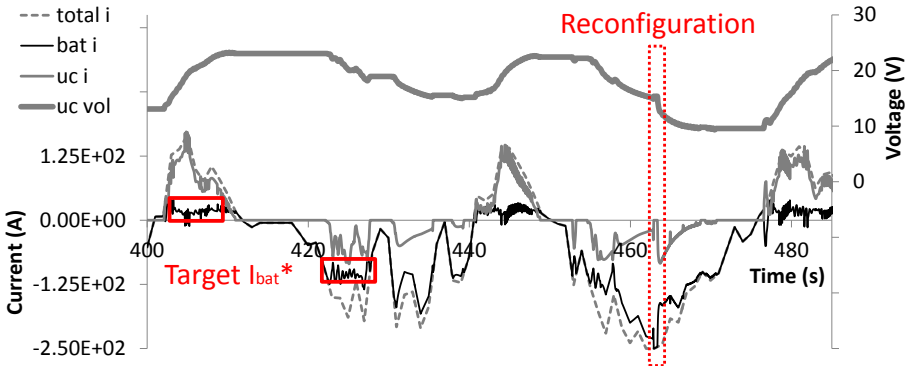

Figure 7.23: Example of discharge/charge current of DRF

Energy Capacity Utilization of UCs

Our HESS introduced in Sections 7.5 and 8.7.1 includes the method to increase the utilization of energy capacity. It actually contributes to the extension of battery life, since increasing the capacity utilization decreases the discharge/charge stress of batteries. We first calculate the target battery discharge current (I^*_{bat}) maximizing UC utilization, and the proposed management policy manipulating UCs current (I_{UC}) to satisfy the target battery discharge current as shown in red boxes in Fig. 7.23. Furthermore, whenever UCs cannot supply the required current due to lack of UC bank voltage, the HESS reconfigures UC-converters to boost the voltage of UC banks to supply a sufficient amount of charge. As shown in dotted red box in Fig. 7.23, our HESS changes the configuration so as to supply charge effectively by allowing a larger voltage swing of the UCs.

7.8 Conclusion

To meet the increasing demand to make EVs financially affordable, BMSes should be able to cope with harsh discharge/charge rate that affects the battery life significantly. A form of switch inputs (frequency and duty cycle) for converters and the HESS configuration are key control knobs for slowing down the battery capacity

degradation, since they have significant impact on the discharge/charge rate of each energy storage device in the HESS. In this chapter, we have presented how to achieve efficient battery management using these control knobs. We proposed a new battery discharge/charge rate management scheme that determines, in real time, the form of input signals and the configuration of the HESS based on the analysis of their impact on the discharge/charge rate of battery cells. To realize this scheme, we also proposed the reconfigurable HESS architecture, which can select the configuration of the HESS. Our evaluation using realistic simulation has shown that the proposed HESS management makes a significant improvement of battery life without increasing cost, over a simple method often seen in the existing BMSes.

It would be interesting to improve the discharge/charge rate management based on the proposed architecture. One direction is to improve the performance of discharge/charge rate management with a power requirement prediction, since it allows BMSes to prepare for supplying or storing energy in advance [68]. Our approaches can also be used for other types of HESSes including fuel cells which have their own power and energy densities. These are matters of our future inquiry.

CHAPTER VIII

Offline Guarantee and Online Management of Power Demand and Supply in Cyber-Physical Systems

8.1 Introduction

Most electric systems, such as electric vehicles, mobile robots, nano satellites, and drones, have to perform various mechanical/electrical operations for their intended applications. For example, a drone needs to (i) operate the flight motors to fly, (ii) power sensors, coolers, and communication modules, (iii) operate the camera and stepper motors to take pictures and deliver parcels, and (iv) perform the computation necessary to maintain its stability (see Fig. 3 in the supplementary file [67]). These *multiple power-demand operations* impose different power demands on the system and may be triggered at different times, requiring the system to effectively provide time-varying supply of power [23, 24, 113, 28, 78, 68]. Existing studies on the power scheduling problem focused on the reduction of peak power by scheduling multiple power-demand operations and analysis thereof [83, 26, 46, 16].

However, a complete solution of the power scheduling problem also needs to characterize energy storages/sources because it affects power capability for the power-demand operations. We address this need by targeting hybrid energy storage systems (HESSes) comprised of *multiple power-supply sources and storages*, such as batteries, supercapacitors, and renewable energy sources, whose concept and implementation

have been proposed and explored in [28, 114, 60, 111, 25, 65, 109]. A combination of high-energy-density batteries and high-power-density supercapacitors enables the system to supply the required time-varying power for a longer time, improving system sustainability. Moreover, renewable power sources (e.g., solar, wind and geothermal energy) enhance the system's power capacity and reduce the load intensity on batteries and supercapacitors, thus prolonging their lifetime [129, 12, 58, 112, 79].

Researchers have studied the optimal design of a HESS to meet the power demands at minimum cost [15, 44, 60, 64, 148]. They first explored possible storage configurations (i.e., size, type, connection) of multiple power-source supplies and storages, and then selected the best configuration by comparing the performance and the energy production cost. Search for an optimal design iterates to generate candidate configurations until one of the candidates satisfies the pre-defined performance and cost criteria [44]. However, these approaches do not guarantee power-sufficiency during operation, as the electric load and criteria are determined based on the load history or the designer's experience and intuition.

To ensure the power sufficiency, we will develop a power scheduling and analysis framework for a reliable energy storage system with multiple power-supply sources and multiple power-demand operations, which achieves the following goals.

G1. **Offline power-supply guarantee:** We provide an offline guarantee to complete every operation before its deadline (i.e., *operation-level power guarantee*) while keeping the amount of power supplied to the entire system no smaller than the sum of power required by individual operations at any time instant (i.e., *system-level power guarantee*).

G2. **Online power management:** We develop online power management that effectively utilizes the difference between the worst-case supplied/demanded

power and the actual one for system performance improvement.

This is a typical *cyber-physical systems* (CPS) problem in that we should address power scheduling and its analysis in the cyber space, based on comprehensive understanding of the physical characteristics of power supply and demand.

To achieve G1, we find similarities between the power-supply guarantee problem and a real-time scheduling problem that determines the execution order of real-time tasks; while the operation-level power guarantee corresponds to the task-level deadline satisfaction, the system-level power guarantee matches the computing platform's capacity constraint. Using the techniques of real-time scheduling, we solve the power-supply guarantee problem in two steps. First, we address the case of multiple power-demand operations with a single, uniform power-supply source (e.g., a battery pack), and develop a scheduling framework and offline power guarantee analysis. Based on the scheduling and analysis framework, we address the general problem—multiple power-demand operations with multiple power-supply sources. For the second step, we develop two scheduling frameworks to utilize additional sporadic power-supply sources: one for sharing additional power-supply sources by all power-demand operations, and the other for assigning the sources to only some of power-demand operations. Our solution for G1 not only demonstrates that the technique of real-time scheduling helps solve a CPS problem, but also addresses the design problem of a HESS by finding a combination of energy storages at minimum cost.

In addition to making the offline power-supply guarantee (G1), we develop online power management (G2), which aims at increasing the utilization of the energy generated by renewable power-supply sources. That is, scheduling multiple power-supply sources and power-demand operations according to G1 necessarily yields sur-

plus energy since G1 considers the worst case, i.e., the largest power demand and the smallest power supply. While we can utilize the surplus energy for improving various performance aspects of a HESS, we focus on the reduction of the peak power of our main energy storage (i.e., a battery pack) to improve its capacity and lifetime [92, 34, 72, 17, 65, 64].

We have prototyped a HESS-powered system (Fig. 8.5 as described in Section 8.7 and Fig. 1 in the supplementary file [67]) to validate the proposed solutions for G1 and G2. The prototype consists of power-consuming components such as wheel motors, stepper motors, coolers, sensors and converters, whose operations are controlled by an application. The prototype is powered by a HESS consisting of Lithium-ion batteries, ultra-capacitors (UCs), and solar panels. When designing this prototype, we determine the sizes of batteries, UCs and solar panels that ensure the worst-case power sufficiency based on the offline power-supply guarantee G1. At run-time, the master board schedules the power-demanding operations with fixed-priority scheduling, and determines the power distribution among batteries, UCs, and solar panels according to online power management G2. Our experimental results show that the prototype not only supplies a sufficient amount of power to the components during their operation, and but also reduces the battery's peak power by 33.1%.

In summary, this chapter makes the following main contributions:

- Design of a power scheduling and analysis framework that consists of (i) offline power-supply guarantee, which is the first power guarantee analysis applicable to the design of a HESS, and (ii) online power management for a HESS to enhance the energy storage's performance,
- Demonstration of the effectiveness of the proposed framework via in-depth, realistic experiments, and

- Solution of an important CPS problem using real-time scheduling techniques.

The chapter is organized as follows. Section 8.2 describes the characteristics of power-supply sources and power-demand operations, and Section 8.3 formally states our main problem. Sections 8.4 and 8.5 present the power scheduling and analysis framework for the offline power-supply guarantee, while Section 8.6 details online power management. Section 8.7 implements our solutions on a prototype and evaluates their power sufficiency and reduction of peak power dissipation. Finally, the chapter concludes with Section 8.8.

8.2 Characteristics of Power-Demand Operations and Power-Supply Sources

As the first step for offline power-supply guarantee and online power management, we investigate the characteristics of power-demand operations and power-supply sources.

8.2.1 Power-demand operations

We consider typical mechanical/electrical operations that are executed repeatedly to complete a given set of tasks. For example, an operation that maintains a constant vehicle speed would accelerate/decelerate motors repeatedly based on the online collected speed data. In this closed-loop control system, the operation updates the required acceleration and requests it to the motor controller at every control period — the operation requires a certain level of power, and must be completed within its control period.

We model the power-demand operations as follows. A system has a set of mechanical/electrical operations $\lambda = \{\lambda_1, \lambda_2, \ldots, \lambda_{n^{\mathtt{d}}}\}$, where $n^{\mathtt{d}}$ is the number of operations.[1] The power usage of λ_i is modeled by the minimum inter-arrival time $T_i^{\mathtt{d}}$, its maximum

[1] Throughout the chapter, we use the superscripts `d` and `s` for power demand and power supply, respectively.

power consumption $P_i^{\mathtt{d}}$, and the maximum length of execution $L_i^{\mathtt{d}}$. Each operation is assumed to be non-preemptive; unlike a computing task executed on a processor, a preemption of an operation on a power system either yields incorrect system behavior or incurs significant cost. The former happens because the physical state of devices before a preemption is not necessarily identical to that after the preemption, e.g., revolutions of a motor per minute. The latter also makes sense in that most power-consuming devices are deployed in a distributed manner, so a preemption and its re-activation entail non-trivial communication/operation overhead such as sending a message via communication channel, pausing the mechanical/electrical operation, and sending back a preemption completion message to the master controller. Each operation is also assumed to be rigid, i.e., providing more power does not reduce the execution length.

Considering the characteristics described so far, λ_i with parameters $T_i^{\mathtt{d}}$, $P_i^{\mathtt{d}}$, and $L_i^{\mathtt{d}}$ invokes its instances as follows. Each instance's release time is separated from the predecessor by at least T_i time units, and each instance should be finished within T_i time units after its release. Once starting to execute, each instance performs its execution during at most L_i time units without any preemption, and the amount of actual power consumption at t within the interval is denoted by $P_i^{\mathtt{d}}(t)$, which is less than or equal to $P_i^{\mathtt{d}}$.[2]

Finally, each operation has its own priority based on the importance of the operation; we consider fixed-priority scheduling [86] using the predefined operation-level priorities.

[2]Throughout the chapter, $P(t)$ implies the actual power demand/supply at t, and P represents the maximum/minimum power demand/supply. Also, we use the term of an "operation" for an "instance" of the operation, when no ambiguity arises.

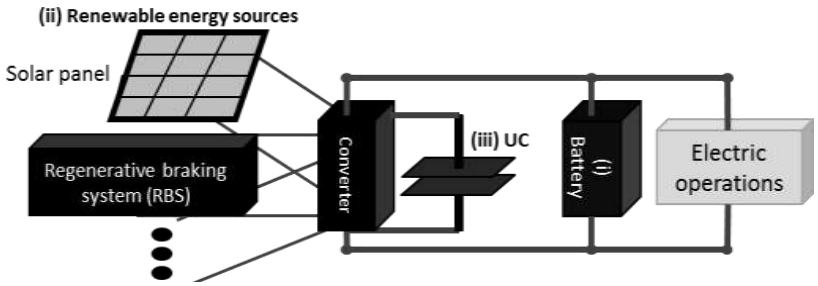

Figure 8.1: Battery-centric hybrid energy storage system model

8.2.2 Power-supply sources

We consider a battery-centric hybrid energy storage system (HESS) that is comprised of three parts: (i) an energy-dense lithium-ion battery pack, (ii) a set of auxiliary renewable energy sources, and (iii) a power-dense energy buffer as shown in Fig. 8.1. Although relatively simple, this architecture contains essential parts for advanced energy management, and each part has been studied extensively [28, 90, 50, 65, 114, 27].

While batteries are widely used as the main energy storage due to their capability to store a large amount of energy and deliver the required power, renewable energy sources such as an RBS (Regenerative Braking System) and a solar panel, supply power sporadically. For instance, an RBS in a vehicle can supply power only when the vehicle decelerates, and the amount of generated power is dependent on braking torque that each brake can provide. A solar panel generates the energy when sunlight strikes a solar cell. On the other hand, the energy buffer accommodates surges of recharging current to protect the battery and provide power when the power requirement is high. Fig. 4 in the supplementary file [67] is an example showing how the energy buffer works for accommodating power supply from renewable energy sources and powering requested operations.

Described below are notations and characteristics of above-mentioned power-

supply sources and storages. Let $\Gamma_{\mathtt{bat}}$ and $\Gamma_{\mathtt{UC}}$ denote the battery pack and the energy buffer corresponding to (i) and (iii), respectively, and they can supply a certain amount of power, which are limited to their individual power capabilities $P^{\mathtt{s}}_{\mathtt{bat}}$ and $P^{\mathtt{s}}_{\mathtt{UC}}$, respectively; $P^{\mathtt{s}}_{\mathtt{bat}}(t)$ ($\leq P^{\mathtt{s}}_{\mathtt{bat}}$) and $P^{\mathtt{s}}_{\mathtt{UC}}(t)$ ($\leq P^{\mathtt{s}}_{\mathtt{UC}}$) denote the actual power supply at t of the corresponding sources. Let $L^{\mathtt{s}}_{\mathtt{UC}}$ denote the minimum time interval for $\Gamma_{\mathtt{UC}}$ to supply power as much as $P^{\mathtt{s}}_{\mathtt{UC}}$ when the system starts, i.e., at $t = 0$, $\Gamma_{\mathtt{UC}}$ has at least $P^{\mathtt{s}}_{\mathtt{UC}} \cdot L^{\mathtt{s}}_{\mathtt{UC}}$ amount of energy.[3] We assume that the target system halts when there is no energy in the battery pack, meaning that we do not need to specify the interval length of $\Gamma_{\mathtt{bat}}$.

As to (ii), let $\Gamma = \{\Gamma_1, \Gamma_2, ...\Gamma_{n^{\mathtt{s}}}\}$ denote a set of auxiliary renewable energy sources, where $n^{\mathtt{s}}$ (≥ 0) is the number of elements in the set. Each energy source Γ_i is modeled with the maximum inter-arrival time $T^{\mathtt{s}}_i$, the minimum supplied power $P^{\mathtt{s}}_i$, and the minimum length of supply duration $L^{\mathtt{s}}_i$. That is, Γ_i generates at least $P^{\mathtt{s}}_i$ amount of power during at least $L^{\mathtt{s}}_i$ time units at the end of every period whose length is no larger than $T^{\mathtt{s}}_i$. Let $P^{\mathtt{s}}_i(t)$ is the actual supplied power at t from Γ_i. Power generation from Γ_i may be unpredictable, which makes it difficult to derive the parameters of Γ_i. However, if we imagine power generation from solar panels during daytime, we can derive the parameters that express conservative behaviors in terms of the amount of power generation; we will show an example of Γ_i using our prototype in the evaluation section (Fig. 2 in the supplementary file [67]). Note that parameters that provide "guarantee" of power supply (i.e., $P^{\mathtt{s}}_{\mathtt{bat}}$ amount of power for all time and $P^{\mathtt{s}}_i \cdot L^{\mathtt{s}}_i$ amount of energy for every $T^{\mathtt{s}}_i$ time units) will be utilized for the offline power guarantee, while any surplus energy (the information which is available only at run-time) will be stored in $\Gamma_{\mathtt{UC}}$ and used for online management for

[3] For example, the battery pack supplies energy to the energy buffer when an electric vehicle turns on the ignition.

minimizing battery peak power. Also, we assume that the energy $\Gamma_{\mathtt{UC}}$ can store is sufficiently large so as to accommodate power generated by all the renewable energy sources.

8.3 Problem Statement and Solution Approach

We first present a formal problem statement for achieving offline power-supply guarantee and online power management. Then, we give high-level explanation how to solve the problem.

Problem statement. Using the characteristics of power-demand operations and power-supply sources described in Section 8.2, we formally state the problem to be solved as:

Given a set of mechanical/electrical operations λ, the battery pack $\Gamma_{\mathtt{bat}}$, the energy buffer $\Gamma_{\mathtt{UC}}$, a set of auxiliary renewable energy sources Γ, and the operation interval $[0, t_{\mathtt{max}})$,

Determine $P^{\mathtt{s}}_{\mathtt{UC}}(t)$ and $\{P^{\mathtt{d}}_i(t)\}_{i=1}^{n^{\mathtt{d}}}$ for all $t \in [0, t_{\mathtt{max}})$ for achieving the following objective function.

$$\text{Minimize (S0)} \int_0^{t_{\mathtt{max}}} P^{\mathtt{s}}_{\mathtt{bat}}(t) + P^{\mathtt{s}}_{\mathtt{bat\text{-}loss}}(t)\, dt,$$

$$\text{Subject to (S1)} \sum_{\lambda_i \in \lambda} P^{\mathtt{d}}_i(t) - P^{\mathtt{s}}_{\mathtt{UC}}(t) - \sum_{\Gamma_i \in \Gamma} P^{\mathtt{s}}_i(t) = P^{\mathtt{s}}_{\mathtt{bat}}(t) \le P^{\mathtt{s}}_{\mathtt{bat}},$$

$$\text{(S2)}\ P^{\mathtt{s}}_{\mathtt{UC}}(t) \le P^{\mathtt{s}}_{\mathtt{UC}},$$

(S3) Every instance of each operation $\lambda_i \in \lambda$ finishes its execution within $T^{\mathtt{d}}_i$ time units after its release.

$\{P^{\mathtt{s}}_i(t)\}_{i=1}^{n^{\mathtt{s}}}$ are not control knobs in that their generated power is immediately stored in $\Gamma_{\mathtt{UC}}$ or served for power-demand operations. $P^{\mathtt{s}}_{\mathtt{bat}}(t)$ is also not, because it

is determined once $P^{\mathsf{s}}_{\mathtt{UC}}(t)$ and $\{P^{\mathsf{d}}_i(t)\}_{i=1}^{n^{\mathsf{d}}}$ are determined as shown in S1. For each $P^{\mathsf{d}}_i(t)$, we determine the time instant at which each λ_i starts to execute. When it comes to $P^{\mathsf{s}}_{\mathtt{UC}}(t)$, we determine the amount of supplied power from $\Gamma_{\mathtt{UC}}$ to λ at each time instant t.

$P^{\mathsf{s}}_{\mathtt{bat\text{-}loss}}(t)$ in S0 denotes the amount of power dissipation at t caused by the power supply of the battery pack; in other words, we lose $P^{\mathsf{s}}_{\mathtt{bat\text{-}loss}}(t)$ of power due to supplying $P^{\mathsf{s}}_{\mathtt{bat}}(t)$ of power from the battery pack at t. Therefore, S0 implies the amount of energy used and dissipated by the battery pack; since the former (i.e., the amount of energy used) is not a control knob, we should reduce the latter (i.e., the amount of energy dissipated) using a simple circuit-based battery model [147]: $P^{\mathsf{s}}_{\mathtt{bat\text{-}loss}}(t) = I^2_{\mathtt{bat}}(t) \cdot R_{\mathtt{bat}}(t)$, where $R_{\mathtt{bat}}(t)$ is a battery's internal resistance, and $I_{\mathtt{bat}}(t)$ is the battery's discharge/charge current for supplying $P_{\mathtt{bat}}(t)$. Since power dissipation is quadratically proportional to discharge/charge battery current, the minimization of battery peak current may reduce energy dissipation of the battery pack, potentially extending the battery operation-time.

Solution approach. To achieve the above objective, we develop a power scheduling and analysis framework that consists of two steps, as shown in Fig. 8.2. In the first step, we focus on satisfaction of constraints S1, S2 and S3, achieving offline power-supply guarantees to complete every operation before its deadline while keeping the amount of power supplied to the entire system no smaller than the sum of power required by individual operations at any time instant. To this end, we consider two sub-steps: one for the single, uniform power-supply source, and the other for the multiple power-supply sources, both of which use parameters that exhibit the worst-case behaviors, e.g., P^{d}_i, not $P^{\mathsf{d}}_i(t)$. First, in Section 8.4 we will consider scheduling of λ only with $\Gamma_{\mathtt{bat}}$, and develop a power scheduling framework and its

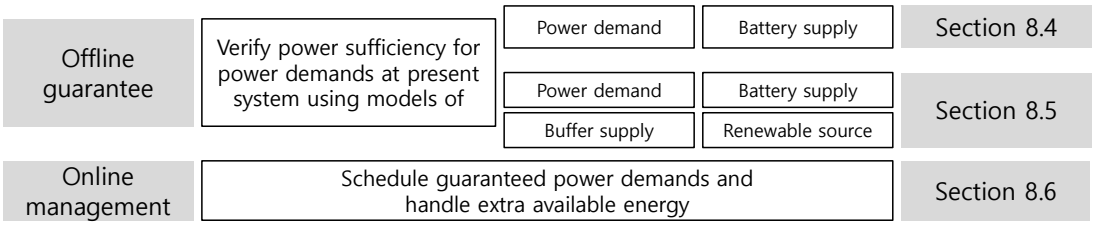

Figure 8.2: Outline of our power scheduling and analysis framework that consists of offline power guarantee and online power management

power guarantee analysis that determines whether or not λ is always scheduled on time without any power shortage under fixed-priority scheduling. Then, we extend the results for considering additional power-supply sources Γ. Adding Γ and using the fact that $\Gamma_{\mathtt{UC}}$ has the minimum energy when the system starts, in Section 8.5 we will suggest two approaches that utilize the power from Γ: one for sharing the power by all operations, and the other for assigning the power to some operations. We also develop the scheduling framework and power guarantee analysis for both approaches.

For the second step, Section 8.6 aims to minimize S0 without compromising S1, S2 and S3. Since the first step is performed based on parameters that exhibit the worst-case behaviors, a lot of energy is actually stored in $\Gamma_{\mathtt{UC}}$, coming from the difference between $P_i^{\mathtt{s}}$ and $P_i^{\mathtt{s}}(t)$. To effectively utilize the difference for minimizing S0, in Section 8.6 we propose an online power management framework to reduce battery peak dissipation, thereby improving battery performance. Since greedy usage of the energy buffer may cause energy shortage when it is needed to mitigate the subsequent surges of power demand, we determine power supply of the energy buffer ($P_{\mathtt{UC}}^{\mathtt{s}}(t)$) effectively, by considering the current status of the energy buffer and the history of power demand.

8.4 Scheduling of Multiple Power-Demand Operations with a Uniform Supply

In this section, we present how to schedule a set of power-demand operations (λ) when the battery pack ($\Gamma_{\texttt{bat}}$) is the sole power-supply source. We first develop a scheduling framework that considers the characteristics of λ and $\Gamma_{\texttt{bat}}$ described in Section 8.2. Under this scheduling framework, we then develop an offline power guarantee analysis that determines whether every operation in λ powered by the battery pack is performed before its deadline without suffering any power shortage.

8.4.1 Scheduling framework

We would like to schedule a set of multiple operations (λ) so as to achieve a system-level and operation-level power guarantee under the uniform supply from the battery pack $\Gamma_{\texttt{bat}}$. By "system-level power guarantee," we mean that the sum of power demand at any time instant should be no larger than maximum power capability of the battery pack, i.e., $\sum_{\lambda_i \in \lambda} P_i^{\texttt{d}}(t) \leq P_{\texttt{bat}}^{\texttt{s}}$, which is equivalent to S1.[4] To achieve the operation-level power guarantee, every operation should receive sufficient power within its period, which is S3.

Our scheduling framework employs the work-conserving policy based on the worst-case power demand and operation-level fixed-priority scheduling policy. The former implies that an operation λ_k can start to execute as long as its worst-case power demand $P_k^{\texttt{d}}$ (as opposed to the actual power demand $P_k^{\texttt{d}}(t)$) is no larger than the difference between the battery capability $P_{\texttt{bat}}^{\texttt{s}}$ and the sum of the worst-case power demand of currently-executing operations $\sum_{\lambda_i \in Q_{\texttt{run}}} P_i^{\texttt{d}}$. The latter implies that the scheduling framework prioritizes the operations that satisfy the above condition.

Since each operation exhibits the non-preemptive behavior as described in Sec-

[4] Since this section considers the sole supply of $\Gamma_{\texttt{bat}}$, we remove terms of the energy buffer and a set of renewable power-supply sources in S1.

Algorithm 13 SCHEDULING FRAMEWORK

The following steps are performed whenever at least one mechanical/electrical operation is finished or released at t:

1: For each λ_k finished at t, $Q_{\texttt{run}} \leftarrow Q_{\texttt{run}} \setminus \{\lambda_k\}$
2: For each λ_k released at t, $Q_{\texttt{ready}} \leftarrow Q_{\texttt{ready}} \cup \{\lambda_k\}$
3: Sort $Q_{\texttt{ready}}$ by given operation-level fixed-priorities
4: **for** $\lambda_k \in Q_{\texttt{ready}}$ (a higher priority operation is chosen earlier) **do**
5: **if** $P_k^{\texttt{d}} \leq P_{\texttt{bat}}^{\texttt{s}} - \sum_{\lambda_i \in Q_{\texttt{run}}} P_i^{\texttt{d}}$ **then**
6: $Q_{\texttt{run}} \leftarrow Q_{\texttt{run}} \cup \{\lambda_k\}$
7: $Q_{\texttt{ready}} \leftarrow Q_{\texttt{ready}} \setminus \{\lambda_k\}$
8: **end if**
9: **end for**

tion 8.2, an operation can start its execution only when it is released or the other operation is finished, and each operation, once started, continues its execution until the completion. Therefore, the scheduling framework can be expressed (as in Algorithm 13) by describing actions for the situations. Lines 1–3 update the ready queue $Q_{\texttt{ready}}$ that contains operations ready to execute, and the running queue $Q_{\texttt{run}}$ for currently-executing operations. Lines 4–9 select operations to be started and move them from $Q_{\texttt{ready}}$ to $Q_{\texttt{run}}$. Although the scheduling framework prioritizes operations based on their priorities, a lower-priority operation λ_j in $Q_{\texttt{ready}}$ can start its execution earlier than a higher-priority operation λ_k in $Q_{\texttt{ready}}$, if the remaining power capability of the system (i.e., $P_{\texttt{bat}}^{\texttt{s}} - \sum_{\lambda_i \in Q_{\texttt{run}}} P_i^{\texttt{d}}$) is larger than $P_k^{\texttt{d}}$ but, no larger than $P_j^{\texttt{d}}$, as described in line 5.

Analogy with real-time scheduling. The scheduling framework presented in Algorithm 13 is similar to gang scheduling [61] in the area of real-time scheduling, where $P_i^{\texttt{d}}$ corresponds to the number of threads to be parallelized for a real-time task, and $L_i^{\texttt{d}}$ matches the WCET (Worst-Case Execution Time) of each thread. Note that $P_i^{\texttt{d}}$ is a continuous variable, but the number of threads is a discrete value. While existing studies for gang scheduling have focused on preemptive scheduling [61, 54, 19], we need non-preemptive gang scheduling. In Section 8.4.2, we will develop an

offline power guarantee analysis, corresponding to the schedulability analysis of non-preemptive gang scheduling, which is, to the best of our knowledge, the first attempt in the real-time scheduling field.

We also note that the similarity to gang scheduling holds for the case of this section—multiple power-demand operations only with the uniform supply; it is a new type of scheduling problem to address the general case of multiple power-demand operations and multiple power-supply sources, which will be addressed in Section 8.5.

8.4.2 Offline power guarantee analysis

Since each operation is non-preemptive, we need to check if each operation λ_k can start its execution no later than $(T_k^{\mathtt{d}} - L_k^{\mathtt{d}})$ time units after its release; once it starts to execute, it completes execution within its period without any preemption. Therefore, we focus on the interval of length $(T_k^{\mathtt{d}} - L_k^{\mathtt{d}} + \epsilon_t)$, which begins at the time of λ_k's release, and check whether the sum of energy consumed by other operations within the interval is strictly less than $(P_{\mathtt{bat}}^{\mathtt{s}} - P_k^{\mathtt{d}} + \epsilon_p) \cdot (T_k^{\mathtt{d}} - L_k^{\mathtt{d}} + \epsilon_t)$, where ϵ_t and ϵ_p denote the time and power quantum (the smallest unit). Since the smallest power that prevents λ_k from execution at each time instant is $(P_{\mathtt{bat}}^{\mathtt{s}} - P_k^{\mathtt{d}} + \epsilon_p)$, the above condition guarantees the start of λ_k's execution to be no later than $(T_k^{\mathtt{d}} - L_k^{\mathtt{d}})$ time units after its release.

The remaining step is then to calculate $I_{k \leftarrow i}(\ell)$, the amount of energy demanded by instances of λ_i within an interval of length ℓ that contributes to prevention of λ_k from starting its execution. Note that for calculation of $I_{k \leftarrow i}(\ell)$, we limit the power demand at each time instant to $(P_{\mathtt{bat}}^{\mathtt{s}} - P_k^{\mathtt{d}} + \epsilon_p)$, since we need to know whether the sum of all power demands at each time instant is no smaller than $(P_{\mathtt{bat}}^{\mathtt{s}} - P_k^{\mathtt{d}} + \epsilon_p)$. Now, we will describe how to calculate an upper bound of $I_{k \leftarrow i}(\ell)$.

First, if λ_i has a higher priority than λ_k, then the upper-bound of $I_{k \leftarrow i}(\ell)$ is the

maximum energy demanded by λ_i in an interval of length ℓ, which is calculated as

$$W_i(\ell) = \min(P_i^{\mathtt{d}}, P_{\mathtt{bat}}^{\mathtt{s}} - P_k^{\mathtt{d}} + \epsilon_p) \times$$
$$\min\Big(\ell, \big(N_i(\ell) \cdot L_i^{\mathtt{d}} + \min(L_i^{\mathtt{d}}, \ell + T_i^{\mathtt{d}} - L_i^{\mathtt{d}} - N_i(\ell) \cdot T_i^{\mathtt{d}})\big)\Big), \tag{8.1}$$

where $N_i(\ell) = \lfloor \frac{\ell + T_i^{\mathtt{d}} - L_i^{\mathtt{d}}}{T_i^{\mathtt{d}}} \rfloor$. This calculation is similar to the workload calculation of real-time scheduling [20]. Briefly, $N_i(\ell)$ implies the number of instances of λ_i, and each of their periods is completely included within the interval of length ℓ (including the first instance of λ_i), which contributes $\min(P_i^{\mathtt{d}}, P_{\mathtt{bat}}^{\mathtt{s}} - P_k^{\mathtt{d}} + \epsilon_p) \cdot N_i(\ell) \cdot L_i^{\mathtt{d}}$ of energy to $W_i(\ell)$. The second part of $W_i(\ell)$ represents the contribution of the operation whose period is partially included in the interval of length ℓ. Fig. 5 in the supplementary file [67] shows an example of $W_i(\ell)$ with $N_i(\ell) = 2$, which contributes $\min(P_i^{\mathtt{d}}, P_{\mathtt{bat}}^{\mathtt{s}} - P_k^{\mathtt{d}} + \epsilon_p) \cdot 2 \cdot L_i^{\mathtt{d}}$ of energy, and the third instance of λ_i contributes $\min(P_i^{\mathtt{d}}, P_{\mathtt{bat}}^{\mathtt{s}} - P_k^{\mathtt{d}} + \epsilon_p) \cdot \min(L_i^{\mathtt{d}}, \ell + T_i^{\mathtt{d}} - L_i^{\mathtt{d}} - N_i(\ell) \cdot T_i^{\mathtt{d}})$ of energy to $W_i(\ell)$.

Second, if λ_i has a lower priority than λ_k, then we consider two sub-cases. Since each operation is non-preemptive, λ_i can execute before the start of λ_k's execution, if λ_i starts its execution before the release of λ_k. In this case, the energy demand is upper-bounded by $\min(P_i^{\mathtt{d}}, P_{\mathtt{bat}}^{\mathtt{s}} - P_k^{\mathtt{d}} + \epsilon_p) \cdot \min(L_i^{\mathtt{d}} - \epsilon_t, \ell)$, which is an upper-bound of $I_{k \leftarrow i}(\ell)$ for the first sub-case of $P_i^{\mathtt{d}} \geq P_k^{\mathtt{d}}$. If $P_i^{\mathtt{d}} < P_k^{\mathtt{d}}$, then an upper-bound of $I_{k \leftarrow i}(\ell)$ can be larger than the first sub-case. That is, due to our worst-case-based work-conserving policy, it is possible for λ_i to start its execution before the start of λ_k's execution, whenever λ_k does not satisfy Line 5 of Algorithm 13 but λ_i does. In this case, we use the general upper-bound $W_i(\ell)$ as an upper-bound of the second sub-case.

Combining all the results discussed so far, we develop a power guarantee analysis as follows.

Lemma VIII.1. *Suppose that every $\lambda_k \in \lambda$ satisfies Eq.* (8.2)*. Then, every instance of every operation $\lambda_k \in \lambda$ finishes its execution within its period of length $T_k^{\mathtt{d}}$, while guaranteeing the sum of power demands at any time instant is no larger than the battery power capability (i.e., S1 and S3 hold).*

$$\sum_{\lambda_i \in \lambda \setminus \{\lambda_k\}} I_{k \leftarrow i}(T_k^{\mathtt{d}} - L_k^{\mathtt{d}} + \epsilon_t)$$

$$< (P_{\mathtt{bat}}^{\mathtt{s}} - P_k^{\mathtt{d}} + \epsilon_p) \cdot (T_k^{\mathtt{d}} - L_k^{\mathtt{d}} + \epsilon_t), \tag{8.2}$$

where $I_{k \leftarrow i}(\ell) = W_i(\ell)$, if λ_k has a higher-priority than λ_i or $P_i^{\mathtt{d}} < P_k^{\mathtt{d}}$; $I_{k \leftarrow i}(\ell) = \min(P_i^{\mathtt{d}}, P_{\mathtt{bat}}^{\mathtt{s}} - P_k^{\mathtt{d}} + \epsilon_p) \cdot \min(L_i^{\mathtt{d}} - \epsilon_t, \ell)$ otherwise.

Proof. As discussed so far, $I_{k \leftarrow i}(T_k^{\mathtt{d}} - L_k^{\mathtt{d}} + \epsilon_t)$ in Eq. (8.2) is an upper-bound of the amount of energy demanded by instances of λ_i in an interval of length $(T_k^{\mathtt{d}} - L_k^{\mathtt{d}} + \epsilon_t)$. Therefore, if Eq. (8.2) holds, then there exists an instant t_1 within the interval, such that the sum of power demands is less than or equal to $(P_{\mathtt{bat}}^{\mathtt{s}} - P_k^{\mathtt{d}})$. This means that λ_k can start its execution no later than $(T_k^{\mathtt{d}} - L_k^{\mathtt{d}})$ time units after its release, implying that λ_k finishes its execution within its period. □

The lemma works not only for an offline power guarantee for the case of the sole supply, but also for a basis to develop an offline power guarantee for the general case to be discussed in Section 8.5. Also, the lemma can be used for addressing a design problem: calculation of the minimum capability of the battery cell that can supply given λ by finding the minimum $P_{\mathtt{bat}}^{\mathtt{s}}$ that satisfies the lemma for given λ.

8.5 Scheduling of Multiple Power-Demand Operations with Multiple Power-Supply Sources

This section addresses a more general situation than Section 8.4, in which additional power is sporadically generated from multiple power-supply sources such as an

RBS and a solar panel, and immediately stored in the energy buffer or used for power-demand operations. We will first address a scheduling challenge due to the existence of sporadic additional power supply. Then, we present two approaches, depending on how to distribute the additional power supply to power-demand operations.

8.5.1 A scheduling challenge

Unlike the situation where a battery pack is the only power-supply source discussed in Section 8.4, a straightforward approach cannot yield a system-level power guarantee, as shown in the following example.

Example VIII.2. Suppose that additional power is supplied by Γ_1 in $[t_1, t_2)$, while the battery pack is the only supply in $[t_0, t_1)$ and $[t_2, t_3)$, where $t_0 < t_1 < t_2 < t_3$, as shown in Fig. 6 (a) in the supplementary file [67]. Also, there are two operations λ_1 and λ_2 ready to execute at t_0, and $\lambda_1 \leq P^{\mathtt{s}}_{\mathtt{bat}}$ and $\lambda_1 + \lambda_2 > P^{\mathtt{s}}_{\mathtt{bat}}$, as shown in Fig. 6 (b) in the supplementary file [67]. Suppose that we apply the worst-case-based work-conserving policy in Algorithm 13, implying we start execution of an operation in the ready queue as long as the system has enough remaining power supply to accommodate the worst-case power demand of the operation. Then, λ_2 can start its execution at t_1, but there is a problem at t_2, at which power supplied by Γ_1 ends. In $[t_2, t_3)$, the total amount of power demand is strictly larger than that of power supply, entailing either eviction of one of "non-preemptive" operations, or risking power shortage in executing operations, both of which are considered as a system failure.

Example VIII.2 shows the need for a more fine-grained way to handle additional sporadic power-supply sources. To meet this need, we consider two policies depending on how to distribute the additional supply as follows.

- Calculate the additional "guaranteed" uniform supply $P^{\mathtt{s}}_{\mathtt{uni}}$, meaning that additional power-supply sources (and the energy buffer) can *always* provide power as much as $P^{\mathtt{s}}_{\mathtt{uni}}$ (as the battery pack provides up to $P^{\mathtt{s}}_{\mathtt{bat}}$). This entails the calculation of $P^{\mathtt{s}}_{\mathtt{uni}}$; once it is calculated, we can reuse the power scheduling and analysis framework presented in Section 8.4, by adding $P^{\mathtt{s}}_{\mathtt{uni}}$ to the existing uniform supply $P^{\mathtt{s}}_{\mathtt{bat}}$. In this case, all operations can share the power generated by additional power-supply sources.
- Assign additional power to a partial set of operations. Power generated by additional power-supply sources (and stored in the energy buffer) is used only when the operations in the partial set are executed. This entails the way to divide power generated by additional power-supply sources for individual power-demand operations.

In what follows, we will detail the above two approaches, including their scheduling frameworks.

8.5.2 Uniform supply approach

In this approach, we calculate the additional guaranteed uniform supply $P^{\mathtt{s}}_{\mathtt{uni}}$ from additional power-supply sources. After calculating $P^{\mathtt{s}}_{\mathtt{uni}}$, we can reuse the scheduling framework in Algorithm 13. That is, we just change the $P^{\mathtt{s}}_{\mathtt{bat}}$ term in Line 5 to $P^{\mathtt{s}}_{\mathtt{bat}} + P^{\mathtt{s}}_{\mathtt{uni}}$. The main issue of this approach is to accurately calculate $P^{\mathtt{s}}_{\mathtt{uni}}$; the larger $P^{\mathtt{s}}_{\mathtt{uni}}$, the more operations to be accommodated.

The basic idea to obtain $P^{\mathtt{s}}_{\mathtt{uni}}$ is to calculate the amount of the minimum supplied energy in $[0, t)$ by considering the fact that the energy buffer has at least $P^{\mathtt{s}}_{\mathtt{UC}} \cdot L^{\mathtt{s}}_{\mathtt{UC}}$ of energy at 0 and each additional supply generates power at the end of its instances' periods. If we divide this amount by t and take the minimum, we guarantee to supply

power as much as $P^{\mathtt{s}}_{\mathtt{uni}}$ in $[0, t)$, as stated in the following lemma.

Lemma VIII.3. *We can calculate P^{s}_{uni} using the following equation.*

$$P^{s}_{\mathit{uni}} = \min_{0 \le t \le \mathit{LCM}} \frac{f(\Gamma_{\mathit{UC}}, t) + \sum_{\Gamma_i \in \Gamma} f(\Gamma_i, t)}{t}, \tag{8.3}$$

where LCM is the least common multiple of $\{T^{s}_{i}\}_{\Gamma_i \in \Gamma}$,

$$f(\Gamma_{\mathit{UC}}, t) = P^{s}_{\mathit{UC}} \cdot \min(t, L^{s}_{\mathit{UC}}), \text{ and} \tag{8.4}$$

$$\begin{aligned} f(\Gamma_i, t) =& P^{s}_{i} \cdot \left\lfloor \frac{t}{T^{s}_{i}} \right\rfloor \cdot L^{s}_{i} \\ &+ P^{s}_{i} \cdot \max\left(0, t - \left\lfloor \frac{t}{T^{s}_{i}} \right\rfloor \cdot T^{s}_{i} - (T^{s}_{i} - L^{s}_{i})\right). \end{aligned} \tag{8.5}$$

Proof. Since the amount of energy in the energy buffer at $t = 0$ is at least $P^{\mathtt{s}}_{\mathtt{UC}} \cdot L^{\mathtt{s}}_{\mathtt{UC}}$, the amount of the supplied energy from the energy buffer in $[0, t)$ is $P^{\mathtt{s}}_{\mathtt{UC}} \cdot t$ if $t \le L^{\mathtt{s}}_{\mathtt{UC}}$, and at least $P^{\mathtt{s}}_{\mathtt{UC}} \cdot L^{\mathtt{s}}_{\mathtt{UC}}$ otherwise, which is recorded in $f(\Gamma_{\mathtt{UC}}, t)$ of Eq. (8.4). For given t, $\lfloor \frac{t}{T^{\mathtt{s}}_{i}} \rfloor$ means the number of instances of λ_i whose periods are completely included in $[0, t)$, and each instance generates energy no smaller than $P^{\mathtt{s}}_{i} \cdot L^{\mathtt{s}}_{i}$. The second term of Eq. (8.5) presents the minimum energy generated by the last instance whose period is partially included in $[0, t)$. Therefore, $\sum_{\Gamma_i \in \Gamma} f(\Gamma_i, t)$ represents the amount of generated energy by Γ in $[0, t)$. Since we assume that the capacity of the energy buffer is sufficiently large, we can always use power as much as the lower-bound of $\frac{f(\Gamma_{\mathtt{UC}}, t) + \sum_{\Gamma_i \in \Gamma} f(\Gamma_i, t)}{t}$ for $0 \le t \le \mathsf{LCM}$. □

If LCM is very large or time-complexity is critically important, e.g., for online admission control for operations, we need a tractable way to calculate $P^{\mathtt{s}}_{\mathtt{uni}}$, which is covered in Lemma 1 of the supplementary file [67].

Finally, we can check a power guarantee of this approach by applying Lemma VIII.1 for all $\lambda_k \in \lambda$ and replacing $P^{\mathtt{s}}_{\mathtt{bat}}$ with $P^{\mathtt{s}}_{\mathtt{bat}} + P^{\mathtt{s}}_{\mathtt{uni}}$.

8.5.3 Dedicated supply approach

In this approach, we can determine $\lambda^{\mathtt{ded}}$, a set of operations completely powered by a set of additional power-supply sources Γ and the energy buffer $\Gamma_{\mathtt{UC}}$. Once we

determine $\lambda^{\texttt{ded}}$, operations in $\lambda \setminus \lambda^{\texttt{ded}}$ can be executed according to Algorithm 13, and their power guarantee is judged by Lemma VIII.1 with $\lambda \setminus \lambda^{\texttt{ded}}$. On the other hand, each operation in $\lambda^{\texttt{ded}}$ is fully supplied by Γ with $\Gamma_{\texttt{UC}}$, and does not use power from $\Gamma_{\texttt{bat}}$. Our policy is to execute each operation in $\lambda^{\texttt{ded}}$ at the end of each period, which accommodates more operations in $\lambda^{\texttt{ded}}$ (because this policy uses less initial energy from the energy buffer). Formally, $\lambda_k \in \lambda^{\texttt{ded}}$ starts its execution at $r+T_k^{\texttt{d}}-L_k^{\texttt{d}}$, where r is the release time of an instance of λ_k, and $\Gamma_{\texttt{UC}}$ supplies $P_k^{\texttt{d}}(t)$ ($\leq P_k^{\texttt{d}}$) amount of power to λ_k in $[r + T_k^{\texttt{d}} - L_k^{\texttt{d}}, r + T_k^{\texttt{d}})$.

Then, the remaining step is to determine $\lambda^{\texttt{ded}}$. The basic idea is to calculate the maximum energy demanded by $\lambda^{\texttt{ded}}$ in $[0, t)$ and the minimum energy supplied by Γ and $\Gamma_{\texttt{UC}}$ in $[0, t)$. We check whether the former is not larger than the latter at all times, which is stated in the following lemma.

Lemma VIII.4. *Every instance of every operation $\lambda_k \in \lambda_{ded}$ finishes its execution at the end of each period (e.g., $[r + T_k^{d} - L_k^{d}, r + T_k^{d})$ where r is the release time of an instance of λ_k), only with Γ and Γ_{UC}, if the following inequality holds for all $t \in [0, LCM)$.*

$$\sum_{\lambda_i \in \lambda^{ded}} f(\lambda_i, t) \leq f(\Gamma_{UC}, t) + \sum_{\Gamma_i \in \Gamma} f(\Gamma_i, t), \text{ and} \tag{8.6}$$

$$\begin{aligned} f(\lambda_i, t) =& P_i^d \cdot \left\lfloor \frac{t}{T_i} \right\rfloor \cdot L_i^d \\ &+ P_i^d \cdot \max\left(0, t - \left\lfloor \frac{t}{T_i^d} \right\rfloor \cdot T_i^d - (T_i^d - L_i^d)\right). \end{aligned} \tag{8.7}$$

Proof. Since $f(\lambda_i, t)$ in Eq. (8.7) exhibits the same formula as Eq. (8.5), it calculates the maximum energy demanded by λ_i in $[0, t)$ when its instances are executed at the end of their periods. Therefore, the LHS (Left-Hand Side) of Eq. (8.6) is the maximum energy demanded by $\lambda^{\texttt{ded}}$ in $[0, t)$. On the other hand, the RHS (Right-Hand Side) of the equation is the minimum energy supplied by Γ and $\Gamma_{\texttt{UC}}$ in $[0, t)$ as explained in Lemma VIII.3. Therefore, the lemma follows. □

Note that if time-complexity is important, we can use another necessary condition presented in Lemma 2 in the supplementary file [67].

The remaining problem is then how to select $\lambda^{\texttt{ded}}$ that satisfies Lemma VIII.4 (or Lemma 2). Here we describe a simple, but effective heuristic. We sort $\lambda_i \in \lambda$, based on the ratio of the LHS to the RHS of Eq. (8.2). If the ratio of λ_i is larger than that of λ_k, we interpret that λ_i is more difficult to satisfy Eq. (8.2) than λ_j. Therefore, starting from $\lambda^{\texttt{ded}} = \emptyset$, we repeat the following step until there is no operation to be moved: we select an operation λ_j with the largest ratio among operations in $\lambda \setminus \lambda^{\texttt{ded}}$ such that $\lambda^{\texttt{ded}} \cup \{\lambda_j\}$ satisfies Lemma VIII.4, and then add λ_j to $\lambda^{\texttt{ded}}$.

Finally, we can check the power guarantee of this approach by checking Lemma VIII.1 only with $\lambda_i \in \lambda \setminus \lambda^{\texttt{ded}}$. Note that for $\lambda_i \in \lambda^{\texttt{ded}}$, we automatically guarantee their power sufficiency in that $\lambda^{\texttt{ded}}$ is constructed so as to supply all power demands in $\lambda^{\texttt{ded}}$ by Γ and $\Gamma_{\texttt{UC}}$ without $\Gamma_{\texttt{bat}}$.

8.6 Online Power Management

If one performs a set of power-demand operations under a set of power-supply sources that satisfy the offline power guarantee analysis in Section 8.5, there will be extra energy stored in the energy buffer as the analysis is based on the minimum (not actual) power supply. Thus, we propose an online power management framework, which adaptively controls power of the energy buffer effectively to reduce the battery's peak power that achieves the goal in Section 8.3.

Our framework periodically controls power of the energy buffer, as shown in Fig. 8.3 and Algorithm 14. At t_0, the beginning of each period (for online power management) of length $t_{\texttt{p}}$, we calculate the amount of energy in $\Gamma_{\texttt{UC}}$, which is necessary for an offline power guarantee for the current period $[t_0, t_0 + t_{\texttt{p}})$ (denoted by

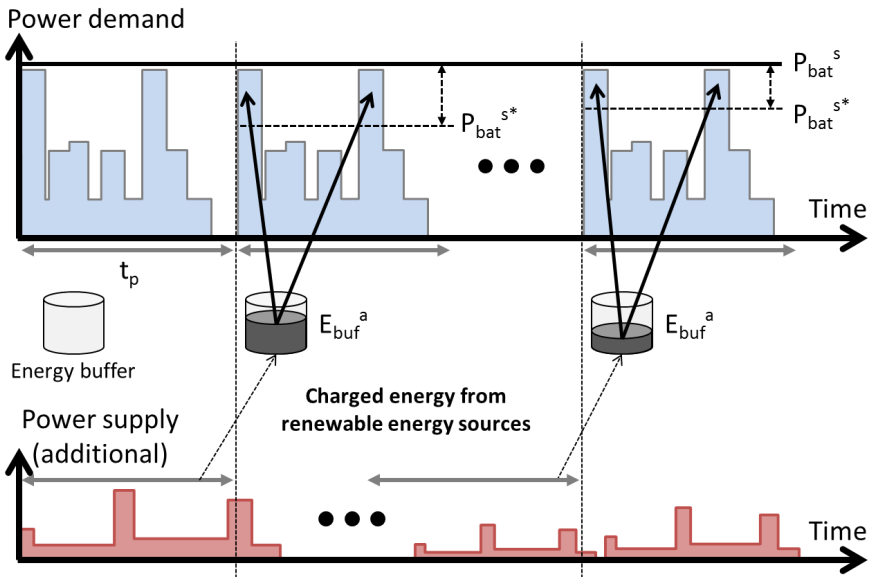

Figure 8.3: Online power management

Algorithm 14 Online Power Management

The following steps are performed at t_0, the beginning of each period of length $t_\mathtt{p}$,

1: Calculate $E^{\mathtt{m}}_{\mathtt{buf}}(t_0)$ depending on the uniform/dedicated supply approach.
2: Calculate $E_{\mathtt{buf}}(t_0)$ by $\frac{1}{2} \cdot C_{\mathtt{buf}} \cdot V^2_{\mathtt{buf}}(t_0)$.
3: // Calculate $P^{\mathtt{s*}}_{\mathtt{bat}}(t_0)$ as follows.
4: $P^{\mathtt{s*}}_{\mathtt{bat}}(t_0) \leftarrow P^{\mathtt{s}}_{\mathtt{bat}}$ // The initial threshold is the battery capacity.
5: $E_{\mathtt{add}} \leftarrow 0$
6: **while** $E_{\mathtt{buf}}(t_0) - E^{\mathtt{m}}_{\mathtt{buf}}(t_0) \geq E_{\mathtt{add}}$ **do**
7: $\quad P^{\mathtt{s*}}_{\mathtt{bat}}(t_0) \leftarrow P^{\mathtt{s*}}_{\mathtt{bat}}(t_0) - \epsilon_p$
8: $\quad E_{\mathtt{add}} = \int_{t_0 - t_p}^{t_0} \mathsf{max}(\Sigma P^{\mathtt{d}}_{\mathtt{i}}(t) - P^{\mathtt{s*}}_{\mathtt{bat}}(t_0), 0)\ dt$
9: **end while**

$E^{\mathtt{m}}_{\mathtt{buf}}(t_0)$) as follows. For the uniform power-supply approach in Section 8.5.2, $E^{\mathtt{m}}_{\mathtt{buf}}(t_0)$ is simply calculated by $t_\mathtt{p} \cdot P^{\mathtt{s}}_{\mathtt{uni}}$ since the offline power guarantee exploits the property that $P^{\mathtt{s}}_{\mathtt{uni}}$ of power is *always* supplied by Γ. For the dedicated supply approach in Section 8.5.3, we calculate $E^{\mathtt{m}}_{\mathtt{buf}}(t_0)$ using the amount of energy consumed by $\lambda^{\mathtt{ded}}$ based on their maximum power demand parameters (i.e., $P^{\mathtt{d}}_i$, not $P^{\mathtt{d}}_i(t)$) during the interval.

Once $E^{\mathtt{m}}_{\mathtt{buf}}(t_0)$ is calculated, we can utilize the energy from $\Gamma_{\mathtt{UC}}$ up to the difference between the amount of total energy stored in $\Gamma_{\mathtt{UC}}$ at t_0 (denoted by $E_{\mathtt{buf}}(t_0)$) and $E^{\mathtt{m}}_{\mathtt{buf}}(t_0)$. Note that we can measure the amount of energy in $\Gamma_{\mathtt{UC}}$ by monitoring the

voltage level of $\Gamma_{\mathtt{UC}}$ at t_0 (denoted by $V_{\mathtt{buf}}(t_0)$), using $E_{\mathtt{buf}}(t_0) = \frac{1}{2} \cdot C_{\mathtt{buf}} \cdot V^2_{\mathtt{buf}}(t_0)$, where $C_{\mathtt{buf}}$ is a constant representing the capacitance of $\Gamma_{\mathtt{UC}}$ [65]. Lines 1 and 2 of Algorithm 14 represent the calculation of $E^{\mathtt{m}}_{\mathtt{buf}}(t_0)$ and $E_{\mathtt{buf}}(t_0)$.

Then, we utilize the extra energy up to as much as $E_{\mathtt{buf}}(t_0) - E^{\mathtt{m}}_{\mathtt{buf}}(t_0)$, for reducing the battery's peak power. We use energy from the energy buffer if the power usage of the battery pack is larger than a threshold $P^{\mathtt{s*}}_{\mathtt{bat}}(t_0)$. We determine $P^{\mathtt{s*}}_{\mathtt{bat}}(t_0)$ for the current period $[t_0, t_0 + t_{\mathtt{p}})$, using the history of the previous period $[t_0 - t_{\mathtt{p}}, t_0)$, which is the amount of actual energy consumption by λ during that period. As shown in Lines 3–9 of Algorithm 14, we repeat the following process: for given $P^{\mathtt{s*}}_{\mathtt{bat}}(t_0)$, we check if the additional amount energy to keep the peak demand no larger than $P^{\mathtt{s*}}_{\mathtt{bat}}(t_0)$ (denoted by $E_{\mathtt{add}}$) is not larger than the available energy $E_{\mathtt{buf}}(t_0) - E^{\mathtt{m}}_{\mathtt{buf}}(t_0)$. If yes, we increase $P^{\mathtt{s*}}_{\mathtt{bat}}(t_0)$ by ϵ_p and repeat the process; otherwise, we stop the process.

Finally, for given $E^{\mathtt{m}}_{\mathtt{buf}}(t_0)$ and $P^{\mathtt{s*}}_{\mathtt{bat}}(t_0)$, the online power management framework controls the energy stored in the energy buffer within a period $[t_0, t_0 + t_{\mathtt{p}})$ as follows. Suppose that the battery pack should supply X amount of power if there is no supply from $\Gamma_{\mathtt{UC}}$ at t for the purpose of the peak power reduction.[5] Then, the energy buffer supplies $X - P^{\mathtt{s*}}_{\mathtt{bat}}(t_0)$ of power, only when $X \geq P^{\mathtt{s*}}_{\mathtt{bat}}(t_0)$ and $E_{\mathtt{buf}}(t) \geq E^{\mathtt{m}}_{\mathtt{buf}}(t_0)$ hold.

8.7 Evaluation

We now evaluate our offline power-supply guarantee analysis and online power management, focusing on whether or not they meet the goals stated in Section 8.3. We first introduce a prototype consisting of sub-devices and a HESS, and the required power-demand operations. We then present experimental results, demonstrating the

[5] The amount of energy $\Gamma_{\mathtt{UC}}$ (the energy buffer) should supply at t for an offline power guarantee is already figured in X.

HESS's power-supply guarantee and reduction of energy dissipation. Fig. 8.4 shows the overall evaluation process.

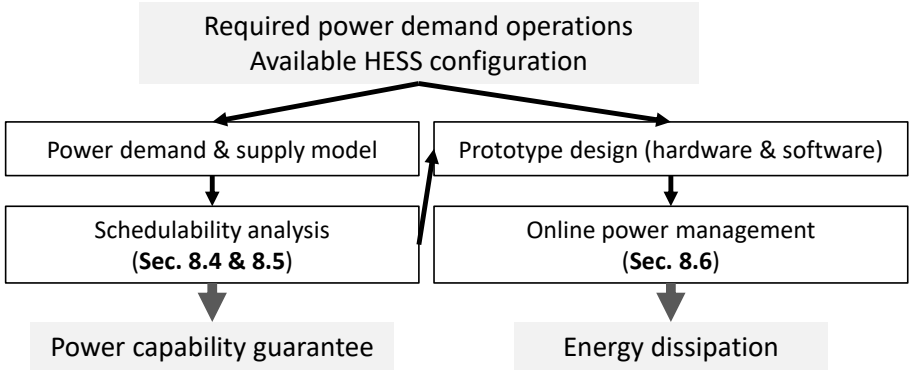

Figure 8.4: The evaluation process used

8.7.1 Prototype design

We have built a prototype which is equipped with wheels, wheel motors, stepper motors, coolers and a HESS including a pack of lithium-ion batteries, a pack of UCs, an RBS and solar panels as shown in Fig. 8.5. The required power demand operations and specifications of energy sources/storage are detailed in Tables 8.1 and 8.2, and the supplementary file [67]. We can determine the parameters of power-demand operations and power-supply sources from their power demand/supply profiles and specifications. Based on the parameters, we determine the optimal number of batteries achieving a power-supply guarantee for the system via the power guarantee analysis in Sections 8.4 and 8.5. We have then executed various sequences of operations while recording battery states to evaluate the proposed system.

System architecture of the prototype

The architecture is required to execute operations of user applications or the system maintenance, and assign the available resources for their execution. Our prototype system consists of a single master and multiple local controllers. The

Tasks	$T^{\mathtt{s}}(s)$	$L^{\mathtt{s}}(s)$	$P^{\mathtt{s}}(W)$
Γ_1	6	2	3
Γ_2	6	1.5	3
Γ_3	1.5	0.2	0.2
$\Gamma_{\mathtt{UC}}$		3	3
$\Gamma_{\mathtt{bat}}$			40

Table 8.1: Power supply

master controller is responsible for scheduling real-time operations using scheduling frameworks in Sections 8.4 and 8.5, and sending messages to the local controller over the CAN bus [36]. Several Arduino boards are used as local controllers to actuate sub-devices according to the messages from the master controller. Our HESS consists of lithium-ion batteries ($\Gamma_{\mathtt{bat}}$), UCs ($\Gamma_{\mathtt{UC}}$), switched-mode converters, regenerative braking system (Γ_3), solar panels (Γ_1, Γ_2), and controllers that can monitor the state of the HESS and communicate with the master controller, all of which are detailed in the supplementary file [67]. The master controller can also regulate power supply of each energy storage via the converter control. Table 8.1 shows power supply models from renewable energy sources.

Applications and tasks

To make our experiments more realistic, we have obtained real driving data from "The US Environmental Protection Agency (EPA)" [3]. Our drive application is programmed to operate wheel motors to achieve the driving profile. Our motor control (λ_1) depends on the PID controller to achieve the required speed, and its control interval ($T_1^{\mathtt{d}}$), maximum acceleration time (time to achieve the target speed, $L_1^{\mathtt{d}}$), and the maximum power ($P_1^{\mathtt{s}}$) are 5s, 1s, and 12W, respectively. To reflect various user applications, we also ran applications that sporadically actuate motors (λ_4 and λ_5). Some applications actuate stepper motors to control position (λ_2), while others (λ_3) use thermal fins to regulate temperature for system thermal stability. The

Tasks	$T^{\mathtt{d}}(s)$	$L^{\mathtt{d}}(s)$	$P^{\mathtt{d}}(W)$
λ_1	5	1	12
λ_2	3	1	9.6
λ_3	2	1	6
λ_4	2	1	6
λ_5	3	2	7.2

Table 8.2: Power demand operations

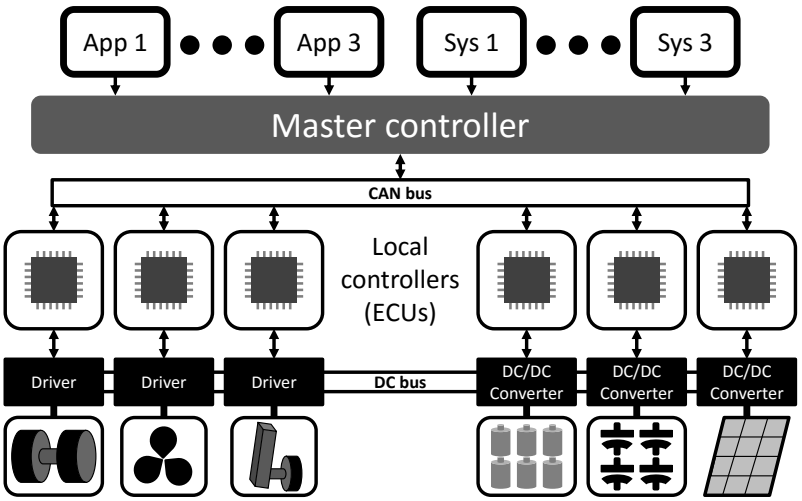

Figure 8.5: Prototype overview

power demand operations are shown in Table 8.2.

8.7.2 Evaluation results

Our offline power-supply guarantee analysis and online power management are evaluated in terms of power guarantee and the amount of energy dissipation reduction, respectively.

Offline power-supply guarantee analysis

As mentioned in the description of our prototype, we schedule the five operations using the three scheduling frameworks in Sections 8.4, 8.5.2 and 8.5.3, and record the minimum battery capability needed to pass the power guarantee analysis, as follows.

- PS1: the minimum required battery capability under the scheduling framework in Section 8.4 (no additional renewable power sources),

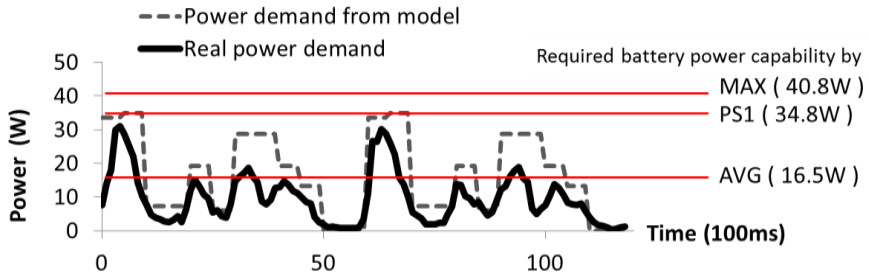

Figure 8.6: Power demand profile when the battery pack is the sole power supply

- PS2-UNI: the minimum required battery capability under the scheduling framework in Section 8.5.2 (uniform supply approach with renewable sources), and
- PS2-DED: the minimum required battery capability under the scheduling framework in Section 8.5.3 (dedicated supply approach with renewable sources).

Fig. 8.6 shows the battery power profile under the scheduling framework in Section 8.4. As references, we compare PS1 with MAX and AVG, which denote the sum of the maximum power demand (i.e., $\sum_{\lambda_i \in \lambda} P_i^{\mathtt{d}}$), and the average of the maximum power demand (i.e., $\sum_{\lambda_i \in \lambda} \frac{P_i^{\mathtt{d}} \cdot L_i^{\mathtt{d}}}{T_i^{\mathtt{d}}}$). AVG could not supply the sufficient power in the worst case, because most electric systems do not require power constantly. While MAX and PS1 guarantee power capability only with the battery pack, PS1 (34.8W) reduces the required battery capability, compared to MAX (40.8W). Note that PS1 can be used as a battery capability when it is difficult to estimate power supply from renewable energy sources.

When it comes to PS2-UNI and PS2-DED, they further reduce the required battery capability (consuming 29.7W and 25.3W, respectively). Between the two, PS2-DED is the most reasonable for a power guarantee, in that it can reduce the required battery capability by 38%, compared to MAX, a naive approach without utilizing renewable energy sources.

Schemes	$P_{\texttt{loss}}(mW)$
PS2-UNI & BE	526
PS2-UNI & OPM	352
PS2-DED & BE	390
PS2-DED & OPM	334

Table 8.3: Average discharge stress energy dissipation $P_{\texttt{loss}}$

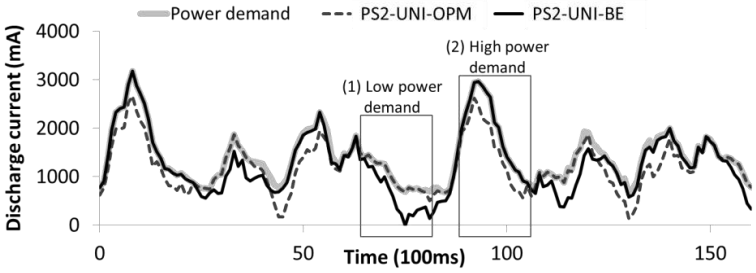

Figure 8.7: Battery discharge current profile under PS2-UNI & BE and PS2-UNI & OPM, which shows that our online power management helps reduce peak battery discharge current considering energy generation rate and power demand history

Online power management

We now compare the average dissipation power in batteries during an operation interval $[0, 600)$, under our online power management (OPM) and the best-effort approach (BE) that enforces the use of buffer energy as long as energy remains in the buffer. Since we have two scheduling frameworks for buffer usage, we have four approaches to compare: PS2-UNI & BE, PS2-UNI & OPM, PS2-DED & BE and PS2-DED & OPM. Note the average dissipation is calculated by $P_{\texttt{loss}} = \frac{1}{t_{\texttt{max}}} \int_0^{t_{\texttt{max}}} P^{\texttt{s}}_{\texttt{bat-loss}}(t)\, dt = \frac{1}{t_{\texttt{max}}} \int_0^{t_{\texttt{max}}} I^2_{\texttt{bat}}(t) \cdot R_{\texttt{bat}}(t)\, dt$, as mentioned in Section 8.3.

Table 8.3 shows the energy dissipation during the operation interval. For a given underlying scheduling framework, OPM significantly reduces the energy dissipation over BE. That is, under PS2-UNI and PS2-DED, the amounts of energy dissipation reduction by OPM over BE are 33.1% and 14.4%, respectively. This observation can be explained using Fig. 8.7 that presents the battery discharge current profile under PS2-UNI & BE and PS2-UNI & OPM. From the figure, we can easily observe that PS2-UNI & BE fails to supply power when the peak current occurs, while PS2-UNI &

OPM effectively reduces the peak current. For example, if we focus on a time instant that exhibits the highest peak current (around $t = 90$), PS2-UNI & OPM successfully reduces the peak current, while PS2-UNI & BE cannot. This is because PS2-UNI & BE consumes much energy when power demand is low (around $t = 80$), as shown in the figure.

On the other hand, if we compare the underlying scheduling frameworks, PS2-DED outperforms PS2-UNI. However, the gap between the two is significantly reduced if we apply OPM (352 versus 334, as opposed to 526 versus 390). This also substantiates the effectiveness of OPM in reducing energy dissipation.

8.8 Conclusion

In this chapter, we have proposed a power scheduling framework—as a guideline for the design of a HESS—that ensures power sufficiency for the worst-case power demand and supply. To improve the runtime performance of the HESS further, we have also designed an online power management framework that utilizes the surplus energy from a real-time power supply, reducing the battery's peak power and hence extending its lifetime. We have validated the design with a HESS-powered prototype system running realistic applications, demonstrating power sufficiency with a lower-cost HESS and higher energy-efficiency.

In future, we would like to develop a design framework for general energy storage systems based on a power guarantee analysis. It will search for the optimal configurations of energy storage systems at their design or replacement time while considering power demand history and power supply's state-of-health. We also plan to build a power/energy management system that not only schedules power demand and supply, but also monitors and pro/diagnoses energy storages/sources.

CHAPTER IX

Conclusion

9.1 Concluding remarks

To meet increasing demands for making EVs less expensive and safer, BMSes should be designed to cope with battery degradation and reliability. In this dissertation, we have proposed a new real-time, integrated BMS that diagnoses the battery states, analyzes the impact of operating conditions on the battery states and regulates the conditions including the operating voltage range, discharge/charge and thermal stress to batteries based on the analysis. This system adaptively analyzes and reacts to real-time changes in charge and temperature. To introduce adaptability into BMSes, we proposed a real-time battery power requirement predictor (PRP) and a data-driven diagnosis/prognosis system. To cope with harsh discharge/charge rates, one of the major operating conditions reducing battery operation-time and life, we presented a reconfigurable hybrid energy storage system (HESS). The HESS consists of multiple energy storages, each with different characteristics. It utilizes a battery discharge/charge rate management algorithm that determines, in real time, the amount of energy needed and identifying the proper configuration of the HESS to efficiently achieve this energy level. Our system also manages and addresses the issues related to battery temperature. Thermal management is key to addressing

a better BMS, because it impacts the electrical state of the battery, as well as its operation-time and lifetime. Using battery thermal management, our BMS can selectively and timely cool/heat battery cells. Although this framework was designed for large-scale EV batteries, it can also be used for other types of batteries, including metal air batteries, Lithium–sulfur batteries and fuel cells. While these batteries have their own thermal characteristics, power and energy densities, the scheduled discharge/charge current can be reconfigured based on other battery behavior models, because battery behavior models are extracted by using behavioral data from the batteries installed in the system.

9.2 Future Directions

This section makes recommendations for future research in building reliable BMSes. More work is needed to improve not only the battery performance, as is the focus of this thesis, but also battery fault detection in a large-scale system and remote/wiress battery management system. For this, we must detect and correct abnormal battery operations to preserve functionality during the warranty period. The International Electrotechnical Commission (IEC) requires that electric vehicles possess certain battery fault diagnosis functions [89]. These functions alarm drivers and service stations of unhealthy batteries and general aging information. The remote/wireless battery management system can facilitate battery data analysis via cloud server/computing resources.

9.2.1 Battery fault model

Most battery fault detection research uses the battery's current and voltage patterns during the charge/discharge period to detect potential faults in a battery pack [132, 133]. These methods require to record the actual battery's voltage and

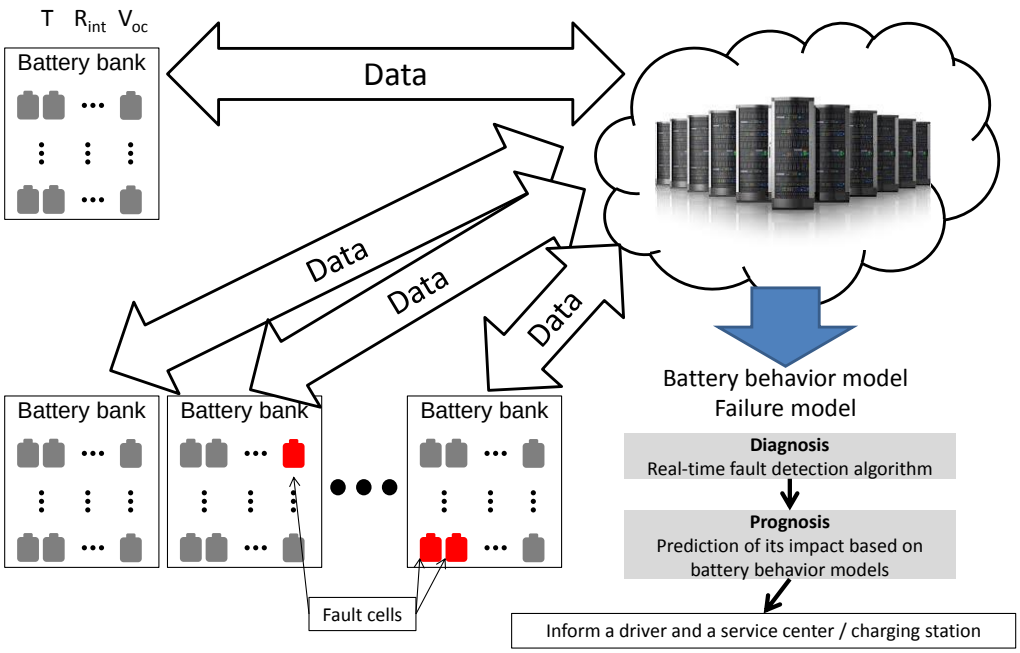

Figure 9.1: Remote battery diagnosis/prognosis system

current data, and then compare the data with current and voltage patterns from a similar healthy battery in the server. This method is based on the idea that battery degradation will result in an abrupt change in the battery's discharge/charge voltage. Other researchers have used fuzzy logic or bayesian techniques to create battery fault diagnosis models [126, 89, 124]. They first analyzed the relationship between the changes in external characteristics throughout a typical battery's life or state. Then, a fault diagnosis model for the battery pack was built using fuzzy mathematical theory or Bayesian statistical estimates to determine the health level of a battery based on changes in external characteristics.

9.2.2 Remote diagnosis/prognosis for large-scale batteries

Currently, fault diagnosis has become a new discipline. However, there are some requirements for a practical diagnosis/prognosis system. Since EVs are equipped with many battery modules and cells – Tesla Motors Model S battery pack (85 KWh

model) consists of 16 modules, each containing 444 battery cells – we cannot measure the voltage, current, and temperature of each cell in a module/pack. Therefore, we need a diagnosis/prognosis and a fault detection system for large-scale batteries with a limited number of sensors. A wireless BMS facilitates the deployment of sensors at the optimal locations while addressing the persistent reliability issues associated with automotive wiring harnesses and connectors in electric and hybrid/electric vehicles. Also, the remote BMS can estimate the battery state-of-health and fault conditions more accurately via data analysis tools and battery behavior data stored in the large data servers.

9.2.3 Battery efficient autonomous driving

We have designed a real-time battery management system that analyzes vehicle power requirements and battery state-of-health. Based on thus analysis, we can propose an adaptive driving and battery control system. In addition to the conventional adaptive (autonomous) driving system that focuses only on safety distance, nearby objects and driving fluency, we can also take into account the battery efficiency and degradation. Furthermore, during autonomous driving, power requirement no longer depends on a driver's driving pattern. This independence of the human factor allows for a more predictable power requirement for autonomous driving, potentially leading to more sophisticated and effective energy component power distribution.

BIBLIOGRAPHY

BIBLIOGRAPHY

[1] Ampacity. http://en.wikipedia.org/wiki/Ampacity.

[2] Digikey. http://www.digikey.com/.

[3] Dynamometer drive schedules.

[4] Carsim simulator, 2012. http://www.carsim.com/products/carsim/index.php.

[5] China publishes plan to boost fuel-efficient and new energy vehicles and domestic auto industry, 2012. http://www.greencarcongress.com/2012/07/china-20120709.html.

[6] Google Map API, 2012. https://developers.google.com/maps/.

[7] Introduction of NGSIM, 2012. http://ngsim-community.org/.

[8] International Energy Agency. Global ev outlook 2013 - understanding the electric vehicle landscape to 2020, 2013. http://www.iea.org/publications/globalevoutlook_2013.pdf.

[9] Ryan Ahmed, Javier Gazzarri, Simona Onori, Saeid Habibi, Robyn Jackey, Kevin Rzemien, Jimi Tjong, and Jonathan LeSage. Model-based parameter identification of healthy and aged li-ion batteries for electric vehicle applications. *SAE Int. J. Alt. Power.*, 4:233–247, 04 2015.

[10] Kyoungho Ahn, Hesham Rakha, Antonio Trani, and Michel Van Aerde. Estimating vehicle fuel consumption and emissions based on instantaneous speed and acceleration levels. *Journal of Transportation Engineering*, 128(2):182–190, 2002.

[11] Douglas Adriano Augusto and Helio JC Barbosa. Symbolic regression via genetic programming. In *Neural Networks, 2000. Proceedings. Sixth Brazilian Symposium on*, pages 173–178. IEEE, 2000.

[12] N. Baldock and M.R. MokhtarzadehDehghan. A study of solarpowered, highaltitude unmanned aerial vehicles. *Aircraft Engineering and Aerospace Technology*, 78(3):187–193, 2006.

[13] Todd M. Bandhauer, Srinivas Garimella, and Thomas F. Fuller. A critical review of thermal issues in lithium-ion batteries. *Journal of The Electrochemical Society*, 2011.

[14] M. Bando, K. Hasebe, A. Nakayama, A. Shibata, and Y. Sugiyama. Dynamics model of traffic congestion and numerical simulation. *Physics Review E*, 51:1035–1042, 1995.

[15] R. Baos, F. Manzano-Agugliaro, F.G. Montoya, C. Gil, A. Alcayde, and J. Gmez. Optimization methods applied to renewable and sustainable energy: A review. *Renewable and Sustainable Energy Reviews*, 15(4):1753 – 1766, 2011.

[16] G. Benetti, M. Delfanti, T. Facchinetti, D. Falabretti, and M. Merlo. Real-time modeling and control of electric vehicles charging processes. *IEEE Transactions on Smart Grid*, 6(3):1375–1385, May 2015.

[17] Luca Benini, Alberto Macii, Enrico Macii, Massimo Poncino, and Riccardo Scarsi. Scheduling battery usage in mobile systems. *IEEE Transactions on VLSI systems*, 11(6):1136–1143, 2003.

[18] D. Bernardi, E. Pawlikowski, and J. Newman. A general energy balance for battery systems. *Journal of the electrochemical society*, 132:5–12, 1985.

[19] Vandy Berten, Pierre Courbin, and Joel Goossens. Gang fixed priority scheduling of periodic moldable real-time tasks. In *Proceedings of the Junior Researcher Workshop Session of the 19th International Conference on Real-Time and Network Systems*, 2011.

[20] Marko Bertogna and Michele Cirinei. Response-time analysis for globally scheduled symmetric multiprocessor platforms. In *Proceedings of IEEE Real-Time Systems Symposium*, 2007.

[21] C. R. Birkl, E. McTurk, M. R. Roberts, P. G. Bruce, and D. A. Howey. A parametric open circuit voltage model for lithium ion batteries. *Journal of The Electrochemical Society*, 162(12):A2271–A2280, 2015.

[22] Peter D. Blair. Modeling energy and power requirements of electric vehicles. *Energy Conversion*, 18(3):127–134, 1978.

[23] Peter D. Blair. Modeling energy and power requirements of electric vehicles. *Energy Conversion*, 18(3):127 – 134, 1978.

[24] Guowei Cai, Lin Feng, Ben M. Chen, and Tong H. Lee. Systematic design methodology and construction of {UAV} helicopters. *Mechatronics*, 18(10):545 – 558, 2008.

[25] J. Cao and A. Emadi. A new battery/ultracapacitor hybrid energy storage system for electric, hybrid, and plug-in hybrid electric vehicles. *Power Electronics, IEEE Transactions on*, 27(1):122–132, Jan 2012.

[26] Davide Caprino, Marco L. Della Vedova, and Tullio Facchinetti. Peak shaving through real-time scheduling of household appliances. *Energy and Buildings*, 75:133 – 148, 2014.

[27] R. Carter and A. Cruden. Strategies for control of a battery/supercapacitor system in an electric vehicle. In *Power Electronics, Electrical Drives, Automation and Motion, 2008. SPEEDAM 2008. International Symposium on*, pages 727–732, June 2008.

[28] C.C. Chan and K.T. Chau. An overview of power electronics in electric vehicles. *Industrial Electronics, IEEE Transactions on*, 44(1):3–13, Feb 1997.

[29] R. E. Chandler, R. Herman, and E. W. Montroll. Traffic dynamics: studies in car following. *Operations Research*, 6:165–184, 1958.

[30] Min Chen and G. A. Rincon-Mora. Accurate electrical battery model capable of predicting runtime and i-v performance. *IEEE Transactions on Energy Conversion*, 21(2):504–511, June 2006.

[31] Min Chen and G. A. Rincon-Mora. Accurate electrical battery model capable of predicting runtime and i-v performance. *IEEE Transactions on Energy Conversion*, 21(2):504–511, June 2006.

[32] Yufei Chen, Li Song, and J.W. Evans. Modeling studies on battery thermal behaviour, thermal runaway, thermal management, and energy efficiency. In *Energy Conversion Engineering Conference, 1996. IECEC 96., Proceedings of the 31st Intersociety*, volume 2, pages 1465–1470 vol.2, 1996.

[33] Yi-Hsien Chiang, Wu-Yang Sean, and Jia-Cheng Ke. Online estimation of internal resistance and open-circuit voltage of lithium-ion batteries in electric vehicles. *Journal of Power Sources*, 196(8):3921 – 3932, 2011.

[34] Soo Seok Choi and Hong S Lim. Factors that affect cycle-life and possible degradation mechanisms of a li-ion cell based on licoo2. *Journal of Power Sources*, 111(1):130 – 136, 2002.

[35] Ford Motor Company. Ford uses innovative liquid-cooled battery system to help focus electric owners maximize range, 2013. http://media.ford.com/article_display.cfm?article_id=33185.

[36] Steve Corrigan. Introduction to the controller area network (can).

[37] Walter J. Culver. High-value energy storage for the grid: A multi-dimensional look. *The Electricity Journal*, 23(10):59–71, 2010.

[38] Matthew Daigle and Chetan S. Kulkarni. End-of-discharge and end-of-life prediction in lithium-ion batteries with electrochemistry-based aging models. *AIAA Infotech*, 2016.

[39] M Dalal, J Ma, and D He. Lithium-ion battery life prognostic health management system using particle filtering framework. *Proceedings of the Institution of Mechanical Engineers, Part O: Journal of Risk and Reliability*, 225(1):81–90, 2011.

[40] Marc Doyle and John Newman. Dualfoil5. http://www.cchem.berkeley.edu/jsngrp/fortran.html.

[41] Matthieu Dubarry, Cyril Truchot, and Bor Yann Liaw. Synthesize battery degradation modes via a diagnostic and prognostic model. *Journal of Power Sources*, 219:204 – 216, 2012.

[42] U.S. EIA. Annual energy outlook 2012 with projections to 2035. Technical report, U.S. Energy Information Administration, 2012.

[43] Electropaedia. Battery life (and death). www.mpoweruk.com/life.htm.

[44] O. Erdinc and M. Uzunoglu. Optimum design of hybrid renewable energy systems: Overview of different approaches. *Renewable and Sustainable Energy Reviews*, 16(3):1412 – 1425, 2012.

[45] O. Erdinc, B. Vural, and M. Uzunoglu. A dynamic lithium-ion battery model considering the effects of temperature and capacity fading. In *Clean Electrical Power, 2009 International Conference on*, pages 383–386, 2009.

[46] T. Facchinetti and M. L. Della Vedova. Real-time modeling for direct load control in cyber-physical power systems. *IEEE Transactions on Industrial Informatics*, 7(4):689–698, Nov 2011.

[47] Eugenio Faggioli, Piergeorgio Rena, Veronique Danel, X Andrieu, Ronald Mallant, and Hans Kahlen. Supercapacitors for the energy management of electric vehicles. *Journal of Power Sources*, 84(2):261 – 269, 1999.

[48] Jason Flinn and M. Satyanarayanan. Managing battery lifetime with energy-aware adaptation. *ACM Transactions on Computer Systems*, 22(2):137–179, 2004.

[49] Hongwei Gao, Yimin Gao, and Mehrdad Ehsani. Design issues of the switched reluctance motor drive for propulsion and regenerative braking in ev and hev. SAE International, 08 2001.

[50] Hongwei Gao, Yimin Gao, and Mehrdad Ehsani. Design issues of the switched reluctance motor drive for propulsion and regenerative braking in ev and hev. SAE International, 08 2001.

[51] Peng Gao, Cuifen Zhang, and Guangwu Wen. Equivalent circuit model analysis on electrochemical impedance spectroscopy of lithium metal batteries. *Journal of Power Sources*, 294(Supplement C):67 – 74, 2015.

[52] Yimin Gao, Liping Chen, and Mehrdad Ehsani. Investigation of the effectiveness of regenerative braking for ev and hev. SAE International, 08 1999.

[53] Yimin Gao and Mehrdad Ehsani. Electronic braking system of ev and hev—integration of regenerative braking, automatic braking force control and abs. SAE International, 08 2001.

[54] Joel Goossens and Vandy Berten. Gang FTP scheduling of periodic and parallel rigid real-time tasks. In *Proceedings of the 18th International Conference on Real-Time Networks and Systems*, 2010.

[55] Liang He, Lipeng Gu, Linghe Kong, Yu Gu, Cong Liu, and Tian He. Exploring adaptive reconfiguration to optimize energy efficiency in large battery systems. In *Proceedings of the 34th IEEE Real-Time Systems Symposium*, 2013.

[56] Liang He, Yu Gu, Cong Liu, Ting Zhu, and Kang G. Shin. SHARE: SoH-aware reconfiguration to enhance deliverable capacity of large-scale battery packs. In *ICCPS'15*, 2015.

[57] Liang He, Eugene Kim, Kang G. Shin, Guozhu Meng, and Tian He. Battery state-of-health estimation for mobile devices. In *The ACM/IEEE 8th International Conference on Cyber-Physical Systems*, 2017.

[58] Mark Z. Jacobson and Mark A. Delucchi. Providing all global energy with wind, water, and solar power, part i: Technologies, energy resources, quantities and areas of infrastructure, and materials. *Energy Policy*, 39(3):1154 – 1169, 2011.

[59] M. Jongerden, B. Haverkort, H. Bohnenkamp, and J. Katoen. Maximizing system lifetime by battery scheduling. In *Dependable Systems Networks, 2009. IEEE/IFIP International Conference on*, pages 63–72, 2009.

[60] Rudi Kaiser. Optimized battery-management system to improve storage lifetime in renewable energy systems. *Journal of Power Sources*, 168(1):58 – 65, 2007.

[61] Shinpei Kato and Yutaka Ishikawa. Gang EDF scheduling of parallel task systems. In *Proceedings of IEEE Real-Time Systems Symposium*, pages 459–468, 2009.

[62] A. Khaligh and Zhihao Li. Battery, ultracapacitor, fuel cell, and hybrid energy storage systems for electric, hybrid electric, fuel cell, and plug-in hybrid electric vehicles: State of the art. *Vehicular Technology, IEEE Transactions on*, 59(6):2806–2814, July 2010.

[63] H.A. Kiehne. *Battery Technology Handbook*. CRC Press, second edition, 2003.

[64] E. Kim, J. Lee, and K. G. Shin. Modeling and real-time scheduling of large-scale batteries for maximizing performance. In *Real-Time Systems Symposium, 2015 IEEE*, pages 33–42, Dec 2015.

[65] E. Kim, K.G. Shin, and Jinkyu Lee. Real-time discharge/charge rate management for hybrid energy storage in electric vehicles. In *Real-Time Systems Symposium (RTSS), 2014 IEEE*, pages 228–237, Dec 2014.

[66] Eugene Kim. Supplement: Modeling and real-time scheduling of large-scale batteries for maximizing performance, 2015. https://kabru.eecs.umich.edu/?page_id=4.

[67] Eugene Kim, Jinkyu Lee, Liang He, Youngmoon Lee, and Kang G. Shin. Supplement: Offline guarantee and online management of power demand and supply in cyber-physical systems, 2016.

[68] Eugene Kim, Jinkyu Lee, and Kang G. Shin. Real-time prediction of battery power requirements for electric vehicles. In *ACM/IEEE 4th International Conference on Cyber-Physical Systems*, Philadelphia, PA, Apr 2013.

[69] Eugene Kim, Jinkyu Lee, and Kang G. Shin. Real-time battery thermal management for electric vehicles. In *ACM/IEEE 5th International Conference on Cyber-Physical Systems*, Berlin, Germany, Apr 2014.

[70] Gi-Heon Kim and A.A. Pesaran. Battery thermal management system design modeling. Yokohama, Japan, Oct 2006.

[71] Hahnsang Kim and Kang G. Shin. On dynamic reconfiguration of a large-scale battery system. In *Proceedings of the 15th IEEE Real-Time and Embedded Technology and Applications Symposium (RTAS)*, pages 87–96, 2009.

[72] Hahnsang Kim and Kang G. Shin. Scheduling of battery charge, discharge, and rest. In *Proceedings of the 30th IEEE Real-Time Systems Symposium (RTSS)*, pages 13–22, 2009.

[73] Hahnsang Kim and Kang G. Shin. Dependable, efficient, scalable architecture for management of large-scale batteries. In *Proceedings of the 1st ACM/IEEE International Conference on Cyber-Physical Systems (ICCPS)*, pages 178–187, 2010.

[74] Younghyun Kim, Sangyoung Park, Yanzhi Wang, Qing Xie, Naehyuck Chang, M. Poncino, and M. Pedram. Balanced reconfiguration of storage banks in a hybrid electrical energy storage system. In *Computer-Aided Design (ICCAD), 2011 IEEE/ACM International Conference on*, pages 624–631, Nov 2011.

[75] John R Koza. *Genetic programming: on the programming of computers by means of natural selection*, volume 1. MIT press, 1992.

[76] Seongjun Lee, Jonghoon Kim, Jaemoon Lee, and B.H. Cho. State-of-charge and capacity estimation of lithium-ion battery using a new open-circuit voltage versus state-of-charge. *Journal of Power Sources*, 185(2):1367 – 1373, 2008.

[77] Seongjun Lee, Jonghoon Kim, Jaemoon Lee, and B.H. Cho. State-of-charge and capacity estimation of lithium-ion battery using a new open-circuit voltage versus state-of-charge. *Journal of Power Sources*, 185(2):1367 – 1373, 2008.

[78] Tae-Kyung Lee, B. Adornato, and Z.S. Filipi. Synthesis of real-world driving cycles and their use for estimating phev energy consumption and charging opportunities: Case study for midwest/u.s. *Vehicular Technology, IEEE Transactions on*, 60(9):4153–4163, 2011.

[79] Steven Letendre, Richard Perez, and Christy Herig. Battery-powered, electric-drive vehicles providing buffer storage for pv capacity value. In *proceedings of the solar conference*, pages 105–110, 2002.

[80] Kun Li, Jie Wu, Yifei Jiang, Zyad Hassan, Qin Lv, Li Shang, and Dragan Maksimovic. Large-scale battery system modeling and analysis for emerging electric-drive vehicles. In *Proceedings of the 16th ACM/IEEE International Symposium on Low Power Electronics and Design (ISLPED)*, pages 277–282, 2010.

[81] Yongfu Li and Dihua Sun. Microscopic car-following model for the traffic flow: the state of the art. *Journal of Control Theory and Applications*, 10:133–143, 2012.

[82] Yonghua Li, R.D. Anderson, Jing Song, A.M. Phillips, and Xu Wang. A nonlinear adaptive observer approach for state of charge estimation of lithium-ion batteries. In *Proceedings of American Control Conference, 2011*, pages 370–375, 2011.

[83] Z. Li, P. C. Huang, A. K. Mok, T. Nghiem, M. Behl, G. Pappas, and R. Mangharam. On the feasibility of linear discrete-time systems of the green scheduling problem. In *Real-Time Systems Symposium (RTSS), 2011 IEEE 32nd*, pages 295–304, Nov 2011.

[84] Xianke Lin, Jonghyun Park, Lin Liu, Yoonkoo Lee, A. M. Sastry, and Wei Lu. A comprehensive capacity fade model and analysis for li-ion batteries. *Journal of The Electrochemical Society*, 160(10):A1701–A1710, 2013.

[85] D. Linden and T.B. Reddy. *Handbook of batteries*. McGraw-Hill, third edition, 2002.

[86] C.L. Liu and James Layland. Scheduling algorithms for multi-programming in a hard-real-time environment. *Journal of the ACM*, 20(1):46–61, 1973.

[87] Nima Lotfi, Poria Fajri, Samuel Novosad, Jack Savage, Robert G. Landers, and Mehdi Ferdowsi. Development of an experimental testbed for research in lithium-ion battery management systems. *Energies*, 6(10):5231–5258, 2013.

[88] Languang Lu, Xuebing Han, Jianqiu Li, Jianfeng Hua, and Minggao Ouyang. A review on the key issues for lithium-ion battery management in electric vehicles. *Journal of Power Sources*, 226:272 – 288, 2013.

[89] Languang Lu, Xuebing Han, Jianqiu Li, Jianfeng Hua, and Minggao Ouyang. A review on the key issues for lithium-ion battery management in electric vehicles. *Journal of Power Sources*, 226:272 – 288, 2013.

[90] Chen Lv, Junzhi Zhang, Yutong Li, and Ye Yuan. Regenerative braking control algorithm for an electrified vehicle equipped with a by-wire brake system. SAE International, 04 2014.

[91] Liqiang Mai, Mengyu Yan, and Yunlong Zhao. Track batteries degrading in real-time. *Nature*, 546(Supplement C):469 – 470, 2017.

[92] Masatoshi Majima, Satoshi Ujiie, Eriko Yagasaki, Keiji Koyama, and Shinji Inazawa. Development of long life lithium ion battery for power storage. *Journal of Power Sources*, 101(1):53 – 59, 2001.

[93] MathWorks. Matlab. http://www.mathworks.com/.

[94] Ahmad A. Pesaran Matthew Zolot and Mark Mihalic. Thermal evaluation of toyota prius battery pack. In *SAE Technical Paper 2002-01-1962*, 2002.

[95] M. McDonald, J. Wu, and M. Brackstone. Development of a fuzzy logic based microscopic motorway simulation model. In *IEEE Conference on Intelligent Transportation System*, pages 82–87, 1997.

[96] Merriam-Webster. http://www.merriam-webster.com/.

[97] A. Millner. Modeling lithium ion battery degradation in electric vehicles. In *Innovative Technologies for an Efficient and Reliable Electricity Supply (CITRES), 2010 IEEE Conference on*, pages 349–356, Sept 2010.

[98] Stephen W. Moore and Peter J. Schneider. A review of cell equalization methods for lithium ion and lithium polymer battery systems. In *SAE Technical Paper*. SAE International, 03 2001.

[99] General Motors. The chevrolet volt cooling/heating systems explained, 2009. http://gmvolt.com/2010/12/09/the-chevrolet-volt-coolingheating-systems-explained/.

[100] Kai Nagel and Michael Schreckenberg. A cellular automaton model for freeway traffic. *J. Phys. I France*, (12):2221–2229, 1992.

[101] Neware. Battery tester. http://www.newarebattery.com/.

[102] Gang Ning, Bala Haran, and Branko N. Popov. Capacity fade study of lithium-ion batteries cycled at high discharge rates. *Journal of Power Sources*, 117(1 - 2):160 – 169, 2003.

[103] Gang Ning and Branko N. Popov. Cycle life modeling of lithium-ion batteries. *Journal of The Electrochemical Society*, 151(10):A1584–A1591, 2004.

[104] Gang Ning, Ralph E. White, and Branko N. Popov. A generalized cycle life model of rechargeable li-ion batteries. *Electrochimica Acta*, 51(10):2012 – 2022, 2006.

[105] Dominic A. Notter, Marcel Gauch, Rolf Widmer, Patrick Wger, Anna Stamp, Rainer Zah, and Hans-Jrg Althaus. Contribution of li-ion batteries to the environmental impact of electric vehicles. *Environmental Science & Technology*, 44(17):6550–6556, 2010. PMID: 20695466.

[106] NREL. Advisor 2002. http://www.nrel.gov/.

[107] U.S. Department of Energy. Alternative fueling station counts by state, 2017. http://www.afdc.energy.gov/fuels/stations_counts.html.

[108] U.S. Department of Energy. Electric vehicle charging station locations, 2017. https://www.afdc.energy.gov/fuels/electricity_locations.html.

[109] M. Ortuzar, J. Moreno, and J. Dixon. Ultracapacitor-based auxiliary energy system for an electric vehicle: Implementation and evaluation. *Industrial Electronics, IEEE Transactions on*, 54(4):2147–2156, Aug 2007.

[110] C. Park and A. Jaura. Dynamic thermal model of li-ion battery for predictive behavior in hybrid and fuel cell vehicles. In *SAE Technical Paper 2003-01-2286*, 2003.

[111] Sangyoung Park, Younghyun Kim, and Naehyuck Chang. Hybrid energy storage systems and battery management for electric vehicles. In *Design Automation Conference (DAC), 2013 50th ACM / EDAC / IEEE*, pages 1–6, May 2013.

[112] Jzef Paska, Piotr Biczel, and Mariusz Kos. Hybrid power systems an effective way of utilising primary energy sources. *Renewable Energy*, 34(11):2414 – 2421, 2009.

[113] E. Pastor, J. Lopez, and P. Royo. Uav payload and mission control hardware/software architecture. *IEEE Aerospace and Electronic Systems Magazine*, 22(6):3–8, June 2007.

[114] S. Pay and Y. Baghzouz. Effectiveness of battery-supercapacitor combination in electric vehicles. In *Power Tech Conference Proceedings, 2003 IEEE Bologna*, volume 3, pages 6 pp. Vol.3–, June 2003.

[115] A.A. Pesaran. Battery thermal management in evs and hevs: Issues and solutions. Las vegas, Nevada, Feb 2001.

[116] A.A. Pesaran, S. Burch, and M. Keyser. An approach for designing thermal management systems for electric and hybrid vehicle battery packs. London, UK, May 1999.

[117] Amhad Pesaran. Ultracapacitor applications and evaluation for hybrid electric vehicles, 2009. http://www.nrel.gov/vehiclesandfuels/energystorage/pdfs/45596.pdf.

[118] Gregory L. Plett. Extended kalman filtering for battery management systems of lipb-based hev battery packs: Part 3. state and parameter estimation. *Journal of Power Sources*, 134(2):277 – 292, 2004.

[119] K. Post, J.H. Kent, J. Tomlin, and N. Carruthers. Fuel consumption and emission modelling by power demand and a comparison with other models. *Transportation Research Part A: General*, 18(3):191–213, 1984.

[120] Daler Rakhmatov and Sarma Vrudhula. Energy management for battery-powered embedded systems. *ACM Transactions on Embedded Computing Systems*, 2:277–324, 2003.

[121] P. Ramadass, Bala Haran, Ralph White, and Branko N. Popov. Mathematical modeling of the capacity fade of li-ion cells. *Journal of Power Sources*, 123(2):230 – 240, 2003.

[122] P. Rodatz, G. Paganelli, A. Sciarretta, and L. Guzzella. Optimal power management of an experimental fuel cell/supercapacitor-powered hybrid vehicle. *Control Engineering Practice*, 13(1):41 – 53, 2005.

[123] Rotronics. Vehicle loads. Technical report, Rotronics, 2009.

[124] B. Saha and K. Goebel. Uncertainty management for diagnostics and prognostics of batteries using bayesian techniques. In *Aerospace Conference, 2008 IEEE*, pages 1–8, March 2008.

[125] Bhaskar Saha and Kai Goebel. Modeling li-ion battery capacity depletion in a particle filtering framework. In *Conference of the Prognostics and Health Management Society*, 2009.

[126] Alvin J Salkind, Craig Fennie, Pritpal Singh, Terrill Atwater, and David E Reisner. Determination of state-of-charge and state-of-health of batteries by fuzzy logic methodology. *Journal of Power Sources*, 80(12):293 – 300, 1999.

[127] Michael Schmidt and Hod Lipson. Distilling free-form natural laws from experimental data. *Science*, 324(5923):81–85, 2009.

[128] Dominic P Searson, David E Leahy, and Mark J Willis. Gptips: an open source genetic programming toolbox for multigene symbolic regression. In *Proceedings of the International multiconference of engineers and computer scientists*, volume 1, pages 77–80. Citeseer, 2010.

[129] J. K. Shiau, D. M. Ma, P. Y. Yang, G. F. Wang, and J. H. Gong. Design of a solar power management system for an experimental uav. *IEEE Transactions on Aerospace and Electronic Systems*, 45(4):1350–1360, Oct 2009.

[130] R. Smith, S. Shahidinejad, D. Blair, and E.L. Bibeau. Characterization of urban commuter driving profiles to optimize battery size in light-duty plug-in electric vehicles. *Transportation Research Part D: Transport and Environment*, 16(3):218 – 224, 2011.

[131] R. Spotnitz. Simulation of capacity fade in lithium-ion batteries. *Journal of Power Sources*, 113(1):72 – 80, 2003.

[132] Yu-Hua Sun, Hurng-Liahng Jou, and Jinn-Chang Wu. Diagnosis method for the degradation of lead-acid battery. In *Industrial Electronics, 2009. ISIE 2009. IEEE International Symposium on*, pages 1397–1402, July 2009.

[133] Yu-Hua Sun, Hurng-Liahng Jou, Jinn-Chang Wu, and Kuen-Der Wu. Auxiliary health diagnosis method for lead-acid battery. *Applied Energy*, 87(12):3691 – 3698, 2010.

[134] Yuxin Tang, Yanyan Zhang, Wenlong Li, Bing Ma, and Xiaodong Chen. Rational material design for ultrafast rechargeable lithium-ion batteries. *Chem. Soc. Rev.*, 44:5926–5940, 2015.

[135] Tenergy. 3.7v 2200mah li-ion 18650 flat top rechargeable battery with pcb.

[136] E.V. Thomas, I. Bloom, J.P. Christophersen, and V.S. Battaglia. Statistical methodology for predicting the life of lithium-ion cells via accelerated degradation testing. *Journal of Power Sources*, 184(1):312 – 317, 2008.

[137] E.V. Thomas, I. Bloom, J.P. Christophersen, and V.S. Battaglia. Rate-based degradation modeling of lithium-ion cells. *Journal of Power Sources*, 206(0):378 – 382, 2012.

[138] Phatiphat Thounthong, Viboon Chunkag, Panarit Sethakul, Suwat Sikkabut, Serge Pierfederici, and Bernard Davat. Energy management of fuel cell/solar cell/supercapacitor hybrid power source. *Journal of Power Sources*, 196(1):313 – 324, 2011.

[139] Uwe Trltzsch, Olfa Kanoun, and Hans-Rolf Trnkler. Characterizing aging effects of lithium ion batteries by impedance spectroscopy. *Electrochimica Acta*, 51(8):1664 – 1672, 2006. Electrochemical Impedance Spectroscopy.

[140] Kotub Uddin, Surak Perera, W. Dhammika Widanage, Limhi Somerville, and James Marco. Characterising lithium-ion battery degradation through the identification and tracking of electrochemical battery model parameters. *Batteries*, 2(2), 2016.

[141] Dong Wang, Qiang Miao, and Michael Pecht. Prognostics of lithium-ion batteries based on relevance vectors and a conditional three-parameter capacity degradation model. *Journal of Power Sources*, 239:253 – 264, 2013.

[142] Eric Wood, Marcus Alexander, and Thomas H. Bradley. Investigation of battery end-of-life conditions for plug-in hybrid electric vehicles. *Journal of Power Sources*, 196(11):5147 – 5154, 2011.

[143] B. Xu, A. Oudalov, A. Ulbig, G. Andersson, and D. Kirschen. Modeling of lithium-ion battery degradation for cell life assessment. *IEEE Transactions on Smart Grid*, PP(99):1–1, 2016.

[144] Hai Yu, Finn Tseng, and R. McGee. Driving pattern identification for ev range estimation. In *Electric Vehicle Conference, 2012 IEEE International*, pages 1–7, 2012.

[145] D Zhang, B.S Haran, A Durairajan, R.E White, Y Podrazhansky, and B.N Popov. Studies on capacity fade of lithium-ion batteries. *Journal of Power Sources*, 91(2):122 – 129, 2000.

[146] Jingliang Zhang and Jay Lee. A review on prognostics and health monitoring of li-ion battery. *Journal of Power Sources*, 196(15):6007 – 6014, 2011.

[147] Jiucai Zhang, Song Ci, H. Sharif, and M. Alahmad. Modeling discharge behavior of multicell battery. *Energy Conversion, IEEE Transactions on*, 25(4):1133–1141, 2010.

[148] Wei Zhou, Chengzhi Lou, Zhongshi Li, Lin Lu, and Hongxing Yang. Current status of research on optimum sizing of stand-alone hybrid solarwind power generation systems. *Applied Energy*, 87(2):380 – 389, 2010.